Spring 5-2018

New Geochemical and Isotopic Approaches to Shallow Crust Landform Evolution

David Decker

APPROVAL PAGE

David D. Decker
Candidate

Earth & Planetary Sciences
Department

This dissertation is approved, and it is acceptable in quality and form for publication:

Approved by the dissertation committee:

Dr. Yemane Asmerom, *chairperson*

Dr. Victor Polyak

Dr. Karl Karlstrom

Dr. Matthew Lachniet

New Geochemical and Isotopic Approaches to Shallow Crust Landform Evolution

by

David D. Decker

Previous Degrees

Associate of Science, University of Phoenix, 1993

Bachelor of Science, University of Southern Illinois – Carbondale, 1994

Master of Science, Naval Postgraduate School, 2003

Dissertation

Submitted in Partial Fulfillment of the Requirements for the Degree of

Doctor of Philosophy

Earth and Planetary Sciences

University of New Mexico

Albuquerque, New Mexico

May, 2018

DEDICATION

To my wife Johanna without whose support, encouragement, patience and understanding I would never have been able to take the time to work through the intricacies of this dissertation. To my mom, Kathi Sands, and dad, Bob Sands, who introduced me to the wonders of nature and taught me to always ask questions. To my Grandma, Trella Romine, who taught me to be persistent, question everything and that just because you know the name of something doesn't mean you know anything about it! And finally, to my aunt Mary "Auntie" Hecker, who encouraged my pursuit of geology and uncle, David Haldeman, who inspired me in all of my scientific pursuits. Thank you all for encouraging me, supporting me and showing me the way!

ACKNOWLEDGEMENTS

Funding for this research has been provided by the National Speleological Foundation (NSF), Cave Research Foundation (CRF), National Speleological Society (NSS), Cleveland Grotto, University of New Mexico Alumni Association, National Speleological Foundation (NSF), and the New Mexico Geological Society (NMGS). I'd also like to thank Carlsbad Caverns National Park (Dale Pate, Stan Allison and Shawn Thomas), Guadalupe Mountains National Park (Jonena Hearst), Bureau of Land Management, Carlsbad Field Office (Jim Goodbar and Aaron Stockton) and U.S. Forest Service, Guadalupe District (Jason Walz) for their help and support during my field work, my field assistants, Garrett Jorgensen and Dr. Michael Queen. Dr. Jane Selverstone provided access to and assistance with the fluid inclusion assemblage analysis, and finally, my Advisors, Dr. Yemane Asmerom and Dr. Victor Polyak, for all the help and guidance along this rocky road.

New Geochemical and Isotopic Approaches to Shallow Crust Landform Evolution

by

David D. Decker

Previous Degrees

A.S., Technology Instruction, University of Phoenix, 1993

B.S., Workforce Education and Development, University of Southern Illinois – Carbondale, 1994

M.S., Physics, Naval Postgraduate School, 2003

ABSTRACT

Many researchers have studied the Guadalupe Mountains in detail and starting with King (1948), many of them have speculated about the timing of the uplift of the Guadalupe block. There are several competing hypotheses including Laramide, Basin and Range, and Rio Grande Rifting uplift scenarios. Using uranium-lead (U-Pb) dating of scalenohedral spar found in small vug caves throughout the study area, I have dated the episodes of spar formation to two major phases, 36 to 33 Ma and 30 to 27 Ma. These two episodes of spar formation are in good agreement with the time frame of the ignimbrite flare up during the formation of the Basin and Range. I have also dated several older phases, all the way back to ~180 Ma, which all correspond to nearby (<100 Km)

known volcanic activity and provide a good argument for the hydrothermal genesis of the spar. By determining the depth of formation of the spar through a new speleogenetic model (supercritical CO_2), age dating the cave spar through U-Pb dating techniques, and finding the temperature of formation of the spar through a newly calibrated $\delta^{88}Sr$ thermometer and fluid inclusion assemblage analysis, I have been able to develop a geothermochronometer in a region that has not had the typical apatite fission track and apatite thorium-helium methods available. This geothermochronometer works because I have been able to constrain the depth and temperature of formation of the spar to a zone 500 ± 250 meters beneath the water table. If major uplift had occurred prior to spar formation, then the water table would have been lowered, taking the cave forming strata of the Capitan Reef out of the spar horizon and no further spar generations would have formed, limiting any uplift to minor local episodes or very broad epeirogenic uplift. Using this new method, along with U-Pb dating of calcite vein spar from the Border Fault Zone (BFZ), I have constrained the timing of the uplift of the Guadalupe block to between 27 and 16 million years ago. This new method has applicability in regions that typically don't have the minerals associated with the apatite methods of geothermochronometry.

TABLE OF CONTENTS

LIST OF FIGURES

LIST OF TABLES

PREFACE

Chapter 2 introduces the new speleogenetic model and the concept of supercritical carbon dioxide dissolution and precipitation of the spar at the "spar horizon". I develop the argument that cave spar, and the vugs in which they form, are two parts to a single process that occurs at 500 ± 250 meters beneath a regional water table, the "spar horizon". I also report the ages of six spar samples, five preliminary $\delta^{88}Sr$ values and eight $^{87}Sr/^{86}Sr$ values for the spar (the majority of this work is in chapter 3). This is a new speleogenetic model and is introduced for the first time in this paper published in "Caves and Karst Across Time, GSA Special Paper 516 (2016). I am the primary author and did all of the field collection and research along with all of the lab work and writing. Dr. Polyak provided assistance in learning the procedures required for the lab work and proofed the manuscript. Dr. Asmerom also provided lab time and supplies, clean reagents, isotope standards, and academic guidance and oversight.

Chapter 3 discusses the temperature of formation of the spar based on the temperature of homogenization of fluid inclusion assemblages and corresponding $\delta^{88}Sr$ values, and uses that information to calibrate a new $\delta^{88}Sr$-calcite thermometer. This new thermometer is based on the research of Fietzke and Eisenhauer (2006b). I show here that the spar is of hydrothermal origin (which is critical to later interpretation) and that $\delta^{88}Sr$ values in cave spar are temperature, rather than rate of growth, dependent. Here I report the $\delta^{88}Sr$ of 15 spar samples, 16 mammillary and dripstone calcites, and two basalt standards. Additionally I

report temperature of homogenization values of fluid inclusions from 17 spar samples. Chapter 3 is still currently under review and will be submitted to Geochimica et Cosmochimica Acta. I am the primary author and did all of the field collection and research along with all of the lab work and writing. Dr. Polyak provided assistance in learning the procedures required for the lab work and proofed the manuscript. Dr. Asmerom also provided assistance in writing and proofing the chapter, lab time and supplies, critical isotope standards and solutions, and academic guidance and oversight.

Chapter 4 is the Landscape Evolution chapter that introduces the age of the spar using U-Pb isotope dating techniques, and then compares the age of the spar to the timing of regional magmatic activity. The ages of 16 additional spar samples are reported in this chapter in addition to the ages reported in chapter 2. I continue to develop the spar thermometer as a proxy for landform evolution based on the previous chapters. Chapter 4 was published in Tectonics, volume 36 (2017). I am the primary author and did all of the field collection and research along with all of the lab work and writing. Dr. Polyak provided assistance in with the procedures required for the lab work and proofed the manuscript. Dr. Asmerom provided lab time and supplies, isotope standards, and solutions, academic guidance and oversight, and assistance in writing the chapter.

Chapter 5 develops the hydrothermal spring concept and brings together the ideas of the previous three chapters to discuss the possibilities of locating ore deposits in the Guadalupe Mountains. This chapter will be submitted to the International Journal of Speleology for publication in May, 2018.

CHAPTER 1 - Introduction

Spar caves can be found throughout the Guadalupe Mountains of southeastern New Mexico and west Texas (Hill, 1987), (Figure 1). These spar caves are essentially large dogtooth spar-lined geodes truncated by sulfuric acid speleogenesis in many cases, and exposed at the surface by erosion and stream down-cutting along entrenched meanders in other cases.

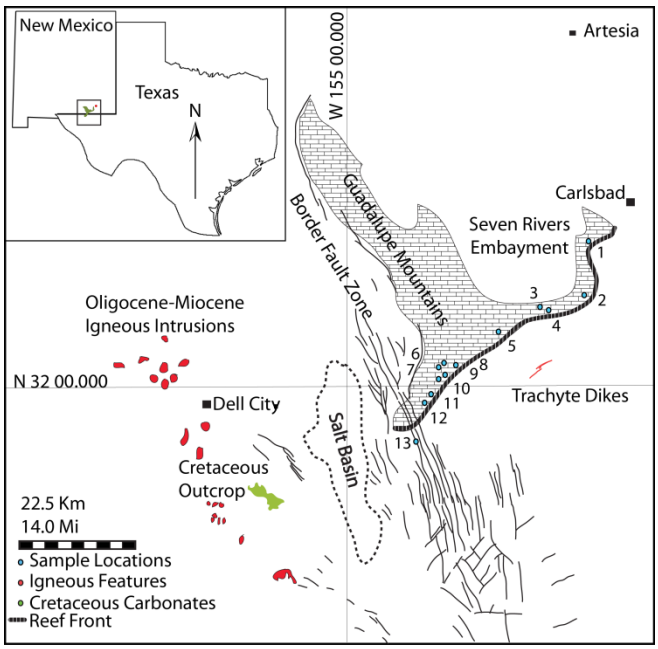

Figure 1: Study area, Guadalupe Mountains of southeastern New Mexico and west Texas. This figure shows known fault zones, igneous intrusions and selected spar collection locations (numbered, Figure 18). The geologic features on this map are compilation from different sources including the Geologic Atlas of Texas - Van Horn El Paso Sheet (Barnes, 1983) and Google Earth.

These caves are less than one to several tens of meters in diameter and are partially to entirely encrusted with euhedral scalenohedral (dogtooth) calcite spar (Figure 2A). This dissertation answers the following questions: When did these spar caves form? What process or processes caused them to be found where they are? Why are they lined with giant crystals of calcite? There is little in the literature on how or when these spar caves formed and what exists is inadequate to explain what is now known to be repeated cycles of spar cave speleogenesis and spar deposition (Chapter 2). Lundberg et al. (2000) published the first U-Pb age of a spar crystal from Big Canyon (90 Ma), Guadalupe Mountains. They

attribute the origin of the spar to tectonic activity and uplift during the Laramide. In this study we used U-Th-Pb and Sr isotope geochemistry to measure the age and interpret the origin of these enigmatic voids.

Geology of the Region

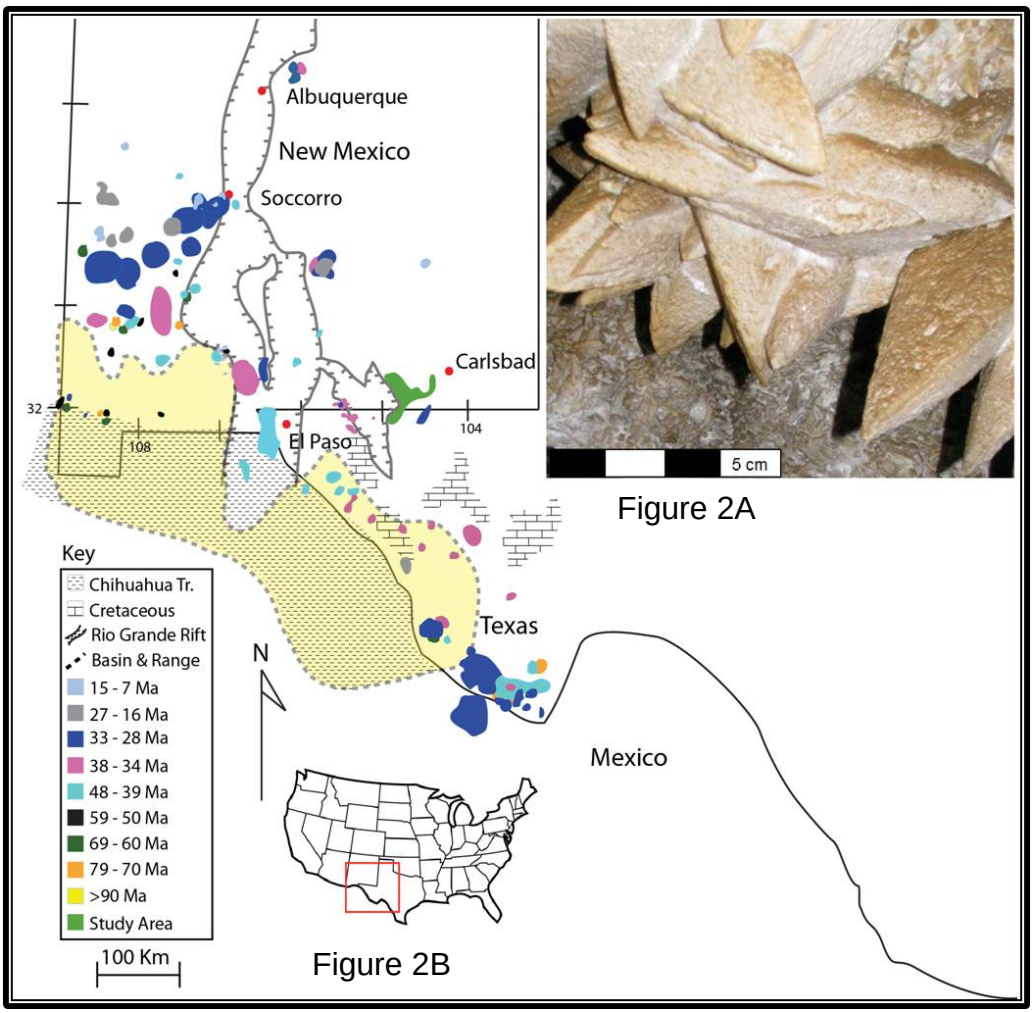

Figure 2: Regional Geology. (A) Representative spar cave from CAVE-005 in Carlsbad Caverns National Park. This Vug is approximately 30 meters in the long axis and the walls, floor and ceiling are entirely covered in euhedral spar up to 30 cm in length. (Photo Credit: Ben Schwarz) (B): Overview of the Guadalupe Mountains of southeastern New Mexico and Trans-Pecos Texas. Here we show the known periods of magmatism in physical relation to our study area. The closest magmatic activity occurred within tens of kilometers of the reef front and quite possibly directly beneath, during both the ignimbrite flare-up and the beginning of the basin and range. We break up the locations and ages of reported igneous activity coincident with periods of spar formation (see key for description). The Cretaceous rocks on the figure show that this entire region was near sea level as late at the Cretaceous. Since then, and up until about 28 Ma, the area was most likely at or just above sea level. References: (Baldridge et al., 1984; Barker et al., 1977; Barnes, 1983; Befus et al., 2008; Breyer et al., 2007; Calzia and Hiss, 1978; Chamberlin et al., 2002; Chapin, 1989; Gilmer et al., 2003; Goff et al., 2011; Gries, 1979; Henry and Price, 1986; Henry et al., 1991; Kelley et al., 2014; Lawton and McMillan, 1999; Lipman et al., 1986; Maynard, 1995; McIntosh et al., 1992; McLemore et al., 1995; Reilinger et al., 1979; Whitmeyer and Karlstrom, 2007; Wilks and Chapin, 1997).

This study's area of interest spans from west Texas to south-eastern New Mexico and includes the Diablo Plateau, the Guadalupe Mountains, the Delaware Basin and the Gypsum Plains (Figure 2B). The region is well known for its petroleum production (Permian Basin), potash deposits, large, well-decorated sulfuric acid type caves and the Waste Isolation Pilot Plant (WIPP), and less well known for the Mississippi Valley Type ore deposits in the Guadalupe Mountains (Hill, 1993). The basement rocks in the region belong to the Texas craton and are mostly granitic. These rocks were emplaced after the Mazatzal orogeny and possibly during the Granite - Rhyolite Province approximately 1.55 to 1.35Ga (Flawn, 1955; Wasserburg et al., 1962; Whitmeyer and Karlstrom, 2007). The Tabosa basin existed in the same location as the Delaware and Midland basins (Hill, 1996) during the late Proterozoic through the Mississippian and was probably formed by continental rifting in the Proterozoic to Cambrian (Hills, 1984). This basin was dissected by the Central Basin Uplift during the late Mississippian Ouachita orogeny. The entire region remained near sea level during this phase and accumulated vast amounts of sediment (Hill, 1996). During the Permian, the area was inundated by the sea forming a restricted basin where the massive Capitan limestones and Artesia Group back reef sediments were deposited followed by the Castile, Salado, Rustler, and Dewey Lake evaporites (Austin, 1978; Hayes and Adams, 1962; Hill, 1987). The area was tectonically quiescent through the remaining Paleozoic and Mesozoic and was not disturbed again until possibly the beginning of the Cenozoic with the onset of the Laramide orogeny (Eaton, 2008). At some point after the Cretaceous, the region was uplifted from

presumably sea level to its current elevation of approximately 2 km. The timing of the rise of the Guadalupe Mountains and the surrounding region is still in dispute with several hypotheses regarding this uplift still in contention, including the Laramide as the main driver (Eaton, 2008) and Rio Grande rifting responsible for ~1000 m of rise (Polyak et al., 1998), and the two events separated by tens of millions of years! The intrusive igneous rocks that are tied to these main structural events and the chemical signatures they've imprinted on secondary mineral formation in the region during these events may help to constrain the uplift history of the region. A third, more likely hypothesis states that the region was uplifted over a long time span by several events including the two mentioned above plus basin and range formation (Karlstrom et al., 2012; Ricketts et al., 2016).

Igneous Activity

Igneous activity in the northwestern Delaware Basin of southeastern New Mexico has been shown little interest by researchers, although activity in Trans-Pecos Texas and nearby southwest New Mexico have volumes of data (Figure 2). The plutonic igneous rocks in the basin, however, bear a great deal of significance when it comes to understanding the genesis of the spar and spar caves in the region, and when added to the research conducted in nearby areas, provides a better picture of the landscape evolution in the Guadalupe Mountains. It most likely has a connection to the speleogenesis that created smaller vug caves lined with giant dogtooth spar crystals that I am studying. Determining when the Yeso Hills and other nearby, unnamed intrusions were emplaced is critical to the

interpretation of the Neogene geology of the Delaware Basin and Guadalupe Mountains and could quite possibly provide definitive evidence to show that the Basin and Range or Rio Grande rifting was active further to the east than originally thought and even constrain the uplift of the Guadalupe Mountains themselves.

Caves of the Region

There are two broad categories of cave formation, epigene speleogenesis and hypogene speleogenesis. Epigene caves are formed from the action of descending water that gets its acidity from surface processes, such as the absorption of carbon dioxide, as the water flows through CO_2 rich soil and then into the bedrock (Klimchouk et al., 2000; Palmer, 2007a; White, 1988). These types of caves exhibit indicative morphology such as dendritic flow patterns, sink holes on the surface, rising streams, and other typical karst features (Klimchouk et al., 2000; Palmer, 2007a; White, 1988). The gypsum caves in the nearby Permian Castile gypsum of the Delaware Basin are epigene caves and are formed as water slightly saturated in carbonic acid from the surface filters into cracks and dissolves the gypsum as it makes its way toward base level (Figure 3).

Hypogene caves on the other hand, gain their acidity from below. For example, CO_2 from magmatic processes that infiltrates an aquifer, or the saturation and mixing of meteoric water that is on the ascending side of its flow path by CO_2 from the decarbonation of limestone and marble, or sulfur dioxide from the biologic action of microbes on petroleum reserves that buoyantly rises and mixes

with the oxygen in an aquifer to form sulfuric acid. Hypogene caves also display diagnostic morphologies such as ascending cupolas, maze-type passageways, and "boneyard", also known as sponge work (Dublyansky, 2000, 2014; Klimchouk, 2007, 2009), a type of speleogen that forms when two or more small, isolated dissolution voids merge (Hill, 1987; Lauritzen and Lundberg, 2000). Hypogene caves are not typically associated with surface features, unlike epigene caves, and usually only intersect the surface when breached by stream down-cutting or surface erosion (Hill, 1996).

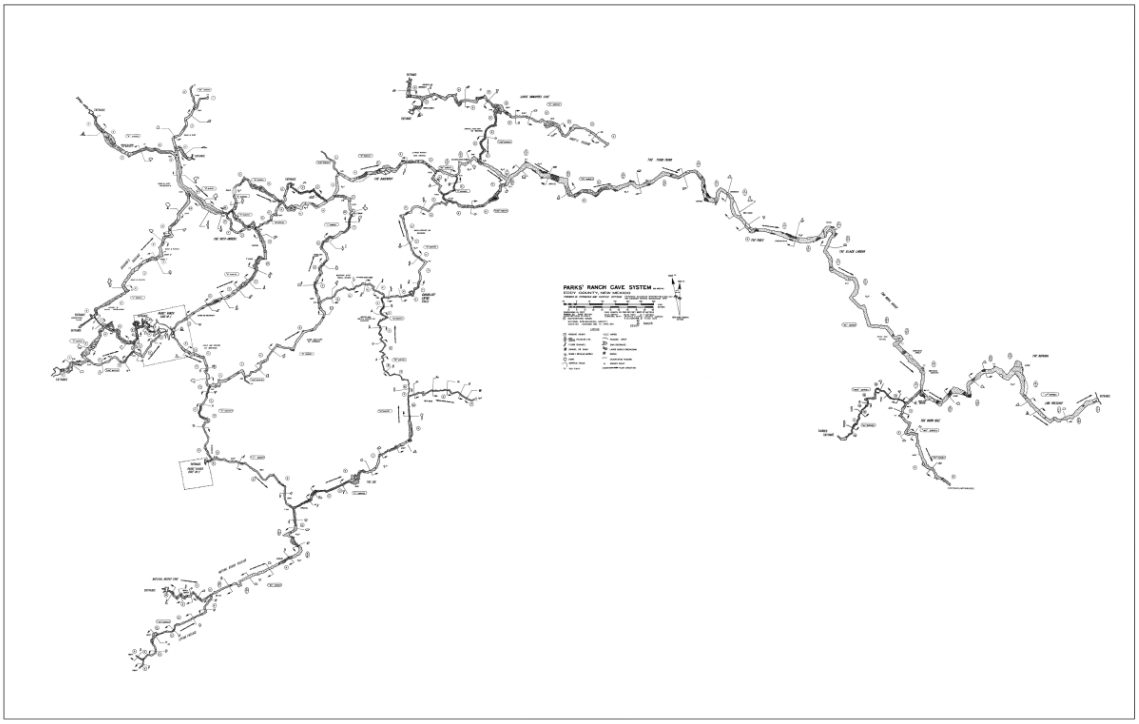

Figure 3: Example of an epigene cave. This is Parks Ranch cave in Eddy County, NM and is an excellent example of a dendritic pattern epigene cave formed in the Castile gypsum (Belski, 1993).

There are two types of hypogene caves in the Guadalupe Mountains, sulfuric acid caves (Hill, 1987; Hill, 1996; Hill, 2000; Jagnow, 1977; Palmer and Palmer, 2000) and carbonic acid caves (Chapter 2; Chapter 4). The sulfuric acid caves within the region are some of the most well-known and studied caves of this type

in the world. Two of the more famous sulfuric acid caves are Carlsbad Cavern and Lechuguilla Cave, both in Carlsbad Caverns National Park (Figure 4). These caves were formed as microbes digested the petroleum reserves in the Delaware Basin forming sulfur dioxide as a waste product of their metabolism. This sulfur dioxide (SO_2) rose along the dip plane through fractures and crevices until it reached the limestone of the Capitan Reef where it mixed with oxygen saturated surface waters to form sulfuric acid (H_2SO_4) (Hill, 1987; Hill, 1996; Jagnow, 1977; Kirkland, 2014; Palmer and Palmer, 2000). Byproducts of the dissolution of limestone by sulfuric acid are still visible in the caves, including, but not limited to, large blocks of gypsum, and a clay called alunite (Polyak, 2000) that is formed right at the water table surface. Alunite is a potassium bearing clay ($KAl_3(SO_4)_2(OH)_6$), which is datable using K-Ar and $^{40}Ar/^{39}Ar$ dating techniques and was used by Polyak et al. (1998) to determine the age of formation of the sulfuric acid caves in the Guadalupe Mountains and the rate of decline of the local water table as the Guadalupe block tilted to its present angle. Because of the work done in the Guadalupe Mountains on hypogene sulfuric acid caves, more and more of these types of caves are being recognized around the world. The sulfuric acid speleogenesis caves are younger than the carbonic acid caves and cross-cut the carbonic acid caves.

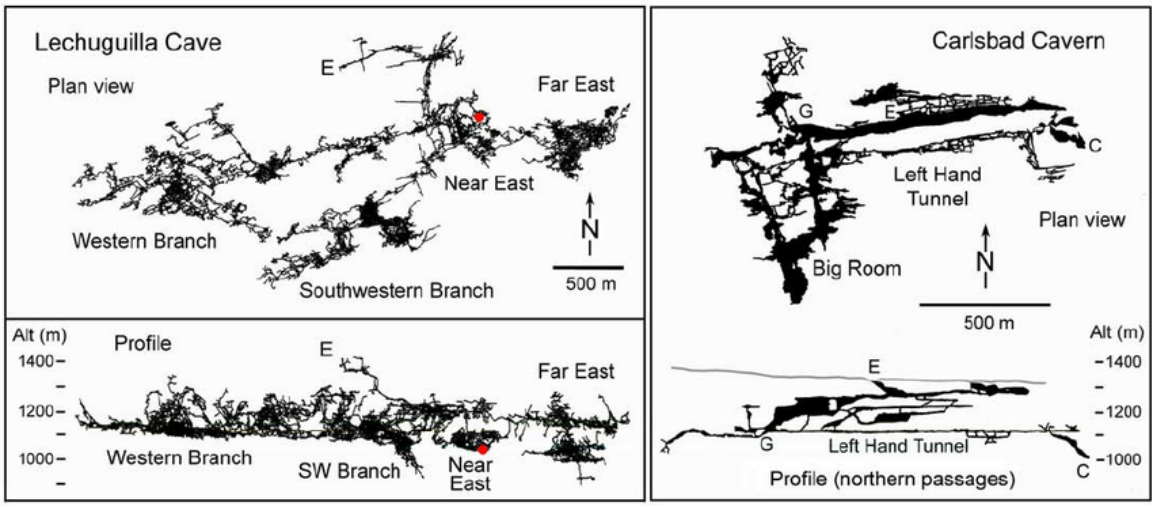

Figure 4: Example of a hypogene cave. These are two well-known caves in the Guadalupe Mountains that exhibit textbook, indeed type locality, hypogene cave morphology. Note the ramiform (mazy) character of the passages as well as the multiple levels (Map from Palmer and Palmer (2012).

The CO_2 caves of the region are much smaller than the sulfuric acid caves, are older, and are cross-cut by the sulfuric acid caves. Many of the CO_2 caves are lined with the scalenohedral spar that is the subject of this study. The carbonic acid caves that are lined with spar are termed "spar caves" by the authors. These caves are described by Hill (1987; 1996; 2000) as stage 2 and 3 (sponge work and thermal karst, respectively) or mesogenetic caves and by Dublyansky (2000) as "thermal" caves. Evidence from this study shows that these spar caves are formed deeper than the sulfuric acid caves, are truncated by the sulfuric acid caves, and are older. As with the sulfuric acid caves, carbonic acid caves are not associated with surface features and are entered through breaches caused by the formation of the sulfuric acid caves, canyon down-cutting, or surface erosion.

Sample Description

For this study 18 spar caves in the Guadalupe Mountains were visited with a total of 27 samples collected, 22 of which were dateable. From these 18 spar caves

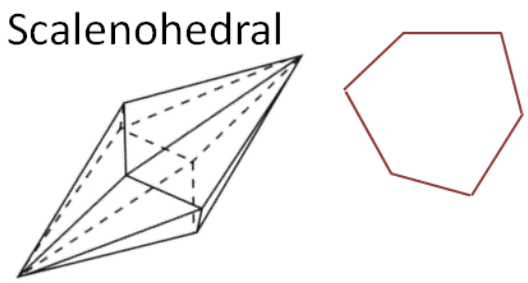

Figure 5: Scalenohedral morphology.

27 spar samples (all samples collected were previously damaged or broken, so no new damage was done to any of the sample sites) were collected for U/Pb geochronology, Sr, O & C isotope geochemistry, and fluid inclusion assemblage (FIA) analysis. Elevation and location data for each spar sample was also collected (APPENDIX A.5 - DESCRIPTION OF COLLECTION LOCATIONS). Of the 27 spar samples collected, 22 samples had the appropriate U to Pb ratio (≥15), based on Thermo X-series mass spectrometer elemental analysis, to proceed with U-Th-Pb chemistry and isotope analyses. The samples range in weight from 16 grams to 2.6 kilograms and in the c-axis from 2 cm to 20 cm. In most instances, the calcite spar was scalenohedral (Figure 5), but there were at least three samples that were indeterminate, and one that was mammillary calcite. Each of the spar crystals collected were encrusted by milky white, non-crystalline calcite, while the interior of the crystals were translucent and ran from white to brown. Several samples also contained bitumen fluid inclusions.

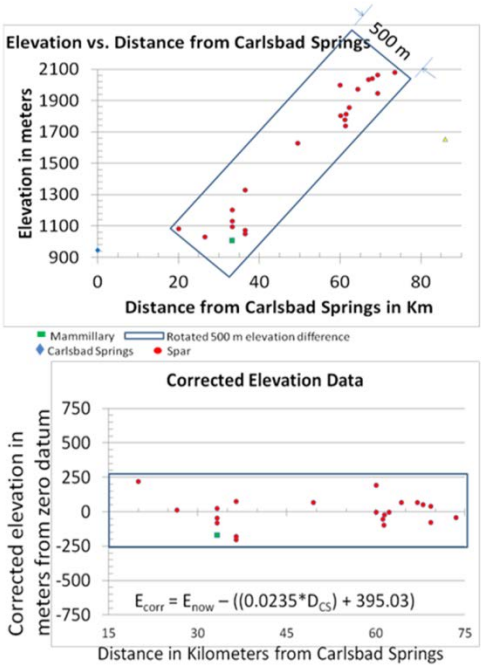

Figure 6: Elevation and location data plotted from Carlsbad Spring in Carlsbad, NM. Assuming level strata, when the elevation data is restored to horizontal, all data points are within 250 meters in elevation of each other.

When the elevation and location data were plotted against the distance from Carlsbad Springs (an artesian spring where the Capitan aquifer intersects the surface) in the town of Carlsbad, NM, and then rotated 1.3 degrees southwest to restore the Guadalupe Mountains tectonic block to a level elevation, all of the sample locations were within 250 meters in elevation of each other (Figure 6), which is half the thickness of the cave-forming strata that includes the Capitan reef and the immediately adjacent backreef and forereef limestones and dolostones (approximately 500 – 750 meters)(Harris and Grover, 1989; Hill, 1996; Zimmerman, 1962).

Current Model

The current CO_2 hypogene speleogenesis model in the literature explains dissolution and precipitation of deeply formed, usually single-chambered caves using standard knowledge about the amount of CO_2 that can be held in solution, which is determined by the temperature and pressure of the water (Andre and Rajaram, 2005; Dublyansky, 2000). Cooler water can hold more CO_2, so as water cools towards shallower depths its increased CO_2 partial pressure results in more acidic conditions and can dissolve more limestone. The source of the additional CO_2 is presumably magmatically derived (Dublyansky, 2000). Since additional capacity does not necessarily mean additional CO_2, it has to be assumed to come from somewhere. At shallower depths (i.e., 500 meters), the pressure is reduced to the point where CO_2 begins to degas so that there is a change in pH precipitating the

calcite (Dublyansky, 2000). This model cannot adequately explain the deposition of cave spar in the voids left behind by dissolution without invoking a reduction in the head of the water column. It also does not explain what happens to the CO_2 in the warmer, deeper brines (beyond that it is less corrosive), or even necessarily where the CO_2 originates (magmatic origin, hydrocarbons, or de-carbonation of limestone). A model that accounts for both the dissolution of the spar caves and the deposition of the spar itself that does not require a lowered water table is needed to explain cave spar speleogenesis. This model must also explain the origin and route travelled of the CO_2 to the spar cave/spar crystal forming depths.

CHAPTER 2 - Depth and Timing of Calcite Spar and 'Spar Cave' Genesis: Implications for Landscape Evolution Studies

(Decker, D.D., Polyak, V.J., Asmerom, Y. (2016). Depth and timing of calcite spar and "spar cave" genesis: Implications for landscape evolution studies", IN Caves and Karst Across Time, GSA Special Publication 516, Feinberg, J.M., Gao, Y., Alexander, E.C. https://doi.org/10.1130/2015.2516(08))

Abstract

Calcite spar (crystals >1 cm in diameter) are common in limestone/dolostone terrains. In the Guadalupe Mountains, New Mexico and West Texas, calcite spar is abundant and lines small geode-like caves. Determining the depth and timing of formation of these large scalenohedral calcite crystals is critical in linking the growth of spar with landscape evolution. In this study we show that large euhedral calcite crystals precipitate deep in the phreatic zone (400-800 meters,) in these small geode-like caves (spar caves), both of which we are proposing are the result of properties of supercritical CO_2 at that depth. U-Pb dating of spar crystals shows that they formed primarily between 36 and 28 Ma. $^{87}Sr/^{86}Sr$ values of the euhedral calcite spar show that the spar has a significantly higher $^{87}Sr/^{86}Sr$ (0.710 - 0.716) than the host Permian limestone (0.706 -0.709). This indicates the spar formed from waters that are mixed with, or formed entirely from, a source other than the surrounding bedrock aquifer, and is consistent with hypogene speleogenesis at significant depth. In addition we conducted highly precise measurements of the variation in non-radiogenic isotopes of strontium, $^{88}Sr/^{86}Sr$, expressed as $\delta^{88}Sr$, which variation has previously been shown to depend on temperature of precipitation. Our preliminary $\delta^{88}Sr$ results from the spar calcite are consistent with formation at 50 to 70° C. Our first U-Pb results

show that the spar was precipitated during the beginning of Basin and Range tectonism in a late Eocene to early Oligocene episode, which is coeval with two major magmatic periods at 36 to 33 Ma, and 32 to 28 Ma. A novel speleogenetic process that includes both the dissolution of the spar caves and precipitation of the spar by the same speleogenetic event is proposed and supports the formation of the spar at 400 to 800 m depth where the transition from supercritical to subcritical CO_2 drive both dissolution of limestone during the main speleogenetic event and precipitation of calcite at the terminal phase of speleogenesis. We suggest that CO_2 is derived from contemporaneous igneous activity. This proposed model suggests that calcite spar can be used for reconstruction of landscape evolution.

Figure 7: Scalenohedral calcite spar location 3 (CAVE-02399-004). Cave spar crystals of this study range from 2 centimeters to 2 meters in length. (Photo credit: Ben Schwarz)

Introduction

Small geode-like caves, referred to herein as spar caves, that are lined with large, scalenohedral dog-tooth spar are well known in the Guadalupe Mountains (Figure 1), yet enigmatic in that they do not fit the standard speleogenetic models. The calcite spar is important because it preserves the geochemical information at the time the spar was formed (Palmer, 2007b, 2011). These

caves and the spar contained within (Figure 7) have been described by Hill (1987; 1996) as both stage II and mesogenetic, meaning that they were formed after the reef system in Late Permian and before Middle Miocene to Pliocene sulfuric acid speleogenesis (Polyak et al., 1998) that formed the large caves like Carlsbad Cavern. Speculation as to when these spar caves were formed range from the late Permian all the way through the Miocene (DuChene and Cunningham, 2006; Hill, 2000; Palmer and Palmer, 2000). The spar on the other hand has been assumed to be of Neogene age as late as the Pliocene (Hill, 1987) and as early at the Cretaceous (Lundberg, 2000) and not necessarily related to the formation of the voids that contain the spar (Hill, 1987). These "spar caves" are relatively small compared to the sulfuric acid caves like Carlsbad Caverns and Lechuguilla Cave, ranging in size from less than a cubic meter to several thousand cubic meters (e.g. Spar City in Lechuguilla Cave, Figure 7). These vug caves have been truncated either by sulfuric acid speleogenesis or by surface erosion and are accessible only for this reason. This paper addresses the origin of spar caves and their calcite spar linings, and the potential importance of these to landscape evolution studies.

The two models suggested for the origin of spar caves in the Guadalupe Mountains infer that these caves were formed either by slowly percolating, CO_2 enriched groundwater in a mixing zone (Hill, 1987) or by hypogene speleogenesis (Klimchouk, 2007, 2009). In the mixing model, supersaturated brines mix with fresh meteoric waters to create an aggressive CO_2 laden mixture that dissolves the limestone creating the voids that will eventually become lined

with crystals. In the hypogene speleogenesis model rising fluids which derive their CO_2 from magma deep below (Klimchouk, 2007; Lowenstern, 2001) dissolve limestone along the way. As they rise, they also cool, which raises the amount of $CaCO_3$ that can be held in solution increasing the amount of dissolution that is occurring. When the water nears the surface, pressure is reduced and the hypogene fluids degas rapidly, raising the pH and precipitating calcite in pores and vugs near the surface (Dublyansky, 2000). Neither of these models can account for both dissolution and precipitation of calcite at several hundred meters depth. We propose that dissolution and precipitation of calcite takes place one right after the other; therefore a better model for the formation of these spar caves is required. Because we can determine the depth of formation of the spar caves and spar, and that that depth is ideal for the transition from supercritical to subcritical CO_2, we propose a supercritical CO_2-based speleogenesis model that can both dissolve the voids and precipitate the calcite in the same rock space within a relatively short time in the deep phreatic zone.

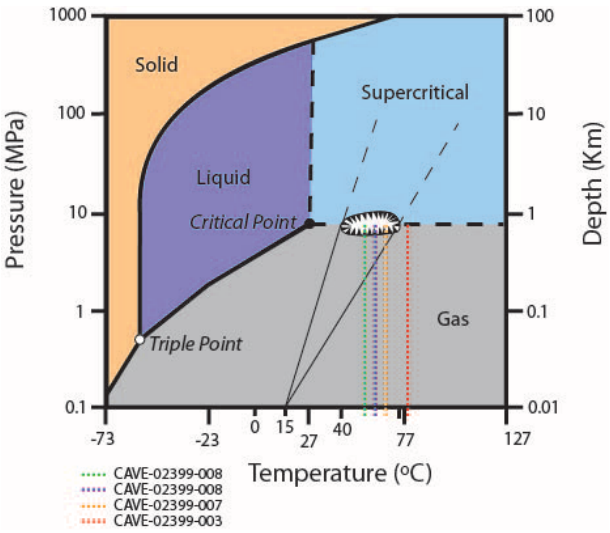

Figure 8: CO_2 phase diagram depicting supercritical gas phase region where dissolution and precipitation occur in the phreatic zone. Dashed lines represent temperatures of several samples from Table 2 based on $\delta^{88}Sr$ and a modified Fietzke & Eisenhauer (2006b) equation (Equation 2). Phase diagram modified from Finney and Jacobs (2010) based on data from Ely et al., (1989).

Supercritical CO_2 ($scCO_2$) is a superfluid phase of carbon dioxide reached at 31° C and 7.4 MPa (Figure 8), (André et al., 2007; Domingo et al., 2004; Kharaka et al., 2006). This temperature and pressure correspond to depths of approximately 350 to 750 meters (m). This phase of CO_2 can be highly aggressive when mixed with aquifer waters, has low resistance to flow allowing it to travel easily from the parent magma through low permeability rock, and a very narrow range of temperature and pressure over which it dissolves or deposits $CaCO_3$ (Domingo et al., 2004).

In this paper we will suggest, using known spar formation depth, and the U-Pb age and Sr-isotope values of the calcite crystals, that these spar caves were formed within a narrow depth range deep beneath a regional water table by dissolution and precipitation via reaction of $scCO_2$ with the aquifer. This model will make a new contribution to landscape evolution studies.

Methods

Uranium-lead (U-Pb) ages were determined by dissolving crushed, cleaned samples in 15 N HNO_3, double spiking with a ^{205}Pb-^{229}Th-^{233}U-^{236}U spike, and then preparing and separating the U, Th, and Pb using the methods described in Asmerom et al. (2006) and Polyak et al. (2008). Pb was eluted first using 6 N HCl from a column with 250 µl of Eichrom/Biorad anion exchange resin. A second set of anion exchange resin columns were used to separate U and Th. The U was eluted with 18 MΩ H_2O and 1 N HBr. The Th was collected using 6 N HCL. Each of the above elements were then dissolved in 3% HNO_3 and then introduced via the CETAC Aridus dry aerosol nebulizer into the Thermo Neptune Multi-Collector

Inductively Coupled Plasma Mass Spectrometer (MC-ICP-MS) at the University of New Mexico Radiogenic Isotopes Lab. Pb samples were run using a static routine where all masses were measured in Faraday cups, and fractionation was corrected using standard-sample-sample-standard bracketing with NBS-981 as the standard. U and Th samples were run after the procedures of Asmerom et al. (2006), where all U isotopes were measured as a static routine in Faraday cups. When this was not possible, ^{234}U was measured in a secondary electron multiplier (SEM) ion detector and NBL-112 was used to determine the gain between the Faraday cups and the SEM. Th isotopes were measured as a static routine where ^{230}Th was measured in the SEM, and an in-house ^{230}Th standard was used to establish the gain between the Faraday cups and SEM. Data reduction was accomplished using PbDat (Ludwig, 1993) and ages were determined by U-Pb concordia using an Excel spreadsheet and Isoplot (Ludwig, 2000).

For strontium (Sr) runs, cleaned pieces of sample were dissolved in 7 N HNO_3, split into two aliquots, with one aliquot from each sample spiked with an in-house ^{84}Sr spike, and the other aliquot unspiked. Sr was separated using Eichrom Sr-spec resin where 3 N HNO_3 was used to condition the columns and clean the sample, and 18 MΩ H_2O was used to collect Sr for analyses on a Thermo Neptune MC-ICP-MS. Runs were monitored using standard NBS-987 which has a $^{87}Sr/^{86}Sr$ of 0.71025. To obtain $^{88}Sr/^{86}Sr$ values, a zirconium ICP standard was added to the unspiked sample aliquots and the $^{90}Zr/^{91}Zr$ (interpolated from the

corrected standard runs) was used to correct mass fractionation. $\delta^{88}Sr$ was determined using equation 1 below.

$$\delta^{88}Sr = (({}^{88}Sr/{}^{86}Sr_{sample} - {}^{88}Sr/{}^{86}Sr_{standard}) - 1) \times 1{,}000 \quad (1)$$

where ${}^{88}Sr/{}^{86}Sr_{standard} = 8.3752094$

The $\delta^{88}Sr$ is then used to obtain the approximate calcite precipitation temperature after Fietzke and Eisenhauer (2006a), equation 2 with modifications based on our fluid inclusion temperature result and their slope used in equation 2 (Table 1):

$$x = (y - 0.0828)/0.0054 \quad (2)$$

where y is the $\delta^{88}Sr$ from the above work, m is the slope adjusted to be -0.1, and x is the temperature of calcite precipitation (Table 1). While our values are

Table 1: $\delta^{88}Sr$ Values and Corresponding Temperatures for Equation (1). Designations are regional, not specific caves (CAVE: Carlsbad Caverns National Park; USFS: US Forest Service, Guadalupe District). FIA - Fluid Inclusion Assemblage Temperature. Temperature is calculated from the Fietzke and Eisenhauer equation (Equation 2), modified to our FIA temperatures.

Sample	$\delta^{88}Sr$	Temp °C (F&E-model)
CAVE-02399-003	0.526	82.2
CAVE-02399-007	0..561	88.5
CAVE-02399-008	0.237	28.6
CAVE-02399-011	0.464	70.6
USFS-11290-008	0.821	105.7

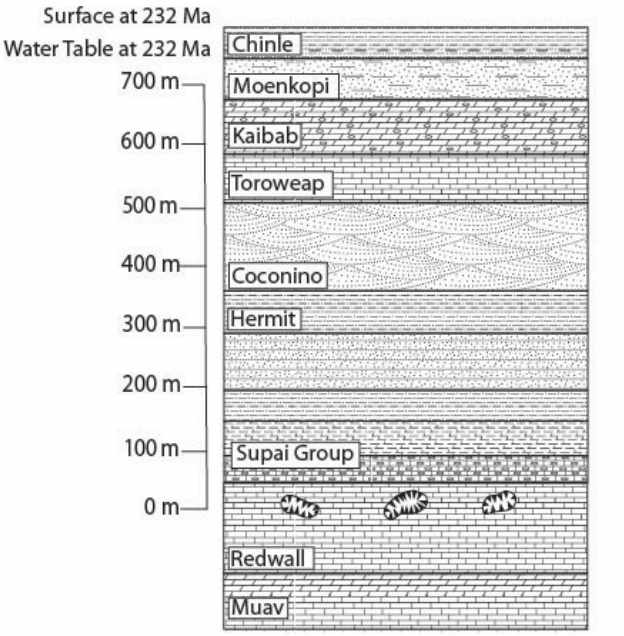

Figure 9: Spar vugs formed in the Redwall limestone at approximately the same time as the upper Moenkopi and lower Chinle formations were being deposited at or very near the water table. This stratigraphic section represents the region above GC-C-17 in Grand Canyon Arizona, near the confluence of the Colorado and Little Colorado rivers on the north rim. The age is 232 ± 2 Ma, and the depth of calcite precipitation is approximately 750 meters. Figure built on data from Blakey and Middleton (2012).

similar to fluid inclusion temperatures for spar calcite reported in the Delaware Basin (Crysdale, 1987), we also note that this method is still not shown to be a robust indicator of temperature as it is still a fairly new technique and few researchers have begun to investigate its potential (Böhm et al., 2012; Fietzke and Eisenhauer, 2006a; Rüggeberg et al., 2008; Shalev et al., 2013; Stevenson et al., In Publication).

Results

We have determined the age of six spar crystals using U-Pb isochrons. Samples and their three dimensional concordia ages are USFS-11290-002 (36.3 ± 0.2 Ma), CAVE-02399-004 (35.1 ± .4 Ma), GUMO-00549-003 (30.6 ± 2.8 Ma), BLMC-20122-005 (31.5 ± 4.3 Ma), CAVE-02399-008 (9.30 ± .95 Ma) and CAVE-02399-003 (12.8 ± 4.4 Ma). See Table 3 and APPENDIX A.3 - SAMPLE DATA PAGES (sample designations are by agency unit e.g. Park Service, US Forest Service, not specific caves, see Tables and Sample Data Pages for more details). The last two samples have been correlated to the water table surface at

- 390 m and - 670 m, respectively, based on alunite data from Polyak et al. (1998). Therefore, their depths of formation from a pre-existing surface are considered minimum depths. Depths of formation of three cave spar sites were determined by U-Pb ages and approximate depth of precipitation below a pre-existing water table or surface. Example 1 comes from Grand Canyon. A small spar cave exposed in Grand Canyon cave C-17 yielded a concordia 3D isochron age of 232 $\pm$ 2 Ma. This is a Triassic age, and rocks from Triassic of this age are of a low-lying terrestrial or shallow near-sea level origin (Blakey and Middleton, 2012). Therefore, the distance from the lower Triassic to the upper Redwall limestone represents the depth of formation of the cave spar. In this case, and according to formation thicknesses (Blakey and Middleton, 2012), the depth is ~750 m (Figure 9). The other two sites come from Carlsbad Cavern, and the depth is estimated using the ages of these two samples and paleo-water tables determined by Polyak et al. (1998) as mentioned above. Depths of spar formation below the paleo-water table are calculated to be ≥ 390 m for sample CAVE-02399-008 (site 1) and ≥ 670 m for sample CAVE-02399-003 (site 2). These depths can also be estimated by determining the thickness of strata and should include some Castile Formation overburden of unknown thickness. Overall, the depth of formation of the calcite spar is ≥ 390 m to 750 m. Both the Grand Canyon and Guadalupe Mountains contain cavernous porosity in limestone and demonstrate that spar formation occurs between 400 and 750 meters below a regional water table and regional surface and that this is not a local phenomenon.

CO_2 becomes supercritical at a temperature ≥ 31° C (395 to 790 m depth depending on the temperature gradient) and at a pressure of 7.4 MPa (280 to 750 m depending on density of water and rock) (André et al., 2007; Domingo et al., 2004; Kharaka et al., 2006), (Figure 8). Since annual average surface temperatures are currently ~ 15° C (NOAA, 2014), an increase in temperature of only 16° C is needed to reach the supercritical CO_2 temperature of 30.9° C, which correlates to a depth of 640 m at a temperature gradient of 25° C/km. However, at the time of formation of the spar, the temperature gradient is interpreted to have been higher due to magmatic activity, anywhere from 30° C to possibly as high as 60° C/Km based on vitrinite reflectance data (Barker and Pawlewicz, 1987). Assuming temperature gradients of 30 to 60° C/km,

Table 2: $^{87}Sr/^{86}Sr$ Values for Samples from the Guadalupe Mountains, NM. Designations are regional, not Specific caves (CAVE: Carlsbad Caverns National Park; GUMO: Guadalupe Mountains National Park; BLMC: Bureau of Land Management, Carlsbad Field Office; USFS: US Forest Service, Guadalupe District). Host rock data from Hill (1996).

Sample	$^{87}Sr/^{86}Sr$	±	Mean	Sr (ppm)	±
GUMO-00549-001a	0.71082	0.00001		389.482	0.014
GUMO-00549-001b	0.71080	0.00001	**0.71095**	251.631	0.008
GUMO-00549-001c	0.71124	0.00001		132.297	0.005
GUMO-00549-002a	0.71336	0.00001		107.514	0.143
GUMO-00549-002b	0.71167	0.00001	**0.71216**	137.464	0.007
GUMO-00549-002c	0.71144	0.00001		110.163	0.003
GUMO-00549-003a	0.71144	0.00001		56.734	0.006
GUMO-00549-003b	0.71138	0.00001	**0.71129**	181.723	0.009
GUMO-00549-003c	0.71104	0.00001		235.138	0.010
CAVE-02399-002a	0.71006	0.00001		109.822	0.007
CAVE-02399-002b	0.71017	0.00001	**0.71003**	196.356	0.007
CAVE-02399-002c	0.70986	0.00001		175.751	0.010
CAVE-02399-004a	0.70931	0.00001		89.491	0.009

CAVE-02399-004b	0.71083	0.00001	**0.71047**	166.114	0.011
CAVE-02399-004c	0.71126	0.00001		93.807	0.005
USFS-11290-007a	0.71257	0.00001		644.485	0.163
USFS-11290-007b	0.71251	0.00001	**0.71257**	654.686	0.094
USFS-11290-007c	0.71263	0.00001		444.905	0.119
BLMC-20122-004d	0.71155	0.00001		139.058	0.026
BLMC-20122-004e	0.71038	0.00001	**0.71116**	160.842	0.011
BLMC-20122-004f	0.71156	0.00001		73.968	0.003
USFS-11290-002a	0.71256	0.00001		76.650	0.007
USFS-11290-002b	0.71129	0.00001	**0.71202**	73.623	0.006
USFS-11290-002c	0.71220	0.00001		97.600	0.007

Host Rock $^{87}Sr/^{86}Sr$	
Capitan	0.70743
Yates	0.70700
Tansill	0.70680
Seven Rivers	0.70824
Bell Canyon	0.70687

and an average mean annual surface temperature similar to the present during the Oligocene and Miocene (Savin, 1977), the minimum depth where $scCO_2$ transforms to subcritical CO_2 ($subCO_2$) is between 266 and 533 meters. Regarding pressure, the lithostatic gradient is approximately 26.5 MPa/km in the continental crust (Fossen, 2010), which yields a depth of 279 m where $scCO_2$ transforms to $subCO_2$. Hydrostatic pressure is a little lower at approximately 10 MPa/km in fresh water, which indicates that depth will be 740 m (Box, 2014). In all, given that the spar caves and cave spar formed at the $scCO_2$ to $subCO_2$ transition zone as we propose, the depth of formation would be somewhere between 266 and 790 m, consistent with our measured depths of formation for

three spar crystals, one from Grand Canyon and two from the Guadalupe Mountains.

Our preliminary $\delta^{88}Sr$ values ranges from 0.237 to 0.821 ‰ (Table 1), which, when plugged into equation (2) yields temperatures of formation of between 56 and 106° C. Additionally, $^{87}Sr/^{86}Sr$ was obtained yielding ratios of 0.709 to 0.713 (Table 2). The Permian limestone ratios range between 0.707 and 0.708 (Burke et al., 1982).

Table 3: U-Pb dates for selected spar samples from the Guadalupe Mountains, southeastern New Mexico and west Texas. Designations are regional, not specific caves (CAVE: Carlsbad Caverns National Park; GUMO: Guadalupe Mountains National Park; BLMC: Bureau of Land Management, Carlsbad Field Office; USFS: US Forest Service, Guadalupe District). Sample C-17 from Grand Canyon National Park. Three dimensional concordia graphs in APPENDIX A.3 - SAMPLE DATA PAGES.

Sample	Spar U-Pb concordia age (Ma)
BLMC-20122-005	31.5 ± 4.3
CAVE-02399-003	12.8 ± 4.4
CAVE-02399-004	35.1 ± 0.4
CAVE-02399-008	9.3 ± 0.95
USFS-11290-002	36.3 ± 0.2
GUMO-00549-003	30.6 ± 2.8
Grand Canyon C-17	232 ± 2

Discussion

Dublyansky (2000) suggests, based on a theoretical equation after Malinin (1979), that there is a depth below the water table at which dissolution stops and rapid precipitation occurs, and these depths are significantly different. We have shown that the cave spar has formed at depths of > 390 m to 750 m below the surface, so the spar caves had to form at or below these depths. $ScCO_2$-speleogenesis not only explains the depth of spar crystal precipitation, but also

the relatively rapid conversion from dissolution to precipitation of calcite at up to a kilometer in depth occurring during a single speleogenesis event.

$ScCO_2$-speleogenesis: A deep hypogene speleogenesis model

Our model suggests that rising $scCO_2$ becomes more aggressive to limestone/dolostone as it rises and cools, and at the depth where $scCO_2$ converts to $subCO_2$, maximum dissolution takes place. In our model, the final phase of speleogenesis is precipitation of large euhedral calcite crystals at a depth of 266 to 790 m. The size of these spar caves is relatively small. They are geode-like chambers up to 10s of meters in diameter, so the speleogenesis is thought to be a short-lived event (half million to a million years). We suggest a model by which $scCO_2$ speleogenesis is related to pulses of $scCO_2$ from magma bodies as a way to explain brief speleogenesis where precipitation marks the end of speleogenesis. As mafic magmas were being generated by decompression melting of the mantle during the Basin and Range tectonism in New Mexico and West Texas, copious amounts of CO_2 were created (Lowenstern, 2001). At the depth that the magma was exsolving fluids, the CO_2 should be a supercritical fluid as it rises along joints and faults. In our model, upward migration of $scCO_2$ eventually intercepts the briny groundwater of the paleo-Capitan aquifer (DuChene, 2009; Huff, 2004) (water in the Capitan reef and immediately adjacent forereef and backreef) near the depth where $scCO_2$ transforms to $subCO_2$ (Figure 10). In an aquifer at and just below that critical depth, $scCO_2$ dissolves more readily in the water until the aquifer water reaches the saturation point of CO_2, which lowers the pH of the water. During this time it begins dissolving the

limestone. The size of the spar cave is probably the result of the difference between rate of displacement of carbonate saturated water (from dissolution of limestone) and rate of fresh supply of $scCO_2$. Essentially, at the point that saturation is reached the dissolution of limestone increases the pH (buffering) to the point where the water can no longer accept more $scCO_2$ and the pH does not promote additional limestone dissolution. Some dissolved carbonate is transported away leaving a void. As the magmatic processes that produce the $scCO_2$ wane, or if even a slight change in temperature or pressure occurs, the $scCO_2$ to $subCO_2$ transformation results in out-gassing of CO_2 as a dissolved gas. This raises the pH of the system allowing precipitation of $CaCO_3$, which at this salinity, temperature, and pressure, produces the scalenohedral spar (Domingo et al., 2004) within the same voids that were previously dissolved at the beginning of the process. For example, at 45° C and 10 MPa, a slight increase in temperature, or a slight decrease in pressure results in a dramatic decrease in the amount of $CaCO_3$ that can be held in solution (Figure

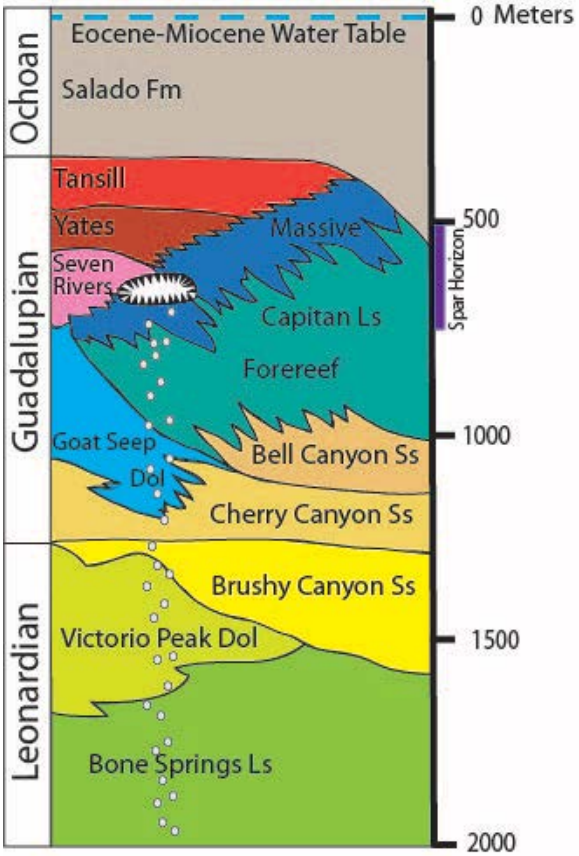

Figure 10: Supercritical CO_2 speleogenesis model. Depth, pressure and temperature scales correspond to spar forming episodes at the Eocene-Oligocene transition. This stratigraphic section is based on the stratigraphy of the Capitan Reef near Carlsbad Caverns National Park, NM, Modified from King (1948).

11) (Domingo et al., 2004). By definition of $scCO_2$, this is predicted to occur over a rather narrow range of 400 to 800 meters below the water table or surface, and this is the depth range that we measured for formation of the spar calcite.

Support for a magma source of CO_2

Previous fluid inclusion data (Crysdale, 1987; Hill, 1987; Hill, 1996) and our $\delta^{88}Sr$ results suggest that the spar formed at temperatures of 50 to 70° C, which correlates to a depth of approximately 2.5 to 3 km using a normal depth/temperature gradient of 20° C/km. The geologic evidence indicates that there was not enough overburden in the region to produce those temperatures under normal thermal gradient conditions. According to Barker and Pawlewicz (1987) there was never more than a kilometer of Ochoan evaporites deposited above the Capitan reef. To obtain these higher temperatures at shallower depths, there must have been an additional heat source. A magma source of heat and CO_2 is supported by our U-Pb ages and Sr isotope ratios of the spar calcite. Most of the

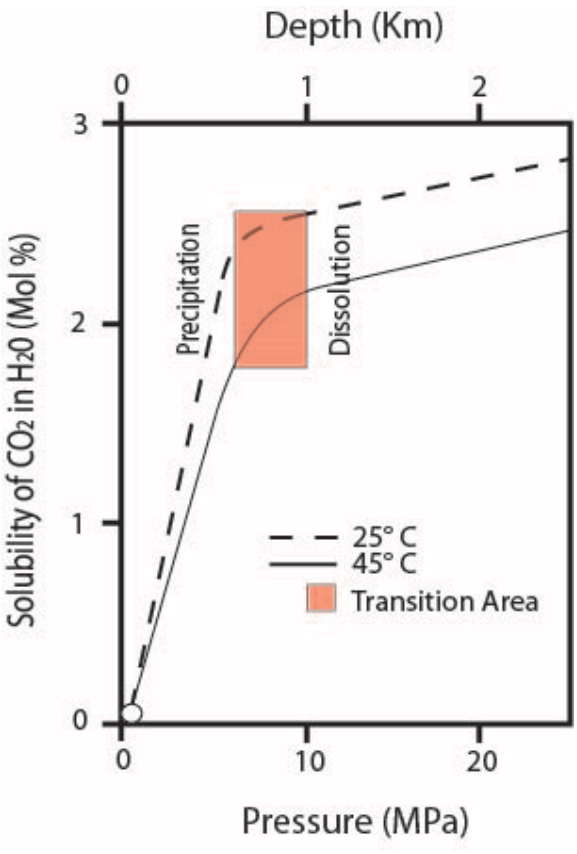

Figure 11: Solubility of CO_2 in H_2O at supercritical temperatures and pressures after Domingo (2004).

U-Pb ages of spar calcite fall between 36 and 28 Ma, coincident with major Basin and Range magmatic activity locally (Barker and Pawlewicz, 1987; Calzia and Hiss, 1978; Chapin et al., 2004). Our $^{87}Sr/^{86}Sr$ isotope ratios (Table 2) are significantly higher than the host rock (Hill, 1996), and support an interpretation that the source fluids originated from greater depths, and circulated through the basement rocks in this region that are approximately 1500 - 3000 m deeper (Flawn, 1955). Together, fluid inclusion data from Hill (1987)and Crysdale (1987) and our $\delta^{88}Sr$, U-Pb, and measured depth results all support deep origin of the caves and spar by rising magmatic-driven fluids. It is at these depths that $scCO_2$ transforms to subcritical CO_2. Based on these constraints, there is a narrow region in which the voids can be created and the spar deposited, approximately 400 to 800 meters deep, forming a “spar horizon” as alluded to by Hill (1987). However, our $scCO_2$ model of speleogenesis is not a simple phreatic story, but rather a low hydrothermal temperature, deep hypogene speleogenesis story.

This newly proposed model of speleogenesis will be incorporated in the landscape evolution of the Guadalupe Mountains, and has potential to be used worldwide to help constrain landform evolution in the regions in which cave spar occurs. A narrow spar horizon suggests minimal tectonic movement in the region during the formation of the spar and suggests a minimum depth for the aquifer in which it formed.

Conclusion

A new model for speleogenesis has been proposed. During the formation of the Basin and Range landscape, decompression melting formed copious amounts of

CO_2, which at the temperature and depth it was released from the magma body was in the supercritical regime. Supercritical CO_2 is highly mobile and made its way upward where it interacted with the Capitan aquifer at the depth where it transforms to subcritical CO_2, creating a low pH carbonic acid that forms geode-like caves in the limestone/dolostone approximately 400 to 800 meters below the water table and/or surface. As the $scCO_2$ diminished at the end of each igneous episode, the acidic waters became more alkaline and began depositing scalenohedral calcite spar in the same vugs that were “recently” dissolved. This is a novel model in that it invokes a different phase of CO_2 that has a narrow pressure and temperature range in which it can both dissolve and precipitate calcite. This new model provides insight into cave formation, carbon sequestration and landform evolution. A spar horizon provides a significant constraint on landform evolution, uplift and faulting.

CHAPTER 3 - δ88Sr of deep phreatic hydrothermal calcite (cave spar) shows temperature dependence between 40 and 80˚ C

(In review and awaiting publication, submitted to Geochimica et Cosmochimica Acta)

Abstract

Determination of the temperature of formation of crystal growth, such as the growth of calcite crystals used in this investigation, can lead to a better understanding of the tectonic, hydrologic, and geomorphologic development of the region under study. From our research of deep phreatic cave calcite (cave spar), we know the depth and timing of spar formation from U-Pb chronologies (Decker et al., 2016; Decker et al., 2017) , and the temperature of spar precipitation can be measured from fluid inclusions in the calcite. However, calcite does not always contain fluid inclusions, and in lower temperature calcites (<40° C) those that do form are single phase and cannot be used to find a temperature of homogenization (T_h). A method for measuring the temperature of formation of calcium carbonate has been offered by Fietzke and Eisenhauer (2006b) using the per mil value differences between aragonite samples and a standard (denoted as $\delta^{88}Sr = ([^{88}Sr/^{86}Sr_{smpl} - {}^{88}Sr/^{86}Sr_{std}]/^{88}Sr/^{86}Sr_{std}) \times 1000)$), in biogenic and non-biogenic aragonite precipitated at known temperatures. They showed a linear correlation between $\delta^{88}Sr$ and the temperature of precipitation, where the slope of this linear trend was different for biogenic and non-biogenic aragonite. This method has since been shown to be a simplification of a more problematic system (Böhm et al., 2012; Halicz et al., 2008) where several other factors are involved in the fractionation. In this study, we test the Fietzke and

Eisenhauer (2006b) method beyond 20° C by determining the temperature of homogenization (T_h) of fluid inclusions from calcite cave spar and comparing those results to the $\delta^{88}Sr$ of the sample, and show that this method has merit if the other factors are considered. Comparison of the values of the temperature of homogenization of sub-samples of the cave spar with $\delta^{88}Sr$ temperatures obtained from the same sub-samples indicate a good correlation (r = 0.64). We then calibrated the $\delta^{88}Sr$-cave spar geothermometer to the T_h and to three low temperature speleothem calcite samples extending the range of temperatures that can be determined using this method. Our results indicate that the spar formed between 40˚ and 80˚ C based on both the T_h and the $\delta^{88}Sr$ temperature curve, and based on the large differences in low and high temperature calcite from the same study area, there seems to be a temperature dependency that may be complicated, but has promise as a geothermometer. While our results suggest a temperature dependence, we cannot completely rule out influence from differing calcite growth rates or other factors that may make this correlation a coincidence.

Introduction

Determining the temperature at which euhedral calcite grows can be an important tool in landform evolution studies. Cave spar, euhedral calcite that lines relatively small geode-like caves (spar caves) in the Guadalupe Mountains, southeastern New Mexico and west Texas, has been proposed and used as a landform evolution tool (Decker et al., 2016; Decker et al., 2017). The calcite cave spar contains fluid inclusions (Figure 12), which provides an opportunity to

compare fluid inclusion temperatures with other promising methods such as clumped isotopes or $^{88}Sr/^{86}Sr$. Knowing accurate temperature of formation of calcite cave spar can provide a better understanding of the tectonic, hydrologic, and geomorphologic development of our study region (Crysdale, 1987; Hill, 1996; Lundberg et al., 2000; Mruk, 1985; Scholle et al., 1992), and can be made applicable to other regions. Cave spar of the study area is modeled to precipitate as a calcite druse as the last phase of "spar cave" genesis that involves upwelling CO_2, and as such, temperature combined with U-Pb ages and depth of formation (Decker et al., 2016; Decker et al., 2017) could offer important advances in surficial studies. Temperatures of homogenization (T_h) of fluid inclusions are the primary way to help narrow the range of temperatures at which calcium carbonate grows in thermal, deep phreatic settings. Carbon, oxygen, and hydrogen stable isotope temperature indicators in calcium carbonate have proved to be less reliable as absolute temperature indicators. Isotopic ratios of carbon and oxygen can, however, support temperature data

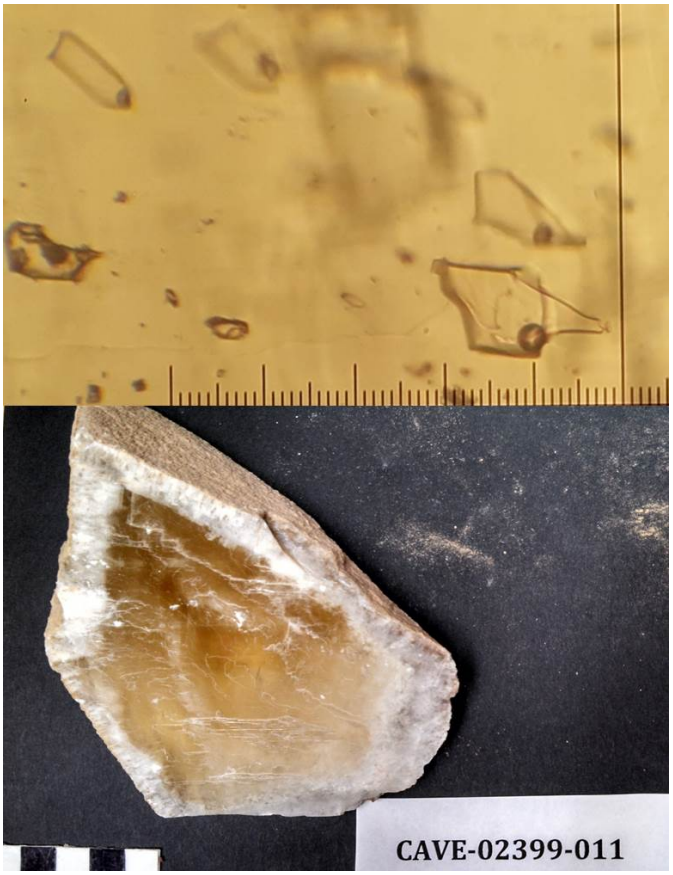

Figure 12: Representative cave spar (below) and associated inclusions (above).

gained by other methods. Recently it has been proposed that strontium (Sr) isotopes can be used as a geothermometer using the difference between the ratio of $^{88}Sr/^{86}Sr$ of a standard to that of a calcium carbonate sample expressed as per mil:

$$(\delta^{88}Sr = (((^{88}Sr/^{86}Sr_{sample} - {}^{88}Sr/^{86}Sr_{standard})/(^{88}Sr/^{86}Sr_{standard})) \text{ X } 1{,}000)$$

of the calcium carbonate (Fietzke and Eisenhauer, 2006b). While promising as a geothermometer, more recent studies indicate that the fractionation factor is heavily influenced by precipitation rate (Böhm et al., 2012; Halicz et al., 2008) and pH of the precipitation fluid (Alkattan et al., 1998; Dietzel et al., 2009; Pokrovksy et al., 2009) rather than the temperature. In this study we show that, while there are numerous factors involved in the stable isotope fractionation between fluids and solids, temperature appears to play a dominant role amongst these factors for natural speleothem calcite. Fluid inclusion temperature analyses have been largely successful, but not all calcium carbonate speleothems contain fluid inclusions, and the T_h only gives a minimum temperature of formation and may be subject to outside influences if the crystal has been reheated during metamorphism or has experienced interaction with high temperature, hydrothermal water (Roedder, 1983b). This study uses fluid inclusion analyses of cave spar calcite to attempt to calibrate the proposed Sr isotope thermometer using the strontium isotope ratio $^{88}Sr/^{86}Sr$ that was previously thought to be unvarying in nature (de Laeter et al., 2003; Faure and Powell, 1972; Herzog et

al., 1958). Because of recent technological advances, this ratio in terrestrial samples has been reported to vary by >0.6 ‰, with 0.4 ‰ measured for the IAPSO sea water standard (Ma et al., 2013). We use scalenohedral calcite cave spar crystals that formed at low-hydrothermal temperatures (35 - 80° C) in the deep phreatic zone to test the strontium isotope thermometer. We also use mammillary calcite formed in the cooler, but still warm, shallow phreatic zone a few meters below the water table, and cool (<25° C) temperature vadose speleothem calcite of stalagmites and pool deposits (shelfstone) for comparison. While the temperature of formation of Grand Canyon and Carlsbad Cavern mammillaries is unknown, shallow phreatic conditions suggest that those temperatures fall between those of the cave spar and vadose speleothems, and water temperature in Devils Hole, where cave mammillaries may be forming today, is 32 to 35° C (Kolesar and Riggs, 2004).

Methods

Strontium isotope analyses

Sub-samples for strontium isotope analyses were 15 to 120 mg powders or pieces. All pieces were selected from samples that were also run for fluid inclusion analyses (see below, 2.2). The strontium was prepared for isotopic analyses by dissolving each sub-sample of calcite in 7 N HNO_3, drying the sub-sample on a hotplate and then preparing a 3 N HNO_3 sample solution for the column resin chemistry. A 2 ml column with 250 µl of Eichrom Sr spec resin was used to retrieve the strontium by chromatographic ion separation with a yield of 81% (Extended Data Figure 16). Sr spec resin shows no tendency for mass

fractionation during collection regardless of the amount recovered (De Muynck et al., 2009; Ohno and Hirata, 2007). Ultrapure water was prepared with a milli-Q Millipore filter system. More detailed separation methods can be found in the extended data text. Each sub-sample, dissolved in 3% HNO_3, was analyzed on a Thermo-Finnegan Neptune Multi-Collector Inductively Coupled Plasma Mass Spectrometer (MC-ICP-MS) using a quartz spray chamber. ^{88}Sr voltage was adjusted to between 60 and 100 volts. The samples and NBS-987 standards were then spiked with zirconium until the $^{88}Sr/^{90}Zr$ ratio was between 30 and 35 to maintain consistency between sample runs. These sub-samples were then run on the MC-ICP-MS using a standard-sample-standard bracketing technique (Ma et al., 2013; Ohno and Hirata, 2007). The $^{90}Zr/^{91}Zr$ was used to monitor both fractionation and machine drift. The bracketing standard was NBS-987, which has an $^{87}Sr/^{86}Sr$ value of 0.71025 (Ma et al., 2013) and an assigned $\delta^{88}Sr$ value of 0 ‰. All runs were corrected by adjusting the Zr-spiked NBS-987 runs to $^{87}Sr/^{86}Sr = 0.71025$. We then normalized to $^{90}Zr/^{91}Zr$ (interpolated from the corrected standard runs) to correct for mass fractionation of the $^{88}Sr/^{86}Sr$ in the samples and measured the $\delta^{88}Sr$ using the mass fractionation equation $(([^{88}Sr/^{86}Sr_{sample}] / [^{88}Sr/^{86}Sr_{standard}]) - 1) \times 1{,}000$ where $^{88}Sr/^{86}Sr_{standard}$ was that measured from the two NBS-987 standard runs bracketing the sample runs, similar to the Zr method described by Scher et al. (2014). The BHVO-2 basalt standard ($^{87}Sr/^{86}Sr = 0.703479$ and $\delta^{88}Sr = 0.25 \pm 0.02$ ‰; Ma et al. 2013) was run with the sample analyses. Our value for BHVO-2 $\delta^{88}Sr = 0.24 \pm 0.03$ ‰ (n = 9)). Another volcanic standard (Table Mountain latite; TML) is an in-house

standard that is used by other groups for U-Th analyses (Sims et al., 2008) yielded a $\delta^{88}Sr = 0.22 \pm 0.07$ ‰ (n = 9).

Fluid Inclusion Assemblage (FIA) Analysis

The FIA analysis was run on all samples for which we had U-Pb ages using a Leica Leitz Laborlux S microscope equipped with a USGS modified fluid inclusion heating/cooling stage attached to a Fluid Inc. Trendicator with a Doric 410A temperature display. Each sub-sample was prepared by using a mortar and pestle to cleave a thin (100 to 500 μm) portion of a piece of crystal selected from the interior of the main sample. This sub-sample was then surveyed for fluid inclusions with notations made when groups of single phase inclusions were found. Photograph and sketch documentation was made of all two phase inclusion assemblages. Fluid inclusion size was determined by using a Dino-Lite calibration slide to find the pitch of the reticules in the Leica microscope at 500X (40X lens, 12.5X eyepiece) magnification. All heating runs for each sample were repeated a minimum of three times, or until the last three runs were within ± 1.0˚ C.

The Doric Trendicator 410A was calibrated per the Fluid Inc. instruction manual (Reynolds, 1994). An ice water bath of 18 MΩ H_2O was prepared for the 0° C calibration. The end of the thermistor was submerged in the ice water bath and allowed to equilibrate. Once the temperature stayed constant on the Doric 410A indicator panel, the zero potentiometer was adjusted to 0.0 ± 0.1˚ C. Liquid

nitrogen (LN) was used to freeze a CO_2 standard (standard #1 synthetic fluid inclusion from Syn Flinc) for the low temperature calibration. Dry N_2 was used to pressurize the liquid nitrogen Dewar. The cold LN flow was set to 14 standard cubic feet per hour (SCFH). After minor adjustment of the span (-) potentiometer, the standard froze at approximately -98˚ C and melted at -56.6 ± 0.2˚ C on the final three runs. The 0° C calibration was checked again in the same manner as above to ensure it had not changed. The high temperature calibration was run using a Powerstat Variable Transformer at a setting of 70 to provide heat. Air flow was provided from a compressor set at 15 SCFH. Ten runs were accomplished using the Syn Flinc standard #4 (pure H_2O), with 374.1 ± 0.2˚ C on the final three runs. The 0° C calibration was checked a final time to ensure that it was still accurate.

Results

Strontium isotope analyses

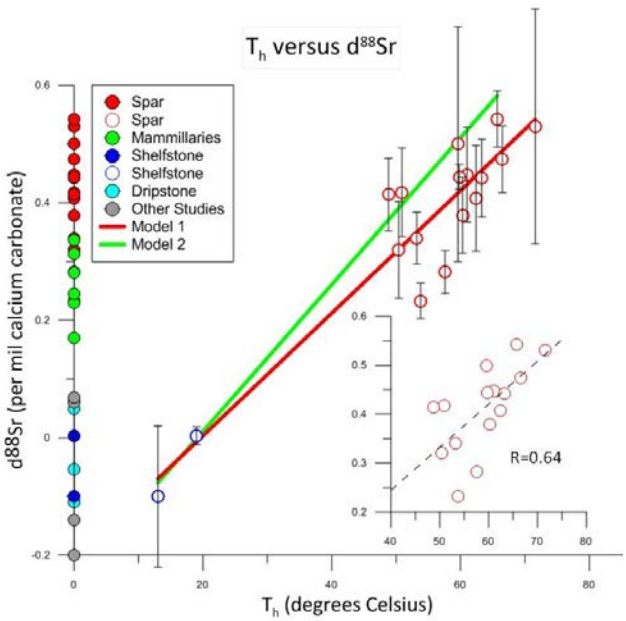

Figure 13: Model 1 uses all samples with fluid inclusion Th below 100° C. This model has an equation of y = 0.01044X - 0.20542. Model 2 uses only samples with the lowest temperatures and highest δ88Sr. This indicates the base of the model at which we expect that

δ^{88}Sr values measured for all of the speleothem samples had a range of 0.64 ‰, from -0.10 ≤ δ^{88}Sr ≤ 0.54 ‰ (Table 5, Figure 13) with the cave spar values spanning from 0.23 ≤ δ^{88}Sr ≤ 0.54 ‰, a range of 0.31 ‰. The lower values are from three cool-water vadose speleothems that include a sub-aqueous shelfstone (LECH VS-1: 0.08 ± 0.04 ‰) and two stalagmites (WBC4-Calcite-2006AD: -0.08 ± 0.07 ‰; and FS-AH1-2mm, 11 ka,: 0.06 ± 0.03 ‰) used because the temperature of formation are known. Sample WBC4 is contemporary calcite precipitated on Plexiglas at 11.6 ± 1.0 °C in Carlsbad Cavern (Rasmussen, 2006). Sample LECH VS-1 is ~4000-yr old subaqueous shelfstone collected deep within Lechuguilla Cave where temperatures today are 20 ± 1 °C (Turin and Plummer, 2000). Stalagmite FS-AH1-2mm was collected from Fort Stanton Cave, New Mexico, where today the temperature is 10.0 ± 0.6 °C (Asmerom et al., 2017). LECH VS-1 and FS-AH1 cool-water speleothem samples are given errors of ± 3 °C to conservatively cover differences in the Holocene. For further comparison, δ^{88}Sr values for mammillary calcite from Lake of the Clouds, Carlsbad Cavern, and from Grand Canyon caves, as well as values for dripstones are included in Figure 13. While cave

spar forms in the deep phreatic, mammillary calcite forms in the very shallow phreatic in hypogene caves, and as such, mammillary calcite is predicted by hypogene cave models (Polyak et al., 2017) to form in warmer water than typical vadose speleothems such as stalagmites, but in cooler water than what cave spar forms in. The more typical dripstone (stalagmites and stalactites), shelfstone, and flowstone form in vadose zones from infiltrating rain waters at the coolest temperatures, and in the study area, these temperatures will be <25 °C. Figure 13 is a compilation of $\delta^{88}Sr$ values for these speleothem types that follows the premise that these values show directly or indirectly a dependency on temperature.

Fluid Inclusion Assemblage (FIA) Analysis

Fluid inclusion assemblage (FIA) analysis temperatures range from 40 to 80˚ C (Table 4**,** Figure 13) with the temperatures of two samples that remain constrained only to above 0˚ C and below 40˚ C (based on single phase inclusions that are fluid between 0˚ C and room temperature and two phase above 40° C). These samples are likely to have formed between 35° and 40° C and have simply stretched the fluid (Roedder, 1983a)) rather than nucleating a vapor bubble. Forced nucleation was attempted by rapidly cooling the sample to 0° C, but nucleation never occurred. Fluid inclusion temperatures could only be measured for the cave spar.

$\delta^{88}Sr$ versus FIA temperatures

$\delta^{88}Sr$ values of the calcite cave spar crystals plotted against the T_h of the fluid inclusions show a positive correlation with increasing temperature (r = 0.64) (Figure 13 and Table 5). When the low temperature vadose speleothem values are included, the correlation improves (r=0.93) because the spread in results is large. Nevertheless, these results are consistent and support a temperature-based relationship similar to what Fietzke & Eisenhauer (2006b) reported. While other factors such as growth rate and inherent $\delta^{88}Sr$ of water before crystallization are present, we suggest that the slope of this curve represents changes driven primarily by temperature. The errors for the FIA were analytical, not empirical, see methods section (2.2) for FIA analysis. Several samples that yielded temperatures above 80˚ C can be explained by poor selection of fluid inclusions during the FIA analysis phase of the study (Figure 14), or these fluid inclusions could have been reheated and stretched during later crustal heating, or even during laboratory heating, resulting in temperature readings that we interpret to be above that at which the crystals formed.

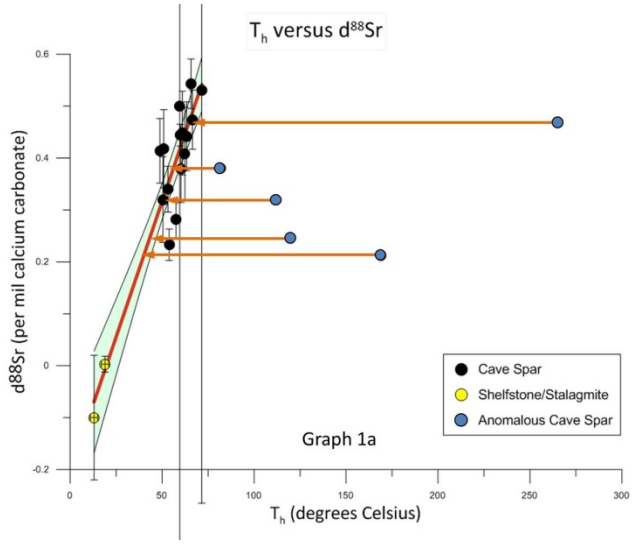

Figure 14: Anomalous high temperature cave spar can be explained by two mechanisms. Rapid addition of heat during laboratory heating stretched the inclusions, or they were overprinted with another thermal geologic event. The orange arrows show the temperatures at which the samples would be, using the model 1 equation.

Our results suggest two temperature curve models.

Model 1 uses a curve that plots through the average of all of the cave spar results. Model 2 suggests that most of the FIA temperatures are slightly above the real temperature, and therefore the line plots along the low temperature edge of the data. We calculated our model 1 equation based on the T_h – $\delta^{88}Sr$ data points (Figure 13) that we plotted for hydrothermal calcite of:

$$x = (y + 0.20542)/0.01044 \quad (1)$$

where x = temperature (°C) and y = $\delta^{88}Sr$. We calculated a second model that assumed even the lower temperatures may have been slightly high and the curve with the steepest slope represents the more likely scenario. This equation is:

$$x = (y + 0.23944)/0.01251) \quad (2)$$

When we plugged all $\delta^{88}Sr$ values of cave spar calcite including five calcite samples that did not contain viable fluid inclusions (anomalous high temperature spar) into this equation, all calculated temperatures from both $\delta^{88}Sr$ curves plotted within the 40° to 80° C range (Figure 14).

Discussion and Conclusions

For our study we were able to find two-phase fluid inclusion assemblages within many of our samples that represented primary formation assemblages. Most fluid inclusion do not leak (Roedder, 1983a), and this is particularly the case for calcite crystals in the small geode-like cave environment in which these crystals

are formed, therefore the fluids within these inclusions are representative of the fluids from which the spar precipitated. The calcite is late stage and has not been buried more than 1 km depth (<180 Ma; (Decker et al., 2017)). Additionally, since these are euhedral crystals and were formed in small, fluid-filled caves and remained so throughout most of their history, there was no differential pressure between the host rock and the spar crystals to form fractures in which to grow secondary inclusions. The majority of the inclusions studied appeared to have formed along crystal growth zones or twin planes, or are large, isolated negative crystal shapes. Based on this evidence, we propose that the fluid inclusion assemblages studied within the cave spar of this study are primary and represent the crystal formation temperatures.

If the pressure at which the sample formed is known or can be determined separately, and the composition of the fluid is known, a precise temperature of formation can be found. In our case we know these crystals formed at approximately 0.5 ± 0.25 km depth, giving us a formation pressure of between 7.4 and 10 MPa (Decker et al., 2016). Based on this pressure of formation we can conclude from our FIA analysis that the spar, unaltered by pressure, formed at temperatures less than 100˚ C. Our analysis supports this with fluid inclusion assemblage temperatures that were consistently between 40° and 80° C and within ± 1.0° C within single crystals over two or more analyses.

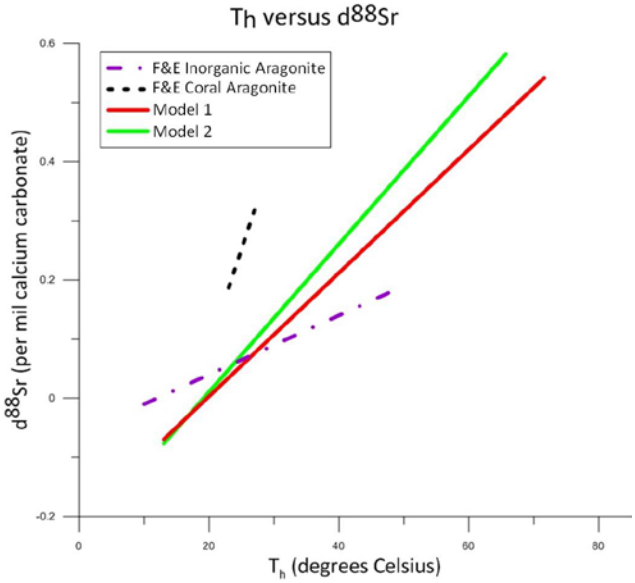

Figure 15: Our models 1 and 2 (red and green lines respectively) non-biogenic calcite cave spar shown with F&E (2006) biogenic (dashed black line) and non-biogenic (dash-dot purple line) aragonite.

Fietzke and Eisenhauer (2006b) and Rüggeberg (2008), showed that $\delta^{88}Sr$ is temperature dependent using aragonite (non-biogenic) and cold water corals (biogenic aragonite, Figure 15). Conversely, Böhm et al. (2012) demonstrated that these changes in $\delta^{88}Sr$ values can be solely due to differences in calcium carbonate growth rate, where faster growth rates cause smaller $\delta^{88}Sr$ values with a spread of values of ~0.3 ‰, similar to the spread observed in all terrestrial samples. Our new calcite-based data set includes geothermal calcite with measured FIA temperatures that vary from 40 to 80˚ C (Table 4), and corresponding $\delta^{88}Sr$ values that produce a co-varying correlation (Figure 13). Our results show a significant correlation between $\delta^{88}Sr$ values of cave spar calcite and measured fluid inclusion temperatures. Temperature dependency is made more significant when the results from cooler temperature calcite is added, for example, $\delta^{88}Sr$ temperature of formation of mammillary calcite from the Lake of the Clouds is estimated to be ~33˚ C ± 6°, which seems reasonable and comparable to Devils Hole, Nevada, which has a measured temperature of 34.25° C (Kolesar and Riggs, 2004). Additionally, qualitative results from comparing $\delta^{88}Sr$ values of cave spar (highest temperature

calcites) to that of mammillaries (medium temperature calcites) and vadose speleothems (cool temperature calcites) are impressive and support a temperature difference (Figure 13).

While there appears to be good evidence for a correlation of $\delta^{88}Sr$ values and temperature of formation in our results, the slope and offset of the slope may also be dependent on the pH of the precipitating solution (Alkattan et al., 1998; Dietzel et al., 2009; Pokrovksy et al., 2009), precipitation rate (DePaolo, 2011; Dietzel et al., 2009; Romanek et al., 1992), vital effects from biological mediation (Böhm et al., 2012; Gussone et al., 2003; Sharp, 2007a; Zeebe, 1999; Zeebe et al., 2006), and initial $\delta^{88}Sr$ value of the precipitating solution. These additional factors have been investigated in several recent studies, however, there is little consensus regarding which of these effects, if any, are dominant. This apparent relationship is dependent on these factors for which Böhm et al. (2012) held constant, except for growth rate. Of these factors, the results of Böhm et al. (2012) that growth rate might play a larger role than temperature, provide the biggest challenge to our study of natural calcite, that the temperature of formation has a dominant effect on the $\delta^{88}Sr$. This relationship would be particularly helpful in paleoclimate studies that use speleothems.

The Böhm et al., (2012) experiments were conducted over days to weeks with very high growth rates and kinetic fractionation (Log (R) = 2.25 to 4.21 $\mu mol/m^2/hr$), whereas our cave spar calcite is presumed to precipitate over tens

of thousands to hundreds of thousands of years in near equilibrium conditions (Decker et al., 2017). In comparison, our fast growing stalagmite, for example, has a $\delta^{88}Sr$ of ~-0.08 ‰ and an overall growth rate of Log (R) = -1.47 μmol/m^2/hr. We've estimated the growth rate of this stalagmite based on the age of the tip and the base, but this is an overall average rate and does not consider the rapid deposition, layer by layer, of calcite upon impact of the drip-water. Stalagmites undoubtedly grow faster than the cave mammillaries and cave spar speleothems, so that all of the samples used in our study likely have growth rates less than Log (R) = -1.47 μmol/m^2/hr. This would seemingly suggest that our sample $\delta^{88}Sr$ values are not affected by their differing growth rates, and that temperature and other factors may be more important than rate fractionation effects for these phreatic speleothems. It is still possible that growth rate is largely controlling changes in $\delta^{88}Sr$ values, but this would suggest that cave spar that formed in warmer water grew slower, which is counter intuitive since that would increase the super-saturation of the water, in turn increasing the rate of precipitation.

Böhm et al. (2012) used the lack of difference in $\Delta\ \delta^{88}Sr_{eq(calcite\text{-}water)}$ values of foraminifera from the Holocene and Late Pleistocene (an age based on mud core depths, a rough estimate at best) that have a 4° C Mg/Ca-derived temperature difference to support the case that temperature does not control this fractionation. Temperature differences between today and the last glacial maximum in the Caribbean are reported to be 2-3° C (Schmidt et al., 2006). Böhm et al. (2012) measured a small non-significant difference in the $\delta^{88}Sr$ of the

samples from the Holocene versus those from the last glacial maximum (0.007 ± 0.009 ‰ difference, which corresponds to 0.5˚ ± 1.0° C by our curve). This is supportive evidence from biogenic calcite that temperature differences are <1.5° C, and that temperature is not playing a role, given that the growth rates of the foraminifera of the two periods are identical. However, natural inorganic calcite samples grow much slower than the experimentally deposited calcite, and it is possible that the slower growth rate negates the rate effect allowing the temperature of the growth medium to imprint itself on the $\delta^{88}Sr$ values. Diffusion of Sr isotopes through water is fast enough (DePaolo, 2011; Watson and Muller, 2009) to allow refreshment of the isotopes being deposited on the crystal face and thus may not be a viable explanation for the fractionation that we are seeing.

Tang et al. (2008) indicates that as temperature increases, the amount of Sr incorporated into the crystal lattice in comparison to the amount of Ca, decreases (T° C ↑:$[Sr^{2+}/Ca^{2+}]$ ↓). Based on the surface entrapment model (SEMO), the Sr is incorporated into the surface layer, but then some escapes back out into solution. This model predicts that the escaping Sr will favor the lighter isotopes and there will be a preferential incorporation of the heavier strontium isotope, ^{88}Sr, over the lighter strontium isotope, ^{86}Sr, in the calcite due to more rapid growth rates, with the value of $\delta^{88}Sr$ depending less on rate of growth and consequently more on temperature. This means that as the temperature increases, even though the amount of strontium incorporated into the crystal decreases, the $\delta^{88}Sr$ in the calcite will increase ($\delta^{88}Sr$ ↑: T° C ↑), (Table 5), opposite of what is expected

from the growth rate experiments (Böhm et al., 2012). This counters the partitioning of Sr thermodynamically and could potentially cause the $\delta^{88}Sr$ to increase as the temperature of formation increases. This SEMO, temperature-dependent scenario is supported by our data over growth rate controls.

Cation dehydration, pH of precipitating solutions, and biological effects may also affect Sr isotope signatures. Dehydration effects (where a hydrated species must rid itself of its surrounding hydration shell) are another mode by which fractionation can occur. Bourg et al., (2010) describes both experimental and modeling approaches using molecular dynamics that suggest isotopes in micropores and possibly at the surface of a forming crystal can be subject to fractionation effects in contradiction to numerous studies that suggest otherwise (Bourg et al., 2010). This effect may be independent of temperature, at least up to the modeled value of 75° C. However, if temperature is a factor, higher temperatures would tend to provide more energy to break the bonds between the heavier molecules driving the isotope ratios to heavier values (more positive). DePaolo (2011) suggests that kinetic effects during dehydration account for the lighter calcium isotopes being favored in mineral deposition, essentially stating that the lighter hydrated cation has a smaller bond to break with the water molecules before it is deposited on the surface of the growing crystal and therefore the crystal growth will favor the lighter isotopes if temperature is not a factor. Given that Sr is affected similarly, then similar to growth rate, kinetic effects will shift $\delta^{88}Sr$ values lower which would show a negative slope if this

were the case suggesting that this is not occurring in our samples or that at a minimum, it is not a dominant factor. In addition, pH affects the rate of precipitation (Nehrke et al., 2007; Tang et al., 2008) within a narrow range of $[Ca^{2+}]/[CO_3^{2-}] \approx 1$ (Nehrke et al., 2007). Biological or vital effects are described by Zeebe et al. (2006) as "offsets from isotopic and elemental equilibrium that were attributed to life processes". There is no evidence in any of our stable isotope data, including the $\delta^{18}O$ (Decker et al., 2017) that the cave spar we are studying was precipitated through biological mediation, and therefore the vital effect is not considered as a factor in the fractionation of Sr isotopes for these crystals.

Another factor that should be considered is the starting $[Sr^{2+}]$ and $\delta^{88}Sr$ of the precipitating solutions. While these variables will not affect local variations to any substantial degree (this factor will not likely change during stalagmite growth), they may have a large influence on differences between regions. The $\delta^{88}Sr$ of water that formed cave spar from one region may be different for the same temperatures of formation for water of another region. Shalev et al. (2013) show that terrestrial waters can vary significantly, but river, stream, and drip waters analyzed have values in the range of 0.263 ± 0.039 ‰ (n=5). Ground waters analyzed by Shalev et al. (2013) are higher and show more variation (0.382 to 0.656; n=4). There could be differences in the value of hydrothermal ground water and vadose ground water that is producing a trend that resembles temperature dependence.

We have argued that many of the factors shown to affect the incorporation of trace elements such as strontium, and the fractionation of their isotopes during building of the crystal lattice by other authors, may not play a significant role in the variation of our speleothem values. We show, both quantitatively and qualitatively, that fractionation of strontium occurs during crystallization due to temperature. Growth rates of speleothem types used in this study are much slower than those reported to affect $\delta^{88}Sr$ experimentally, and therefore, may not contribute greatly to $\delta^{88}Sr$ values in speleothems. Therefore, the $\delta^{88}Sr$ for slowly forming, abiogenic calcite in speleothems may be useful for determining the temperature of formation.

Summary

The cave spar formed in deep phreatic conditions in small geode-like caves during igneous episodes under hydrothermal conditions likely formed at similar growth rates. Temperature data from cave spar fluid inclusions co-varies with the $\delta^{88}Sr$ of the cave spar, suggesting that temperature, not growth rate, is controlling fractionation of strontium isotopes. $\delta^{88}Sr$ of cool water speleothems from the same study area further suggest a $\delta^{88}Sr$ versus temperature correlation. Qualitative comparison of $\delta^{88}Sr$ of high temperature, medium temperature, and low temperature speleothems also support the temperature driven fractionation of strontium in natural calcite. However, we cannot rule out that the higher-temperature cave spar calcite could have grown slower than the medium-temperature mammillary calcite, which grew slower than the cool-

temperature stalagmites and a shelfstone, producing a coincidental correlation. The correlation within the cave spar samples, which probably formed very similarly (including growth rates), is the best evidence for a temperature relationship. Therefore, our equation may be useful to determine the temperature of formation of cave spar samples that have no fluid inclusions, or that have inclusions that are not useful due to any number of circumstances. Mammillary calcite temperature of formation may also be estimated. For example, the Lake of the Clouds mammillary $\delta^{88}Sr$ temperature is ~33˚ C ± 6°, which seems reasonable and comparable to mammillaries from Devils Hole, Nevada.

Tables

Table 4: Fluid inclusion size (volume is estimated volume of vapor phase to volume of inclusion), T_h, T_{mi}, T_{mf}.

	Size (µm)	Size (µm)	%Volume	T_h (˚C)	±	T_{mi} (˚C)	±	T_{mf} (˚C)	±
BLMC-002A	7	20	11	69.5	1.0	-14.2	0.5	-0.3	0.5
BLMC-002B	10	29	8	61.0	0.5	-21.6	0.5	0.0	0.5
BLMC-005A1	10	29	10	54.3	1.0	N/O	-	-0.2	0.5
BLMC-005A2	5	14	8	63.3	0.5				
BLMC-005D	4	11	5	53.8	0.5	N/O	-	N/O	-
BLMC-011A	3	9	50	50.4	0.5	-3.5	0.5	-1.2	0.5
BLMC-011D	3	9	80	50.7	0.5				
CAVE-003A	25	72	18	66.7	0.5	-1.0	0.5	0.0	0.5
CAVE-003B	15	43	25	71.6	0.5				
CAVE-006A	30	86	10	66.0	0.5	N/O	-	N/O	-
CAVE-006B	45	129	8	65.7	0.5	N/O	-	N/O	-
CAVE-007A	3	9	20	81.9	0.5	-32.1	0.5	-14.2	0.5
CAVE-007B	5	14	15	82.1	0.5				
CAVE-009A	5	14	15	75.2	0.5	-13.6	0.5	-2.0	0.5
CAVE-009B	15	43	15	71.9	0.5	-4.8	0.5	-0.6	0.5
CAVE-011A	80	229	15	71.6	0.5	-4.0	0.5	-0.2	0.5
CAVE-011B	10	29	10	66.5	1.0				
GUMO-001A	15	43	3	65.3	0.5	-9.9	0.5	-0.4	0.5
GUMO-001B	20	57	3	57.6	0.5				
GUMO-003A	20	57	5	65.6	0.7	-5.0	0.5	-1.9	0.5
GUMO-003B	3	9	5	53.2	2.2				
USFS-002A	20	57	9	38.5	0.5	N/O	-	N/O	-
USFS-002B	40	114	20	71.8	0.5	-10.0	1.0	0.0	0.5
USFS-006A	6	17	8	50.9	0.5				
USFS-007A	4	11	8	62.4	0.5	N/O	-	0.0	0.5
USFS-008B	28	80	8	81.8	0.5				
USFS-009A	10	29	8	81.5	0.5				
USFS-009B	2	6	5	59.8	0.5				
USFS-010(Y)A	10	29	10	74.7	0.5	-34.0	0.5	0.0	0.5
USFS-010(Y)C	7	20	8	53.9	0.5				
USFS-010(Y)B	15	43	5	53.6	6.0				
USFS-010(W)	50	143	10	58.0	2.0				
USFS-011A	10	29	10	48.8	0.5	-0.2	0.5	1.0	0.5
USFS-011B	10	29	10	59.8	0.5				

Table 5: Weighted average of $\delta^{88}Sr$ for each sample and corresponding temperature of formation. We have also included the $\delta^{88}Sr$ of two igneous standards, BHVO and TML, along with speleothem results from other studies.

	$\delta^{88}Sr$ (‰)	2σ error	n	Temp (°C)	U/Pb Age (Ma)
Guadalupe Mountains cave spar					
BLMC-002	0.45	0.08	6	61 ± 1	68.3 ± 2.9
BLMC-005	0.23	0.03	6	54 ± 1	29.8 ± 1.2
BLMC-011	0.32	0.08	7	50 ± 1	34.4 ± 1.2
CAVE-003	0.52	0.07	2	72 ± 1	13.1 ± 0.3
CAVE-006	0.54	0.05	6	66 ± 1	44.6 ± 1.6
CAVE-007	0.38	0.06	6	60 ± 1	77.2 ± 1.2
CAVE-009	0.44	0.07	7	63 ± 1	62.4 ± 2.8
CAVE-011	0.47	0.06	8	67 ± 1	36.1 ± 2.1
GUMO-001	0.28	0.04	6	58 ± 1	33.2 ± 0.7
GUMO-003	0.34	0.04	6	53 ± 1	27.6 ± 1.3
USFS-006	0.42	0.08	4	51 ± 1	53.6 ± 0.5
USFS-007	0.41	0.09	4	62 ± 1	37.9 ± 1.8
USFS-009	0.44	0.02	6	60 ± 1	54.5 ± 1.3
USFS-010(Y)	0.50	0.19	2	60 ± 1	112.8 ± 1.0
USFS-011	0.41	0.06	4	49 ± 1	29 ± 2
Lake of Clouds mammillary - Carlsbad Cavern					
CBM (LOC)	0.17	0.07	4	nr	
Grand Canyon mammillaries					
Bida7	0.23	0.03	5	nr	nr
GCC	0.34	0.06	3	nr	nr
GnC2-3	0.25	0.05	3	nr	nr
Lean	0.31	0.05	3	nr	nr
Bob4	0.28	0.07	3	nr	nr

nr = none reported
n/a = not applicable

	$\delta^{88}Sr$ (‰)	2σ error	n	Temp (°C)	U/Pb Age (Ma)
Fort Stanton Cave stalagmite (early Holocene)					
AH1-2mm	0.06	0.03	6	13 ± 3	nr
Lechuguilla Cave shelfstone calcite (late Holocene)					
LECH VS-1	0.08	0.04	8	20 ± 3	nr
WBC4-Calcit	-0.08	0.07	7	12 ± 3	nr
CaCa-BC7-14mm (late Holocene)					
stalagmite	-0.05	0.07	3	nr	nr
CaCa-BC21-8to12cm (glacial age)					
stalagmite	0.05	0.05	7	nr	nr
CaCa-BC5-108_5d (glacial age)					
stalagmite	-0.11	0.16	4	nr	nr
Other studies					
Soreq Cave, Israel (Shalev et al., 2016, 2017)					
stalagmite	0.6	0.29	4	nr	nr
stalagmite	0.68	0.31	4	nr	nr
Israel caves (Halicz et al., 2008, 2009)					
speleothem	-1.4	1.7	3	nr	nr
speleothem	-2	0.8	3	nr	nr
Volcanic Standards					
BHVO-2	0.22	0.01	9	n/a	n/a
TML	0.21	0.06	9	n/a	n/a

Extended Data

Text

Strontium Chromatographic Separation:

Column Preparation:

250 µl Eichrom Sr-spec resin (part #: Sr-B50-A; LOT: SRA 121517)

Wash with two column full's (CF) (~4 ml) of 18 MΩ cm^{-1} ultrapure H_2O

Condition with one CF (~2 ml) 3 N HNO_3

Sample Preparation:

Select 3 sub-samples, each <50mg and place in separate beakers

Add 3 drops of 7 N HNO_3 from bottle dropper to dissolve

Load sample into columns and clean beakers from which the samples came

Sample Collection

Rinse with 2 CF (~2 ml) of 3 N HNO_3

Collect with 1000 µl (4 column volumes (CV) 18 $M\Omega^{-1}$ cm ultrapure H_2O

Dry down on low heat

Add 500 µl 3% HNO_3 and dissolve

Transfer to vial

Extended Data Figures

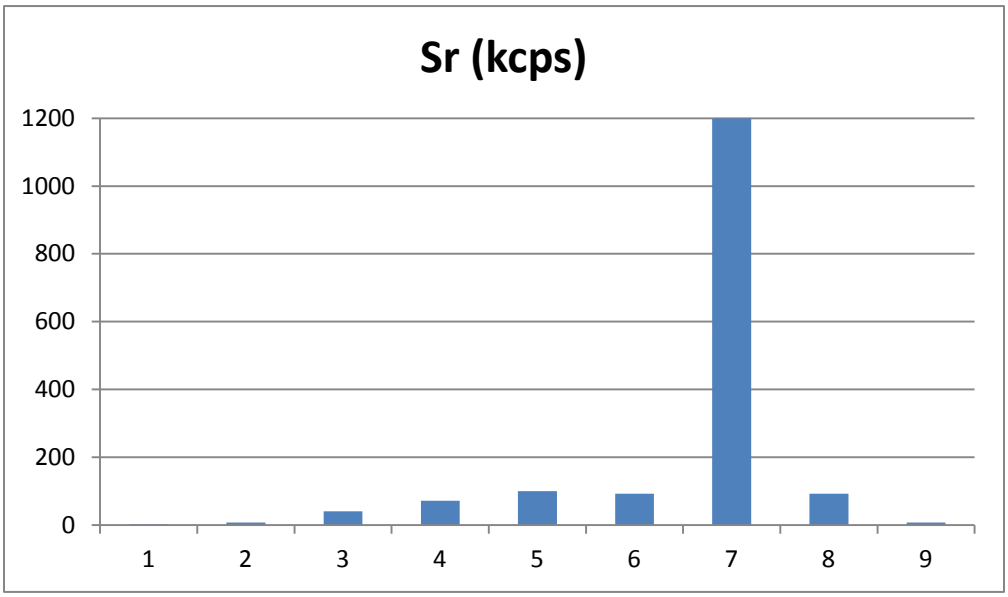

Figure 16: Strontium column calibration graph. Y-axis, kilo-counts per second. X-axis: Number of elutions captured (1000 µl each collection). Step 1, measure background count, step 2, load sample (0.5 ml 3 M HNO3), steps 3-6, clean sample with 1 ml 3N HNO3 each, step.

Figure 17: $^{90}Zr/^{91}Zr$ Drift

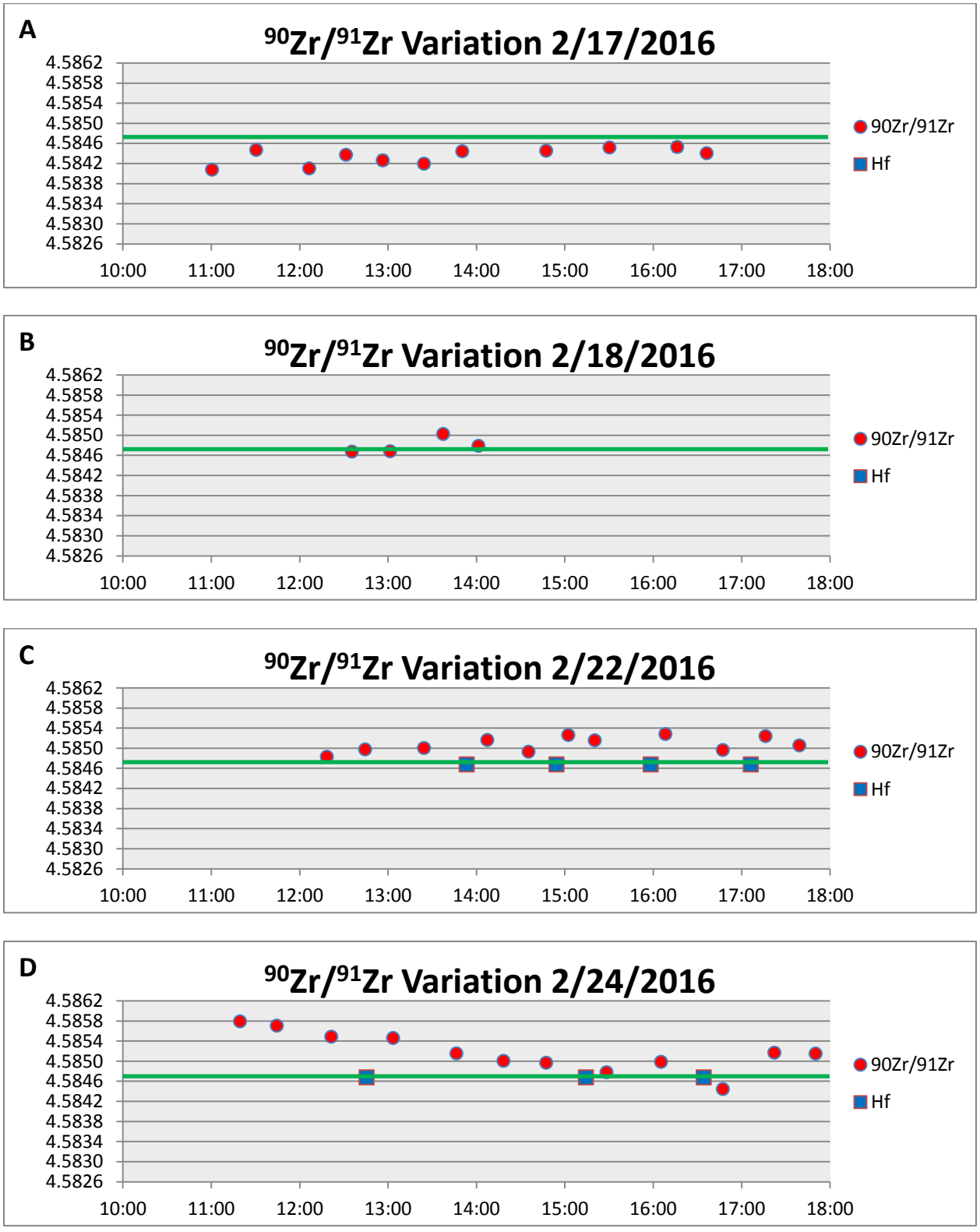

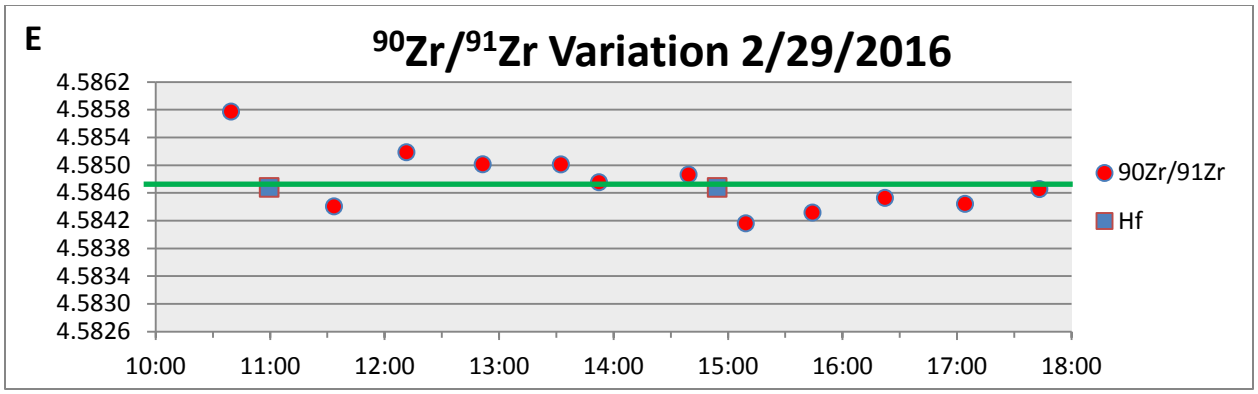
E
90Zr/91Zr Variation 2/29/2016
4.5862
4.5858
4.5854
4.5850
4.5846
4.5842
4.5838
4.5834
4.5830
4.5826
10:00
11:00
12:00
13:00
14:00
15:00
16:00
17:00
18:00
90Zr/91Zr
Hf

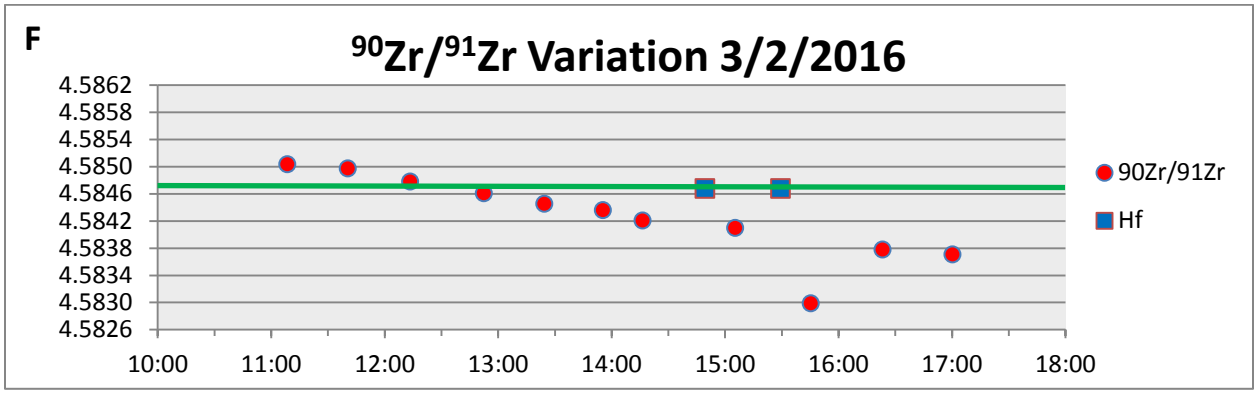
F
90Zr/91Zr Variation 3/2/2016
4.5862
4.5858
4.5854
4.5850
4.5846
4.5842
4.5838
4.5834
4.5830
4.5826
10:00
11:00
12:00
13:00
14:00
15:00
16:00
17:00
18:00
90Zr/91Zr
Hf

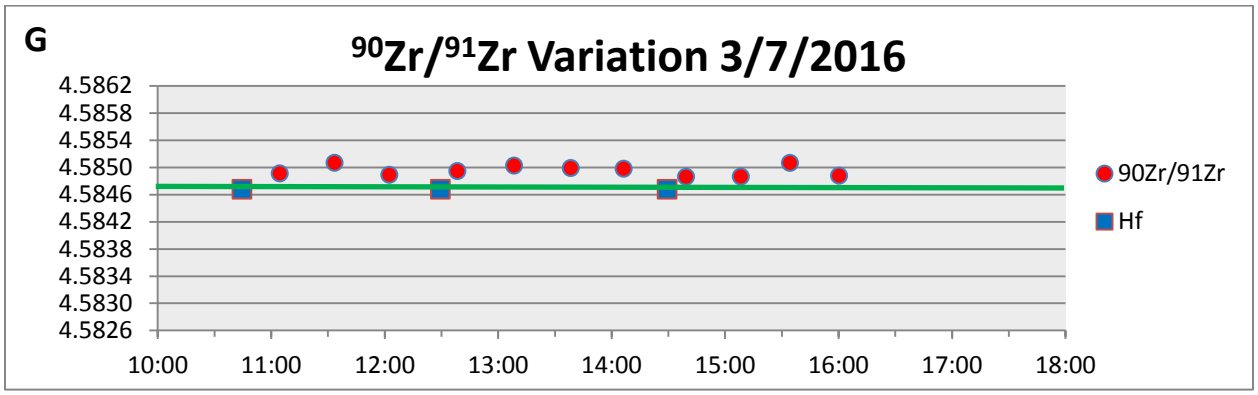
G
90Zr/91Zr Variation 3/7/2016
4.5862
4.5858
4.5854
4.5850
4.5846
4.5842
4.5838
4.5834
4.5830
4.5826
10:00
11:00
12:00
13:00
14:00
15:00
16:00
17:00
18:00
90Zr/91Zr
Hf

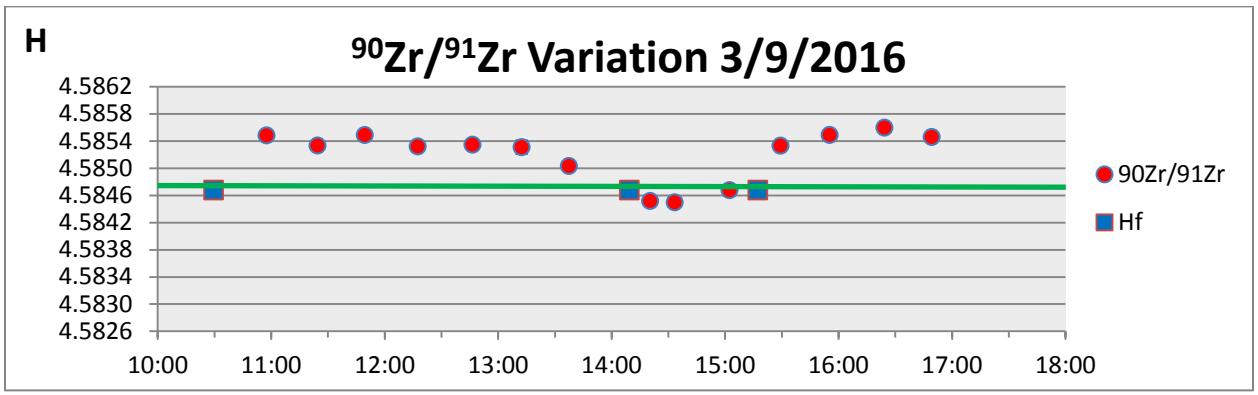
H
90Zr/91Zr Variation 3/9/2016
4.5862
4.5858
4.5854
4.5850
4.5846
4.5842
4.5838
4.5834
4.5830
4.5826
10:00
11:00
12:00
13:00
14:00
15:00
16:00
17:00
18:00
90Zr/91Zr
Hf

I

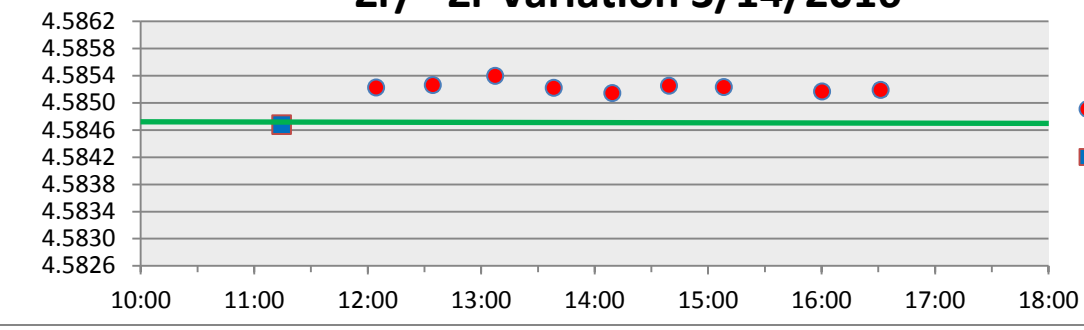
90Zr/91Zr Variation 3/14/2016
4.5862
4.5858
4.5854
4.5850
4.5846
4.5842
4.5838
4.5834
4.5830
4.5826
10:00
11:00
12:00
13:00
14:00
15:00
16:00
17:00
18:00
90Zr/91Zr
Hf

J

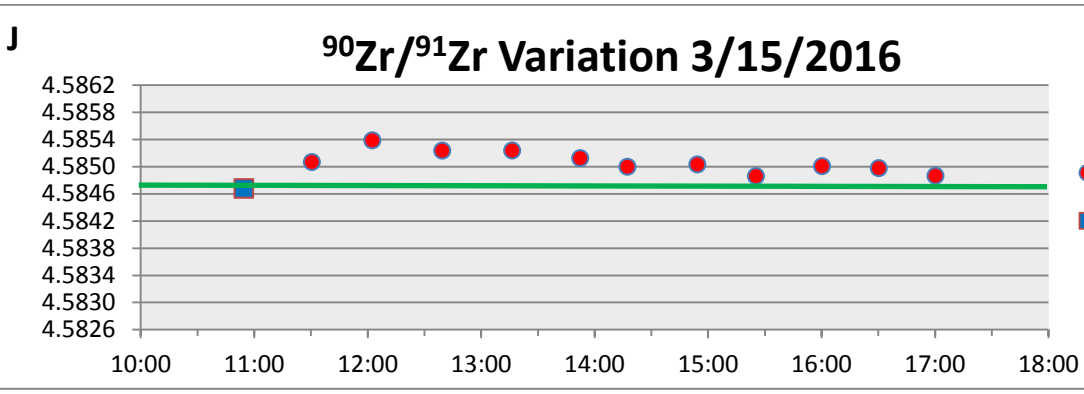
90Zr/91Zr Variation 3/15/2016
4.5862
4.5858
4.5854
4.5850
4.5846
4.5842
4.5838
4.5834
4.5830
4.5826
10:00
11:00
12:00
13:00
14:00
15:00
16:00
17:00
18:00
90Zr/91Zr
Hf

K

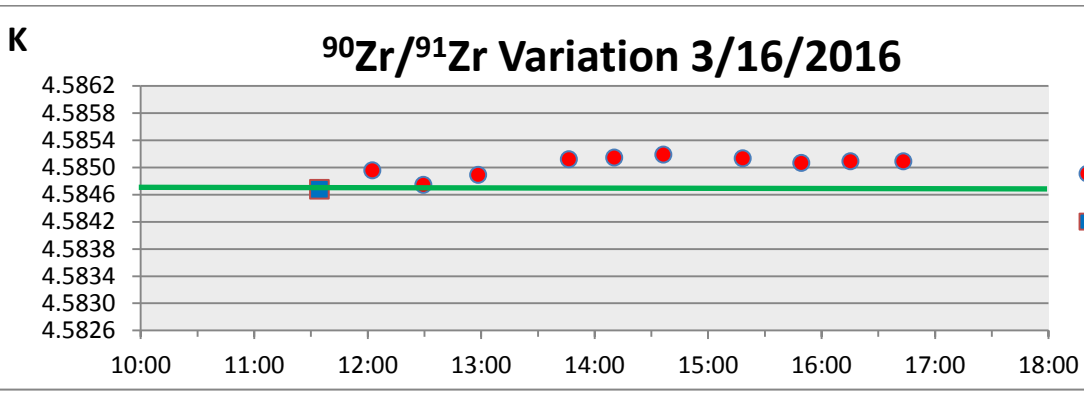
90Zr/91Zr Variation 3/16/2016
4.5862
4.5858
4.5854
4.5850
4.5846
4.5842
4.5838
4.5834
4.5830
4.5826
10:00
11:00
12:00
13:00
14:00
15:00
16:00
17:00
18:00
90Zr/91Zr
Hf

L

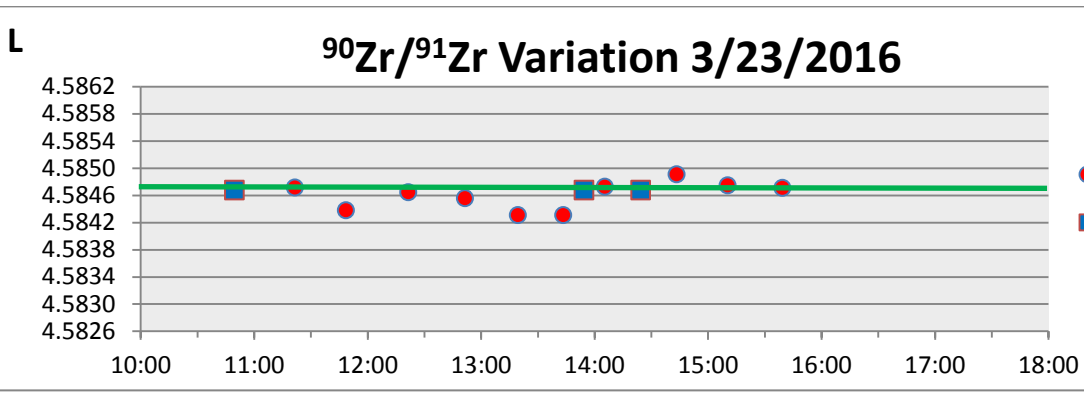
90Zr/91Zr Variation 3/23/2016
4.5862
4.5858
4.5854
4.5850
4.5846
4.5842
4.5838
4.5834
4.5830
4.5826
10:00
11:00
12:00
13:00
14:00
15:00
16:00
17:00
18:00
90Zr/91Zr
Hf

M

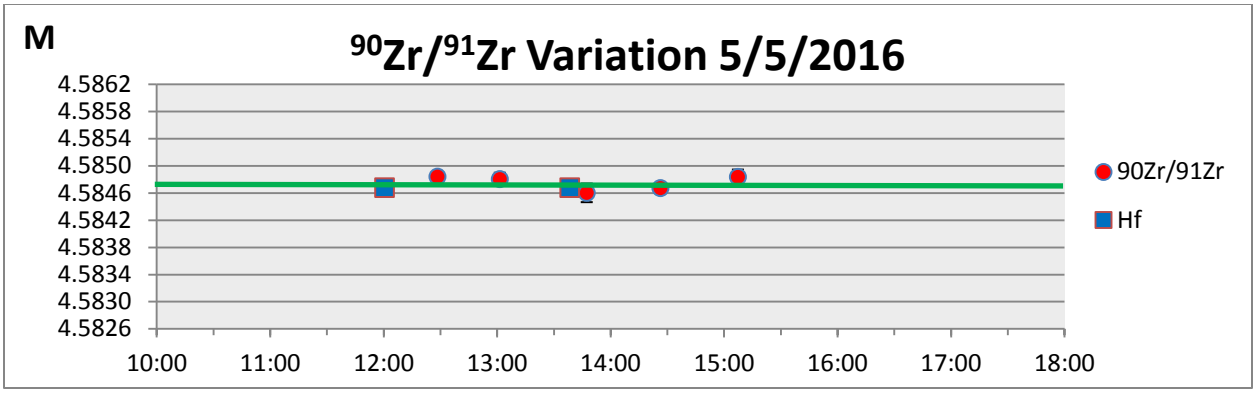
90Zr/91Zr Variation 5/5/2016
4.5862
4.5858
4.5854
4.5850
4.5846
4.5842
4.5838
4.5834
4.5830
4.5826
10:00
11:00
12:00
13:00
14:00
15:00
16:00
17:00
18:00
90Zr/91Zr
Hf

N

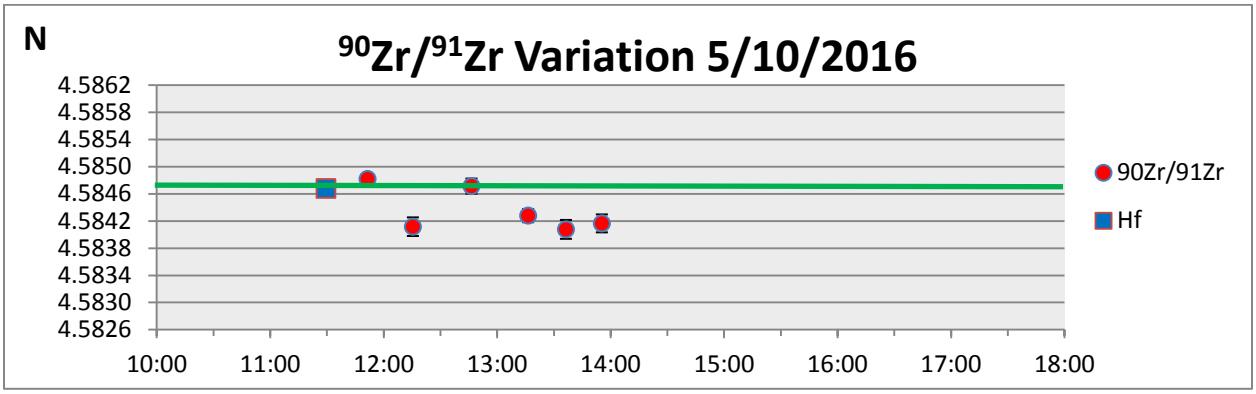
90Zr/91Zr Variation 5/10/2016
4.5862
4.5858
4.5854
4.5850
4.5846
4.5842
4.5838
4.5834
4.5830
4.5826
10:00
11:00
12:00
13:00
14:00
15:00
16:00
17:00
18:00
90Zr/91Zr
Hf

O

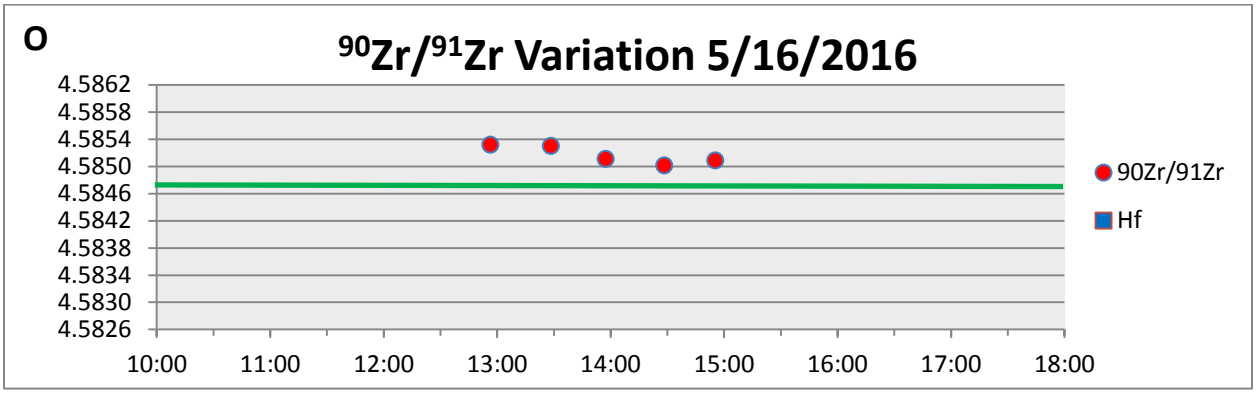
90Zr/91Zr Variation 5/16/2016
4.5862
4.5858
4.5854
4.5850
4.5846
4.5842
4.5838
4.5834
4.5830
4.5826
10:00
11:00
12:00
13:00
14:00
15:00
16:00
17:00
18:00
90Zr/91Zr
Hf

Extended Data Tables

Table 6: Sr column calibration

		^{88}Sr (kcps)	$^{88}Sr\ (kcps)_{corr}$	^{115}In (kcps)	Notes	
1	Background	2.9	0	9	Background cps in thousands.	
2	SR01	8	5	850	Load	500 µl 1 ppm Sr
3	SR02	41	38	840	Clean	1 ml 3 N HNO_3
4	SR03	72	69	850	Clean	1 ml 3 N HNO_3
5	SR04	100	97	820	Clean	1 ml 3 N HNO_3
6	SR05	93	90	830	Clean	1 ml 3 N HNO_3
7	SR06	1,200	1197	850	1st Collect	1 ml 18 MΩ H_2O
8	SR07	93	90	810	2nd Collect	1 ml 18 MΩ H_2O
9	SR08	7.4	5	800	3rd Collect	1 ml 18 MΩ H_2O

Table 7: MC-ICP-MS strontium program and typical set up.

UNM_Sr_Zr.met program

Cup	Isotope	Resistor
L3	^{83}Kr	10^{12}
L2	^{84}Sr	10^{11}
L1	^{85}Rb	10^{12}
C	^{86}Sr	10^{11}
H1	^{87}Sr	10^{11}
H2	^{88}Sr	10^{10}
H3	^{90}Zr	10^{11}
H4	^{91}Zr	10^{11}

Integration Time: 16.777 (s)
Integrations: 1
Idle Time: 10.0 (s)
Cycles: 20

Typical MC-ICP-MS Set Up

HV	9.33E-08	mbar
FV	2.31E-04	mbar
IGP	2.79E-09	mbar
OP	1299.10	W
SGF	1.097	l/m
AGF	0.97	l/m

CHAPTER 4 - U-PB DATING OF CAVE SPAR: A NEW SHALLOW CRUST LANDSCAPE EVOLUTION TOOL

(Decker, D.D., Polyak, V.J., Asmerom, Y. & Lachniet, M.S. (2017). U-Pb dating of cave spar: A new shallow crust landscape evolution tool. Tectonics, 36. https://doi.org/10.1002/2017TC004675)

Abstract

In carbonate terranes, rocks types that provide apatite are not available to effectively use apatite fission track (AFT) or (U/Th)-He chronometry (AHe). Here we suggest that calcite cave spar can be an effective chronometer and complimentary to AFT and AHe thermochronometers in carbonate regions such as our study area, the Guadalupe Mountains of southeastern New Mexico and west Texas. Our measured depth of cave spar deposition is 500 ± 250 meters beneath the regional water table, formed at temperatures of 40˚ to 80˚ C, indicating these caves and their spar crystals form near the supercritical CO_2-subcritical CO_2 boundary where we interpret the origin of both the caves and spar to occur. This depth-temperature relationship suggests a higher than normal geotherm, likely associated with regional magmatic activity. As a case study we examined the timing of uplift of the Guadalupe Mountains previously attributed to the compressional Laramide orogeny (ca. 90 to 50 Ma), later extensional tectonics associated with Basin and Range (ca. 36 to 28 Ma) or the opening of the Rio Grande Rift (ca. 20 Ma to present). We show that most of the spar origin is coeval with the ignimbrite flare-up between 36 – 28 Ma. Our results constrain the initiation of Guadalupe Mountains block uplift, relative to the surrounding terrain, to between 27-16 Ma and reconstruct the evolution of a low-lying regional landscape prior to block uplift from 185 to 28 Ma, in support of

models that attribute regional surface uplift to extensional tectonics and associated volcanism.

Introduction

Background. Two shallow crust (<3 km) thermochronometric methods, apatite fission track (Donelick et al., 2005; Reiners et al., 2005) and apatite (U-Th)/He or AHe thermochronometry, are currently commonly used in shallow landscape evolution studies (Ehlers and Farley, 2003; Farley, 2002; Farley and Stockli, 2002). There are a number of geologic settings in which these techniques are not useable due to lack of the rocks that contain the minerals used in these methods (Donelick et al., 2005). Moreover, these techniques have led to some disparate conclusions regarding interpretations of shallow depth data (Donelick et al., 2005; Flowers and Farley, 2012, 2013; Green et al., 2006; Hendricks and Redfield, 2005, 2006; Karlstrom et al., 2013; Karlstrom et al., 2014; Larson et al., 2006). In this study we show that large calcite crystals, herein referred to as cave spar (euhedral druses of calcite crystals 2 – 30 cm in length, lining small geode-like caves, Figure 2) can be used as an effective depth and time indicator for landscape evolution studies, complimentary to the apatite fission track and apatite (U/Th)-He thermochronometers for use in landscape evolution studies (Decker et al., 2016). This method is not based on the temperature at which fission tracks heal themselves, or the amount of gaseous daughter nuclides accumulated in the crystal structure, rather we are able to determine the timing of crystal formation with U/Pb isotopes (this study) and directly measure depth of

formation of the crystals (Decker et al., 2016). Thus, a

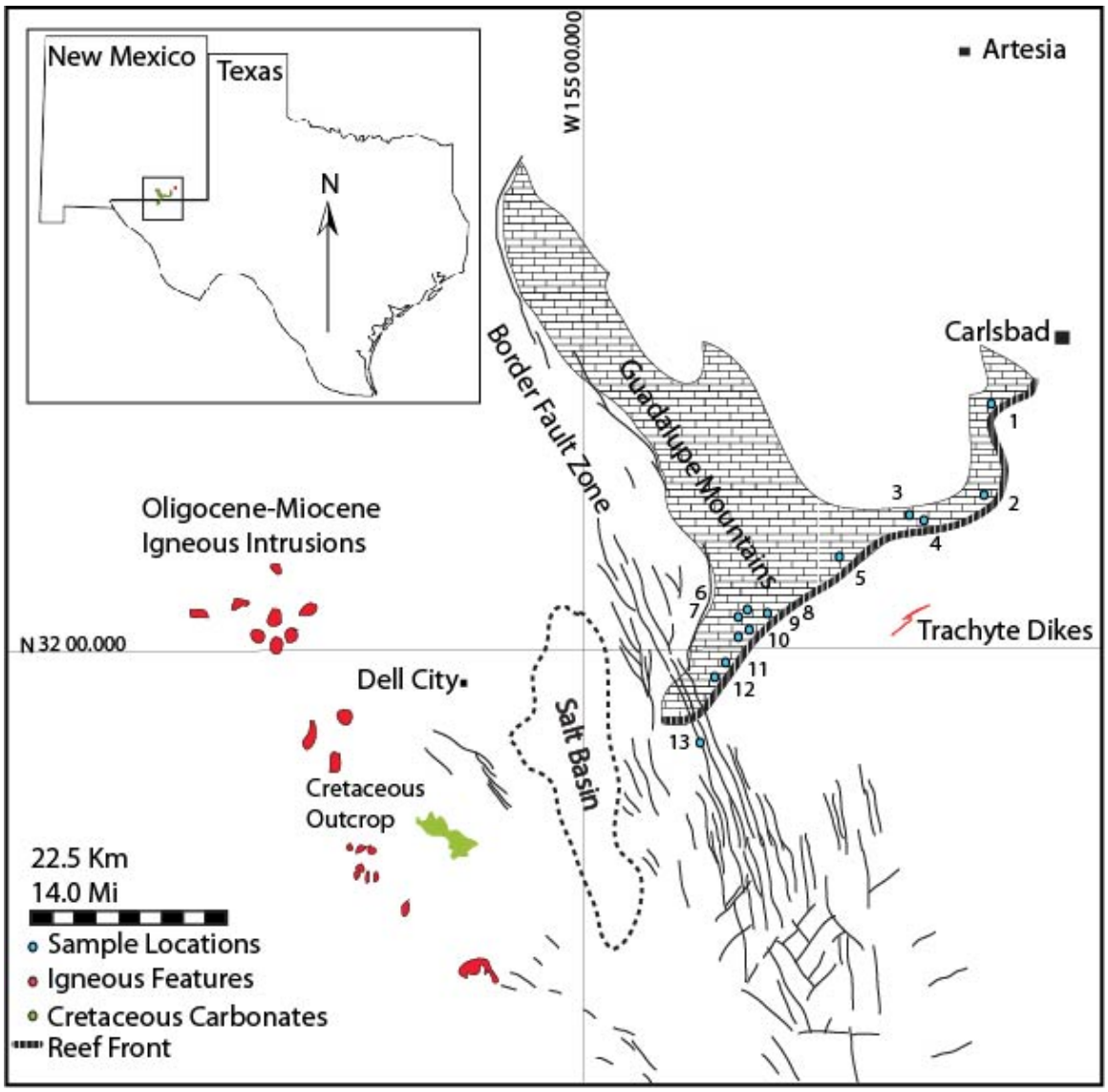

Figure 18: Selected sample locations and nearby igneous features in the Guadalupe Mountains, southeastern New Mexico and west Texas. 1: BLMC-005, 2: BLMC-002, 3: CAVE-004 & -006, 4: CAVE-002, -003, -007, -008 & CC-001, 5: CAVE-011, 6: USFS-006, 7: USFS-002 & -007, 8: USFS-008, 9: USFS-009, 10: BLMC-011, 11: GUMO-002 & -003, 12: GUMO-001, 13: GUPA-001. The geologic features on this map are a compilation from different sources (Geologic Atlas of Texas - Van Horn El Paso Sheet (Barnes, 1983), Google Earth.

single isochron age is coupled to the depth of origin of spar crystals, and multiple samples provide multiple ages that correspond to that spar depth. We demonstrate the potential of this new method using the Guadalupe Mountains of southeastern New Mexico and west Texas (Figure 2B and Figure 18), as a proof

of concept where our measured U-Pb spar ages are used to constrain the timing of the initiation of the rotation of the Guadalupe Mountains tectonic block (Guadalupe block) as well as the evolution of the landscape prior to block movement relative to the surrounding terrain.

Cave Spar Model. From depths of formation of three cave spar samples, one from Grand Canyon and two from the Guadalupe Mountains (Decker et al., 2016), we constructed a new cave genesis (speleogenesis) model that explains the origin of these small (<30 m in diameter) geode-like caves (spar caves) and the cave spar that lines them. The three depths show that spar cave speleogenesis and its final phase, cave spar deposition, takes place at 500 ± 250 meters below a regional water table, which corresponds to the effective pressure (P_e) of the supercritical CO_2-subcritical CO_2 boundary (Decker et al., 2016). We determined a measured depth using a Grand Canyon cave spar that formed in the Redwall Limestone 232.3 ± 1.8 Ma (U-Pb age of spar) and based the measured depth on near-sea level Triassic Moenkopi lithology positioned 750 meters above the cave spar (Decker et al., 2016). The two Guadalupe Mountains spar sample depths were derived by extrapolating the elevation of the water table based on the alunite-age water table position (Polyak et al., 1998) (alunite is formed at/near the water table, therefore dating the alunite provides the time and elevation of the paleo-water table). In addition to depth of formation of cave spar (Crysdale, 1987; Mruk, 1985), the cave spar temperature of homogenization (T_h) (Crysdale, 1987; Mruk, 1985, 1989) using fluid inclusion assemblage (FIA) analysis of the spar within the spar caves in the Capitan formation and back reef

equivalents (cave-forming strata) yield formation temperatures between 40˚ and 80˚ C and can be used to determine the hydrostatic pressure at which these minerals formed. These temperatures and pressures are consistent with a supercritical CO_2 speleogenesis model for the spar caves and the calcite cave spar lining them (Decker et al., 2016).

Our model states that during episodes of magmatic activity, CO_2 is released from the magma body in a supercritical state. Since $scCO_2$ is much less dense and more fluid than the surrounding rock, it makes its way toward the surface relatively easy. In its supercritical state, the CO_2 is not absorbed into water as it encounters the water table. At a point roughly 500 meters below the water table surface, however, due to decreases in both temperature and pressure, the CO_2 transforms states from supercritical to subcritical and is immediately absorbed into the aquifer where it acidifies the water and consequently dissolves the limestone. This dissolved limestone is carried away by the hydrologic flow and is replaced by more acidic water as long as the magmatically driven hydrothermal system is active, continuing to dissolve voids at a $scCO_2$-$subCO_2$ horizon. Once the magmatic activity ceases, the waters within the voids become slightly supersaturated, and at the temperatures and pressure at that depth, form the scalenohedral spar of interest. Because we can measure and model the depth (pressure), timing, and temperature of calcite spar formation, our results are used in a similar manner as low temperature apatite thermochronometers (Chew and Spikings, 2015; Dumitru, 2000; Renne, 2000).

Regional Geologic History. The Guadalupe Mountains have been heavily studied over the past seventy years, indeed, they are the type location for Permian reef systems. Numerous authors have produced large, in-depth volumes on the geology of the region (Austin, 1978; Flawn, 1956; Garber et al., 1989; Hayes, 1964; Hayes and Adams, 1962; Hill, 1987; Hill, 1996; Kelley, 1971; King, 1948; Kirkland, 2014; Meyer, 1966) and therefore we will only briefly cover it here. Our area of interest spans from south-eastern New Mexico into west Texas and includes the Diablo Plateau, the Guadalupe Mountains, the Delaware Basin and the Gypsum Plains (Figure 2 and Figure 18**)**. The region is well known for its petroleum production (Permian Basin), potash deposits, large, well decorated sulfuric acid type caves, and the Waste Isolation Pilot Plant (WIPP); and less well known for the Mississippi Valley Type ore deposits in the Guadalupe Mountains (Hill, 1993). The basement rocks in the region belong to the Texas craton and are mostly granitic. These rocks were emplaced in two episodes, the Mazatzal orogeny between 1.69 and 1.65 Ga and the Granite-Rhyolite Province starting approximately 1.55 Ga (Whitmeyer and Karlstrom, 2007) and are found approximately 3.3 km below the surface (Flawn, 1956). The Tabosa basin existed in the same location as the Delaware and Midland basins (Hill, 1996) during the late Proterozoic through the Mississippian and was probably formed by continental rifting in the Proterozoic to Cambrian (Hills, 1984). This basin was dissected by the Central Basin Uplift during the late Mississippian Ouachita orogeny. The entire region remained near sea level during this phase and accumulated vast amounts of sediment (Hill, 1996). During the Permian, the area

was inundated by the sea forming a restricted basin where the massive Capitan limestones and Artesia Group back reef sediments were deposited followed by the Castile, Salado, Rustler and Dewey Lake evaporites (Austin, 1978; Hayes and Adams, 1962; Hill, 1987). The area was tectonically quiescent through the remaining Paleozoic and Mesozoic and was not disturbed again until possibly the beginning of the Cenozoic during the initiation of the Laramide orogeny (Eaton, 2008). At some point after the Cretaceous, the region was uplifted from sea level to its current elevation of approximately 2.66 km at its highest point.

There are competing models that describe the timing of the uplift of the Guadalupe block. One model measured one kilometer of relative Guadalupe block uplift from 12 Ma to present coeval with Rio Grande rifting (Polyak et al., 1998). Other models suggests that the area arose primarily during the Laramide Orogeny (Cather et al., 2012; DuChene and Cunningham, 2006; Eaton, 2008) or during the Oligocene-Miocene (King, 1948). Pre-Laramide crustal thickening has been suggested based on petrographic evidence (Scholle et al., 1992). With the exception of the phase of apparent uplift during Rio Grande rifting, a more robust tectonic history of the Guadalupe Mountains region, in which absolute timing of events is critical, is lacking.

The Guadalupe Mountains spar caves examined in this study are largely confined within the cave-forming strata (Hill, 1996) of the Capitan Limestone and the backreef equivalents of the Yates, Tansill, and Seven Rivers formations. With no known topographic expression for this region before the Guadalupe Mountains tectonic block was uplifted relative to the Salt Basin (Figure 18), our

cave spar U-Pb ages are indications of when the cave-forming strata was 500 ± 250 m below a regional water table, and likely near this depth below the paleo-surface. Since block uplift and tilting would have moved the cave-forming region out of the spar forming depths, we can use the thermochronometry and the U-Pb age results from these crystals to reconstruct a deep time history of the Guadalupe Mountains region landscape.

Methods

Sample Selection

Samples were selected from 'spar' caves located in the Permian Capitan Reef and immediate backreef and forereef deposits of the Artesia Group (the spar cave-forming strata) along the reef escarpment in the Guadalupe Mountains of New Mexico and Texas (Figure 18). The caves have been described by Decker et al. (2016). The exact cave locations are considered sensitive resource information and can be obtained through the appropriate resource personnel at Carlsbad Caverns National Park, Guadalupe Mountains National Park, Bureau of Land Management, Carlsbad, and the US Forest Service, Guadalupe District office. Each sample was selected based on its size and lack of visual surface alteration. We collected samples that were already broken or physically damaged to minimize the negative impact to the sampled caves. The samples ranged in size from 4 cm (long axis) to 25 cm. All cave spar samples collected are the mesogenetic spar (formed after the reef stopped growing and before the beginning of H_2SO_4 speleogenesis) described by Hill (1996). Sample location descriptions are available upon request.

Isotopic Methods

U-Pb Chronology. U-Pb and uranium-series dating methods were used to determine the ages of 22 cave spar crystals, a sample of cave mammillary, and a sample of fault-filling vein calcite. For each spar sample a 1 cm^2 sized piece was extracted from the interior of each spar sample. Surfaces of these pieces were cleaned, placed in clean-room napkins, and broken into smaller subsample pieces. Of these subsamples, 25 to 75 mg pieces were used for the U-Pb geochronology. The high precision U-Pb, in combination with uranium-series isotope ratios (used to test for open system behavior), was completed using standard isotope dilution anion resin chemistry and mass spectrometry (Denniston et al., 2008; Polyak et al., 1998). Separation of elements was achieved by conventional ion chromatography of spiked samples using Eichrom/Bio-Rad anion exchange resin. A mixed spike containing ^{205}Pb-^{229}Th-^{233}U-^{236}U was used to generate U, Th, and Pb isotope ratios. The U-Pb and uranium-series isotope ratios were measured using the Thermo Neptune Multi-Collector, Inductively Coupled Plasma Mass Spectrometer (MC-ICP-MS) coupled with the Cetac Aridus II desolvating nebulizer at the University of New Mexico Radiogenic Isotope Lab. U, Th, and Pb aliquots were measured separately. All Pb isotopes were measured using faraday cups with ^{205}Pb (the spike) measured in the center cup using a standard (NBS-981)-sample-sample-standard routine. ^{230}Th and ^{234}U were measured in the center position using the secondary electron multiplier (SEM) or a faraday cup-10^{12}-ohm resistor set up. Gain between the faraday cups and SEM were measured using the NBL-112 U-

standard and an in-house ^{230}Th standard. Decay constants for ^{234}U and ^{230}Th were 2.82206 ± 0.00302 X 10^{-6} a^{-1} and 9.1705 ± 0.0138 X 10^{-6} a^{-1}, respectively, from Cheng et al. (2013), and for ^{235}U and ^{238}U were 9.8569 ± 0.0017/0.0110 X 10^{-10} a^{-1} and 1.54993 ± 0.00026/0.00219 X 10^{-10} a^{-1}, respectively, from Schoene (2006). Data reduction and isochron ages were calculated using PbDat (Ludwig, 1993) and Isoplot (Ludwig, 2000). One ^{207}Pb-^{206}Pb age was calculated for our oldest sample. Model age routines were written in Excel for the ^{235}U/^{204}Pb-^{207}Pb/^{204}Pb, ^{238}U/^{204}-^{206}Pb/^{204}Pb, and ^{238}U/^{208}Pb-^{206}Pb/^{208}Pb decay systems, using isochron-derived initial ^{235}U/^{207}Pb, ^{238}U/^{204}Pb, and ^{238}U/^{208}Pb ratios, and their associated 2σ absolute errors. While these samples are tens of millions of years old, ^{230}Th/^{238}U and δ^{234}U were monitored to test for secular equilibrium and obvious evidence of crystal alteration.

Stable Isotope Methods

Strontium Isotopes. Sub-samples for strontium isotope analyses were 15 to 120 mg powders or pieces. Some pieces were also run for fluid inclusion analyses (see paragraph 2.4). The strontium was prepared for isotopic analyses by dissolving each sub-sample of calcite in 7 N HNO_3, drying the sub-sample on a hotplate and then preparing a 3 N HNO_3 sample solution for the column resin chemistry. A 2 ml column with 250 µl of Eichrom Sr spec resin was used to retrieve the strontium by chromatographic ion separation with a yield of 81%. Sr spec resin shows no tendency for mass fractionation of ^{87}Sr/^{86}Sr during collection regardless of the amount recovered (De Muynck et al., 2009)]. Each sub-sample,

dissolved in 3% HNO_3, was then run on the MC-ICP-MS. The standard was NBS-987, which has an $^{87}Sr/^{86}Sr$ value of 0.71025 (Ma et al., 2013).

Carbon and Oxygen Isotopes. Carbonate samples were reacted at 70°C with three drops of phosphoric acid in a Kiel IV automated carbonate preparation system connected to a Delta V Plus stable isotope ratio mass spectrometer via dual inlet. Isotope values were calibrated to the in-house USC-1 calcite standard, which was calibrated to international calcite standards NBS-18 and NBS-19. Analytical precision is better than 0.08‰ and 0.05‰ for $\delta^{18}O$ and $\delta^{13}C$, respectively, based on long-term standard analyses, and values are reported in ‰ notation relative to the VPDB (Vienna Pee Dee Belemnite) scale (Lachniet, 2009)

Fluid Inclusion Assemblage Methods

Calibration. The Fluid Inclusion Assemblage (FIA) analysis was run on samples for which we had ages using a Leica Leitz Laborlux S microscope equipped with a USGS modified fluid inclusion heating/cooling stage attached to a Fluid Inc. Trendicator with a Doric 410A temperature display. The Doric Trendicator 410A was calibrated per the Fluid Inc. instruction manual (Reynolds, 1994). An ice water bath of 18 MΩ H_2O was prepared for the 0˚ C calibration. The end of the thermistor was submerged in the ice water bath and allowed to equilibrate. Once the temperature stayed constant on the Doric 410A indicator panel, the zero potentiometer was adjusted to 0.0 ± 0.1˚ C. Liquid nitrogen (LN) was used to freeze a CO_2 standard (standard #1 synthetic fluid inclusion from Syn Flinc) for the low temperature calibration.

Dry N_2 was used to pressurize the liquid nitrogen Dewar. The cold LN flow was set to 14 standard cubic feet per hour (SCFH). After minor adjustment of the span (-) potentiometer, the standard froze at approximately -98˚ C and melted at -56.6 ± 0.2˚ C on the final three runs. The zero calibration was checked again in the same manner as above to ensure it had not changed. The high temperature calibration was run using a Powerstat variable transformer at a setting of 70 to provide heat. Air flow was provided from a compressor set at 15 SCFH. Ten runs were accomplished using the Syn Flinc standard #4 (pure H_2O), with homogenization occurring at 374.1 ± 0.2˚ C on the final three runs. The zero calibration was checked a final time to ensure that it was still accurate.

Analysis. Each sub-sample was prepared using a mortar and pestle to gently cleave a thin (100 to 500 µm) piece of crystal selected from the interior of the main sample. This sub-sample was then surveyed for fluid inclusions with notations made when groups of single phase inclusions were found. Once a two phase inclusion assemblage was located a photograph was taken and sketch completed of each inclusion or assemblage used for the analysis. Fluid inclusion size was determined by using a Dino-Lite calibration slide to find the pitch of the reticules in the Leica microscope at 500X (40X lens, 12.5X eyepiece) magnification. All heating runs for each sample were repeated a minimum of three times, or until the last three runs were within ± 1.0˚ C.

Results

Isotopic Data

U-Pb System. Twenty-two U-Pb-dated spar samples (Table 8) from eighteen different caves located throughout the Guadalupe Mountains (Figure 18) yielded ages between 180 and 9 Ma. Greater than 50% of the spar ages are between 36 and 28 Ma. In addition to our cave spar results, fibrous fault-filling calcite sampled from the Border Fault zone in Guadalupe Pass, Texas yielded an isochron age of 15.8 ± 1.0 Ma that was used as an absolute and direct constraint on the earliest timing of block fault activity (Roberts and Walker, 2016). $^{238}U/^{206}Pb$, $^{235}U/^{207}Pb$ and 3D-Conchordia ages were all within analytical error (Table 8). Spar ages from two of the caves (Carlsbad Caverns and Lechuguilla Cave) indicate multi-generational spar deposition events within the same cave. For example, Carlsbad Cavern spar had the oldest, 180 Ma, and the youngest, 9 Ma, spar dates. While the spar that yielded these dates are currently located within the same cave, they are from two different vugs, separated by nearly a kilometer horizontally. and are only part of the same cave in that younger sulfuric-acid speleogenesis breached both voids and connected them. This is also the case for other vugs within both caves.

U-Series Data. U-series data was monitored during this research to ensure isotopic equilibrium. All samples used in this study have measured values of $^{230}Th/^{238}U$ and $\delta^{234}U$ that indicate the calcite is in or very near isotopic equilibrium, showing that there had been little to no U, Th, and Pb gain or loss,

nor any other events that could have "reset the clock", within the timeframe applicable to U-series dating.

Table 8: U-Pb ages for 22 spar samples, a cave mammillary and vein filling calcite.

		Concordia		$^{238}U/^{206}Pb$		$^{235}U/^{207}Pb$		$^{207}Pb/^{206}Pb$	
IGSN	**Sample #**	**Age**	**(My)**	**Age**	**(My)**	**Age**	**(My)**	**Age**	**(My)**
	97-CAH	91.3	±7.8	(Lundberg et al., 2000)					
IESWG0001	BLMC-20122-002	68.3	±2.9	68.2	±2.9	66.1	±2.9		
IESWG0002	BLMC-20122-005	29.8	±1.2	29.7	±3.5	28.28	±0.67		
IESWG0003	BLMC-20122-011	34.4	±1.2	34.75	±0.40	34.36	±0.73		
IESWG0004	CAVE-02399-002	184.2	±7.8	184.0	±7.9	184.9	±7.4	185	±47
IESWG0005	CAVE-02399-003	13.08	±0.29	13.22	±0.98	14.3	±2.4		
IESWG0006	CAVE-02399-004	34.82	±0.38	34.78	±0.22	34.76	±0.34		
IESWG0007	CAVE-02399-006	44.6	±1.6	47.9	±1.9	44.6	±3.9		
IESWG0008	CAVE-02399-007	77.2	±1.2	80.4	±4.5	76.9	±1.5		
IESWG0009	CAVE-02399-008	9.23	±0.36	9.19	±0.55	9.45	±0.14		
IESWG000A	CAVE-02399-009	62.4	±2.8	63.9	±1.4	61.73	±0.56		
IESWG000B	CAVE-02399-011	36.1	±2.1	37.29	±0.13	36.46	±0.51		
IESWG000C	CC-001	2.13	±0.24	1.95	±0.27	2.0	±6.8		
IESWG000D	GUMO-00549-001	33.21	±0.70	35.6	±8.0	33.5	±1.4		
IESWG000E	GUMO-00549-002	28.1	±1.6	28.0	±1.6	27.5	±1.6		
IESWG000F	GUMO-00549-003	27.6	±1.3	28.01	±0.31	27.9	±1.7		
IESWG000G	GUPA-00001-001	16.11	±0.43	17.04	±0.55	15.8	±1.0		
IESWG000H	USFS-11290-002	35.69	±0.67	35.90	±0.91	35.76	±0.30		
IESWG000I	USFS-11290-006	53.57	±0.42	54.90	±0.46	53.58	±0.79		
IESWG000J	USFS-11290-007	37.9	±1.8	39.6	±0.4	36.5	±1.7		
IESWG000K	USFS-11290-008	33.5	±2.0	33.08	±0.41	33.06	±0.48		
IESWG000L	USFS-11290-009	54.5	±1.3	56.1	±1.4	55.0	±1.4		
IESWG000M	USFS-11290-010	112.8	0.96	116.4	±1.5	116.8	±1.5	118.8	±0.71
IESWG000N	USFS-11290-011	29.0	±2	27.6	±3.6	26.0	±6.8		

Table 9: Strontium, carbon, and oxygen isotopes for both spar and non-spar calcite.

	$^{87}Sr/^{86}Sr$[1]	Abs. Err.	$\delta^{18}O_{CaCO3\text{-}VPDB}$	$\delta^{18}O_{H20\text{-}VSMOW}$	$\delta^{13}C_{CaCO3\text{-}VPDB}$	$\delta^{13}C_{CO2}$[2]
BLMC-002A	0.708940	6.43E-05	-15.51	-7.4	-3.24	-6.9
BLMC-002B	0.708940	6.43E-05	-15.51	-8.7	-3.24	-7.9
BLMC-005A1	0.709523	4.28E-05	-12.85	-7.1	-1.30	-6.7
BLMC-005A2	0.709523	4.28E-05	-12.85	-5.6	-1.30	-5.7
BLMC-005D	0.709523	4.28E-05	-12.85	-7.1	-1.30	-6.8
BLMC-011A	0.710446	3.40E-05	-13.84	-8.8	0.14	-5.8
BLMC-011D	0.710446	3.40E-05	-13.84	-8.6	0.14	-5.7
CAVE-002	0.708390	2.50E-04	-12.11	DNA[3]	1.94	NC[3]
CAVE-003A	0.710200	1.10E-03	-14.38	-6.7	-1.94	-5.9
CAVE-003B	0.710200	1.10E-03	-14.38	-5.9	-1.94	-5.3
CAVE-004	0.709787	2.88E-06	-9.21	DNA[3]	-4.98	NC[3]
CAVE-006A	0.710669	6.20E-05	-12.43	-4.8	0.17	-3.9
CAVE-006B	0.710669	6.20E-05	-12.43	-4.9	0.17	-3.9
CAVE-007A	0.708770	5.30E-05	-16.19	-6.3	-1.17	-3.3
CAVE-007B	0.708770	5.30E-05	-16.19	-6.3	-1.17	-3.3
CAVE-008	0.709717	2.02E-06	-7.39	DNA[3]	-0.98	NC[3]
CAVE-009A	0.708695	5.16E-05	-12.34	-3.4	1.18	-1.8
CAVE-009B	0.708695	5.16E-05	-12.34	-3.8	1.18	-2.2
CAVE-011A	0.710483	4.02E-05	-15.28	-6.9	-1.22	-4.6
CAVE-011B	0.710483	4.02E-05	-15.28	-7.6	-1.22	-5.2
GUMO-001A	0.710750	1.19E-04	-13.97	-6.5	0.63	-3.5
GUMO-001B	0.710750	1.19E-04	-13.97	-7.7	0.63	-4.4
GUMO-002	0.712894	8.36E-05	-10.11	DNA[3]	0.22	NC[3]
GUMO-003A	0.712351	2.55E-05	-12.40	-4.8	0.50	-3.6
GUMO-003B	0.712351	2.55E-05	-12.40	-6.8	0.50	-5.1
USFS-002A	0.710875	7.44E-05	-14.10	-11.0	-0.65	-8.0
USFS-002B	0.710875	7.44E-05	-14.10	-5.6	-0.65	-4.0
USFS-006	0.713842	5.80E-05	-13.89	-8.7	-1.70	-7.5
USFS-007	0.712373	2.70E-05	-14.62	-7.6	0.67	-3.8
USFS-008	0.711094	2.63E-05	-14.11	-4.2	-0.24	-2.4
USFS-009A	0.716033	2.70E+00	-13.53	-3.7	-2.66	-4.8
USFS-009B	0.716033	2.70E+00	-13.53	-6.9	-2.66	-7.4
USFS-010(W)	0.708653	4.15E-05	DNA[3]	NC[3]	DNA[3]	NC[3]
USFS-010(Y)	0.708272	3.81E-06	DNA[3]	NC[3]	DNA[3]	NC[3]
USFS-011A	0.712901	1.03E-05	-12.60	-7.7	1.10	-5.0
USFS-011B	0.712901	1.03E-05	-12.60	-5.9	1.10	-3.7
Non-spar Calcite						
CaCa-BC21-	0.708523	1.40E-05	DNA[3]	NC[3]	DNA[3]	NC[3]
CBM-001 (light)	0.708214	9.90E-06	-8.18	DNA[3]	-6.76	NC[3]
CBM-004 (dark)	0.708042	2.80E-05	-8.48	DNA[3]	-2.26	NC[3]
GUPA-00001-001	DNA[3]	DNA[3]	-8.93	DNA[3]	-24.37	NC[3]
LECH VS-1	0.708782	1.30E-05	DNA[3]	NC[3]	DNA[3]	NC[3]
WBC4-Calcite	0.708428	2.10E-05	DNA[3]	NC[3]	DNA[3]	NC[3]

Note 1: Average $^{87}Sr/^{86}Sr$ value for the limestone bedrock 0.707

Note 2: $\delta^{13}C_{CO2}$ calculated from Romanek et al. [1992]: $\varepsilon_{CaCO3\text{-}CO2} = 11.98 - 0.12 * T(°C)$

Note 3: DNA - Data Not Avail.; NC - Not Computed

$^{87}Sr/^{86}Sr$, $\delta^{13}C$, and $\delta^{18}O$. Strontium, carbon, and oxygen isotope data were also collected. Strontium ratios ($^{87}Sr/^{86}Sr$) ranged from 0.708042 in mammillary calcite up to 0.716033 in the cave spar. The $\delta^{13}C_{CaCO3\text{-}VPDB}$ ranged from -24.4 ‰ in the vein spar from Guadalupe Pass up to 1.94 ‰ in the cave spar and the $\delta^{18}O_{CaCO3\text{-}VPDB}$ ranged from -16.2 to -7.4 ‰ (Figure 25, Table 9).

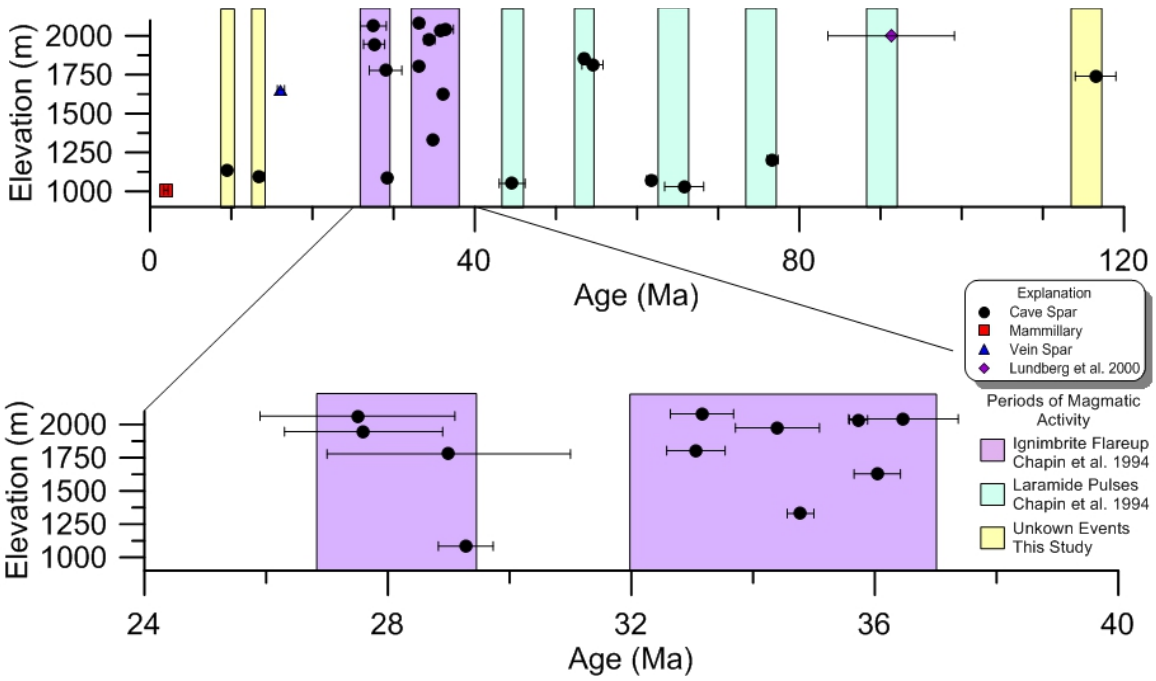

Figure 19: Age vs. elevation data for spar crystals. Blue bars are times of known magmatic activity in the region. Figure modified from Decker et al., 2017, igneous data from Chapin et al., (1994).

Fluid Inclusion Assemblage Data. Fluid inclusion assemblage (FIA) analysis temperatures range from 40 to 80˚ C (Table 4) with the temperatures of two samples that remain constrained only to above 0˚ C and below 30˚ C (based on single phase inclusions that are fluid between 0˚ C and room temperature and two phase above 30° C). These samples are likely to have formed between 35° and 40° C and have simply stretched the fluid (Roedder, 1983a)) rather than

nucleating a vapor bubble. Forced nucleation was attempted by rapidly cooling the sample to 0° C, but nucleation never occurred.

Discussion and Conclusion

Spar age temporal association with magmatic activity. The bulk of our U-Pb ages (Table 8) cluster with the $^{40}Ar/^{39}Ar$ ages in the two major ignimbrite flare-up sub-episodes (Chapin et al., 2004) (Figure 2B and Figure 19) between 36 – 28 Ma. The remainder are coeval with regional igneous events at 45 Ma (Henry et al., 1991), 55 Ma (Todd et al., 1975), 65 Ma (Gilmer et al., 2003), 75 Ma (Befus et al., 2008; Breyer et al., 2007), and 90 Ma (Befus et al., 2008), linking them temporally to the igneous episodes associated with Rio Grande rifting (Figure 2B and Figure 19) and other magmatic events, providing evidence that the origin of these caves and the calcite spar that lines them are related to pulses of regional magmatic activity (Figure 2B). The closest surface expression of magmatic activity occurring near the Guadalupe Mountains is within only eleven kilometers of the reef front**.** These consist of three parallel mafic dikes emplaced during the ignimbrite flare-up (Barker and Pawlewicz, 1987; King, 1948) which continue several kilometers just below the surface to the northeast (intersected by a local potash mine at depth), and likely continue beneath the cliffs of the reef front to the southwest. Our dataset also includes younger spar ages at 14.3 ± 2.4 and 9.45 ± 0.14 Ma in Carlsbad Cavern (Table 8). Our two oldest spar ages of 184.9 ± 7.4 and 116.8 ± 1.5 Ma, are not coincident with known periods of magmatic activity.

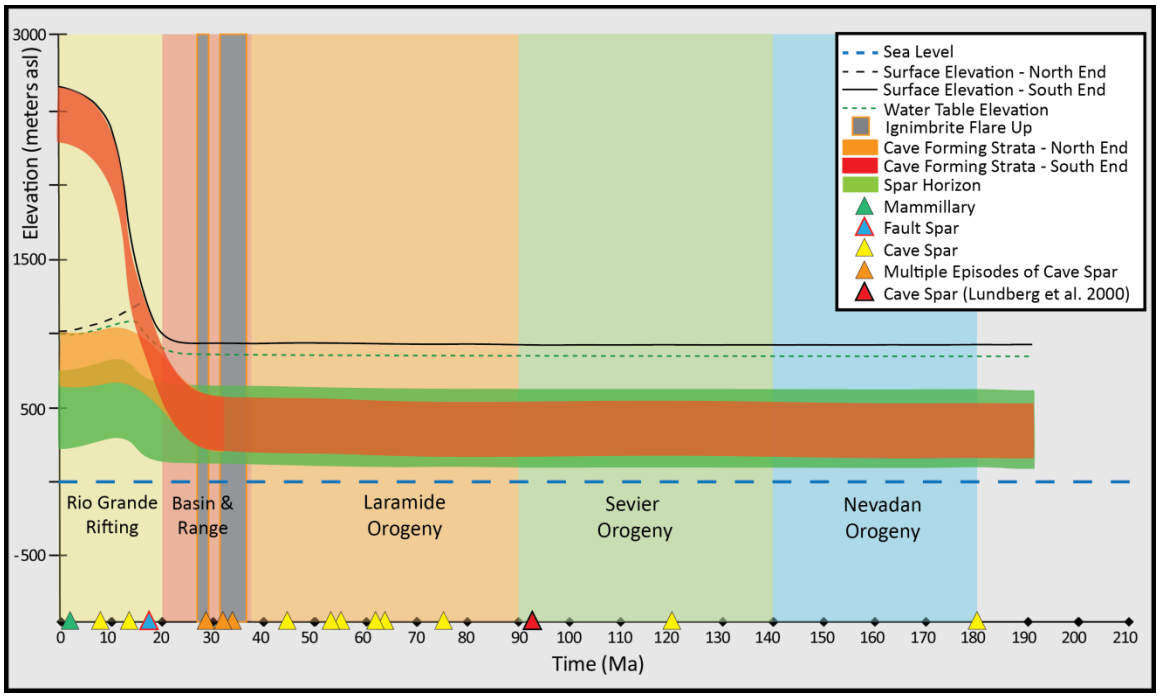

Figure 20: Spar chronology model. Here we show the spar horizon (green ribbon) elevation relative to sea level as far back as the Jurassic Period. We also show U-Pb spar ages (yellow, orange and blue triangles). The red and orange in this graphic represent the southwest end nearest the Border Fault zone will experience greater uplift than the northeast end near the fault hinges (see Figure 6B). The green area is the spar horizon. Different orogenic events are an average estimate from many different sources.

In Figure 2B we break up the locations and ages of reported igneous activity coincident with periods of spar formation (also see Figure 19. The nearest Cretaceous rocks (green) in Figure 2B show that this entire region was likely close to sea level as late at the Cretaceous. Using the speleogenesis model from Decker et al., (2016), spar dates older than 65 Ma support this evidence for a low-relief, near-sea level landscape. Since then, and up until about 28 Ma, the area was also most likely at or just above sea level. If any significant (> 1 km) local rock uplift had occurred, the area where the spar formed would have been lifted out of the spar forming region and no cave spar could have formed (Figure 20 and Figure 21). Every spar date is an indication of when the spar cave-forming strata were buried to shallow depths of ~0.5 km,

and since significant regional uplift would have disturbed the regional water table, it suggests that the surface remained at or near sea level during spar formation.

Strontium, carbon, and oxygen isotope interpretation.

Strontium. The strontium isotope ratios, ranging from 0.708 to 0.716 (Table 9) are well above that of the local limestones (0.706 - .708, (Hill, 1996)) indicating the fluid that formed the spar was not in complete equilibrium with the Capitan formation or any of the back reef equivalents. This suggests that a component of the groundwater was deeply circulating through, and in contact with, though not in equilibrium with, the basement rock ($^{87}Sr/^{86}Sr$ = 0.82, (Barker et al., 1977)), which in this region is approximately 3.3 km below the surface (Flawn, 1956). One way to explain this is to set up buoyant circulation in a localized hydrothermal plume by heating water at depth and circulating lower Sr ratio waters through higher Sr ratio rocks for a short time. Another way is to have a regional aquifer supplied from a distant highland that flows for long periods through high Sr ratio basement rocks. The later seems less likely and would be reflected in the more meteoric secondary precipitates.

Carbon and Oxygen. The $\delta^{13}C_{spar}$ values for which we have fluid inclusion temperatures range between -3.24 and +1.18 ‰. We estimated the $\delta^{13}C_{CO2}$ of waters forming the calcite assuming equilibrium isotopic fractionation using the measured spar $\delta^{13}C$ values and estimated fluid inclusion temperatures with the enrichment factor equation of Romanek et al. (1992):

$$\varepsilon_{CaCO3\text{-}CO2} = 11.98 - 0.12 * T(°C) \quad (1)$$

Solving for the $\delta^{13}C$ of CO_2 gives a range of -8.0 to -1.8 ‰, with a mean and standard deviation of -4.9 ± 1.7 ‰ VPDB (Table 9). These values overlap, but are slightly higher than a typical magmatically derived CO_2 signature (-7 ‰ to -5 ‰, Figure 25) (El Desouky et al., 2015). The bias toward slightly higher $\delta^{13}C$ values suggests a mix with a high-$\delta^{13}C$ bedrock-derived source. Our observations and estimates are consistent with a locally derived carbon source that is circulating buoyantly, driven by a magmatic heat source, and mixing with meteoric waters.

Similarly, we estimated the $\delta^{18}O$ values of formation water assuming isotopic equilibrium at the estimated spar formation temperatures and the measured $\delta^{18}O$ of spar calcites using the equation of Coplen (2007):

$$1000 \ln \Delta_{calcite\text{-}water} = 17.4 (1000/T (°C)) - 28.6 \quad (2)$$

and solving for $\delta^{18}O$ of water. The range of the spar $\delta^{18}O$ of -3.4 ‰ to -11.0 ‰ (VPDB) (Table 9) falls directly in line with the thermal spar of Hill (1996) and the thermally derived cements of Loyd (2013) and Budd (2013) (Figure 23). Further, estimated formation water $\delta^{18}O$ values (in VSMOW) range from -3.4 to -11.0 ‰, with a mean and standard deviation of -6.6 ± 1.7 ‰ (Table 9). These values are consistent with a meteoric water source located proximal to an oceanic moisture source relatively unimpeded by significant orographic barriers, and are similar to the $\delta^{18}O$ values of summer moisture reaching New Mexico today (Sharp, 2007b),

and support a mixing of magmatically-derived CO_2 with meteorically-derived ground waters.

Fluid inclusion assemblage interpretation. The fluid inclusion assemblage temperatures of homogenization (40 to 80° C) (Table 4) indicate that the spar formed at temperatures higher than those expected for non-thermal meteoric-derived water, or possibly that the calcite was reset during a post-depositional event. Based on several interpretations of the depth of burial after formation of the reef (Barker and Pawlewicz, 1987; Budd et al., 2013; Loyd et al., 2013; Mruk, 1985, 1989; Scholle et al., 1992),(Table 10), the Capitan formation, and thus the cave-forming strata, was never buried more than about 1 km. Assuming a 15 to 20° C average surface temperature, a local geothermal gradient of between 40 to 60° C/km would have to have been required during the times of spar formation. This strongly suggests geothermal activity, and paired with the timing of formation, magmatically driven geothermal activity. Vitrinite reflectance data from Barker, 1987 suggests a regional geotherm of 50° C/km during the ignimbrite flare-up, with steeper gradients likely in areas of hydrothermal upwelling. Present day geothermal gradients in the region average 25˚ C/km (Ruppel et al., 2005), supporting our hypothesis that the water from which the cave spar precipitated was thermal. Since the cave spar was formed in vugs where differential pressure is low to non-existent, and the associated temperatures and pressures of formation were not exceedingly high, it is unlikely that the fluid within the inclusions was reset during higher temperature excursions of events subsequent to the formation of the individual crystals (Roedder, 1983b). Additionally, calcite

formation along hydrothermal pathways tends to cement these pathways closed (Budd et al., 2013; Loyd et al., 2013; Mruk, 1985; Scholle et al., 1992), keeping them from being used by later plumes and forcing new pathways to form along unobstructed fractures. This suggests that the T_h for the cave spar in our study is representative of the temperature of formation rather than peak temperatures for the region.

The U-Pb age, $^{87}Sr/^{86}Sr$, $\delta^{18}O$, and $\delta^{13}C$, and data fluid inclusion T_h (Tables Table 4,8, and 9) indicate that the cave spar was formed by mixing of meteoric-derived aquifer water with upwelling deeply circulated meteoric water that was in contact with basement rocks. The calcite formed at elevated temperatures (40 to 80° C) tied to magmatically derived CO_2-related speleogenesis.

Landscape evolution of Guadalupe Mountains region. Two significant findings come from these results: 1. U-Pb ages of cave spar likely defines periods of magmatically driven hydrothermal (40 to 80˚ C) activity responsible for the hypogene speleogenesis (Dublyansky, 2014) of these vugs, and 2. these ages represent periods when the cave-forming strata were not buried deeper than 1 km below a regional water table (based on our speleogenetic model), linking age and depth of formation, and therefore can be used to constrain the landscape evolution back into the Cretaceous. These findings are important to any debate regarding the timing and evolution of the rotation of the Guadalupe Mountains tectonic block, and the pre-uplift history of the Delaware Basin region. Our study area is positioned marginal to regional Jurassic rifting (Chihuahua Trough), the Laramide orogeny, Basin and Range extension, and Rio Grande rifting proper

(Figure 2B), allowing for many magmatically-driven hydrologic and $scCO_2$ pathways of communication throughout the region, and possibly explaining why our cave spar ages cover the full range of tectono-physiographic history of the region.

Spar ages are sporadic prior to the ignimbrite flare-up, but predominantly match the history of magmatic activity in southwestern New Mexico (Chapin et al., 2004) and west Texas (Befus et al., 2008; Breyer et al., 2007; Gilmer et al., 2003; Henry et al., 1991) (Figure 2B). $^{235}U/^{207}Pb$ spar ages at 44.6 ± 3.9, 53.58 ± 0.79, 55.0 ± 1.4, 61.73 ± 0.56, 66.1 ± 2.9 and 76.9 ± 1.5 Ma are coincident within error of individual intrusive dates of regional back-arc magmatism in Trans-Pecos, Texas and in southwestern New Mexico during the Laramide Orogeny (Befus et al., 2008; Breyer et al., 2007; Chapin et al., 2004; Gilmer et al., 2003; Henry et al., 1991; McLemore et al., 1995). Our interpretation is that these regional scale magmatic events periodically raised the local thermal gradient and produced copious amounts of CO_2 contributing to the formation of the spar caves and spar linings at ~0.5 km depths. However, our landscape evolution model presented here (Figure 20) suggests that none of these events prior to rifting seemed to result in development of significant topographic relief, otherwise the area in which the spar caves formed would have been lifted out of the spar horizon during any uplift/down-drop event, precluding the formation of spar younger than the uplift event (Figure 21).

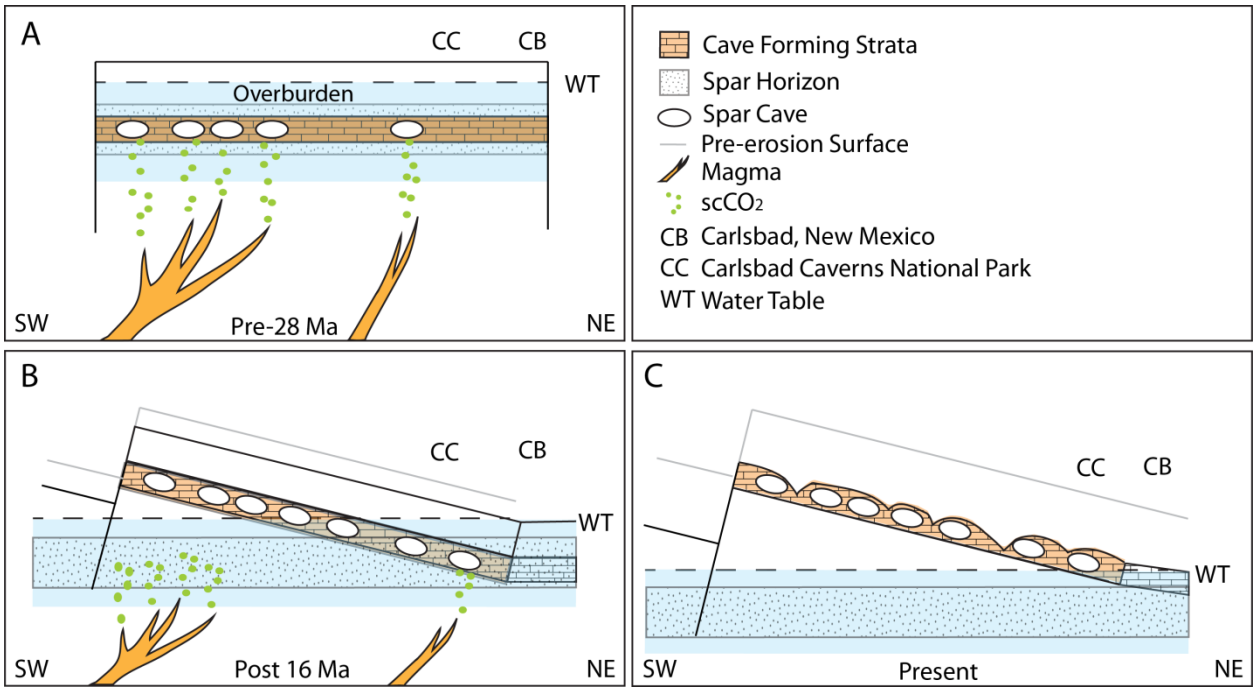

Figure 21: Graphic representation of the formation of the spar caves and spar crystals over time. (A) Volcanism prior to 28 Ma created spar caves and cave spar at the spar horizon ~500 m +/- 250 m depth through the release and reaction of supercritical CO2. (B) As uplift of the Guadalupe Block began post-27 Ma, the SW end of the Guadalupe Mountains began to rise and the Capitan Reef was lifted out of the spar horizon to the south as the Guadalupe Block began to dewater and erode. To the NE, the spar horizon and cave forming strata remained below the water table. (C) Presently, the Guadalupe Mountains are undergoing erosion and the water table is well below the surface except at the city of Carlsbad where the Capitan Aquifer reaches the surface in the bed of the Pecos River.

Given a scenario in which the surface of the Delaware Basin-Guadalupe Mountains region was moderately uplifted prior to Rio Grande Rift block faulting during the period of interest (185 to 28 Ma), then it would have required a broad epeirogenic uplift to have lifted the regional water table across a large area without changing the gradient drastically, allowing the Capitan reef complex to remain in the spar horizon. Because our U-Pb ages spread between 185 and 28 Ma before Guadalupe block uplift, it seems unlikely that any Laramide or pre-Laramide regional uplift would have been significant (i.e., > 1 km) which is consistent with broader scale estimates of uplift (Hay, 1984). We interpret the

landscape to have been at low elevation (i.e., <500 m above sea level) during much of the Jurassic, Cretaceous, and Paleogene (Figure 20) based on our spar forming model (Decker et al., 2016), however, our results and model explained in more detail below, enables broad regional deviations of the landscape elevation of ±500 m, allowing for interpretations that place the landscape near sea level during the Cretaceous, or near 1000 m above sea level during the Laramide Orogeny.

We use the age of vein calcite from the Border Fault Zone (BFZ, depicted by the red triangle in Figure 20, GUPA-00001-001, Table 8) to constrain the minimum age of block uplift in the region (Roberts and Walker, 2016). Therefore, between 27 Ma (age of youngest spar near BFZ) and 16 Ma (age of BFZ vein calcite), Rio Grande rift normal faulting and block rotation began lifting the southwestern end of the Guadalupe Mountains tectonic block above and out of the cave spar-forming horizon. The water table at the southwestern end of the mountain range could no longer be supported in the karstic environment and dropped dramatically relative to the strata (Polyak et al., 1998). Considering uplift rates of ~0.11 km/Ma from Polyak et al. (2008) and assuming that rate back to initiation of block rotation at 27 Ma or 16 Ma, total uplift along the Border Fault Zone (BFZ) of 2970 (27 Ma) or 1760 m (16 Ma) would have occurred, placing the spar horizon between ~ 0 and 1000 m above sea level prior to block uplift (Figure 20). This is close to the present-day elevation of the cave-forming strata and water table near the city of Carlsbad. Two post-flare-up spar ages at 14.3 ± 2.4 and 9.45 ± 0.14 Ma in Carlsbad Cavern indicate that the northeastern end of the Guadalupe

Mountains remained in the spar horizon long after the southwestern end started rising (Figure 21a). It is likely that magmatic events at 14.3 and 9.5 Ma (Seager and Morgan, 1978) coeval with our two youngest spar ages resulted in late spar growth nearer the hinge lines of the Guadalupe block rotation on the southeast end (Figure 21b) that were not yet uplifted. As a result, the areas to the northeast near the hinge line remained well below the water table during the first half of the block uplift period, allowing for continued spar growth after 16 Ma at 14.3 and 9.5 Ma. Eventually, as uplift continued, the water table dropped below even these vugs and is currently approximately 120 meters lower than the lowest known spar caves in the Carlsbad Cavern area. We use the age of a cave mammillary (water table indicator speleothem) from Lake of the Clouds in Carlsbad Cavern (CC001, 2.13 ± 0.24 Ma, Table 8), and the present-day water table to constrain and project the timing of water table descent on the block hinge end of the mountain range.

Conclusions. We have shown that accurate and precise U-Pb ages can be retrieved from calcite cave spar. Retrieving U-Pb and uranium-series dates from speleothems has been done in the past, but has been largely restricted to stalagmites and other sub-aerial deposits. Although a spar crystal was dated by Lundberg et al. [2001], this is the first effort attempting to retrieve this information from a set of deep phreatic speleothems, and combined with both stable isotope and fluid inclusion data, develop a landscape evolution model. We have also shown that the cave spar can be used as a shallow-crust landscape evolution tool based on its deposition in a spar horizon at a known time and a consistent

temperature range and depth. Our two oldest spar ages of 185 Ma and 115 Ma in combination with the 91.3 ± 7.8 Ma 3D-conchordia age reported by Lundberg et al. (2000), and our results from 77 to 28 Ma, seemingly demonstrate that the study area was at or just above sea level since the Jurassic. On the southwestern end of the mountains in the area of the Border Fault zone along which the Guadalupe Mountains tectonic block was uplifted, two of our results, a cave spar (28 Ma) near the Border Fault zone and fault-filling calcite (16 Ma) in the Border Fault zone, place an absolute constraint on when the block began rising. These results constrain the initiation of uplift of the mountain block to between 28 and 16 Ma. While the Laramide Orogeny is considered as a period of uplift in our study area, there is little known about the extent of Laramide uplift and the pre-Laramide landscape. Some reports suggest the surface of the region was uplifted as much as one kilometer during the Laramide, but the absolute timing of the remaining 2 km of uplift is less well known (Chapin and Cather, 1994; DuChene and Cunningham, 2006; Hill, 1996; Horak, 1985). Overall, our model of spar cave speleogenesis and measured depth results indicate that the paleo-surface of the Guadalupe Mountains and Delaware Basin region was 500 ± 250 m above the spar horizon, and this, along with nearby occurrences of Cretaceous strata (Figure 18) and lack of tectonic evidence for a strong compressional regime during the Laramide supports a relatively low-lying terrane ~ ≤1 km above sea level from 180 to 28 Ma, after which the Guadalupe tectonic block rose an additional 2 km above the adjacent Salt Basin graben on the west end near the fault zone.

The cave spar chronometry model, based on the supercritical CO_2 model of spar cave speleogenesis (Decker et al., 2016), proposes that the most likely time spar caves can form is when the cave forming strata (Capitan Reef, Yates, Tansil, Seven Rivers formations, etc. in our case) intersects the spar horizon (depth at which spar caves and cave spar form). Figure 20 illustrates our proposed model that the landscape in the Guadalupe Mountains remained stable and low-lying during the Cretaceous and through the Laramide, and did not begin major uplift until Rio Grande rifting. We demonstrate how cave spar, used as a landscape evolution tool, will augment or compliment AFT analysis and (U-Th)/He data in apatite from regions of igneous and metamorphic provenance as well as provide data in terranes that only have carbonate strata (Farley and Flowers, 2012). The two common shallow crust methods (AHe and AFT) are not useful in our carbonate dominated study area due to lack of apatite, illustrating the importance of our new method. In areas where data based on shallow crust thermochronometers can be interpreted in more than one way, our newly proposed method of determining landscape evolution could provide the data necessary to resolve the discrepancy.

Tables

Table 10: Vein and vug filling spar temperatures from McKittrick and Dark Canyons, Guadalupe Mountains, southeastern New Mexico and west Texas.

Sample	$\delta^{13}C$ (‰ VPDB)	$\delta^{18}O$ (‰ VPDB)	Temp (°C)	Reference
6107-A	-8.4	-11.4	22	1
6107-F	-12.3	-12.8	70	1
6107-I	-12.6	-14.4	74	1
6610-A	-15.4	-15.3	73	1
6610-C	-14.5	-13	71	1
6617-A	-0.6	-15.8	81	1
6617-E	1	-13.9	81	1
6619-A	0.1	-9.9	32	1
6619-C	-1.8	-14	31	1
6626-C	-14.4	-14.9	70	1
6626-E	-16.9	-15.3	75	1
6626-G	-16.8	-15.5	78	1
6626-I	-17.1	-13.6	90	1
6602-A	0.7	-8.8	16	1
6602-D	1	-11.9	65	1
6603-F	-5.4	-12.3	59	1
MC1	1.15	-11.97	72.7	2
MC2	1.16	-11.69	61.6	2
MC3	1.18	-11.6	65.8	2
MC4	1.25	-11.59	63.9	2
MC5	1.34	-11.34	57.8	2
MC6	1.33	-11.41	54.4	2
MC7	1.22	-11.49	58.9	2
MC8	0.53	-8.87	34.8	2
MC9	-5.57	-12.26	40.5	2
MC10	0.86	-11.74	60.1	2
MC11	-1.93	-13.94	50.1	2
MC12	1.18	-11.6	65.8	2
MC13	1.27	-11.82	55.3	2
MC14	-0.81	-14.99	56.5	2
MC15	0.33	-13.77	71.3	2
MC16	0.21	-12.15	67.9	2
MC17	0.82	-11.16	49.7	2
MC18	0.41	-13.23	62.5	2
MC19	-1.38	-16.66	41.2	2
MC20	-0.75	-13.33	55.2	2
DC1	-14.42	-12.88	30.5	2
DC2	-8.12	-11.32	46.7	2
DC3	-17.1	-13.56	58.1	2
DC4	-12.22	-12.65	47.2	2

1. Budd et al., 2013. Temperatures derived from Δ_{47}
All samples from Dark Canyon
2. Loyd et al., 2013. Temperatures derived from Δ_{47}
DC - Dark Canyon, MC - McKittrick Canyon

CHAPTER 5 - Spar Caves as Fossil Hydrothermal Systems in the Guadalupe Mountains of Southeast New Mexico and West Texas: Implications for timing and origin of Ore Deposits

(Submitted to the journal "International Journal of Speleology" special edition "Processes and Manifestations of Hypogene Karstification" to be published in May, 2018.)

Abstract

The timing of the uplift and the tectonic events that may have contributed to the uplift of the Guadalupe Mountains of west Texas and southeastern New Mexico have been constrained to between 27 and 16 Ma.. The concept of sulfuric acid hypogene speleogenesis has added results important to the history of the mountain range for the last 12 Ma. The concept of supercritical CO_2 spar cave genesis has potential to help explain the landscape evolution of this region back into deep time (e.g., 180 Ma). This new spar cave speleogenesis model is based on U-Pb age dating of the dogtooth calcite cave spar crystals, and reveals that the crystals from different spar caves have different ages. More than half of the spar cave crystals dated indicate that precipitation took place within the two distinct episodes of the ignimbrite flare-up during the end of the Basin and Range tensional tectonics (36 - 28 Ma) and the beginning of the Rio Grande Rift formation (~28 Ma). Many other older spar ages also coincide with magmatic events. Fluid inclusion assemblage analyses show that the cave spar formed between 40 and 80° C, and three measured depths of formation show that the spar formed deep in the phreatic zone between 250 and 750 meters depth. These findings indicate that geothermal gradients were high (50° to 70° C/km) during cave spar formation, and that these were low temperature hydrothermal systems. Stable isotope data including $\delta^{13}C$, $\delta^{18}O$, and $\delta^{88}Sr$ indicate that the

waters the spar formed from were hydrothermal and mixed with gases emanating from shallow magma conduits. Nearby outcrops of Tertiary igneous dikes the same age as the spar supports this hypothesis.

Fossil hydrothermal systems active sporadically during basin and range formation and Rio Grande rifting driven by magmatic intrusions on the fringes of the Delaware Basin likely were responsible for both the formation of the spar and the small caves in which it is found (supercritical CO_2 spar cave hypogene speleogenesis). The origin of these spar caves, and the temperatures and depth at which the spar forms, indicate that the region was tectonically stable for tens of millions of years, possibly as far back as 185 Ma, and that the majority of the uplift of the Guadalupe Mountains did not occur until after the beginning of the Rio Grande rifting. Since these spar caves that formed several hundred meters below the surface are now at the surface, any indication of fossil hydrothermal systems such as travertine deposits on the surface have long since been eroded away. These spar caves are remnants of hydrothermal processes from the time period between 180 to 28 Ma, and the timing of the origin of ore/hydrocarbon deposits are likely coeval with the timing of origin of spar caves. This relationship may help to determine more about the timing and origin of the economic epithermal deposits in the region.

Introduction

The Guadalupe Mountains region (Figure 1) is well studied, but little about the actual landscape evolution of the area is known. King (1948) states that the region was of “post-cretaceous age, most probably Oligocene to Miocene” and may have been composed of up to three periods of uplift. Hills (1984) and McKnight (1986) suggests that there has been little to no uplift in the region since the end of the Permian. Eaton (1986) concluded that the area was uplifted during the formation of the Basin and Range producing a topographic high to the west called the Alvarado Ridge, which subsequently subsided along a central basin during Rio Grande rifting. Lundberg, et al. (2000) obtained a U-Pb date of 90.7 ± 2.8 Ma from a spar crystal in Big Canyon and concluded that a deep seated hydrothermal event during the Laramide produced the spar cave, spar deposition, and hydrocarbon maturation; and may have been responsible for post-Permian uplift of the region. Duchene and Martinez (2000) believe the Alvarado Ridge arose during the Laramide, based on the paleobotanical evidence of Gregory and Chase (1992) from farther north in the southern Rockies. The landscape evolution of this region may seem simple, but based on the wide

Figure 22: Large spar cave truncated by the formation of Lechuguilla Cave near Carlsbad Caverns, NM. These spar crystals range in size from 2 cm to 20 cm along the c-axis.

range of views proffered by the above authors it is not settled and is more complex than expected. Since few outcrops exist that are related to landscape evolution and ore generation, it becomes even more difficult to determine the absolute timing of the history of this mountain range, making proxies for these processes valuable resources. Spar caves in the Guadalupe Mountains are essentially large geodes lined with druses of macro-crystalline calcite that had formed long before the sulfuric acid cave genesis events (Hill, 1996). The large calcite crystals are called 'cave spar' in this paper, and are phreatically precipitated deposits (Gary et al., 2002). Cave spar growth in these spar caves of the Guadalupe Mountains and adjacent Delaware basin (Figure 22) has been largely defined by Hill (1996), Mruk (1985) and Lloyd et al. (2013). Euhedral thermal spar used in this study fits the mesogenetic spar of Hill (1996) and the spar II of Mruk (1985). Decker et al. (2016) determined that these spar caves formed in the deep phreatic zone, a model that evolved from the direct measurement of depth of formation of three spar samples using U-Pb ages of the calcite spar crystals (Decker et al., 2017) and known paleosurface elevations relative to the spar caves, for which two of the paleosurfaces were from alunite-based paleo-water table elevations determined by Polyak et al. (1998) and one paleosurface from a Grand Canyon example (Decker et al., 2016; Decker et al., 2017). In Decker et al., (2017), the beginning of the uplift and rotation of the Guadalupe block was constrained to between 27 and 16 Ma.

The Guadalupe Mountains are located at the boundary of three significant Cenozoic tectonic terranes, (1) the northeastern margin of the Basin and Range, (2) the southeastern margin of the Rio Grande Rift zone, and (3) the eastern extreme of the Laramide Orogeny. The relative importance and absolute timing of each of these tectonic/magmatic events in the evolution of the regional landforms is vaguely known because of the lack of dateable materials present in the Guadalupe Mountains and Delaware Basin region. Some speleothem types can be used to make inferences on landscape evolution(Bakalowicz et al., 1987; Decker et al., 2016; Polyak et al., 1998), and growth of these speleothems can record the processes that shaped this landscape and preserve evidence of the timing and role of each providing that there is an understanding of the type and origin of the speleothems. For example, Bakalowicz (1987) used nail head spar speleothems to model the landscape above Jewel Cave; Polyak et al. (2008) using water table type speleothems (folia, mammillaries, and gypsum rinds) to reconstruct past water tables in Grand Canyon; and Decker et al. (2016) modelled the depth of origin of cave spar crystals to determine when significant changes in landscape took place in the Guadalupe Mountains. Decker et al. (2017) showed the coincidence of the timing of cave spar formation and magmatic events, and that the cave spar formed at low hydrothermal temperatures. This not only supports the idea that spar caves are forming during magmatic events, but also shows that past hydrothermal processes linked with hydrocarbon/ore deposition probably took place during these periods when cave spar formed. Most spar ages are coeval with systems that are heavily entwined

with the last two events of the ignimbrite flare-up that occurred in this region from 36 to 28 Ma (Decker et al., 2017).

U-Pb dating of cave spar shows that most ages fall coeval with the ignimbrite flare-up, but that there are multiple other generations of euhedral spar crystal formation in the Guadalupe Mountains (possibly up to five). This spar is hydrothermally generated (Dublyansky, 2000) at depths between 250 and 1000 meters during phase changes associated with supercritical carbon dioxide that is highly dependent on pressure and temperature (Decker et al., 2016; Decker et al., 2017).

This paper uses isotopic evidence (U/Pb, $\delta^{18}O$, $\delta^{13}C$) to link the formation of the spar caves and growth of the spar during hydrothermal activity to known magmatic events in southeastern New Mexico and west Texas, providing evidence that, at a minimum, the two latest spar forming events were derived from fossil hydrothermal systems during the basin and range tectonic events and the Rio Grande rifting.

Methods

U-Pb and U-series dating methods and stable isotope analyses methods are previously published in Decker et al. (2016; 2017). Calcite cave spar samples from 16 caves, a sample of mammillary calcite from Lake of the Clouds, Carlsbad Cavern, and a sample of fault-filling vein calcite from the Border fault zone (site 13 of Figure 1). Sample descriptions and tabulated data are also found in APPENDIX A.3 - SAMPLE DATA PAGES and APPENDIX A.4 - SAMPLE DESCRIPTIONS AND

TRIP REPORTS. Evidence for hydrothermal origin of the cave spar comes from fluid inclusion assemblage analyses and carbon and oxygen stable isotope values reported in Decker et al. (2017).

Figure 23: In situ scalenohedral spar crystal in small ceiling vug. Photo by Jason Waltz.

Samples were selected from caves throughout the Guadalupe Mountains. Each sample was selected based on lack of visual surface alteration (Figure 23). If available, fist sized up to football sized crystals were collected to ensure that the center had not been leached. Visible surface alteration is generally a sign that the crystal surface had been re-dissolved in subsequent speleogenetic episodes, most likely during the late stage H_2SO_4 speleogenesis. The majority of samples were already broken and therefore the interior of samples could be examined for pristineness, and no additional damage was done to the sampled caves. The sampled crystals ranged in size from 2 to 25 cm along the crystallographic axis. All cave spar samples collected are interpreted to be the mesogenetic spar (formed after the reef stopped growing and before the beginning of H_2SO_4 speleogenesis) described by Hill (1996). A typical spar cave is approximately 10 to 20 meters in diameter, and entirely lined by scalenohedral spar. These vugs have been found as small as 10 cm in diameter with 2 to 3 cm long crystals and as large as 50 meters long by 30 meters wide and 10 meters tall (Spar City in Lechuguilla Cave,

Figure 22) and crystals as large as 2 meters long in other, smaller Guadalupe caves.

Results

U-Pb ages of cave spar calcite from 22 locations (16 different caves, Figure 1) cluster between 64 to 54 Ma, 40 to 34, Ma and 30 to 28 Ma (Figure 19). There are three outliers, one at 91 Ma (Lundberg et al., 2000) and two others at 9.23 ± 0.36 and 13.1 ± 0.3 Ma (Decker et al., 2017). Fibrous fault filling spar sampled from the Border Fault zone in Guadalupe Pass, Texas yielded an isochron age of 16.1 ± 0.4 Ma, putting constraints on the timing of block fault activity. A cave mammillary (a phreatic speleothem formed at or just below the water table, (Coplen, 2007)) from the deepest part of Carlsbad Cavern in Lake of the Clouds was dated at 1.95 ± 0.2 Ma places the water table well below the majority of the spar locations by the late Pliocene.

Depth of formation of cave spar was measured for a cave spar sample from a Grand Canyon cave, and two cave spar samples from the Guadalupe Mountains, one from the New Mexico Room and another from the Bell Room of Carlsbad Cavern, as absolute indicators of depth of formation of these deep, phreatically formed crystals. The sample from Grand Canyon yielded a U-Pb age of 232 ± 2 Ma. The cave is in the Redwall Limestone, located ~750 m below Triassic-aged, near-sea-level sediments. From this, we can infer that the cave spar formed ~750 m below a paleo-water table (Decker et al., 2016; Decker et al., 2011). In Carlsbad Cavern, sample CAVE-02399-003 yielded an age of 13.1 ± 0.3 Ma, and

CAVE-02399-008 yielded an age of 9.23 ± 0.36 Ma. The elevation of these samples are ~500 and 800 m below a 9 and 13 My-old paleo-water table defined by Polyak et al. (1998). All three samples provide absolute depths of 500-800 m below water tables for the origin of the calcite spar (Decker et al., 2016). Dublyansky (2000) approached the depth of spar formation from an analytical point of view and determined that large scalenohedral spar should form between 500 and 1000 meters below the water table consistent with our results. This depth of formation of cave spar is also the depth of the supercritical/subcritical CO_2 boundary where carbonate rocks are reported to dissolve (see (Decker et al., 2016; Decker et al., 2017)). The advantage of knowing this depth of formation is that it is coincident with the supercritical/subcritical CO_2 boundary, which can be used to explain both the origin of the spar caves and the cave spar that lines them. Because the cave spar ages are coeval with magmatic events in the region, and that have formed at higher temperatures than expected, the magmatic events can be used to explain why spar caves form, and during the end of this event, why the cave spar precipitates.

Temperatures derived from fluid inclusions (Decker et al., 2017; Decker et al., 2018), and from vitrinite reflectance data (Barker and Pawlewicz, 1987), yielded a maximum geothermal gradient for the region during the time of these magmatic events. The results suggest that the spar was deposited in temperatures ranging from 45 to 80° C and possibly as high as 90°C. While these temperatures are not considered hot for geothermal purposes, and the depths are not deep for tectonic purposes, these temperatures and depths can provide us with insight

into near surface processes that are not available by other means, and suggest that the region experienced hydrothermal events coeval with spar cave speleogenesis events at temperatures high enough to allow maturation of hydrocarbons.

Discussion

Hydrothermal buoyancy driven flow exists over thermal point sources such as upwelling magma creating advective heat flow ((Ingebritsen et al., 2006), Figure 24). Typical continental heat flow ranges from 40 mW/m^2 or temperature gradients in the range of 20° to 35° C. Most often variations from these ranges are due to shallow magma, groundwater flow, or both (Ingebritsen et al., 2006). Fluid flow near magma bodies is driven in part by thermal convection, fluid density changes, and volatiles (CO_2 and water vapor, plus other minor constituents). The route that the ascending fluid takes is determined by pressure gradients, heat gradients, permeability of the surrounding rocks, which is itself determined by tectonic faults, fractures that include fractures caused by the strain of intrusion, and in the case of the Guadalupe Mountains, cavernous porosity. These paths of flow can be opened and closed by any of the above mentioned forces and tend to change over time due to mineralization and diagenesis (Ingebritsen et al., 2006).

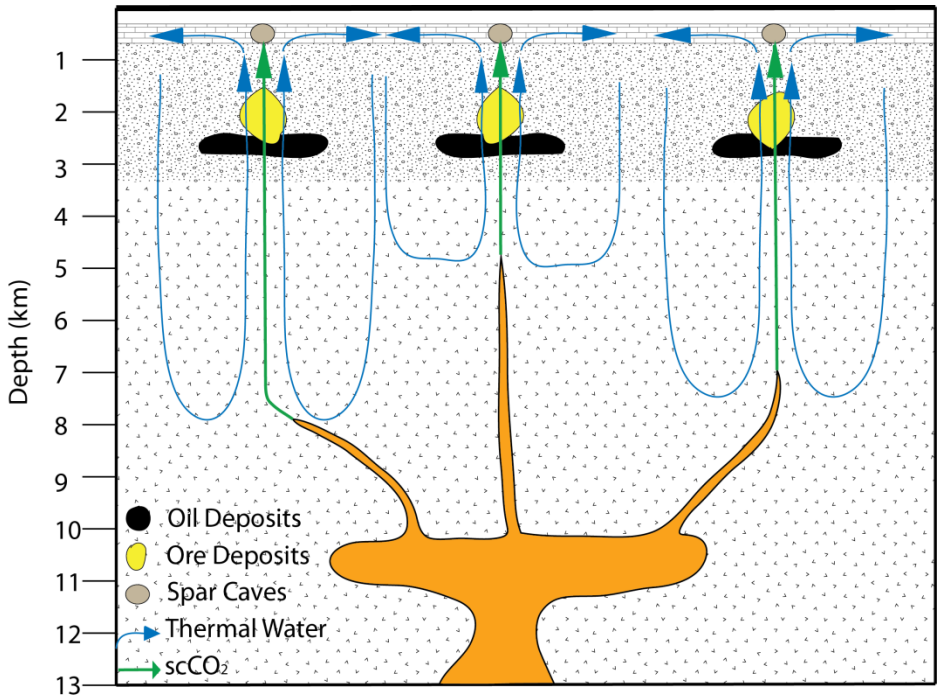

Figure 24: Hydrothermal flow graphic. This graphic depicts the hydrothermal flow set up and driven by magmatic processes. Heated groundwater scavenges and mobilizes metals from the host rock and then later deposits it as shallower depths as the temperature and pressure regimes change. As the fluids get closer to the surface, supercritical CO_2 changes to sub-critical CO_2 forming the small voids. The flow of groundwater near the surface removes the $CaCO_3$ saturated water allowing further dissolution of the vugs. As the magmatic activity ceases and the flow of $scCO_2$ wanes, the hydrologic flow changes and allows slightly $CaCO_3$ saturated waters to remain in the area to precipitate the scalenohedral spar in the voids.

Epithermal economic deposits exist due to mobilization and transport of metals from the surrounding country rock by groundwater heated through magmatism, which then deposits the metals in mineable quantities due to changes in temperature, pressure, or ground water mixing (Ingebritsen et al., 2006). We interpret this to happen beneath the spar forming horizon in which the spar caves are formed, between 10 and 1 km in depth (Figure 24; (Ingebritsen et al., 2006). Trace element analysis of nearby basalt dikes and the spar crystals are, however, inconclusive and show widely varying results suggesting different source areas, different scavenging mechanisms, or possibly different routes to

the surface. Known mineral deposits in the Guadalupe Mountains include: iron, copper, sulfur, and fluorite (Hill, 1990; Hill, 1996; Polyak and Provencio, 2001), all of which can be deposited hydrothermally. Hill (1996) provides a thorough review of elemental sulfur and Mississippi Valley Type (MVT) deposits of the Guadalupe

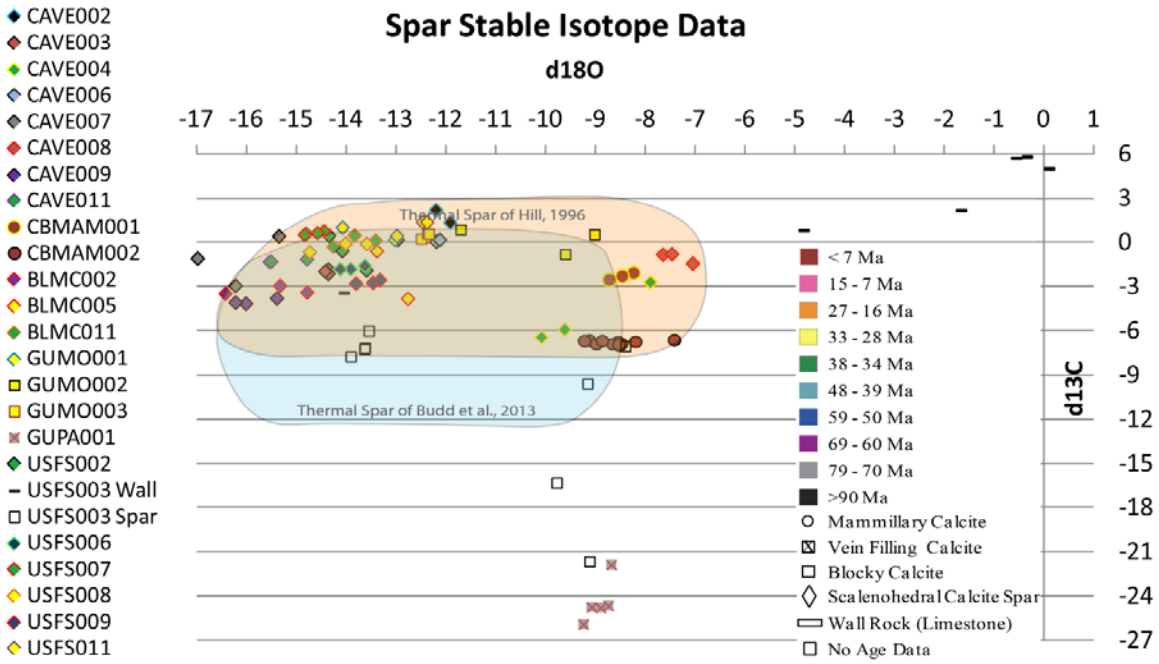

Figure 25: Stable isotope data from scalenohedral spar formed in the Guadalupe Mountains. Thermal spar fields from Hill (1996) and Budd et al., (2013).

Mountains. In other studies it is shown that MVT deposits form at shallow depth (<800 m) and moderate temperatures (83° to 101° C, (Ingebritsen et al., 2006)). While MVT deposits in the United States are thought to occur from regional scale hydrologic flow and transport of metals over long distances, other types of MVT deposits, such as the "Irish" MVTs, are associated with volcanism and make for good analogs of the processes that may have occurred in the Guadalupe Mountains (Ingebritsen et al., 2006).

Based on the age of the spar and the correlation to known magmatic events (discussed below) in the region for some of the spar dates (Figure 19), along with $^{87}Sr/^{86}Sr$ and $\delta^{13}C$ values of the $CaCO_3$ (Decker et al., 2017), it is evident that the provenance of the CO_2 that formed the spar caves and cave spar was hypogene magmatic rather than soil derived. What causes spar to precipitate? It is a combination of several factors, specifically temperature, pressure and salinity changes that are modeled to take place at the end of CO_2 spar cave speleogenesis, all of which directly contribute to the saturation or super-saturation of the fluid from which the $CaCO_3$ is dissolving or precipitating. Dogtooth spar reportedly precipitates from just barely supersaturated thermal solutions (R: 1.01 - 1.20 or so (Gary et al., 2002)). CO_2 goes from supercritical to subcritical over a very narrow range of temperatures and pressures (Domingo et al., 2004). The change from $scCO_2$ to $subCO_2$ causes gas to exsolve and escape the system, causing a shift from under saturated in $CaCO_3$ and aggressive to slightly super-saturated in $CaCO_3$ and precipitating. This shift can be caused by very slight temperature variations over a certain pressure range which corresponds to 500 ± 250 meters in depth (Decker et al., 2016). Cave spar can grow relatively rapidly (a football sized crystal can grow in less than a million years for example and within the timeframes of the lifetime of a typical magmatic episode (Goff et al., 1988). These episodes of magmatic activity are interpreted to be the same episodes that drive hydrocarbon maturation and ore deposition.

The age range of most of the cave spar is between 180 to 28 Ma. Two more recent cave spar sites are located to the east towards the Guadalupe tectonic block hinge(s) in Carlsbad Cavern. Overall the landscape of the Guadalupe Mountains/Delaware Basin region must have been relatively stable from 180 to 28 Ma (Decker et al., 2017); otherwise the cave-forming strata would have been too deep or too shallow for precipitation of cave spar. This suggests that Laramide compression and Basin and Range extension did not contribute significantly to the elevation of the study area prior to about 28 Ma, and may not as a whole contributed to origin of regional ore deposits. However, individual magmatic events, many represented by our cave spar dates, may have been largely responsible for maturation and migration of hydrocarbon, elemental sulfur, and MVT ores. For example, the Delaware basin has large hydrocarbon reservoirs and is a major source of oil and gas production and, contains economic deposits of elemental sulfur, and small mostly non-economical deposits of MVT ores.

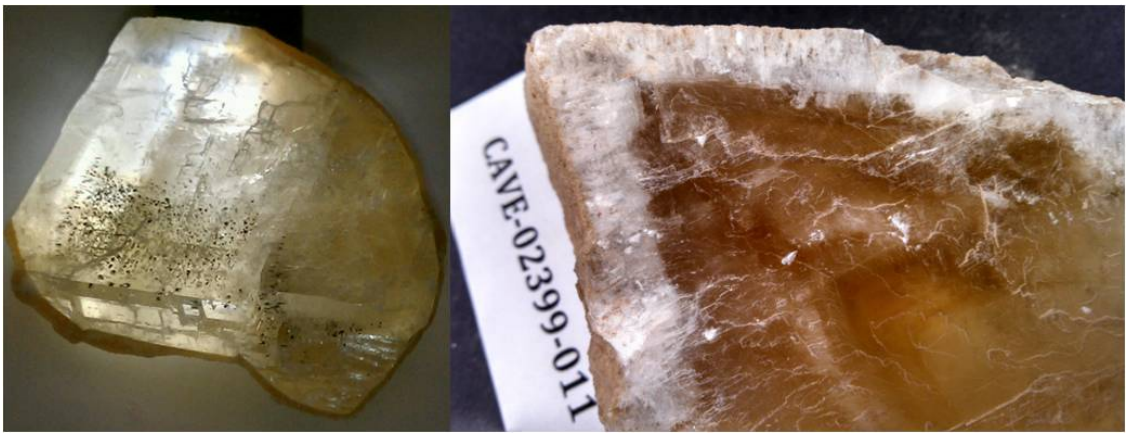

Figure 26: Cave spar samples from the Guadalupe Mountains contain numerous bitumen inclusions. These two samples come from widely separated locations. The sample on the left is from cave BLM-NM-060-030 and is 29.8 ± 1.2 Ma. The sample on the right is from cave CAVE-C-10 20 km to the southwest and is 36.1 ± 2.1 Ma.

Hill (1996) states numerous times that the depths required for the temperature to be high enough to begin cracking the hydrocarbons was deeper than the formation rocks were buried, using a local, modern day geothermal gradient of 20° C/km. The only way to account for this is that a much higher temperature gradient existed during the time of petroleum maturation (50° to 70° C/km). We can assume that the magmatic events that drove the spar cave dissolution and spar formation may also have been responsible for the maturation and possible migration of the oils from the source rocks to the traps. Bitumen inclusions in spar formed during the ignimbrite flare-up support this conclusion (Figure 26).

Elemental sulfur was first reported in the larger sulfuric acid caves such as Carlsbad Cavern and Lechuguilla Cave by Davis (1973), and in more detail by Hill (1995; 1996), showing that sulfuric acid speleogenesis can form elemental sulfur deposits. The larger economic deposits are also interpreted to form from H_2S (Hill, 1996) in the Delaware Basin and are found in areas where hydrothermally driven fluids would likely ascend from depth, e.g. the graben-

boundary faults in the Castile gypsum (Hill, 1996; Kirkland, 2014). It is likely that magmatic/tectonic events related to spar cave speleogenesis also play an important role in sulfuric acid cave speleogenesis, and that these larger basinal deposits of elemental sulfur are related to these magmatic pulses.

MVT ore deposits exist in the Guadalupe Mountains and Delaware Basin, but are small (Hill, 1996). Gossans are typically related to hydrothermal springs and are heavily enriched in mineral such as iron, manganese, zinc, silver and copper. A well-known gossan within the Guadalupe Mountains is the Queen of the Guadalupe's Mine which is known to contain molybdenum, lead, and zinc (Hill, 1996). Other metals found there include trace amounts of barium, copper, and iron (Thompson, 1983). Knowing that spar caves and spar are formed by degassing thermal waters that derive their heat and CO_2 from magma bodies, we can use spar locations on the surface to guide searches for epithermal ores such as copper, silver, gold, and molybdenum that are precipitated from rising hydrothermal plumes (Brown and Simmons, 2003; Simmons and Brown, 2006). In areas such as the Guadalupe Mountains where there are no obvious volcanic features to guide us and any surface expression of a hydrothermal play such as travertine mounds, hot springs, and seeps have long since been eroded away, we can use these spar caves to locate areas of fossil hydrothermal systems that may lead to ore bodies of economic value at depth.

The Border Fault zone vein spar in Guadalupe Pass indicates that the faults responsible for tilting of the Guadalupe tectonic block were active as early as 16.1 ± 0.4 Ma. This pushes back the timing of the uplift from 12 Ma (Polyak et al.,

1998) to 16 Ma. The youngest cave spar dated thus far on the western end of the Guadalupe tectonic block is 28 Ma (sample GUMO-00549-002). Our previous study (Decker et al., 2017) indicates that the uplift of this tectonic block, the rise of the cave-forming strata above the water table, began between 28 and 16 Ma and probably marks the end of major ore deposition in the region, although some deposits may have formed to the east of the study area later.

Summary

Scalenohedral calcite spar can be used to interpret both the tectonic and geothermal history of a region. This cave spar only precipitates at shallow crustal depths and limited temperature and pressure ranges creating a spar horizon. This spar horizon can then be used as a constraining factor on uplift since there is a delicate balance between uplift and location of the water table in a karst environment such as the Guadalupe Mountains. Since hydrothermal deposits are ephemeral and disappear from the landscape quickly, having a proxy for their locations can help to determine past histories of a region including possible volcanic activity and ore deposition. Dating of the spar and determination of the temperature of precipitation can further constrain uplift rates and help to determine the age and location of possible economic epithermal ore deposits and the timing of petroleum maturation. In this paper, we have linked magmatic intrusion, through hydrothermal activity, to the growth of spar caves and subsequent precipitation of cave spar, the possible timing of maturation and movement of petroleum plays, and the origin of minor ore deposits found throughout the region.

CHAPTER 6 - Summary

The Guadalupe Mountains region (Figure 1) is well studied, but little about the actual landscape evolution of the area is known. King (1948) states that the region was of “post-cretaceous age, most probably Oligocene to Miocene” and may have been composed of up to three periods of uplift. Hills (1984) suggests that there has been little to no uplift in the region since the end of the Permian. Eaton (1986) concluded that the area was uplifted during the formation of the Basin and Range producing a topographic high to the west called the Alvarado Ridge, which subsequently subsided along a central basin during Rio Grande rifting. Lundberg, et al. (2000) obtained a U-Pb date of 90.7 ± 2.8 Ma from a spar crystal in Big Canyon and concluded that a deep seated hydrothermal event during the Laramide produced cave formation, spar deposition and hydrocarbon maturation and may have been responsible for post-Permian uplift of the region. Duchene and Martinez (2000) believe the Alvarado Ridge arose during the Laramide, based on the paleo-botanical evidence of Gregory and Chase (1992) from farther north in the southern Rockies. The landscape evolution of this region may seem simple, but based on the wide range of views proffered by the above authors it is more complicated than the above mentioned authors would have you believe. Since few outcrops exist that are related to landscape evolution and ore generation, it becomes even more difficult to determine the absolute timing of the history of this mountain range, making proxies for these processes valuable resources. Spar caves in the Guadalupe Mountains are essentially large geodes lined with macro-crystalline calcite that have formed

long before the sulfuric acid cave genesis events (Hill, 1996). The large calcite crystals are called 'cave spar', and are phreatically precipitated deposits (Gary et al., 2002). Calcite spar deposits in the caves and in small vugs of the Guadalupe Mountains and adjacent Delaware basin (Figure 2A) have been categorized by Hill (1996), Mruk (1985) and Lloyd et al. (2013) Cave spar used in this study fits the mesogenetic spar of Hill (1996) and the spar II of Mruk (1985). Decker et al. (2016), (CHAPTER 2) showed that these spar formed in the deep phreatic zone, which is demonstrated by U-Pb ages (Table 8), δ^{88}Sr temperature values (Table 5) and the previous alunite-based paleo-water table elevations determined by Polyak et al. (1998), (Figure 19). In this study, we showed that the two latest spar forming events were derived from a fossil hydrothermal system driven by magmatic events that occurred during the basin and range extension and the Rio Grande rifting.

The relative importance and absolute timing of the tectonic/magmatic events in the evolution of the regional landforms is vaguely known because of the lack of dateable materials present in the Guadalupe Mountains. Some speleothem types can be used to make inferences on landscape evolution (Bakalowicz et al., 1987), and growth of these speleothems can record the processes that shaped this landscape and preserve evidence of the timing and role of each. Hydrothermal systems are heavily entwined with the last two events that occurred in this region and have been connected temporally to well-known Cenozoic magmatic events (Decker et al., 2012).

U-Pb dating of cave spar shows that there are multiple generations of cave spar formation in the Guadalupe Mountains. This spar is hydrothermally generated (Dublyansky, 2000) at depths between 250 and 1000 meters during phase changes associated with carbon dioxide (Decker et al., 2016) and highly dependent on pressure and temperature.

Twenty-two U-Pb ages of cave spar calcite from 18 locations (16 different caves, Figure 1) cluster between 30 to 28 Ma, 40 to 34 Ma and 64 to 54 Ma (Figure 19). There are four outliers, one at 180 Ma (this study), one at 91 Ma (Lundberg et al., 2000) and two others at 9.45 ± 0.14 and 13.08 ± 0.29 Ma (Also this study, Table 8). Fibrous fault filling spar sampled from the Border Fault zone in Guadalupe Pass, Texas yielded an isochron age of 16.11 ± 0.43 Ma, putting constraints on the timing of block fault activity. A mammillary (a phreatic speleothem formed at or just below the water table) dated at 2.13 ± 0.24 million years places the water table at the bottom level of Carlsbad Caverns and well below the majority of the spar locations by the late Pliocene.

Depth of formation of cave spar is determined via several methods. We used a cave spar sample from a Grand Canyon cave, and two cave spar samples, one from the New Mexico Room and another from the Bell Room of Carlsbad Cavern, as absolute indicators of depth of formation of these euhedral crystals. The sample from Grand Canyon yielded a U-Pb age of 232 ± 2 Ma. The cave is in the Redwall Limestone, located ~750 m below Triassic-aged, near-sea-level sediments. From this, we can infer that the cave spar formed ~750 m below a paleo-water table (Decker et al., 2011). In Carlsbad Cavern, sample CAVE-

02399-003 yielded an age of 13.08 ± 0.29 Ma, and CAVE-02399-008 yielded an age of 9.45 ± 0.14 Ma.

The elevation of these samples are ~500 and 800 m below a 9 and 13 My-old paleo-water table defined by Polyak et al. (1998). All three samples provide absolute depths of 500-800 m below water tables for the origin of this type of cave spar (Decker et al., 2016). Additionally, Dublyansky (2000) approached the depth of spar formation from an analytical point of view and determined that large scalenohedral spar should form between 500 and 1000 meters below the water table.

Temperatures are based on three different thermometers: fluid inclusions and strontium isotopes, derived directly from the calcite crystals (Decker et al., 2016), and vitrinite reflectance data (Barker and Pawlewicz, 1987), which gave us a maximum geothermal gradient for the region during the time of interest. All three thermometers suggest that the spar was deposited in temperatures ranging from 45 to 80° C and possibly as high as 90°C. While these temperatures are not considered hot for geothermal purposes, and the depths are not deep for tectonic regimes, these temperatures and depths can provide us insight into near surface processes that are not available by other means.

Limestone has an $^{87}Sr/^{86}Sr$ ratio that is in equilibrium with the water from which it was precipitated (Albarede, 2006), as do speleothems (Banner et al., 1996). The Sr isotope values of the spar are all well above those of the host bedrock and suggest that these spar caves and the cave spar were formed, at least partially,

by rising deep-seated water, and that supercritical CO_2 ($scCO_2$) associated with the rising water mixed with an overlying briny aquifer forming an aggressive solution that formed the small caves and then subsequently deposited the spar in a spar horizon (Decker et al., 2016). The cave spar has values significantly higher than the Permian limestones, and likely formed as the terminal phase of this small-scaled speleogenesis that we interpret as being linked to magmatic activity. Precipitation of calcite took place as the thermal events diminished and the CO_2 dwindled, allowing precipitation rather than dissolution.

Based on the age of the spar and the correlation to known magmatic events in the region for some of the spar dates (Figure 2B), along with $\delta^{13}C$ values of the $CaCO_3$ (Figure 25), it is evident that the provenance of the gas was magmatic rather than soil derived. The isotopic evidence, including $\delta^{18}O$, further supports the hypothesis that magma derived, super critical CO_2 was instrumental in both dissolving the vug space and precipitating the spar in the voids (Figure 10). Spar precipitates due to a combination of several factors, specifically temperature, pressure and salinity, all of which directly contribute to the saturation or super-saturation of the fluid from which the $CaCO_3$ is dissolving or precipitating. Scalenohedral spar precipitates from just barely supersaturated thermal solutions (R: 1.01 - 1.20 or so (Gary et al., 2002)). CO_2 goes from supercritical to subcritical over a very narrow range of temperatures and pressures (Domingo et al., 2004). The change from $scCO_2$ to $subCO_2$ causes gas to exsolve and escape the system, causing a shift from under saturated in $CaCO_3$ and aggressive to slightly super-saturated in $CaCO_3$ and precipitating. This shift can

be caused by very slight temperature variations over a certain pressure range which corresponds to 500 ± 250 meters in depth (Decker et al., 2016). Cave spar can grow relatively rapidly, a football sized crystal can grow in less than a million years and within the timeframes of the lifetime of a typical magmatic system (Goff et al., 1988). (Part of our study dated the core and rim of a crystal approximately 15 cm in length along the c-axis and 10 cm in diameter. The age of the core and the age of the rim were the same within error (± 0.97 Ma)). Euhedral scalenohedral spar is hypothesized to form from slightly supersaturated, thermal waters at depths of approximately 500 meters (Dublyansky, 2000). This is supported by our findings.

Most of our cave spar ages are coincident with two periods of major volcanic events that occurred in southeastern and southwestern New Mexico and the Trans-Pecos region of west Texas during Basin and Range development ~36 to 28 Ma. Only 12 km due east of our study area, and 30 km due west (Figure 1), several basaltic intrusions have been dated at ~35 to 30 Ma (Barker et al., 1977). Further to the south and to the west, volcanic activity took place during this same period (Chamberlin et al., 2002; Chapin et al., 2004; McIntosh et al., 1992)(Figure 2B). In southwestern New Mexico large calderas formed during a bimodal period similar to our cave spar age results at 32 to 28 and 36 to 34 Ma (Chamberlin et al., 2002; Chapin et al., 2004) and an arc of volcanism dated at the same time underlies our study area (McIntosh et al., 1992). The similarity in timing of these events supports an interpretation that origin of the cave spar, and

possibly the small caves themselves, took place due to thermally activated groundwater.

The Guadalupe tectonic block is tilted about 1.2° (DuChene and Cunningham, 2006) to the east. The block includes the Guadalupe Mountains and Delaware basin (King, 1948)). The block is reportedly hinged on the east end near the area of the Pecos River and is highest on its west end (King, 1948). Well data places the hinge just east of Carlsbad, New Mexico (Hiss, 1976). About 1000 meters of uplift of this tilted block, between 12 and 4 Ma (at least relative to the local water table) has been worked out by absolute means ($^{40}Ar/^{39}Ar$ dating of cave alunite; Polyak et al. 1998). That study does not extend westward to the 'border' faults, and depending on when faulting was initiated and the extent of regional uplift before block tilting, an additional >1500 meters (1000 + 1500 = 2500 m elevation of cave-forming strata today) of pre-12 Ma rise of the western edge of the block needs explanation. Knowing that cave spar grows ~300 to 800 meters below the water table, any significant uplift of the region would likely cause the paleo-water table to drop, which would cease formation of the spar. A paleo-water table needs to be maintained several hundred meters above the cave-forming strata for the cave spar to form.

The Border Fault Zone vein spar in Guadalupe Pass indicates that the faults responsible for tilting of the Guadalupe tectonic block were active as early as 16.1 ± 0.5 Ma. This pushes back the timing of the uplift from 12 Ma (Polyak et al., 1998)) to 16 Ma. The youngest cave spar dated thus far on the western end of the Guadalupe tectonic block is 28 Ma (sample GUMO-00549-002). Our study

indicates that the uplift of this tectonic block, the rise of the cave-forming strata above the water table, began between 28 and 16 Ma. Extending the trend of H_2SO_4-cave genesis elevation (Polyak et al., 1998) back to 16 Ma places the cave-forming strata at an elevation of 3000 m. The elevation of the cave-forming strata at the Guadalupe tectonic block hinge is ~1000 m, showing that the western end of the block rose 2000 m in the last 16 Ma by our interpretation. Most of the tilting (uplift) of the Guadalupe tectonic block occurred during Rio Grande rift tectonic activity.

The age range of most of the cave spar is between 90 to 28 Ma. The landscape must have been stable during this time; otherwise the cave-forming strata would have been too deep or too shallow for precipitation of cave spar. This suggests that Laramide compression and Basin and Range extension did not contribute significantly to the elevation of the study area prior to about 28 Ma.

Knowing that spar caves and spar are formed by degassing thermal waters that derive their heat and CO_2 from magma bodies, we can use spar locations on the surface to guide searches for epithermal ores such as copper, silver, gold, and molybdenum that are precipitated from rising hydrothermal plumes (Brown and Simmons, 2003; Simmons and Brown, 2006). In areas such as the Guadalupe Mountains where there are no obvious volcanic features to guide us and any surface expression of a hydrothermal play such as travertine mounds, hot springs and seeps have long since been eroded away, we can use these spar caves to locate areas of fossil hydrothermal systems that may lead to ore bodies of economic value at depth.

APPENDIX A.1 - GLOSSARY

Ac. *Analcime*
Ae. *Aenigmatite*
Af. *Arfvedsonite*
AF. *Alkali Feldspar*
Am. *Amphibole*
An. *Anorthite*
Ap. *Apatite*
Ba. *Bastnaesite*
BFZ. *Border Fault Zone*
BHVO. *Basalt - Hawaii Volcanic Observatory*
Bi. *Biotite*
BLMC. *Bureau of Land Management - Carlsbad Feild Office*
CAVE. *Carlsbad Caverns National Park*
CB. *City of Carlsbad*
CC. *Carlsbad Caverns*
Ch. *Chlorophaeite*
Cl. *Chlorite*
Cp. *Cryptoperthite*
CRF. *Cave Research Foundation*
Ct. *Catapleiite*
DP. *Diablo Plateau*
eP. *East of the Pecos*
Eu. *Eudialyte*
F&E. *Fietzke and Eisenhauer*
FIA. *Fluid Inclusion Assemblage*
Fr. *Ferroedenite*
Fy. *Fayalite*
GUMO. *Guadalupe Mountains National Park*
Hb. *Hornblende*
Il. *Ilminite*
IUGS. *International Union of Geological Sciences*
kcps. *1000 counts per second*
LECH. *Lechuguilla Cave*
LN. *Liquid Nitrogen*
L-V. *Liquide to Vapor*
Ma. *million years*
MC-ICP-MS. *Multicollector Inductively Coupled Plasma Mass Spectrometer*
Mg. *Magnetite*
Mp. *Microperthite*
NG. *Not Given*
NMGS. *New Mexico Geological Society*
NOAA. *National Oceanic and Atmospheric Administration*
Np. *Nepheline*
NSF. *National Science Foundation*
NSN. *No Sample Number*
NSS. *National Speleological Society*
Nt. *Natrolite*
Ol. *Olivine*
Or. *Orthoclase*
Pl. *Plagioclase*
Px. *Pyroxene*
Rb. *Rubidium*
REE. *Rare Earth Element*
scCO_2. *Supercritical Carbon Dioxide*
SCFH. *Standard Cubic Feet per Hour*
SEM. *Secondary Electron Multiplier*
So. *Sodalite*
subCO_2. *Subcritical Carbon Dioxide*
T_h. *Temperature of Homogenization*
T_{mf}. *Temperature of Final Melting*
T_{mi}. *Temperature of Initial Melting*
TML. *Table Mountain Latite*
Unk. *Unknown*
USFS. *US Forest Service - Guadalupe District*
USGS. *US Geological Survey*
WIPP. *Waste Isolation Pilot Plant*
WT. *Water Table*
YH. *Yeso Hills*
Zr. *Zircon*
δ^{88}Sr. *difference between the ratio of 88Sr/86Sr of a standard to that of a calcium carbonate sample expressed as per mil calcium carbonate*

Cave Number	Sample Name	Sample Weight (g)	Spike Weight (g)	U conc. ppm*	%error 2σ	^{232}Th conc. ppb‡	%error 2σ	Pb conc. ppb*
CAVE-C-1	CAVE-02399-002d	0.0912	0.2589	0.428	± 0.026	N/A	–	13.656
CCBR#1	CAVE-02399-002e	0.1040	0.2989	0.800	± 0.016	N/A	–	23.561
	CAVE-02399-002f	0.1557	0.1882	0.804	± 0.017	N/A	–	23.641
«	CAVE-02399-002x	0.0266	0.1074	0.521	± 0.108	242.458	± 1.452	18.630
	CAVE-02399-002y	0.0139	0.0915	1.444	± 0.966	242.879	± 2.740	39.853
	CAVE-02399-002z	0.0157	0.0994	0.866	± 0.107	196.022	± 3.028	24.358
CAVE-C-1	CAVE-02399-003a	0.0669	0.1220	0.265	± 0.114	20.454	± 0.721	3.174
CCBR#2	CAVE-02399-003b	0.0558	0.1285	0.249	± 0.114	17.222	± 1.020	2.474
	CAVE-02399-003c	0.0460	0.1192	0.195	± 0.131	20.791	± 1.013	2.066
	CAVE-02399-003d	0.0528	0.1045	0.254	± 0.119	28.485	± 0.670	2.247
	CAVE-02399-003e	0.0845	0.1162	0.247	± 0.105	19.814	± 0.602	3.458
	CAVE-02399-003x	0.0714	0.1040	0.222	± 0.104	11.082	± 1.2	2.661
	CAVE-02399-003y	0.0765	0.1169	0.145	± 0.105	28.900	± 0.6	1.743
	CAVE-02399-003z	0.0451	0.1595	0.124	± 0.114	41.624	± 0.5	1.552
CAVE-C-5	CAVE-02399-004a	0.0800	0.1500	1.295	± 0.101	118.121	± 0.265	44.403
LCHSC	CAVE-02399-004b	0.0460	0.1513	2.190	± 0.103	35.469	± 0.738	16.917
	CAVE-02399-004c	0.1355	0.1518	2.716	± 1.160	9.910	± 0.763	20.083
	CAVE-02399-004d	0.0712	0.1543	1.851	± 0.104	37.286	± 0.688	16.942
	CAVE-02399-004e	0.0540	0.1472	1.714	± 0.102	51.488	± 0.424	16.867
CAVE-C-5	CAVE-02399-006a	0.0266	0.1045	0.094	± 0.157	1.614	± 21.616	2.979
LCHWB	CAVE-02399-006b	0.0194	0.0847	0.023	± 0.644	2.544	± 19.215	1.483
	CAVE-02399-006c	0.0544	0.1294	0.050	± 0.149	1.491	± 11.487	1.523
	CAVE-02399-006d	0.0188	0.0654	0.045	± 0.401	7.114	± 7.144	1.992
	CAVE-02399-006e	0.0294	0.0896	0.030	± 0.353	4.524	± 7.260	1.036
	CAVE-02399-006x	0.0172	0.0951	0.353	± 0.118	7.266	± 7.446	3.251
	CAVE-02399-006y	0.0239	0.0906	0.054	± 0.241	1.359	± 28.551	0.602
	CAVE-02399-006z	0.0148	0.0964	0.026	± 0.675	8.910	± 7.150	0.379
CAVE-C-1	CAVE-02399-007a	0.0962	0.1431	0.160	± 0.114	235.020	± 0.212	2.380
CCGRC	CAVE-02399-007b	0.0675	0.1522	0.158	± 0.115	366.902	± 2.302	3.512
	CAVE-02399-007c	0.0348	0.1602	0.104	± 0.130	356.010	± 1.578	2.615
	CAVE-02399-007d	0.0566	0.1588	0.102	± 0.119	523.851	± 0.544	31.694
	CAVE-02399-007e	0.0973	0.1471	0.185	± 0.109	621.915	± 0.418	7.159
	CAVE-02399-007x	0.0552	0.1450	0.081	± 0.117	614.956	± 0.332	3.091
	CAVE-02399-007y	0.0433	0.1214	0.137	± 0.111	342.423	± 0.271	2.933
	CAVE-02399-007z	0.0628	0.1213	0.127	± 0.107	408.650	± 0.575	2.871
CAVE-C-1	CAVE-02399-008a	0.1237	0.1202	7.171	± 0.108	8.165	± 0.938	142.960
CCNMR	CAVE-02399-008b	0.1464	0.1042	0.650	± 0.105	201.816	± 0.218	1.647
	CAVE-02399-008c	0.1095	0.0853	5.795	± 0.127	19.702	± 0.493	71.183

Cave Number	Sample Name	%error 2σ	U/Pb	$\delta^{234}U^{\ddagger}$	%error 2σ	$[^{230}Th/^{238}U]^{\ddagger}$	%error 2σ	$^{238}U/^{204}Pb$	%error 2σ	$^{206}Pb/^{204}Pb$	%error 2σ
CAVE-C-1	CAVE-02399-002d	± 0.271	31.4	N/A	--	N/A	--	9204.2	± 3.89	270.194	± 3.630
CCBR#1	CAVE-02399-002e	± 0.133	34.0	N/A	--	N/A	--	20298.0	± 4.02	605.734	± 3.890
	CAVE-02399-002f	± 0.107	34.0	N/A	--	N/A	--	21448.0	± 2.83	641.931	± 2.740
«	CAVE-02399-002x	± 0.510	27.9	-17.6	± 1.0	1.01377	± 0.002	3392.7	± 0.42	82.073	± 0.299
	CAVE-02399-002y	± 0.504	36.2	-4.0	± 1.0	1.01623	± 0.010	30664.0	± 2.57	882.789	± 2.340
	CAVE-02399-002z	± 0.508	35.6	0.4	± 1.0	1.01077	± 0.003	24910.0	± 2.87	720.392	± 2.800
CAVE-C-1	CAVE-02399-003a	± 0.621	83.5	3.8	± 1.0	1.08019	± 0.003	6367.4	± 0.72	32.143	± 0.276
CCBR#2	CAVE-02399-003b	± 0.731	100.5	2.5	± 1.0	1.00093	± 0.004	7912.2	± 1.12	34.853	± 0.470
	CAVE-02399-003c	± 0.905	94.1	0.9	± 1.3	0.09239	± 0.002	7559.5	± 1.66	36.473	± 0.705
	CAVE-02399-003d	± 0.772	113.1	1.3	± 1.0	1.00457	± 0.004	9366.9	± 1.33	38.705	± 0.600
	CAVE-02399-003e	± 0.583	71.5	1.1	± 1.0	0.99748	± 0.003	5325.4	± 0.55	30.208	± 0.239
	CAVE-02399-003x	± 0.644	83.6	2.2	± 1.0	0.23675	± 0.001	6387.0	± 0.79	32.362	± 0.275
	CAVE-02399-003y	± 0.741	83.5	1.6	± 1.0	1.03483	± 0.004	6712.3	± 1.15	35.859	± 0.453
	CAVE-02399-003z	± 1.150	80.2	3.1	± 1.0	4.45713	± 0.015	6468.3	± 2.28	35.959	± 0.867
CAVE-C-5	CAVE-02399-004a	± 0.509	29.2	0.3	± 1.0	1.00777	± 0.002	2101.3	± 0.19	27.572	± 0.072
LCHSC	CAVE-02399-004b	± 0.530	129.4	-1.0	± 1.0	0.99888	± 0.002	22265.0	± 1.18	137.316	± 0.999
	CAVE-02399-004c	± 0.505	135.2	-3.0	± 1.0	0.99256	± 0.036	25591.0	± 1.22	156.393	± 0.327
	CAVE-02399-004d	± 0.517	109.2	-0.6	± 1.0	0.99330	± 0.003	14474.0	± 0.61	93.927	± 0.463
	CAVE-02399-004e	± 0.542	101.6	-0.7	± 1.0	0.98125	± 0.002	12602.0	± 0.82	84.196	± 0.636
CAVE-C-5	CAVE-02399-006a	± 1.010	31.4	8.4	± 2.4	1.00979	± 0.006	5615.3	± 3.15	55.569	± 2.230
LCHWB	CAVE-02399-006b	± 2.840	15.4	13.6	± 5.0	1.08136	± 0.026	1557.2	± 6.29	27.838	± 1.690
	CAVE-02399-006c	± 0.971	32.5	19.2	± 2.0	1.06609	± 0.008	6967.0	± 3.18	66.675	± 2.180
	CAVE-02399-006d	± 2.070	22.5	2.8	± 4.0	1.19055	± 0.018	2702.1	± 4.98	35.049	± 2.060
	CAVE-02399-006e	± 2.500	28.9	5.6	± 3.5	1.06181	± 0.016	4778.6	± 8.21	47.640	± 4.500
	CAVE-02399-006x	± 0.770	108.5	0.8	± 1.1	1.00295	± 0.003	23486.0	± 5.43	174.819	± 4.780
	CAVE-02399-006y	± 2.740	89.7	6.5	± 2.0	1.01212	± 0.012	12049.0	± 15.80	91.210	± 11.300
	CAVE-02399-006z	± 16.700	68.6	14.2	± 2.9	0.98976	± 0.019	7905.5	± 195.00	62.153	± 122.000
CAVE-C-1	CAVE-02399-007a	± 0.631	67.3	0.4	± 1.0	1.02774	± 0.003	22748.0	± 4.02	195.288	± 3.630
CCGRC	CAVE-02399-007b	± 0.653	45.0	1.7	± 1.0	1.04512	± 0.014	12270.0	± 3.14	143.550	± 2.700
	CAVE-02399-007c	± 1.260	39.8	1.1	± 1.4	1.06846	± 0.010	23332.0	± 17.90	289.213	± 16.500
	CAVE-02399-007d	± 0.514	3.2	1.5	± 1.4	1.08628	± 0.005	221.7	± 0.21	20.597	± 0.071
	CAVE-02399-007e	± 0.533	25.9	0.2	± 1.0	1.06180	± 0.005	3916.0	± 0.63	64.790	± 0.425
	CAVE-02399-007x	± 1.130	26.2	3.1	± 1.1	1.05927	± 0.007	31955.0	± 21.80	410.001	± 20.700
	CAVE-02399-007y	± 1.820	46.8	1.4	± 1.0	1.03001	± 0.005	15934.0	± 17.40	176.329	± 15.000
	CAVE-02399-007z	± 0.523	44.3	1.5	± 1.0	1.04234	± 0.006	62872.0	± 5.88	751.832	± 5.750
CAVE-C-1	CAVE-02399-008a	± 0.505	50.2	-0.8	± 1.0	1.01505	± 0.002	3403.6	± 0.14	23.246	± 0.061
CCNMR	CAVE-02399-008b	± 0.621	394.7	-2.6	± 1.0	1.01697	± 0.003	200580.0	± 8.33	467.944	± 7.980
	CAVE-02399-008c	± 0.504	81.4	-1.6	± 1.0	1.00597	± 0.002	5769.4	± 0.16	26.575	± 0.062

Cave Number	Sample Name	$^{238}U/^{208}Pb$	%error 2σ	$^{206}Pb/^{208}Pb$	%error 2σ	$^{235}U/^{204}Pb$	%error 2σ	$^{207}Pb/^{204}Pb$	%error 2σ	$^{238}U/^{206}Pb$
CAVE-C-1	CAVE-02399-002d	223.105	± 3.905	6.549	± 3.38	66.794	± 3.89	28.113	± 1.75	34.065
CCBR#1	CAVE-02399-002e	478.388	± 4.042	14.276	± 3.55	147.300	± 4.02	44.912	± 2.63	33.510
	CAVE-02399-002f	505.349	± 2.850	15.125	± 2.50	155.640	± 2.83	46.718	± 1.89	33.412
«	CAVE-02399-002x	86.710	± 0.442	2.096	± 0.28	24.620	± 0.42	18.746	± 0.16	41.337
	CAVE-02399-002y	717.270	± 2.616	20.637	± 2.06	222.530	± 2.57	58.716	± 1.81	34.735
	CAVE-02399-002z	575.927	± 2.930	16.646	± 2.43	180.770	± 2.87	50.673	± 2.07	34.578
CAVE-C-1	CAVE-02399-003a	163.412	± 0.437	0.811	± 0.206	46.208	± 0.72	16.260	± 0.24	200.832
CCBR#2	CAVE-02399-003b	202.833	± 0.653	0.876	± 0.358	57.418	± 1.12	16.399	± 0.37	230.612
	CAVE-02399-003c	193.162	± 0.960	0.915	± 0.580	54.859	± 1.66	16.450	± 0.52	210.257
	CAVE-02399-003d	236.014	± 0.767	0.955	± 0.478	67.974	± 1.33	16.600	± 0.42	246.100
	CAVE-02399-003e	136.811	± 0.357	0.764	± 0.162	38.646	± 0.55	16.179	± 0.25	178.454
	CAVE-02399-003x	164.203	± 0.804	0.818	± 0.232	46.350	± 0.79	16.259	± 0.22	200.072
	CAVE-02399-003y	168.274	± 1.170	0.885	± 0.372	48.710	± 1.15	16.435	± 0.32	189.623
	CAVE-02399-003z	161.837	± 2.305	0.886	± 0.710	46.940	± 2.28	16.477	± 0.58	182.133
CAVE-C-5	CAVE-02399-004a	54.209	± 0.226	0.711	± 0.074	15.249	± 0.19	16.005	± 0.10	76.210
LCHSC	CAVE-02399-004b	569.612	± 1.206	3.513	± 0.955	161.580	± 1.18	21.123	± 0.46	162.144
	CAVE-02399-004c	657.951	± 1.229	4.024	± 0.316	185.710	± 1.22	22.005	± 0.18	163.632
	CAVE-02399-004d	371.557	± 0.630	2.411	± 0.441	105.400	± 0.61	19.102	± 0.23	154.098
	CAVE-02399-004e	320.026	± 0.941	2.138	± 0.589	91.451	± 0.82	18.667	± 0.47	149.674
CAVE-C-5	CAVE-02399-006a	43.492	± 4.104	0.430	± 1.250	40.750	± 3.15	17.754	± 1.69	101.051
LCHWB	CAVE-02399-006b	21.861	± 6.675	0.390	± 1.160	11.300	± 6.29	16.227	± 1.45	55.938
	CAVE-02399-006c	44.020	± 3.960	0.421	± 0.555	50.559	± 3.18	17.969	± 1.16	104.492
	CAVE-02399-006d	31.863	± 5.577	0.413	± 0.982	19.609	± 4.98	16.581	± 1.54	77.095
	CAVE-02399-006e	38.876	± 9.729	0.387	± 1.580	34.678	± 8.21	16.860	± 2.81	100.306
	CAVE-02399-006x	604.110	± 5.494	4.486	± 4.620	170.440	± 5.43	23.367	± 2.29	134.344
	CAVE-02399-006y	322.787	± 15.935	2.438	± 11.600	87.438	± 15.80	19.413	± 4.65	132.102
	CAVE-02399-006z	198.911	± 195.225	1.560	± 117.000	54.596	± 195.00	19.476	± 38.10	127.194
CAVE-C-1	CAVE-02399-007a	148.820	± 0.723	1.278	± 0.602	165.080	± 4.02	24.475	± 1.88	116.486
CCGRC	CAVE-02399-007b	87.637	± 0.612	1.025	± 0.430	89.039	± 3.14	21.786	± 1.27	85.471
	CAVE-02399-007c	68.478	± 1.409	0.849	± 0.800	169.320	± 17.90	29.126	± 9.32	80.672
	CAVE-02399-007d	5.250	± 0.181	0.488	± 0.064	1.609	± 0.21	15.722	± 0.10	10.762
	CAVE-02399-007e	44.214	± 0.236	0.732	± 0.100	28.418	± 0.63	17.835	± 0.23	60.441
	CAVE-02399-007x	33.902	± 30.131	0.434	± 0.231	231.890	± 21.80	33.766	± 12.70	77.939
	CAVE-02399-007y	88.023	± 21.901	0.973	± 1.700	115.630	± 17.40	23.571	± 7.10	90.365
	CAVE-02399-007z	79.596	± 8.141	0.950	± 0.147	456.250	± 5.88	50.643	± 4.27	83.625
CAVE-C-1	CAVE-02399-008a	88.610	± 0.143	0.605	± 0.062	24.700	± 0.14	15.848	± 0.09	146.414
CCNMR	CAVE-02399-008b	2400.068	± 3.422	5.599	± 3.400	1455.600	± 8.33	35.388	± 5.10	428.659
	CAVE-02399-008c	150.231	± 0.157	0.692	± 0.064	41.868	± 0.16	16.000	± 0.09	217.101

Cave Number		Sample Name	%error 2σ	$^{207}Pb/^{206}Pb$	%error 2σ	$^{204}Pb/^{206}Pb$	%error 2σ	Concordia age (Ma)	error (Ma)	MSWD
CAVE-C-1		CAVE-02399-002d	± 5.314	0.10404	± 4.021	0.003701	± 3.630	184.2	± 7.8	0.45
CCBR#1		CAVE-02399-002e	± 5.594	0.07413	± 4.696	0.001651	± 3.890			
		CAVE-02399-002f	± 3.939	0.07277	± 3.329	0.001558	± 2.740			
	«	CAVE-02399-002x	± 0.514	0.22839	± 0.340	0.012184	± 0.299			
		CAVE-02399-002y	± 3.476	0.06650	± 2.958	0.001133	± 2.340			
		CAVE-02399-002z	± 4.010	0.07033	± 3.482	0.001388	± 2.800			
CAVE-C-1		CAVE-02399-003a	± 0.483	0.51278	± 0.179	0.031111	± 0.276	13.08	± 0.29	1.15
CCBR#2		CAVE-02399-003b	± 0.745	0.47788	± 0.316	0.028692	± 0.470			
		CAVE-02399-003c	± 1.122	0.45744	± 0.499	0.027417	± 0.705			
		CAVE-02399-003d	± 0.904	0.43605	± 0.435	0.025837	± 0.600			
		CAVE-02399-003e	± 0.392	0.54208	± 0.140	0.033104	± 0.239			
		CAVE-02399-003x	± 0.833	0.50925	± 0.354	0.030900	± 0.275			
		CAVE-02399-003y	± 1.236	0.46423	± 0.552	0.027887	± 0.453			
		CAVE-02399-003z	± 2.439	0.46390	± 1.041	0.027810	± 0.867			
CAVE-C-5		CAVE-02399-004a	± 0.199	0.58043	± 0.122	0.036268	± 0.072	34.82	± 0.38	2.4
LCHSC		CAVE-02399-004b	± 1.546	0.15377	± 1.101	0.007282	± 0.999			
		CAVE-02399-004c	± 1.263	0.14065	± 0.372	0.006394	± 0.327			
		CAVE-02399-004d	± 0.763	0.20332	± 0.517	0.010647	± 0.463			
		CAVE-02399-004e	± 1.040	0.22166	± 0.789	0.011877	± 0.636			
CAVE-C-5		CAVE-02399-006a	± 3.859	0.31946	± 2.798	0.017996	± 2.230	44.6	± 1.6	0.96
LCHWB		CAVE-02399-006b	± 6.513	0.58287	± 2.227	0.035922	± 1.690			
		CAVE-02399-006c	± 3.855	0.26947	± 2.469	0.014998	± 2.180			
		CAVE-02399-006d	± 5.389	0.47305	± 2.572	0.028531	± 2.060			
		CAVE-02399-006e	± 9.362	0.35386	± 5.305	0.020991	± 4.500			
		CAVE-02399-006x	± 7.234	0.13362	± 5.300	0.005720	± 4.780			
		CAVE-02399-006y	± 19.425	0.21279	± 12.219	0.010964	± 11.300			
		CAVE-02399-006z	± 230.020	0.31331	± 127.811	0.016089	± 122.000			
CAVE-C-1		CAVE-02399-007a	± 0.941	0.12529	± 2.080	0.005121	± 3.630	77.2	± 1.4	28
CCGRC		CAVE-02399-007b	± 0.748	0.15174	± 1.750	0.006966	± 2.700			
		CAVE-02399-007c	± 1.620	0.10068	± 8.050	0.003458	± 16.500			
		CAVE-02399-007d	± 0.192	0.76332	± 0.034	0.048550	± 0.071			
		CAVE-02399-007e	± 0.257	0.27526	± 0.324	0.015435	± 0.425			
		CAVE-02399-007x	± 30.062	0.08233	± 24.285	0.002439	± 20.700			
		CAVE-02399-007y	± 22.973	0.13365	± 16.595	0.005671	± 15.000			
		CAVE-02399-007z	± 8.224	0.06733	± 7.162	0.001330	± 5.750			
CAVE-C-1		CAVE-02399-008a	± 0.156	0.68169	± 0.031	0.043018	± 0.061	9.23	± 0.36	± 34
CCNMR		CAVE-02399-008b	± 4.824	0.07548	± 3.230	0.002137	± 7.980			
		CAVE-02399-008c	± 0.169	0.60199	± 0.034	0.037630	± 0.062			

Cave Number		Sample Name	^{238}U-$^{206}Pb(^{204}Pb)$ age	error (Ma)	MSWD	^{238}U-$^{206}Pb(^{208}Pb)$ age	error (Ma)	MSWD	^{235}U-$^{207}Pb(^{204}Pb)$ age
CAVE-C-1		CAVE-02399-002d	184.0	± 7.90	± 1.02	183.7	7.9	± 1.14	184.9
CCBR#1		CAVE-02399-002e							
		CAVE-02399-002f							
	«	CAVE-02399-002x							
		CAVE-02399-002y							
		CAVE-02399-002z							
CAVE-C-1		CAVE-02399-003a	13.46	± 0.52	0.75	12.42	± 0.36	0.27	14.3
CCBR#2		CAVE-02399-003b							
		CAVE-02399-003c							
		CAVE-02399-003d							
		CAVE-02399-003e							
		CAVE-02399-003x							
		CAVE-02399-003y							
		CAVE-02399-003z							
CAVE-C-5		CAVE-02399-004a	34.78	± 0.22	2.6	35.10	± 0.95	3.1	34.76
LCHSC		CAVE-02399-004b							
		CAVE-02399-004c							
		CAVE-02399-004d							
		CAVE-02399-004e							
CAVE-C-5		CAVE-02399-006a	44.4	± 1.8	1.14	46.7	± 3.4	0.47	44
LCHWB		CAVE-02399-006b							
		CAVE-02399-006c							
		CAVE-02399-006d							
		CAVE-02399-006e							
		CAVE-02399-006x							
		CAVE-02399-006y							
		CAVE-02399-006z							
CAVE-C-1		CAVE-02399-007a	76.70	± 0.68	0.14	70	± 13	± 0.2	76.9
CCGRC		CAVE-02399-007b							
		CAVE-02399-007c							
		CAVE-02399-007d							
		CAVE-02399-007e							
		CAVE-02399-007x							
		CAVE-02399-007y							
		CAVE-02399-007z							
CAVE-C-1		CAVE-02399-008a	9.45	± 0.57	47	9.43	± 0.50	46	9.45
CCNMR		CAVE-02399-008b							
		CAVE-02399-008c							

Cave Number		Sample Name	error (Ma)	MSWD	^{207}Pb-$^{206}Pb(^{204}Pb)$ age	error (Ma)	MSWD	$^{238}U/^{206}$ Pb Model Ages	error (%)	Average
CAVE-C-1		CAVE-02399-002d	7.4	± 0.95	185	± 47	0.011			187.5
CCBR#1		CAVE-02399-002e								
		CAVE-02399-002f								
	«	CAVE-02399-002x						187.45	± 4.45	
		CAVE-02399-002y						186.70	± 8.54	
		CAVE-02399-002z						188.36	± 10.60	
CAVE-C-1		CAVE-02399-003a	± 2.4	1.12				13.21	± 0.69	13.41
CCBR#2		CAVE-02399-003b						12.84	± 0.69	
		CAVE-02399-003c						14.82	± 0.90	
		CAVE-02399-003d						13.49	± 0.61	
		CAVE-02399-003e						13.46	± 0.63	
		CAVE-02399-003x								
		CAVE-02399-003y								
		CAVE-02399-003z								
CAVE-C-5		CAVE-02399-004a	± 0.34	1.7				35.14	± 0.37	35.18
LCHSC		CAVE-02399-004b						35.35	± 0.85	
		CAVE-02399-004c						35.60	± 0.59	
		CAVE-02399-004d						34.90	± 0.55	
		CAVE-02399-004e						35.06	± 0.73	
CAVE-C-5		CAVE-02399-006a	± 3.9	0.06				47.95	± 3.95	48.0
LCHWB		CAVE-02399-006b						48.84	± 8.58	
		CAVE-02399-006c						49.61	± 3.77	
		CAVE-02399-006d						46.87	± 5.17	
		CAVE-02399-006e						45.05	± 7.82	
		CAVE-02399-006x						43.35	± 15.31	
		CAVE-02399-006y								
		CAVE-02399-006z								
CAVE-C-1		CAVE-02399-007a	± 1.5	0.12				79.85	± 9.91	81.7
CCGRC		CAVE-02399-007b						79.66	± 34.08	
		CAVE-02399-007c						81.76	± 10.92	
		CAVE-02399-007d						81.80	± 1.58	
		CAVE-02399-007e						83.65	± 46.04	
		CAVE-02399-007x								
		CAVE-02399-007y								
		CAVE-02399-007z								
CAVE-C-1		CAVE-02399-008a	± 0.14	0.75				9.65	± 1.94	9.54
CCNMR		CAVE-02399-008b						9.55	± 2.67	
		CAVE-02399-008c						9.45	± 1.15	

Cave Number		Sample Name	error (%)	$^{235}U/^{207}$ Pb Model Ages	error (%)	Average	error (%)
CAVE-C-1		CAVE-02399-002d	± 0.5			187.4	± 9.1
CCBR#1		CAVE-02399-002e					
		CAVE-02399-002f					
	«	CAVE-02399-002x		187.40	± 6.95		
		CAVE-02399-002y		186.68	± 9.18		
		CAVE-02399-002z		188.52	± 10.79		
CAVE-C-1		CAVE-02399-003a	± 0.72	13.91	± 3.67	14.25	± 0.71
CCBR#2		CAVE-02399-003b		13.62	± 3.42		
		CAVE-02399-003c		15.18	± 4.14		
		CAVE-02399-003d		14.48	± 3.09		
		CAVE-02399-003e		14.52	± 4.35		
		CAVE-02399-003x					
		CAVE-02399-003y					
		CAVE-02399-003z					
CAVE-C-5		CAVE-02399-004a	± 0.31	34.85	± 2.27	34.73	± 0.43
LCHSC		CAVE-02399-004b		34.83	± 1.12		
		CAVE-02399-004c		35.03	± 0.73		
		CAVE-02399-004d		34.31	± 0.79		
		CAVE-02399-004e		34.81	± 1.43		
CAVE-C-5		CAVE-02399-006a	± 1.8	44.54	± 7.12	44.3	± 2.4
LCHWB		CAVE-02399-006b		45.30	± 45.11		
		CAVE-02399-006c		44.31	± 10.18		
		CAVE-02399-006d		44.04	± 27.48		
		CAVE-02399-006e		42.04	± 22.52		
		CAVE-02399-006x					
		CAVE-02399-006y					
		CAVE-02399-006z					
CAVE-C-1		CAVE-02399-007a	± 1.2	3.58	± 0.00	76.8	± 1.7
CCGRC		CAVE-02399-007b		0.53	± 0.00		
		CAVE-02399-007c		4.01	± 1.20		
		CAVE-02399-007d		1.37	± 0.00		
		CAVE-02399-007e		9.84	± 0.00		
		CAVE-02399-007x					
		CAVE-02399-007y					
		CAVE-02399-007z					
CAVE-C-1		CAVE-02399-008a	± 0.06	9.57	± 1.24	9.42	± 1.54
CCNMR		CAVE-02399-008b		9.41	± 0.21		
		CAVE-02399-008c		9.29	± 0.75		

Cave Number	Sample Name	Sample Weight (g)	Spike Weight (g)	U conc. ppm*	%error 2σ	^{232}Th conc. ppb‡	%error 2σ	Pb conc. ppb*
	CAVE-02399-008d	0.1154	0.0747	4.297	± 0.119	41.222	± 0.327	9.563
	CAVE-02399-008e	0.0952	0.0946	0.579	± 0.108	226.100	± 0.211	1.479
CAVE-C-5	CAVE-02399-009a	0.0433	0.0969	0.422	± 0.107	26.115	± 0.844	14.540
LCHBS	CAVE-02399-009b	0.0849	0.1285	0.070	± 0.125	20.071	± 0.813	1.047
	CAVE-02399-009c	0.1402	0.1689	0.376	± 0.110	24.108	± 0.298	12.204
	CAVE-02399-009d	0.1020	0.1498	0.315	± 0.118	27.711	± 0.376	4.268
	CAVE-02399-009e	0.0815	0.1087	0.246	± 0.116	26.209	± 0.486	2.574
	CAVE-02399-009x	0.0568	0.1244	0.147	± 0.108	20.867	± 0.877	1.531
	CAVE-02399-009y	0.0546	0.1257	0.484	± 0.103	16.517	± 1.060	12.785
	CAVE-02399-009z	0.0652	0.1448	0.191	± 0.123	22.915	± 0.650	1.928
CAVE-C-1	CC-001-A	0.0592	0.1181	0.999	± 0.110	0.083	± 189.800	1415.100
CCLOC	CC-001-B	0.0467	0.1250	1.490	± 0.108	0.089	± 222.300	903.230
	CC-001-C	0.0413	0.1245	2.148	± 0.102	0.118	± 190.400	349.150
	CC-001-D	0.0421	0.1255	0.968	± 0.105	0.062	± 375.200	328.070
	CC-001-E	0.0605	0.1188	1.045	± 0.104	0.111	± 138.300	1527.900
CAVE-C-10	CAVE-02399-011a	0.0338	0.0974	3.687	± 0.107	607.950	± 0.189	41.324
CCCRS	CAVE-02399-011b	0.0362	0.0945	4.984	± 0.103	986.142	± 0.142	33.866
	CAVE-02399-011c	0.0187	0.0955	2.357	± 0.104	397.921	± 0.254	28.581
	CAVE-02399-011d	0.0447	0.0910	3.689	± 0.108	739.350	± 0.160	32.691
	CAVE-02399-011e	0.0297	0.0969	2.295	± 0.106	366.806	± 0.205	23.844
BLM-NM-060-0021	BLMC-20122-002a	0.0412	0.1482	0.967	± 0.017	N/A	—	13.313
BLMWN	BLMC-20122-002b	0.0412	0.1714	0.956	± 0.229	N/A	—	9.588
	BLMC-20122-002c	0.0391	0.2056	0.249	± 0.108	N/A	—	2.246
	BLMC-20122-002d	0.0325	0.1982	0.866	± 0.102	N/A	—	2.971
	BLMC-20122-002e	0.0436	0.1994	0.011	± 1.060	N/A	—	0.517
	BLMC-20122-002x	0.0767	0.0970	0.789	± 0.107	103.414	± 0.2	8.616
	BLMC-20122-002y	0.0532	0.1032	0.827	± 0.103	109.437	± 0.2	8.508
	BLMC-20122-002z	0.0536	0.1134	0.994	± 0.112	106.330	± 0.2	9.886
BLM-NM-060-0030	BLMC-20122-005a	0.0584	0.1598	1.698	± 0.103	11.817	± 1.4	12.648
BLMLR	BLMC-20122-005b	0.0851	0.1497	1.265	± 0.103	311.120	± 0.6	5.165
	BLMC-20122-005c	0.0816	0.1429	1.770	± 0.179	526.185	± 0.3	9.994
	BLMC-20122-005d	0.0681	0.1409	1.623	± 0.102	455.343	± 0.2	14.168
	BLMC-20122-005e	0.0612	0.1457	1.606	± 0.107	235.011	± 0.2	8.314
	BLMC-20122-005x	0.1097	0.1278	1.917	± 0.101	526.233	± 0.1	9.635
	BLMC-20122-005y	0.1130	0.1285	1.577	± 0.101	112.627	± 0.1	10.222
	BLMC-20122-005z	0.1094	0.1279	1.434	± 0.106	355.205	± 0.1	6.277
BLM-NM-060-27	BLMC-20122-011a	0.1439	0.1500	1.556	± 0.109	42.857	± 0.9	9.816

Cave Number	Sample Name	%error 2σ	U/Pb	$\delta^{234}U^{‡}$	%error 2σ	$[^{230}Th/^{238}U]^{‡}$	%error 2σ	$^{238}U/^{204}Pb$	%error 2σ	$^{206}Pb/^{204}Pb$	%error 2σ
	CAVE-02399-008d	± 0.518	449.3	-1.5	± 1.0	0.99981	± 0.002	71140.0	± 0.62	122.532	± 0.508
	CAVE-02399-008e	± 0.797	391.4	-5.7	± 1.0	1.00503	± 0.002	710370.0	± 53.10	1754.939	± 52.700
CAVE-C-5	CAVE-02399-009a	± 0.504	29.0	5.5	± 1.0	1.00795	± 0.002	2519.8	± 0.17	42.898	± 0.095
LCHBS	CAVE-02399-009b	± 0.532	66.5	6.2	± 1.8	1.02438	± 0.006	19519.0	± 2.42	244.771	± 2.280
	CAVE-02399-009c	± 0.502	30.8	10.8	± 1.0	1.00852	± 0.002	2741.7	± 0.14	45.134	± 0.066
	CAVE-02399-009d	± 0.503	73.8	5.6	± 1.0	1.00678	± 0.002	14731.0	± 0.35	159.859	± 0.293
	CAVE-02399-009e	± 0.505	95.7	4.9	± 1.0	1.00627	± 0.002	104460.0	± 3.62	1081.769	± 3.580
	CAVE-02399-009x	± 0.528	96.3	6.7	± 1.0	1.03068	± 0.005	503430.0	± 44.80	5324.893	± 44.800
	CAVE-02399-009y	± 0.591	37.9	6.7	± 1.0	1.03394	± 0.007	3607.3	± 0.90	52.082	± 0.520
	CAVE-02399-009z	± 0.515	99.0	9.2	± 1.0	1.02840	± 0.003	124610.0	± 7.48	1252.849	± 7.390
CAVE-C-1	CC-001-A	± 0.501	0.7	-3.6	± 1.0	1.00340	± 0.002	45.9	± 0.13	20.162	± 0.061
CCLOC	CC-001-B	± 0.505	1.6	4.3	± 1.0	1.00607	± 0.002	107.3	± 0.14	20.165	± 0.061
	CC-001-C	± 0.507	6.2	-0.5	± 1.0	1.00023	± 0.001	400.9	± 0.16	20.267	± 0.064
	CC-001-D	± 0.507	2.9	-3.5	± 1.4	1.02329	± 0.009	192.0	± 0.16	10.189	± 0.064
	CC-001-E	± 0.501	0.7	-2.9	± 1.1	1.00407	± 0.003	44.5	± 0.13	20.161	± 0.060
CAVE-C-10	CAVE-02399-011a	± 0.508	89.2	-1.1	± 1.0	1.00036	± 0.002	11134.0	± 0.33	80.446	± 0.236
CCCRS	CAVE-02399-011b	± 0.506	147.2	-1.1	± 1.0	1.00828	± 0.002	51772.0	± 0.96	306.950	± 0.892
	CAVE-02399-011c	± 0.542	82.5	2.3	± 1.0	1.00623	± 0.002	9548.9	± 0.76	71.260	± 0.531
	CAVE-02399-011d	± 0.540	112.9	1.1	± 1.0	1.00929	± 0.002	19387.0	± 0.42	126.711	± 0.338
	CAVE-02399-011e	± 0.522	96.3	1.1	± 1.0	1.00768	± 0.002	12975.0	± 0.66	90.612	± 0.504
BLM-NM-060-0021	BLMC-20122-002a	± 0.691	72.6	N/A	---	N/A	---	171300.0	± 15.90	1715.284	± 15.800
BLMWN	BLMC-20122-002b	± 0.525	99.7	N/A	---	N/A	---	77172.0	± 5.35	797.998	± 5.210
	BLMC-20122-002c	± 0.625	110.8	N/A	---	N/A	---	45018.0	± 7.56	422.035	± 7.270
	BLMC-20122-002d	± 0.829	291.4	N/A	---	N/A	---	279970.0	± 29.90	914.561	± 29.300
	BLMC-20122-002e	± 2.970	20.8	N/A	---	N/A	---	1792.5	± 8.44	40.655	± 3.420
	BLMC-20122-002x	± 0.506	91.6	0.7	± 1.0	1.00602	± 0.001	107220.0	± 4.04	1198.422	± 3.990
	BLMC-20122-002y	± 0.511	97.2	2.3	± 1.0	1.00944	± 0.002	228700.0	± 11.70	2458.702	± 11.600
	BLMC-20122-002z	± 0.510	100.5	-2.7	± 1.0	1.00898	± 0.001	121400.0	± 5.07	1247.883	± 5.010
BLM-NM-060-0030	BLMC-20122-005a	± 0.506	134.2	0.0	± 1.0	1.00277	± 0.001	171570.0	± 4.06	1319.144	± 4.010
BLMLR	BLMC-20122-005b	± 0.515	244.9	-0.5	± 1.0	0.99524	± 0.019	131410.0	± 2.87	470.742	± 2.770
	BLMC-20122-005c	± 0.571	177.1	4.2	± 1.0	1.14290	± 0.003	67454.0	± 1.39	318.220	± 1.290
	BLMC-20122-005d	± 0.509	114.6	-0.1	± 1.0	1.01297	± 0.002	13010.0	± 0.32	66.118	± 0.217
	BLMC-20122-005e	± 0.511	193.2	-0.3	± 1.0	1.00824	± 0.002	102250.0	± 2.49	488.487	± 2.400
	BLMC-20122-005x	± 0.503	199.0	-0.3	± 1.0	1.01548	± 0.001	141390.0	± 1.49	653.974	± 1.450
	BLMC-20122-005y	± 0.507	154.3	0.3	± 1.0	1.01165	± 0.001	36117.0	± 0.49	195.825	± 0.432
	BLMC-20122-005z	± 0.510	228.4	-0.2	± 1.0	1.01399	± 0.001	108890.0	± 1.66	417.716	± 1.600
BLM-NM-060-27	BLMC-20122-011a	± 0.503	158.5	-0.8	± 1.0	1.00413	± 0.005	43485.0	± 0.47	242.125	± 0.418

Cave Number	Sample Name	$^{238}U/^{208}Pb$	%error 2σ	$^{206}Pb/^{208}Pb$	%error 2σ	$^{235}U/^{204}Pb$	%error 2σ	$^{207}Pb/^{204}Pb$	%error 2σ	$^{238}U/^{206}Pb$
	CAVE-02399-008d	1828.764	± 0.504	3.150	± 0.470	516.260	± 0.62	20.448	± 0.31	580.566
	CAVE-02399-008e	2812.938	± 7.377	6.949	± 7.350	5155.100	± 53.10	91.713	± 45.70	404.783
CAVE-C-5	CAVE-02399-009a	64.753	± 0.231	1.102	± 0.105	18.286	± 0.17	16.772	± 0.11	58.740
LCHBS	CAVE-02399-009b	321.174	± 3.277	4.028	± 1.980	141.650	± 2.42	26.759	± 1.61	79.744
	CAVE-02399-009c	70.287	± 0.187	1.157	± 0.069	19.896	± 0.14	16.872	± 0.09	60.745
	CAVE-02399-009d	345.077	± 0.438	3.745	± 0.294	106.900	± 0.35	22.330	± 0.20	92.150
	CAVE-02399-009e	1337.174	± 4.657	13.847	± 2.310	758.040	± 3.62	66.729	± 3.03	96.564
	CAVE-02399-009x	1747.657	± 59.529	18.456	± 5.710	3653.300	± 44.80	274.860	± 42.60	94.543
	CAVE-02399-009y	93.137	± 0.914	1.343	± 0.489	26.178	± 0.90	17.208	± 0.27	69.261
	CAVE-02399-009z	1435.731	± 8.668	14.411	± 3.130	904.300	± 7.48	75.362	± 6.10	99.461
CAVE-C-1	CC-001-A	1.195	± 0.178	0.525	± 0.061	0.333	± 0.13	15.712	± 0.09	2.278
CCLOC	CC-001-B	2.795	± 0.187	0.525	± 0.061	0.778	± 0.14	15.698	± 0.09	5.319
	CC-001-C	10.435	± 0.202	0.527	± 0.062	2.909	± 0.16	15.718	± 0.09	19.782
	CC-001-D	4.997	± 0.204	0.525	± 0.062	1.394	± 0.16	15.715	± 0.09	18.847
	CC-001-E	1.158	± 0.175	0.524	± 0.060	0.323	± 0.13	15.714	± 0.09	2.207
CAVE-C-10	CAVE-02399-011a	267.189	± 0.249	1.931	± 0.205	80.796	± 0.33	18.588	± 0.14	138.400
CCCRS	CAVE-02399-011b	903.525	± 0.584	5.357	± 0.570	375.710	± 0.96	29.323	± 0.52	168.667
	CAVE-02399-011c	231.315	± 0.518	1.726	± 0.462	69.296	± 0.76	18.152	± 0.26	134.001
	CAVE-02399-011d	425.086	± 0.305	2.779	± 0.269	140.690	± 0.42	20.790	± 0.18	152.993
	CAVE-02399-011e	307.672	± 0.468	2.149	± 0.431	94.156	± 0.66	19.069	± 0.25	143.188
BLM-NM-060-0021	BLMC-20122-002a	1746.391	± 16.674	17.487	± 5.020	1242.800	± 15.90	81.143	± 14.30	99.867
BLMWN	BLMC-20122-002b	1070.466	± 6.148	11.069	± 3.030	559.910	± 5.35	46.604	± 3.77	96.707
	BLMC-20122-002c	612.782	± 8.167	5.745	± 3.090	326.620	± 7.56	19.112	± 4.31	106.669
	BLMC-20122-002d	2184.876	± 30.993	7.138	± 8.160	2031.700	± 29.90	58.050	± 22.50	306.125
	BLMC-20122-002e	43.799	± 8.889	0.993	± 2.790	13.008	± 8.44	17.290	± 1.97	44.091
	BLMC-20122-002x	1228.629	± 4.767	13.712	± 1.620	778.050	± 4.04	70.645	± 3.31	89.468
	BLMC-20122-002y	1651.144	± 14.622	17.724	± 3.050	1659.600	± 11.70	128.917	± 10.50	93.017
	BLMC-20122-002z	1539.417	± 5.811	15.798	± 2.330	881.010	± 5.07	72.603	± 4.13	97.285
BLM-NM-060-0030	BLMC-20122-005a	4199.178	± 4.133	32.286	± 3.710	1245.000	± 4.06	78.984	± 3.34	130.062
BLMLR	BLMC-20122-005b	1661.588	± 3.262	5.952	± 1.260	953.640	± 2.87	36.825	± 1.79	279.155
	BLMC-20122-005c	908.790	± 1.702	4.287	± 0.537	489.510	± 1.39	30.590	± 1.01	211.973
	BLMC-20122-005d	301.234	± 0.356	1.531	± 0.173	94.414	± 0.32	17.816	± 0.14	196.769
	BLMC-20122-005e	1718.025	± 2.710	8.208	± 1.460	741.990	± 2.49	38.381	± 1.63	209.320
	BLMC-20122-005x	1574.920	± 1.745	7.258	± 0.584	1026.100	± 1.49	45.330	± 1.04	216.201
	BLMC-20122-005y	864.933	± 0.544	4.675	± 0.378	262.100	± 0.49	24.087	± 0.27	184.435
	BLMC-20122-005z	1490.602	± 1.948	5.693	± 0.738	790.180	± 1.66	34.214	± 1.13	260.680
BLM-NM-060-27	BLMC-20122-011a	1061.179	± 0.496	5.909	± 0.377	315.560	± 0.47	26.155	± 0.24	179.598

Cave Number	Sample Name	%error 2σ	$^{207}Pb/^{206}Pb$	%error 2σ	$^{204}Pb/^{206}Pb$	%error 2σ	Concordia age (Ma)	error (Ma)	MSWD
	CAVE-02399-008d	± 0.689	0.16668	± 0.346	0.008161	± 0.508			
	CAVE-02399-008e	± 10.414	0.05212	± 0.828	0.000570	± 52.700			
CAVE-C-5	CAVE-02399-009a	± 0.197	0.39095	± 0.145	0.023311	± 0.095	62.1	± 3.8	95
LCHBS	CAVE-02399-009b	± 3.325	0.10929	± 2.791	0.004085	± 2.280			
	CAVE-02399-009c	± 0.154	0.37380	± 0.114	0.022156	± 0.066			
	CAVE-02399-009d	± 0.454	0.13965	± 0.356	0.006256	± 0.293			
	CAVE-02399-009e	± 5.091	0.06165	± 4.690	0.000924	± 3.580			
	CAVE-02399-009x	± 63.357	0.05159	± 61.821	0.000188	± 44.800			
	CAVE-02399-009y	± 1.035	0.33038	± 0.588	0.019200	± 0.520			
	CAVE-02399-009z	± 10.515	0.06012	± 9.582	0.000798	± 7.390			
CAVE-C-1	CC-001-A	± 0.144	0.77928	± 0.109	0.049598	± 0.061	2.13	± 0.24	1.09
CCLOC	CC-001-B	± 0.155	0.77848	± 0.109	0.049591	± 0.061			
	CC-001-C	± 0.173	0.77556	± 0.113	0.049342	± 0.064			
	CC-001-D	± 0.176	1.54240	± 0.113	0.098148	± 0.064			
	CC-001-E	± 0.141	0.77941	± 0.109	0.049600	± 0.060			
CAVE-C-10	CAVE-02399-011a	± 0.322	0.23101	± 0.172	0.012431	± 0.236	36.1	± 2.1	47
CCCRS	CAVE-02399-011b	± 0.816	0.09547	± 0.436	0.003258	± 0.892			
	CAVE-02399-011c	± 0.694	0.25419	± 0.405	0.014033	± 0.531			
	CAVE-02399-011d	± 0.406	0.16401	± 0.227	0.007892	± 0.338			
	CAVE-02399-011e	± 0.636	0.21040	± 0.367	0.011036	± 0.504			
BLM-NM-060-0021	BLMC-20122-002a	± 22.415	0.04727	± 21.310	0.000583	± 15.800	68.3	± 2.9	0.97
BLMWN	BLMC-20122-002b	± 7.468	0.05837	± 6.431	0.001253	± 5.210			
	BLMC-20122-002c	± 10.488	0.04525	± 8.452	0.002369	± 7.270			
	BLMC-20122-002d	± 41.863	0.06337	± 36.942	0.001093	± 29.300			
	BLMC-20122-002e	± 9.107	0.42527	± 3.947	0.024597	± 3.420			
	BLMC-20122-002x	± 5.678	0.05892	± 5.184	0.000834	± 3.990			
	BLMC-20122-002y	± 16.476	0.05240	± 15.646	0.000407	± 11.600			
	BLMC-20122-002z	± 7.128	0.05815	± 6.493	0.000801	± 5.010			
BLM-NM-060-0030	BLMC-20122-005a	± 5.706	0.05983	± 5.219	0.000758	± 4.010	29.8	± 1.2	4.5
BLMLR	BLMC-20122-005b	± 3.989	0.07813	± 3.298	0.002124	± 2.770			
	BLMC-20122-005c	± 1.896	0.09606	± 1.638	0.003142	± 1.290			
	BLMC-20122-005d	± 0.389	0.26940	± 0.260	0.015124	± 0.217			
	BLMC-20122-005e	± 3.458	0.07850	± 2.901	0.002047	± 2.400			
	BLMC-20122-005x	± 2.079	0.06924	± 1.784	0.001529	± 1.450			
	BLMC-20122-005y	± 0.654	0.12294	± 0.511	0.005107	± 0.432			
	BLMC-20122-005z	± 2.306	0.08182	± 1.959	0.002394	± 1.600			
BLM-NM-060-27	BLMC-20122-011a	± 0.627	0.10796	± 0.484	0.004130	± 0.418	34.4	± 1.2	2.3

Cave Number	Sample Name	^{238}U-$^{206}Pb(^{204}Pb)$ age	error (Ma)	MSWD	^{238}U-$^{206}Pb(^{208}Pb)$ age	error (Ma)	MSWD	^{235}U-$^{207}Pb(^{204}Pb)$ age
	CAVE-02399-008d							
	CAVE-02399-008e							
CAVE-C-5	CAVE-02399-009a	61.7	± 1.4	16	60.7	± 1.4	11.4	61.73
LCHBS	CAVE-02399-009b							
	CAVE-02399-009c							
	CAVE-02399-009d							
	CAVE-02399-009e							
	CAVE-02399-009x							
	CAVE-02399-009y							
	CAVE-02399-009z							
CAVE-C-1	CC-001-A	1.95	± 0.27	2.2	1.92	± 0.27	1.4	2.0
CCLOC	CC-001-B							
	CC-001-C							
	CC-001-D							
	CC-001-E							
CAVE-C-10	CAVE-02399-011a	36.04	± 0.38	0.48	34.71	± 0.30	1.2	36.46
CCCRS	CAVE-02399-011b							
	CAVE-02399-011c							
	CAVE-02399-011d							
	CAVE-02399-011e							
3LM-NM-060-0021	BLMC-20122-002a	68.2	± 2.9	1.6	66.8	± 2.6	1.9	66.1
BLMWN	BLMC-20122-002b							
	BLMC-20122-002c							
	BLMC-20122-002d							
	BLMC-20122-002e							
	BLMC-20122-002x							
	BLMC-20122-002y							
	BLMC-20122-002z							
3LM-NM-060-0030	BLMC-20122-005a	28.3	± 3.5	9.4	29.28	± 0.45	2.4	28.28
BLMLR	BLMC-20122-005b							
	BLMC-20122-005c							
	BLMC-20122-005d							
	BLMC-20122-005e							
	BLMC-20122-005x							
	BLMC-20122-005y							
	BLMC-20122-005z							
BLM-NM-060-27	BLMC-20122-011a	34.36	± 0.69	0.46	34.35	± 0.67	0.64	34.36

Cave Number	Sample Name	error (Ma)	MSWD	^{207}Pb-$^{206}Pb(^{204}Pb)$ age	error (Ma)	MSWD	$^{238}U/^{206}$ Pb Model Ages	error (%)	Average
	CAVE-02399-008d						9.54	± 0.21	
	CAVE-02399-008e						9.55	± 35.80	
CAVE-C-5	CAVE-02399-009a	± 0.56	2.1				64.97	± 4.28	64.20
LCHBS	CAVE-02399-009b						62.40	± 3.92	
	CAVE-02399-009c						65.15	± 3.89	
	CAVE-02399-009d						64.21	± 0.59	
	CAVE-02399-009e						66.04	± 10.65	
	CAVE-02399-009x								
	CAVE-02399-009y								
	CAVE-02399-009z								
CAVE-C-1	CC-001-A	± 6.8	0.02				2.87	± 3.13	2.36
CCLOC	CC-001-B						1.53	± 1.35	
	CC-001-C						2.23	± 0.37	
	CC-001-D						2.81	± 59.94	
	CC-001-E								
CAVE-C-10	CAVE-02399-011a	± 0.51	0.30				37.84	± 0.69	37.79
CCCRS	CAVE-02399-011b						37.67	± 0.82	
	CAVE-02399-011c						37.64	± 1.08	
	CAVE-02399-011d						37.84	± 0.43	
	CAVE-02399-011e						37.76	± 0.67	
BLM-NM-060-0021	BLMC-20122-002a	± 2.9	1.8						68.1
BLMWN	BLMC-20122-002b								
	BLMC-20122-002c								
	BLMC-20122-002d								
	BLMC-20122-002e						65.09	± 6.96	
	BLMC-20122-002x						70.67	± 6.08	
	BLMC-20122-002y						68.63	± 18.08	
	BLMC-20122-002z						68.57	± 13.38	
BLM-NM-060-0030	BLMC-20122-005a	± 0.67	2.3				50.50	± 4.29	
BLMLR	BLMC-20122-005b						23.96	± 1.45	
	BLMC-20122-005c						30.42	± 0.92	
	BLMC-20122-005d						25.58	± 0.34	
	BLMC-20122-005e						31.38	± 1.62	
	BLMC-20122-005x								
	BLMC-20122-005y								
	BLMC-20122-005z								
BLM-NM-060-27	BLMC-20122-011a	± 0.73	0.33				35.59	± 1.11	35.67

Cave Number	Sample Name	error (%)	$^{235}U/^{207}$ Pb Model Ages	error (%)	Average	error (%)
	CAVE-02399-008d		9.41	± 0.21		
	CAVE-02399-008e		9.41	± 0.21		
CAVE-C-5	CAVE-02399-009a	± 0.36	61.46	± 42.67	62.4	± 3.8
LCHBS	CAVE-02399-009b		59.38	± 31.73		
	CAVE-02399-009c		61.43	± 39.13		
	CAVE-02399-009d		61.64	± 7.87		
	CAVE-02399-009e		64.85	± 11.17		
	CAVE-02399-009x					
	CAVE-02399-009y					
	CAVE-02399-009z					
CAVE-C-1	CC-001-A	± 35				
CCLOC	CC-001-B					
	CC-001-C					
	CC-001-D					
	CC-001-E					
CAVE-C-10	CAVE-02399-011a	± 0.11	36.44	± 1.10	± 36.04	± 0.24
CCCRS	CAVE-02399-011b		36.28	± 0.89		
	CAVE-02399-011c		36.24	± 1.73		
	CAVE-02399-011d		36.50	± 0.80		
	CAVE-02399-011e		36.36	± 1.30		
BLM-NM-060-0021	BLMC-20122-002a	± 2.8			67.3	± 3.9
BLMWN	BLMC-20122-002b					
	BLMC-20122-002c					
	BLMC-20122-002d					
	BLMC-20122-002e		68.31	± 2.82		
	BLMC-20122-002x		62.67	± 6.68		
	BLMC-20122-002y		66.50	± 17.18		
	BLMC-20122-002z		65.61	± 35.23		
BLM-NM-060-0030	BLMC-20122-005a		49.50	± 4.34		
BLMLR	BLMC-20122-005b		21.16	± 1.56		
	BLMC-20122-005c		28.38	± 1.47		
	BLMC-20122-005d		12.09	± 2.62		
	BLMC-20122-005e		29.20	± 1.88		
	BLMC-20122-005x					
	BLMC-20122-005y					
	BLMC-20122-005z					
BLM-NM-060-27	BLMC-20122-011a	± 0.15	34.27	± 1.31	34.3	± 0.21

Cave Number	Sample Name	Sample Weight (g)	Spike Weight (g)	U conc. ppm*	%error 2σ	^{232}Th conc. ppb‡	%error 2σ	Pb conc. ppb*
BLMSH	BLMC-20122-011b	0.0532	0.1294	2.518	± 0.124	20.849	± 0.8	14.249
	BLMC-20122-011c	0.1055	0.1554	2.234	± 0.104	30.390	± 0.3	11.803
	BLMC-20122-011d	0.0649	0.1608	3.081	± 0.104	11.289	± 1.3	18.013
	BLMC-20122-011e	0.0545	0.1316	1.402	± 0.102	10.957	± 1.6	8.602
FSGD-C-90	USFS-11290-002a	0.0444	0.2060	8.125	± 0.116	994.997	± 0.2	61.171
USFVI	USFS-11290-002b	0.0557	0.2176	3.484	± 0.102	373.946	± 1.4	37.652
	USFS-11290-002c	0.0425	0.2128	10.853	± 0.102	1695.679	± 0.1	76.929
	USFS-11290-002d	0.0524	0.2192	0.236	± 0.109	36.837	± 2.2	2.557
	USFS-11290-002e	0.0489	0.2253	0.696	± 0.107	95.098	± 2.0	5.216
FSGD-C-202	USFS-11290-006a	0.0495	0.1775	0.675	± 0.101	0.298	± 63.4	8.339
USFDL	USFS-11290-006b	0.0722	0.1721	0.907	± 0.103	0.649	± 103.6	12.788
	USFS-11290-006c	0.0568	0.1645	0.840	± 0.104	0.312	± 54.0	8.179
	USFS-11290-006d	0.0490	0.1306	0.770	± 0.103	0.318	± 60.4	9.601
	USFS-11290-006e	0.0489	0.1506	0.775	± 0.105	0.397	± 48.6	17.487
	USFS-11290-006x	0.0238	0.0871	0.681	± 0.103	0.263	± 148.2	6.500
	USFS-11290-006y	0.0167	0.0971	0.784	± 0.109	0.368	± 151.0	7.405
	USFS-11290-006z	0.0147	0.0953	0.880	± 0.106	0.230	± 275.2	7.769
FSGD-C-72	USFS-11290-007a	0.0785	0.1689	0.042	± 4.130	0.379	± 36.8	13.576
USFEM	USFS-11290-007b	0.1046	0.1572	0.255	± 0.102	2.301	± 3.9	10.669
	USFS-11290-007c	0.0970	0.1394	0.065	± 0.113	0.533	± 18.0	13.072
	USFS-11290-007d	0.0827	0.1364	0.107	± 0.106	0.800	± 14.1	11.408
	USFS-11290-007e	0.1407	0.1581	0.054	± 0.116	0.519	± 15.1	14.244
FSGD-C-40	USFS-11290-008a	0.0280	0.1371	1.664	± 0.147	69.438	± 1.5	28.085
USFCL	USFS-11290-008b	0.0166	0.1255	1.698	± 0.147	99.660	± 1.0	43.456
	USFS-11290-008c	0.0739	0.1227	2.454	± 0.101	173.016	± 0.4	15.462
	USFS-11290-008d	0.0511	0.0466	1.713	± 0.107	72.205	± 1.1	29.728
	USFS-11290-008e	0.0236	0.0931	1.136	± 0.104	55.369	± 1.4	12.812
	USFS-11290-008f	0.0871	0.0799	2.200	± 0.103	77.328	± 2.3	19.168
FSGD-C-62	USFS-11290-009a	0.0483	0.1471	1.322	± 0.107	1.906	± 10.1	14.019
USFFR	USFS-11290-009b	0.0308	0.1148	0.855	± 0.129	0.142	± 212.7	9.218
	USFS-11290-009c	0.0514	0.0955	1.584	± 0.119	0.470	± 38.4	15.377
	USFS-11290-009d	0.0406	0.0817	2.611	± 0.140	1.705	± 13.4	27.645
	USFS-11290-009e	0.0523	0.1028	1.342	± 0.108	0.551	± 32.2	13.306
	USFS-11290-009f	0.0419	0.0873	1.995	± 0.104	0.680	± 32.6	17.435
	USFS-11290-009g	0.0383	0.0986	1.344	± 0.110	0.772	± 31.4	13.805
	USFS-11290-009x	0.0517	0.1092	1.332	± 0.117	0.581	± 30.9	12.652
	USFS-11290-009y	0.0492	0.1058	1.771	± 0.113	0.857	± 22.0	21.454
	USFS-11290-009z	0.0478	0.1127	1.351	± 0.104	0.236	± 82.2	14.181

Cave Number	Sample Name	%error 2σ	U/Pb	$\delta^{234}U^{\ddagger}$	%error 2σ	$[^{230}Th/^{238}U]^{\ddagger}$	%error 2σ	$^{238}U/^{204}Pb$	%error 2σ	$^{206}Pb/^{204}Pb$	%error 2σ
BLMSH	BLMC-20122-011b	± 0.507	176.7	-1.8	± 1.0	1.00689	± 0.002	86202.0	± 1.49	470.901	± 1.420
	BLMC-20122-011c	± 0.503	189.3	-1.0	± 1.0	1.00781	± 0.001	174130.0	± 1.69	930.401	± 1.650
	BLMC-20122-011d	± 0.503	171.0	-1.4	± 1.0	1.00564	± 0.001	67282.0	± 0.79	370.825	± 0.740
	BLMC-20122-011e	± 0.513	162.9	-0.7	± 1.0	1.00689	± 0.002	49402.0	± 1.48	274.234	± 1.370
FSGD-C-90	USFS-11290-002a	± 0.502	132.8	-0.6	± 1.0	1.01857	± 0.001	29202.0	± 0.24	183.522	± 0.183
USFVI	USFS-11290-002b	± 0.503	92.5	-1.5	± 1.0	1.02003	± 0.002	11921.0	± 0.21	87.684	± 0.147
	USFS-11290-002c	± 0.502	141.1	0.0	± 1.0	1.01473	± 0.002	37472.0	± 0.29	229.770	± 0.262
	USFS-11290-002d	± 0.775	92.3	-11.7	± 1.0	1.01606	± 0.004	15949.0	± 3.59	129.105	± 3.150
	USFS-11290-002e	± 0.570	133.3	-0.8	± 1.0	1.01867	± 0.003	42975.0	± 3.69	291.707	± 3.540
FSGD-C-202	USFS-11290-006a	± 0.516	81.0	7.8	± 1.0	1.26964	± 0.017	26926.0	± 1.91	310.830	± 1.790
USFDL	USFS-11290-006b	± 0.507	71.0	-1.9	± 1.0	1.05306	± 0.195	10076.0	± 0.39	102.781	± 0.305
	USFS-11290-006c	± 0.530	102.7	-2.2	± 1.0	1.00310	± 0.020	31617.0	± 2.54	281.250	± 2.470
	USFS-11290-006d	± 0.518	80.2	-1.4	± 1.0	1.01438	± 0.015	13677.0	± 0.88	133.391	± 0.737
	USFS-11290-006e	± 0.511	44.3	-1.4	± 1.0	0.99691	± 0.018	4310.9	± 0.32	54.860	± 0.189
	USFS-11290-006x	± 0.622	104.7	-15.3	± 1.0	1.11511	± 0.003	58555.0	± 10.20	555.218	± 9.840
	USFS-11290-006y	± 0.704	105.9	-19.7	± 1.0	1.00130	± 0.003	34397.0	± 7.45	300.609	± 6.940
	USFS-11290-006z	± 0.562	113.3	-16.4	± 1.0	1.00850	± 0.003	54082.0	± 5.91	465.042	± 5.670
FSGD-C-72	USFS-11290-007a	± 0.577	3.1	-0.4	± 3.6	0.99706	± 0.042	200.8	± 4.14	20.695	± 0.078
USFEM	USFS-11290-007b	± 0.513	23.9	-2.4	± 1.0	1.00893	± 0.005	1784.3	± 0.23	29.722	± 0.089
	USFS-11290-007c	± 0.516	4.9	-1.4	± 1.0	1.01624	± 0.011	327.5	± 0.23	21.430	± 0.073
	USFS-11290-007d	± 0.525	9.4	-1.3	± 1.0	1.00352	± 0.005	641.7	± 0.27	23.237	± 0.083
	USFS-11290-007e	± 0.510	3.8	-1.0	± 1.1	2.12099	± 0.255	249.3	± 0.18	21.098	± 0.068
FSGD-C-40	USFS-11290-008a	± 0.526	59.2	7.1	± 1.3	1.00782	± 0.003	5321.7	± 0.41	47.116	± 0.215
USFCL	USFS-11290-008b	± 0.538	39.1	7.0	± 1.0	1.00557	± 0.003	3121.7	± 0.43	35.986	± 0.176
	USFS-11290-008c	± 0.507	158.7	5.5	± 1.0	1.00620	± 0.001	43139.0	± 0.77	241.426	± 0.707
	USFS-11290-008d	± 0.530	57.6	7.5	± 1.0	1.01149	± 0.003	5197.7	± 0.28	47.245	± 0.126
	USFS-11290-008e	± 0.591	88.7	3.3	± 1.0	1.00238	± 0.003	10642.0	± 1.27	79.485	± 0.927
	USFS-11290-008f	± 0.513	114.8	1.4	± 1.0	1.00875	± 0.004	14041.0	± 0.28	81.873	± 0.182
FSGD-C-62	USFS-11290-009a	± 0.508	94.3	2.8	± 1.0	1.00209	± 0.002	23678.0	± 0.89	219.941	± 0.806
USFFR	USFS-11290-009b	± 0.539	92.8	4.2	± 1.2	1.00036	± 0.002	21157.0	± 2.00	195.514	± 1.810
	USFS-11290-009c	± 0.507	103.0	3.8	± 1.0	1.00241	± 0.002	34160.0	± 1.03	306.562	± 0.965
	USFS-11290-009d	± 0.504	94.4	0.9	± 1.0	1.00290	± 0.002	23138.0	± 0.57	213.795	± 0.502
	USFS-11290-009e	± 0.507	100.8	-0.3	± 1.0	1.00276	± 0.002	30593.0	± 1.05	276.361	± 0.972
	USFS-11290-009f	± 0.507	114.4	2.2	± 1.0	1.00056	± 0.002	72214.0	± 2.06	628.197	± 2.010
	USFS-11290-009g	± 0.515	97.4	0.0	± 1.0	1.00139	± 0.002	26181.0	± 1.26	239.315	± 1.160
	USFS-11290-009x	± 0.507	105.3	-0.3	± 1.0	1.03354	± 0.002	40196.0	± 1.31	361.348	± 1.240
	USFS-11290-009y	± 0.504	82.6	1.5	± 1.0	1.37451	± 0.002	43135.0	± 1.15	516.969	± 1.110
	USFS-11290-009z	± 0.507	95.3	-0.3	± 1.0	1.01887	± 0.002	24085.0	± 0.84	222.436	± 0.761

Cave Number	Sample Name	%error 2σ	$^{207}Pb/^{206}Pb$	%error 2σ	$^{204}Pb/^{206}Pb$	%error 2σ	Concordia age (Ma)	error (Ma)	MSWD
BLMSH	BLMC-20122-011b	± 2.058	0.07829	± 1.705	0.002124	± 1.420			
	BLMC-20122-011c	± 2.362	0.06281	± 2.088	0.001075	± 1.650			
	BLMC-20122-011d	± 1.079	0.08666	± 0.873	0.002697	± 0.740			
	BLMC-20122-011e	± 2.017	0.10103	± 1.567	0.003647	± 1.370			
FSGD-C-90	USFS-11290-002a	± 0.298	0.12736	± 0.231	0.005449	± 0.183	36.25	± 0.23	2.1
USFVI	USFS-11290-002b	± 0.252	0.21542	± 0.209	0.011405	± 0.147			
	USFS-11290-002c	± 0.393	0.11119	± 0.368	0.004352	± 0.262			
	USFS-11290-002d	± 4.776	0.16327	± 4.104	0.007746	± 3.150			
	USFS-11290-002e	± 5.113	0.09802	± 4.660	0.003428	± 3.540			
FSGD-C-202	USFS-11290-006a	± 2.618	0.09394	± 2.065	0.003217	± 1.790	53.57	± 0.42	0.47
USFDL	USFS-11290-006b	± 0.498	0.19082	± 0.350	0.009729	± 0.305			
	USFS-11290-006c	± 3.543	0.09952	± 3.430	0.003556	± 2.470			
	USFS-11290-006d	± 1.145	0.15784	± 0.817	0.007497	± 0.737			
	USFS-11290-006e	± 0.367	0.31628	± 0.231	0.018228	± 0.189			
	USFS-11290-006x	± 14.173	0.07407	± 11.904	0.001801	± 9.840			
	USFS-11290-006y	± 10.182	0.09690	± 7.966	0.003327	± 6.940			
	USFS-11290-006z	± 8.190	0.07914	± 6.760	0.002150	± 5.670			
FSGD-C-72	USFS-11290-007a	± 4.141	0.75986	± 0.132	0.048322	± 0.078	37.9	± 1.8	144
USFEM	USFS-11290-007b	± 0.250	0.54326	± 0.138	0.033645	± 0.089			
	USFS-11290-007c	± 0.237	0.73514	± 0.126	0.046664	± 0.073			
	USFS-11290-007d	± 0.284	0.68175	± 0.139	0.043034	± 0.083			
	USFS-11290-007e	± 0.196	0.74623	± 0.119	0.047398	± 0.068			
FSGD-C-40	USFS-11290-008a	± 0.466	0.36017	± 0.264	0.021224	± 0.215	33.5	± 2.0	37
USFCL	USFS-11290-008b	± 0.460	0.45643	± 0.231	0.027789	± 0.176			
	USFS-11290-008c	± 1.045	0.10781	± 0.845	0.004142	± 0.707			
	USFS-11290-008d	± 0.311	0.35811	± 0.171	0.021166	± 0.126			
	USFS-11290-008e	± 1.572	0.23271	± 1.053	0.012581	± 0.927			
	USFS-11290-008f	± 0.332	0.22659	± 0.221	0.012214	± 0.182			
FSGD-C-62	USFS-11290-009a	± 1.201	0.11459	± 0.916	0.004547	± 0.806	54.5	± 1.3	± 0.8
USFFR	USFS-11290-009b	± 2.697	0.12247	± 2.098	0.005115	± 1.810			
	USFS-11290-009c	± 1.411	0.09540	± 1.137	0.003262	± 0.965			
	USFS-11290-009d	± 0.756	0.11606	± 0.591	0.004677	± 0.502			
	USFS-11290-009e	± 1.431	0.10065	± 1.123	0.003618	± 0.972			
	USFS-11290-009f	± 2.878	0.07083	± 2.473	0.001592	± 2.010			
	USFS-11290-009g	± 1.713	0.10899	± 1.348	0.004179	± 1.160			
	USFS-11290-009x	± 1.804	0.08834	± 1.459	0.002767	± 1.240			
	USFS-11290-009y	± 1.598	0.07566	± 1.364	0.001934	± 1.110			
	USFS-11290-009z	± 1.133	0.11371	± 0.866	0.004496	± 0.761			

Cave Number	Sample Name	^{238}U-$^{206}Pb(^{204}Pb)$ age	error (Ma)	MSWD	^{238}U-$^{206}Pb(^{208}Pb)$ age	error (Ma)	MSWD	^{235}U-$^{207}Pb(^{204}Pb)$ age
BLMSH	BLMC-20122-011b							
	BLMC-20122-011c							
	BLMC-20122-011d							
	BLMC-20122-011e							
FSGD-C-90	USFS-11290-002a	35.73	± 0.15	0.45	34.72	± 0.18	2.0	35.76
USFVI	USFS-11290-002b							
	USFS-11290-002c							
	USFS-11290-002d							
	USFS-11290-002e							
FSGD-C-202	USFS-11290-006a	53.49	± 0.45	0.23	53.38	± 0.46	0.23	53.63
USFDL	USFS-11290-006b							
	USFS-11290-006c							
	USFS-11290-006d							
	USFS-11290-006e							
	USFS-11290-006x							
	USFS-11290-006y							
	USFS-11290-006z							
FSGD-C-72	USFS-11290-007a	36.47	± 0.90	38	36.39	± 0.68	23	36.5
USFEM	USFS-11290-007b							
	USFS-11290-007c							
	USFS-11290-007d							
	USFS-11290-007e							
FSGD-C-40	USFS-11290-008a	33.03	± 0.91	46	32.55	± 0.92	40	33.06
USFCL	USFS-11290-008b							
	USFS-11290-008c							
	USFS-11290-008d							
	USFS-11290-008e							
	USFS-11290-008f							
FSGD-C-62	USFS-11290-009a	54.5	± 1.3	0.43	54.4	± 1.3	0.33	55.0
USFFR	USFS-11290-009b							
	USFS-11290-009c							
	USFS-11290-009d							
	USFS-11290-009e							
	USFS-11290-009f							
	USFS-11290-009g							
	USFS-11290-009x							
	USFS-11290-009y							
	USFS-11290-009z							

Cave Number	Sample Name	error (Ma)	MSWD	^{207}Pb-$^{206}Pb(^{204}Pb)$ age	error (Ma)	MSWD	$^{238}U/^{206}$ Pb Model Ages	error (%)	Average
BLMSH	BLMC-20122-011b						35.66	± 1.46	
	BLMC-20122-011c						35.28	± 1.40	
	BLMC-20122-011d						35.76	± 0.58	
	BLMC-20122-011e						35.66	± 1.07	
FSGD-C-90	USFS-11290-002a	± 0.30	0.38				35.85	± 0.26	35.80
USFVI	USFS-11290-002b						35.34	± 0.39	
	USFS-11290-002c						36.00	± 0.29	
	USFS-11290-002d								
	USFS-11290-002e								
FSGD-C-202	USFS-11290-006a	± 0.79	0.44				10.18	7.97	55.26
USFDL	USFS-11290-006b						1.57	1.05	
	USFS-11290-006c						0.00	0.00	
	USFS-11290-006d						0.21	0.13	
	USFS-11290-006e						1.27	0.92	
	USFS-11290-006x						0.00	0.00	
	USFS-11290-006y								
	USFS-11290-006z								
FSGD-C-72	USFS-11290-007a	± 1.7	0.32				38.28	± 6.76	39.94
USFEM	USFS-11290-007b						39.99	± 0.69	
	USFS-11290-007c						39.28	± 3.09	
	USFS-11290-007d						39.89	± 4.23	
	USFS-11290-007e						41.92	± 10.55	
FSGD-C-40	USFS-11290-008a	± 0.48	0.85				33.11	± 1.84	33.71
USFCL	USFS-11290-008b						33.19	± 2.97	
	USFS-11290-008c						33.46	± 0.71	
	USFS-11290-008d						34.05	± 0.67	
	USFS-11290-008e						36.34	± 1.17	
	USFS-11290-008f						28.76	± 0.33	
FSGD-C-62	USFS-11290-009a	± 1.4	± 1.0				56.78	± 2.46	56.33
USFFR	USFS-11290-009b						55.90	± 3.91	
	USFS-11290-009c						56.24	± 2.17	
	USFS-11290-009d						56.36	± 0.73	
	USFS-11290-009e						56.23	± 1.26	
	USFS-11290-009f								
	USFS-11290-009g								
	USFS-11290-009x								
	USFS-11290-009y								
	USFS-11290-009z								

Cave Number	Sample Name	error (%)	$^{235}U/^{207}Pb$ Model Ages	error (%)	Average	error (%)
BLMSH	BLMC-20122-011b		34.39	± 1.55		
	BLMC-20122-011c		34.05	± 1.41		
	BLMC-20122-011d		34.39	± 1.19		
	BLMC-20122-011e		34.51	± 1.94		
FSGD-C-90	USFS-11290-002a	± 0.74	35.68	± 0.60	35.73	± 0.14
USFVI	USFS-11290-002b		35.73	± 1.28		
	USFS-11290-002c		35.78	± 0.63		
	USFS-11290-002d					
	USFS-11290-002e					
FSGD-C-202	USFS-11290-006a	± 0.26	53.33	± 9.08	53.53	± 0.47
USFDL	USFS-11290-006b		53.47	± 1.27		
	USFS-11290-006c		53.12	± 4.41		
	USFS-11290-006d		53.74	± 1.65		
	USFS-11290-006e		53.53	± 2.32		
	USFS-11290-006x		53.25	± 6.89		
	USFS-11290-006y					
	USFS-11290-006z					
FSGD-C-72	USFS-11290-007a	± 0.26	36.24	± 20.80	36.49	± 0.84
USFEM	USFS-11290-007b		36.55	± 2.21		
	USFS-11290-007c		34.44	± 11.21		
	USFS-11290-007d		36.38	± 6.10		
	USFS-11290-007e		39.60	± 14.20		
FSGD-C-40	USFS-11290-008a	± 0.62	33.39	± 1.40	33.02	± 0.18
USFCL	USFS-11290-008b		32.91	± 2.23		
	USFS-11290-008c		33.00	± 0.71		
	USFS-11290-008d		32.84	± 1.21		
	USFS-11290-008e		36.37	± 1.95		
	USFS-11290-008f		28.22	± 0.53		
FSGD-C-62	USFS-11290-009a	± 0.32	55.17	± 3.03	54.42	± 0.71
USFFR	USFS-11290-009b		53.69	± 4.87		
	USFS-11290-009c		54.37	± 2.58		
	USFS-11290-009d		54.19	± 2.72		
	USFS-11290-009e		54.35	± 2.75		
	USFS-11290-009f					
	USFS-11290-009g					
	USFS-11290-009x					
	USFS-11290-009y					
	USFS-11290-009z					

Cave Number	Sample Name	Sample Weight (g)	Spike Weight (g)	U conc. ppm*	%error 2σ	^{232}Th conc. ppb‡	%error 2σ	Pb conc. ppb*
FSGD-C-011	USFS-11290-010(W)a	0.0384	0.1074	0.734	± 0.121	43.775	± 0.6	41.418
USFGS	USFS-11290-010(W)b	0.0435	0.1091	0.712	± 0.105	6.403	± 3.3	73.500
	USFS-11290-010(W)c	0.0479	0.1044	0.429	± 0.105	26.177	± 0.8	32.225
	USFS-11290-010(Y)a	0.0324	0.1016	13.343	± 0.106	0.076	± 376.3	284.440
	USFS-11290-010(Y)b	0.0510	0.0997	49.957	± 0.136	0.290	± 62.8	826.970
	USFS-11290-010(Y)c	0.0463	0.0940	3.933	± 0.103	0.701	± 28.6	68.001
	USFS-11290-010(Y)d	0.0314	0.0897	0.378	± 0.109	0.173	± 170.9	1.290
	USFS-11290-010(Y)e	0.0392	0.0946	3.477	± 0.102	-0.027	± 881.9	69.530
GUMO-GEO-00111	GUMO-00549-001a	0.0649	0.1084	5.114	± 0.103	N/A	---	18.064
GUMDT	GUMO-00549-001b	0.0402	0.1223	1.275	± 0.101	N/A	---	16.691
	GUMO-00549-001c	0.0707	0.1183	0.376	± 0.103	N/A	---	3.878
	GUMO-00549-001d	0.0328	0.1102	1.230	± 0.101	N/A	---	45.408
	GUMO-00549-001e	0.0516	0.1063	0.658	± 0.102	N/A	---	4.331
GUMO-GEO-00564	GUMO-00549-002a	0.0272	0.1170	4.013	± 0.104	N/A	---	28.518
GUMHA	GUMO-00549-002b	0.0267	0.0755	3.992	± 0.104	N/A	---	15.235
	GUMO-00549-002c	0.0281	0.1083	5.330	± 0.110	N/A	---	20.595
	GUMO-00549-002d	0.0406	0.2444	3.268	± 0.101	N/A	---	14.737
	GUMO-00549-002e	0.0225	0.1118	4.609	± 2.290	N/A	---	20.117
GUMO-GEO-00108	GUMO-00549-003a	0.0270	0.1983	2.290	± 0.102	2.844	± 12.1	9.923
GUMTH	GUMO-00549-003b	0.0430	0.1986	1.351	± 0.102	2.391	± 9.0	7.686
	GUMO-00549-003c	0.0648	0.2037	3.187	± 0.102	2.962	± 4.8	15.132
	GUMO-00549-003d	0.0624	0.1871	1.349	± 0.101	1.667	± 8.9	7.175
	GUMO-00549-003e	0.0466	0.2289	2.024	± 0.120	3.194	± 6.2	13.483
Surface Sample	GUPA-00001-001a	0.0262	0.1891	0.440	± 0.291	N/A	---	6.173
From Road Cut	GUPA-00001-001b	0.0184	0.1411	0.175	± 0.311	N/A	---	1.422
GUPA	GUPA-00001-001c	0.0148	0.1576	0.304	± 0.225	N/A	---	1.819
	GUPA-00001-001d	0.1575	0.1639	0.194	± 0.035	N/A	---	6.766
	GUPA-00001-001e	0.1824	0.2145	0.380	± 0.015	N/A	---	3.734
	GUPA-00001-001f	0.1912	0.1954	0.249	± 0.030	N/A	---	4.361

*From Neptune after PbDat correction

‡From Victor's U-Th Redux Sheets

«Not used for various reasons noted in detail on sample data page

Cave Number	Sample Name	%error 2σ	U/Pb	$\delta^{234}U^{‡}$	%error 2σ	$[^{230}Th/^{238}U]^{‡}$	%error 2σ	$^{238}U/^{204}Pb$	%error 2σ	$^{206}Pb/^{204}Pb$	%error 2σ
FSGD-C-011	USFS-11290-010(W)a	± 0.509	17.7	-1.7	± 1.0	1.02385	± 0.002	2163.4	± 0.38	82.368	± 0.269
USFGS	USFS-11290-010(W)b	± 0.505	9.7	0.6	± 1.0	1.03451	± 0.002	817.4	± 0.18	41.657	± 0.090
	USFS-11290-010(W)c	± 0.512	13.3	-19.3	± 1.0	1.01736	± 0.002	1320.7	± 0.33	57.299	± 0.200
	USFS-11290-010(Y)a	± 0.501	46.9	1.4	± 1.0	1.01874	± 0.002	11758.0	± 0.15	225.803	± 0.094
	USFS-11290-010(Y)b	± 0.501	60.4	2.0	± 1.0	1.61210	± 0.005	574930.0	± 0.67	10490.134	± 0.659
	USFS-11290-010(Y)c	± 0.501	57.8	1.3	± 1.0	1.03306	± 0.002	20775.0	± 0.35	346.040	± 0.318
	USFS-11290-010(Y)d	± 0.501	293.0	-30.2	± 1.0	1.03570	± 0.004	18.6	± 0.13	18.562	± 0.060
	USFS-11290-010(Y)e	± 0.502	50.0	0.3	± 1.0	1.02291	± 0.002	14830.0	± 0.34	276.656	± 0.300
GUMO-GEO-00111	GUMO-00549-001a	± 0.505	283.1	N/A	---	N/A	---	196870.0	± 1.43	704.617	± 1.390
GUMDT	GUMO-00549-001b	± 0.516	76.4	N/A	---	N/A	---	8233.4	± 0.42	65.303	± 0.273
	GUMO-00549-001c	± 0.684	96.9	N/A	---	N/A	---	15994.0	± 1.89	129.381	± 1.630
	GUMO-00549-001d	± 0.508	27.1	N/A	---	N/A	---	2108.0	± 0.19	33.954	± 0.084
	GUMO-00549-001e	± 0.564	151.9	N/A	---	N/A	---	54368.0	± 4.00	324.517	± 3.780
GUMO-GEO-00564	GUMO-00549-002a	± 0.667	140.7	N/A	---	N/A	---	21369.0	± 1.46	117.775	± 1.260
GUMHA	GUMO-00549-002b	± 4.76	262.0	N/A	---	N/A	---	337370.0	± 13.80	1325.055	± 10.100
	GUMO-00549-002c	± 1.65	258.8	N/A	---	N/A	---	802630.0	± 7.31	3346.680	± 6.700
	GUMO-00549-002d	± 0.525	221.8	N/A	---	N/A	---	201100.0	± 7.14	944.666	± 7.020
	GUMO-00549-002e	± 0.607	229.1	N/A	---	N/A	---	262340.0	± 6.55	1207.579	± 6.030
GUMO-GEO-00108	GUMO-00549-003a	± 0.559	230.7	-1.5	± 1.0	1.00163	± 0.002	201200.0	± 11.00	898.505	± 10.800
GUMTH	GUMO-00549-003b	± 0.555	175.8	-1.7	± 1.0	1.00659	± 0.001	41376.0	± 2.42	205.660	± 2.180
	GUMO-00549-003c	± 0.506	210.6	17.8	± 2.1	1.12205	± 0.044	181580.0	± 3.10	889.653	± 3.050
	GUMO-00549-003d	± 0.529	188.0	-0.3	± 1.0	1.00668	± 0.001	51730.0	± 2.09	249.074	± 1.930
	GUMO-00549-003e	± 0.519	150.1	0.6	± 1.0	1.00914	± 0.001	26441.0	± 0.97	141.046	± 0.824
Surface Sample	GUPA-00001-001a	± 4.1	71.3	N/A	---	N/A	---	5732.3	± 9.62	35.992	± 4.160
From Road Cut	GUPA-00001-001b	± 19.7	123.4	N/A	---	N/A	---	12065.0	± 82.10	55.013	± 47.900
GUPA	GUPA-00001-001c	± 16.6	167.1	N/A	---	N/A	---	20245.0	± 90.50	78.672	± 63.900
	GUPA-00001-001d	± 0.785	28.7	N/A	---	N/A	---	2015.2	± 1.36	25.249	± 0.324
	GUPA-00001-001e	± 0.887	101.8	N/A	---	N/A	---	8802.6	± 2.29	41.817	± 1.210
	GUPA-00001-001f	± 0.873	57.0	N/A	---	N/A	---	4321.8	± 1.75	30.882	± 0.638

Cave Number	Sample Name	$^{238}U/^{208}Pb$	%error 2σ	$^{206}Pb/^{208}Pb$	%error 2σ	$^{235}U/^{204}Pb$	%error 2σ	$^{207}Pb/^{204}Pb$	%error 2σ	$^{238}U/^{206}Pb$
FSGD-C-011	USFS-11290-010(W)a	54.909	± 0.407	2.090	± 0.252	15.661	± 0.69	18.694	± 0.14	26.265
USFGS	USFS-11290-010(W)b	21.337	± 0.222	1.087	± 0.085	5.925	± 0.28	16.739	± 0.05	19.623
	USFS-11290-010(W)c	33.837	± 0.359	1.467	± 0.187	9.564	± 0.60	17.467	± 0.10	23.049
	USFS-11290-010(Y)a	306.829	± 0.193	5.887	± 0.093	85.323	± 0.15	25.715	± 0.10	52.072
	USFS-11290-010(Y)b	15118.994	± 0.695	275.604	± 0.654	4172.200	± 0.67	524.904	± 0.65	54.807
	USFS-11290-010(Y)c	542.173	± 0.379	9.022	± 0.313	150.760	± 0.35	31.475	± 0.21	60.036
	USFS-11290-010(Y)d	0.486	± 0.175	0.484	± 0.060	0.135	± 0.13	15.632	± 0.09	1.003
	USFS-11290-010(Y)e	387.388	± 0.366	7.220	± 0.296	107.620	± 0.34	28.189	± 0.19	53.604
GUMO-GEO-00111	GUMO-00549-001a	5016.819	± 1.606	17.956	± 1.310	1428.600	± 1.43	47.831	± 1.03	279.400
GUMDT	GUMO-00549-001b	204.506	± 0.441	1.622	± 0.246	59.749	± 0.42	17.780	± 0.16	126.080
	GUMO-00549-001c	408.771	± 2.529	3.307	± 1.690	116.070	± 1.89	20.862	± 1.58	123.619
	GUMO-00549-001d	54.456	± 0.231	0.877	± 0.078	15.297	± 0.19	16.296	± 0.10	62.084
	GUMO-00549-001e	972.838	± 4.000	5.807	± 2.430	394.540	± 4.00	29.969	± 2.50	167.535
GUMO-GEO-00564	GUMO-00549-002a	555.544	± 1.781	3.062	± 0.769	157.030	± 1.46	20.149	± 1.06	181.439
GUMHA	GUMO-00549-002b	4250.706	± 15.088	16.696	± 5.280	2448.300	± 13.80	73.649	± 8.27	254.608
	GUMO-00549-002c	16063.845	± 8.144	66.980	± 5.640	5824.600	± 7.31	167.339	± 6.19	239.829
	GUMO-00549-002d	5051.495	± 7.298	23.730	± 6.640	1459.400	± 7.14	58.376	± 5.44	212.880
	GUMO-00549-002e	6755.421	± 6.922	31.097	± 5.880	1903.800	± 6.55	70.324	± 4.97	217.245
GUMO-GEO-00108	GUMO-00549-003a	5262.745	± 5.263	23.502	± 10.600	1460.100	± 11.00	57.460	± 8.30	223.927
GUMTH	GUMO-00549-003b	1078.342	± 5.641	5.360	± 2.130	300.260	± 2.42	24.477	± 1.09	201.187
	GUMO-00549-003c	4748.058	± 2.153	23.264	± 3.020	1317.700	± 3.10	56.641	± 2.43	204.102
	GUMO-00549-003d	1350.335	± 4.363	6.502	± 1.890	375.400	± 2.09	26.500	± 1.05	207.689
	GUMO-00549-003e	686.654	± 4.203	3.663	± 0.796	191.880	± 0.97	21.483	± 0.40	187.463
Surface Sample	GUPA-00001-001a	149.462	± 9.626	0.936	± 4.240	41.599	± 9.62	16.438	± 0.63	159.265
From Road Cut	GUPA-00001-001b	323.675	± 82.173	1.470	± 50.700	87.554	± 82.10	17.337	± 7.91	219.312
GUPA	GUPA-00001-001c	537.759	± 90.606	2.081	± 66.300	146.910	± 90.50	18.608	± 14.20	257.334
	GUPA-00001-001d	52.221	± 1.376	0.653	± 0.326	14.624	± 1.36	15.990	± 0.17	79.814
	GUPA-00001-001e	227.952	± 2.300	1.079	± 1.220	63.880	± 2.29	16.763	± 0.24	210.505
	GUPA-00001-001f	111.802	± 1.763	0.797	± 0.640	31.363	± 1.75	16.248	± 0.18	139.945

Cave Number	Sample Name	%error 2σ	$^{207}Pb/^{206}Pb$	%error 2σ	$^{204}Pb/^{206}Pb$	%error 2σ	Concordia age (Ma)	error (Ma)	MSWD
FSGD-C-011	USFS-11290-010(W)a	± 0.467	0.22857	± 0.308	0.012141	± 0.269	112.83	± 0.96	17
USFGS	USFS-11290-010(W)b	± 0.205	0.40293	± 0.135	0.024006	± 0.090			
	USFS-11290-010(W)c	± 0.388	0.30673	± 0.240	0.017452	± 0.200			
	USFS-11290-010(Y)a	± 0.176	0.11386	± 0.136	0.004429	± 0.094			
	USFS-11290-010(Y)b	± 0.941	0.05002	± 0.923	0.000095	± 0.659			
	USFS-11290-010(Y)c	± 0.475	0.09094	± 0.379	0.002890	± 0.318			
	USFS-11290-010(Y)d	± 0.141	0.84214	± 0.108	0.053873	± 0.060			
	USFS-11290-010(Y)e	± 0.453	0.10187	± 0.354	0.003615	± 0.300			
GUMO-GEO-00111	GUMO-00549-001a	± 1.994	0.06779	± 1.730	0.001419	± 1.390	33.06	± 0.81	5.0
GUMDT	GUMO-00549-001b	± 0.498	0.27222	± 0.314	0.015313	± 0.273			
	GUMO-00549-001c	± 2.496	0.16121	± 2.270	0.007729	± 1.630			
	GUMO-00549-001d	± 0.211	0.47991	± 0.131	0.029451	± 0.084			
	GUMO-00549-001e	± 5.503	0.09229	± 4.532	0.003082	± 3.780			
GUMO-GEO-00564	GUMO-00549-002a	± 1.929	0.17102	± 1.647	0.008491	± 1.260	29.3	± 2.1	0.04
GUMHA	GUMO-00549-002b	± 17.101	0.05550	± 13.054	0.000755	± 10.100			
	GUMO-00549-002c	± 9.916	0.04992	± 9.122	0.000299	± 6.700			
	GUMO-00549-002d	± 10.013	0.06172	± 8.881	0.001059	± 7.020			
	GUMO-00549-002e	± 8.903	0.05816	± 7.814	0.000828	± 6.030			
GUMO-GEO-00108	GUMO-00549-003a	± 15.416	0.06387	± 13.621	0.001113	± 10.800	27.6	± 1.3	0.02
GUMTH	GUMO-00549-003b	± 3.257	0.11895	± 2.437	0.004862	± 2.180			
	GUMO-00549-003c	± 4.349	0.06360	± 3.900	0.001124	± 3.050			
	GUMO-00549-003d	± 2.845	0.10633	± 2.197	0.004015	± 1.930			
	GUMO-00549-003e	± 1.274	0.15225	± 0.916	0.007090	± 0.824			
Surface Sample	GUPA-00001-001a	± 10.481	0.45666	± 4.207	0.027784	± 4.160	16.16	± 0.68	1.9
From Road Cut	GUPA-00001-001b	± 95.052	0.31507	± 48.549	0.018178	± 47.900			
GUPA	GUPA-00001-001c	± 110.786	0.23644	± 65.459	0.012711	± 63.900			
	GUPA-00001-001d	± 1.398	0.63326	± 0.364	0.039606	± 0.324			
	GUPA-00001-001e	± 2.590	0.40080	± 1.234	0.023914	± 1.210			
	GUPA-00001-001f	± 1.863	0.52610	± 0.664	0.032381	± 0.638			

Cave Number	Sample Name	^{238}U-$^{206}Pb(^{204}Pb)$ age	error (Ma)	MSWD	^{238}U-$^{206}Pb(^{208}Pb)$ age	error (Ma)	MSWD	^{235}U-$^{207}Pb(^{204}Pb)$ age
FSGD-C-011 USFGS	USFS-11290-010(W)a USFS-11290-010(W)b USFS-11290-010(W)c USFS-11290-010(Y)a USFS-11290-010(Y)b USFS-11290-010(Y)c USFS-11290-010(Y)d USFS-11290-010(Y)e	116.4	± 1.5	26300	116.4	± 7.2	50	116.8
GUMO-GEO-00111 GUMDT	GUMO-00549-001a GUMO-00549-001b GUMO-00549-001c GUMO-00549-001d GUMO-00549-001e	33.16	± 0.52	1.9	32.19	± 0.51	2.3	33.5
GUMO-GEO-00564 GUMHA	GUMO-00549-002a GUMO-00549-002b GUMO-00549-002c GUMO-00549-002d GUMO-00549-002e	29.3	± 2.1	0.05	29.3	± 2.1	0.05	29.0
GUMO-GEO-00108 GUMTH	GUMO-00549-003a GUMO-00549-003b GUMO-00549-003c GUMO-00549-003d GUMO-00549-003e	27.6	± 1.4	0.03	27.7	± 2.2	0.02	27.5
Surface Sample From Road Cut GUPA	GUPA-00001-001a GUPA-00001-001b GUPA-00001-001c GUPA-00001-001d GUPA-00001-001e GUPA-00001-001f	15.80	± 0.52	0.71	15.65	± 0.52	0.84	15.8

Cave Number	Sample Name	error (Ma)	MSWD	^{207}Pb-$^{206}Pb(^{204}Pb)$ age	error (Ma)	MSWD	$^{238}U/^{206}$ Pb Model Ages	error (%)	Average
FSGD-C-011	USFS-11290-010(W)a	± 1.5	1692	118.80	± 0.71	20	114.35	± 12.71	
USFGS	USFS-11290-010(W)b						116.72	± 1.81	
	USFS-11290-010(W)c						101.93	± 7.76	
	USFS-11290-010(Y)a						832.39	± 4756.60	
	USFS-11290-010(Y)b						112.66	± 10.61	
	USFS-11290-010(Y)c						192.01	± 21.71	
	USFS-11290-010(Y)d						191.21	± 54.23	
	USFS-11290-010(Y)e						193.69	± 34.44	
GUMO-GEO-00111	GUMO-00549-001a	± 1.4	1.11				32.88	± 0.82	33.02
GUMDT	GUMO-00549-001b						32.92	± 1.75	
	GUMO-00549-001c						35.60	± 3.24	
	GUMO-00549-001d								
	GUMO-00549-001e								
GUMO-GEO-00564	GUMO-00549-002a	± 2.1	0.08				28.36	± 1.30	28.3
GUMHA	GUMO-00549-002b						25.17	± 7.05	
	GUMO-00549-002c						27.00	± 4.10	
	GUMO-00549-002d						29.80	± 4.61	
	GUMO-00549-002e						29.38	± 4.00	
GUMO-GEO-00108	GUMO-00549-003a	± 1.6	0.07				28.49	± 7.30	28.40
GUMTH	GUMO-00549-003b						28.32	± 2.48	
	GUMO-00549-003c						31.18	± 2.25	
	GUMO-00549-003d						28.18	± 1.29	
	GUMO-00549-003e						28.24	± 0.70	
Surface Sample	GUPA-00001-001a	± 1.0	0.095						
From Road Cut	GUPA-00001-001b								
GUPA	GUPA-00001-001c								
	GUPA-00001-001d								
	GUPA-00001-001e								
	GUPA-00001-001f								

Cave Number	Sample Name	error (%)	$^{235}U/^{207}Pb$ Model Ages	error (%)	Average	error (%)
FSGD-C-011	USFS-11290-010(W)a		117.86	± 19.58	116.8	± 2.0
USFGS	USFS-11290-010(W)b		116.89	± 1.88		
	USFS-11290-010(W)c		103.96	± 11.80		
	USFS-11290-010(Y)a		1455.52	± 1467.15		
	USFS-11290-010(Y)b		115.56	± 16.09		
	USFS-11290-010(Y)c		192.48	± 4.28		
	USFS-11290-010(Y)d		192.30	± 8.21		
	USFS-11290-010(Y)e		194.72	± 6.03		
GUMO-GEO-00111	GUMO-00549-001a	± 0.73	33.35	± 3.19	34.30	± 2.40
GUMDT	GUMO-00549-001b		33.59	± 11.21		
	GUMO-00549-001c		35.80	± 3.80		
	GUMO-00549-001d					
	GUMO-00549-001e					
GUMO-GEO-00564	GUMO-00549-002a	± 1.1	27.42	± 3.98	28.2	± 2.1
GUMHA	GUMO-00549-002b		23.63	± 6.74		
	GUMO-00549-002c		26.00	± 3.98		
	GUMO-00549-002d		29.10	± 4.76		
	GUMO-00549-002e		28.58	± 4.10		
GUMO-GEO-00108	GUMO-00549-003a	± 0.93	28.83	± 7.93	30.73	± 0.62
GUMTH	GUMO-00549-003b		30.50	± 5.33		
	GUMO-00549-003c		31.29	± 2.89		
	GUMO-00549-003d		29.78	± 4.32		
	GUMO-00549-003e		32.13	± 6.43		
Surface Sample	GUPA-00001-001a		16.38	± 5.51	15.78	± 0.20
From Road Cut	GUPA-00001-001b		18.08	± 158.77		
GUPA	GUPA-00001-001c		19.44	± 318.81		
	GUPA-00001-001d		15.83	± 4.77		
	GUPA-00001-001e		15.77	± 1.64		
	GUPA-00001-001f		15.66	± 2.52		

APPENDIX A.3 - SAMPLE DATA PAGES

A.3.1 - CAVE

Figure 27: Sample CAVE-02399-001. Calcite spar. Scale bar is in cm. (Photo Credit: Dave Decker).

Cave ID Number: CAVE-C-1
Sample Number: CAVE-02399-001
Collection Date: 28 October, 2011
Collected By: Dave Decker

X-series U (ppm): 0.039
X-series Th (ppm): 0.247
X-series Pb (ppm): 0.029
U/Pb: 1.34

Weight (Kg): 0.095
Size (cm): 4 x 11
Curation Location: University of New Mexico

Figure 28: Sample CAVE-02399-005. Calcite spar. Scale bar is in cm. (Photo Credit: Dave Decker).

Cave ID Number: CAVE-C-5
Sample Number: CAVE-02399-005
Collection Date: 19 July, 2012
Collected By: Dave Decker

X-series U (ppm): 0.004
X-series Th (ppm): 0.004
X-series Pb (ppm): 0.008
U/Pb: 0.5

Weight (Kg): 1.15
Size (cm): 20 x 9
Curation Location: University of New Mexico

Figure 29: Sample CAVE-02399-010. Calcite spar. Scale bar is in cm. (Photo Credit: Dave Decker).

Cave ID Number:	CAVE-C-76
Sample Number:	CAVE-02399-010
Collection Date:	10 May, 2014
Collected By:	Dave Decker
X-series U (ppm):	0.121
X-series Th (ppm):	0.073
X-series Pb (ppm):	0.158
U/Pb:	0.766
Weight (Kg):	1.41
Size (cm):	15.9 x 11.4 x 7.0
Curation Location:	University of New Mexico

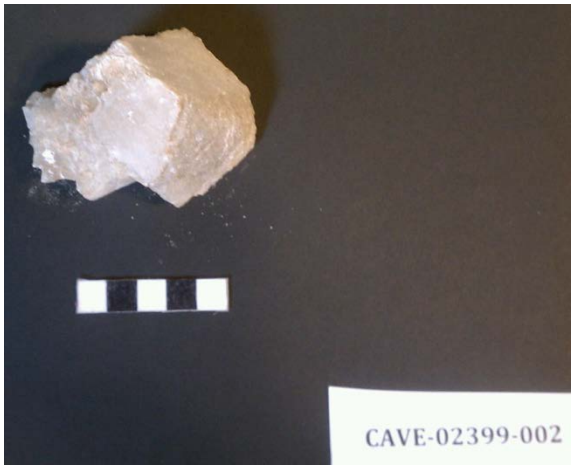

Figure 30: Sample CAVE-02399-002. Calcite spar. Scale bar is in cm. (Photo Credit: Dave Decker).

Cave ID Number: CAVE-C-1
Sample Number: CAVE-02399-002
Collection Date: 28 October, 2011
Collected By: Dave Decker

X-series U (ppm): 0.559
X-series Th (ppm): 0.153
X-series Pb (ppm): 0.031
U/Pb: 18.0

Weight (Kg): 0.210
Size (cm): 5 x 8
Curation Location: University of New Mexico

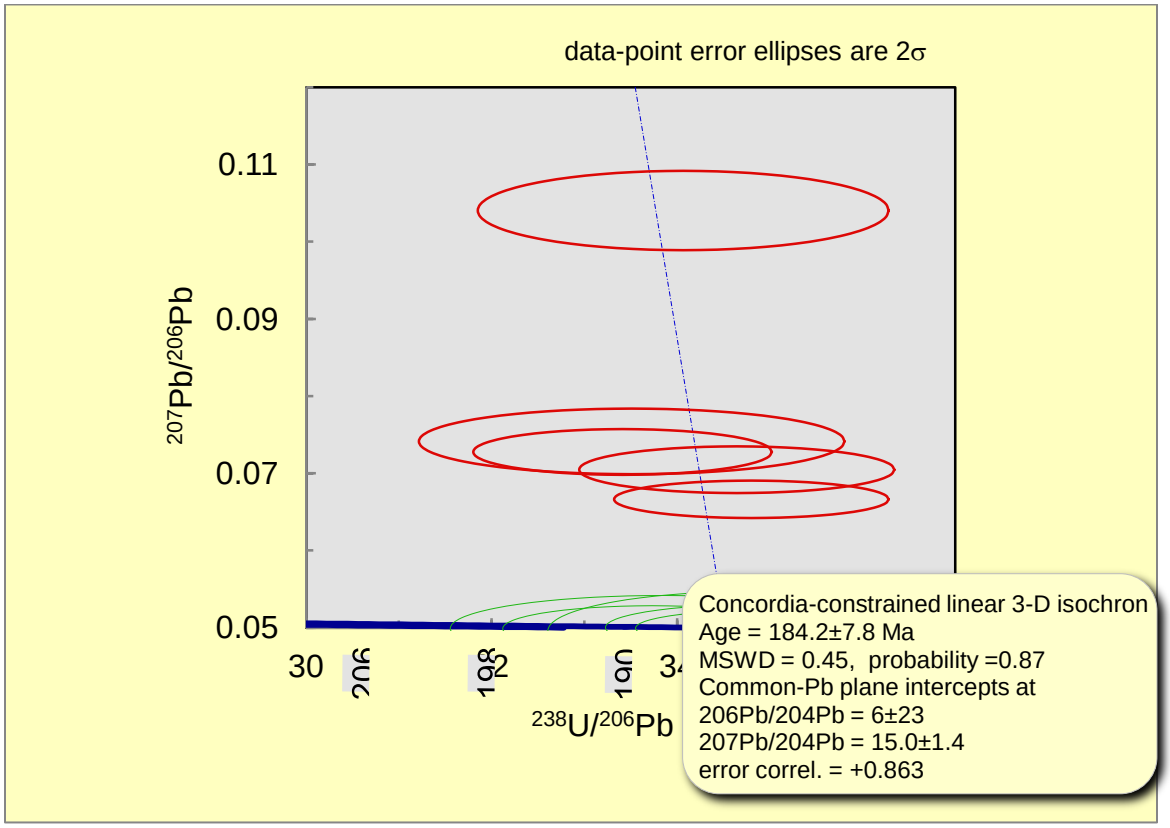

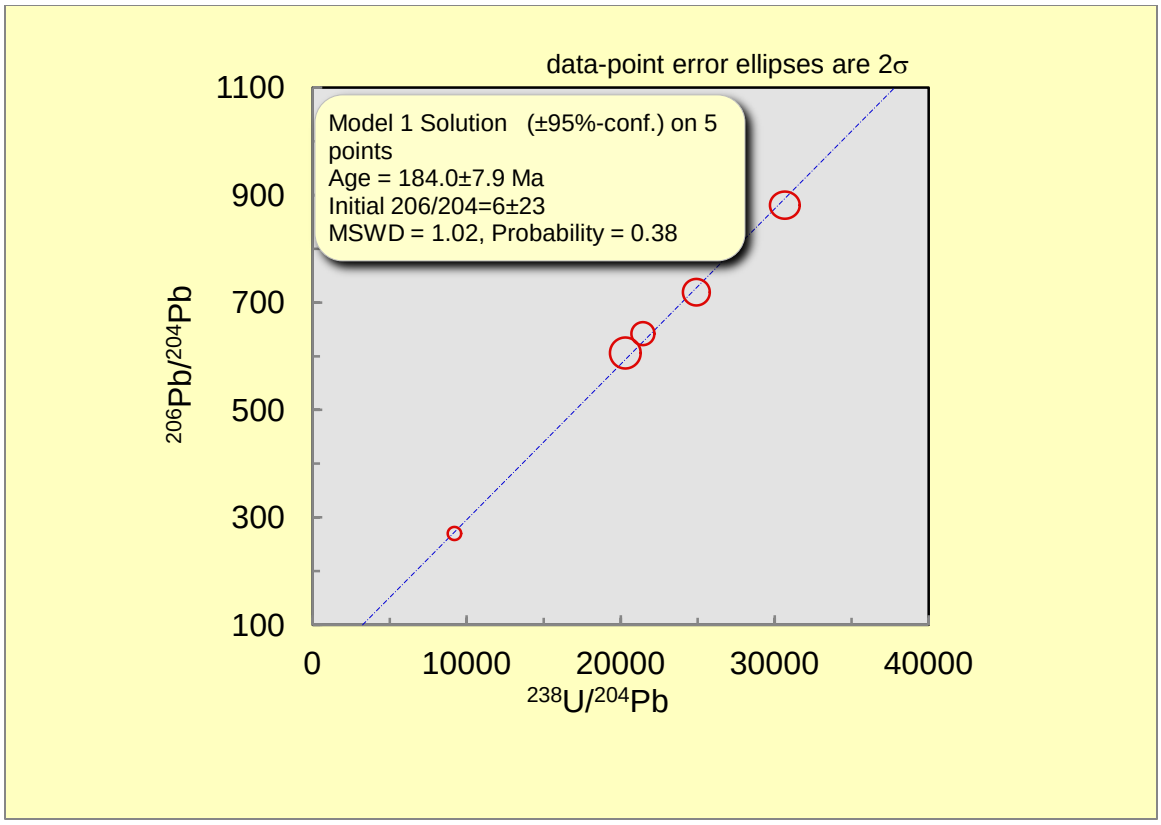
data-point error ellipses are 2σ
Model 1 Solution (±95%-conf.) on 5 points
Age = 184.0±7.9 Ma
Initial 206/204=6±23
MSWD = 1.02, Probability = 0.38
1100
900
700
500
300
100
0
10000
20000
30000
40000
206Pb/204Pb
238U/204Pb

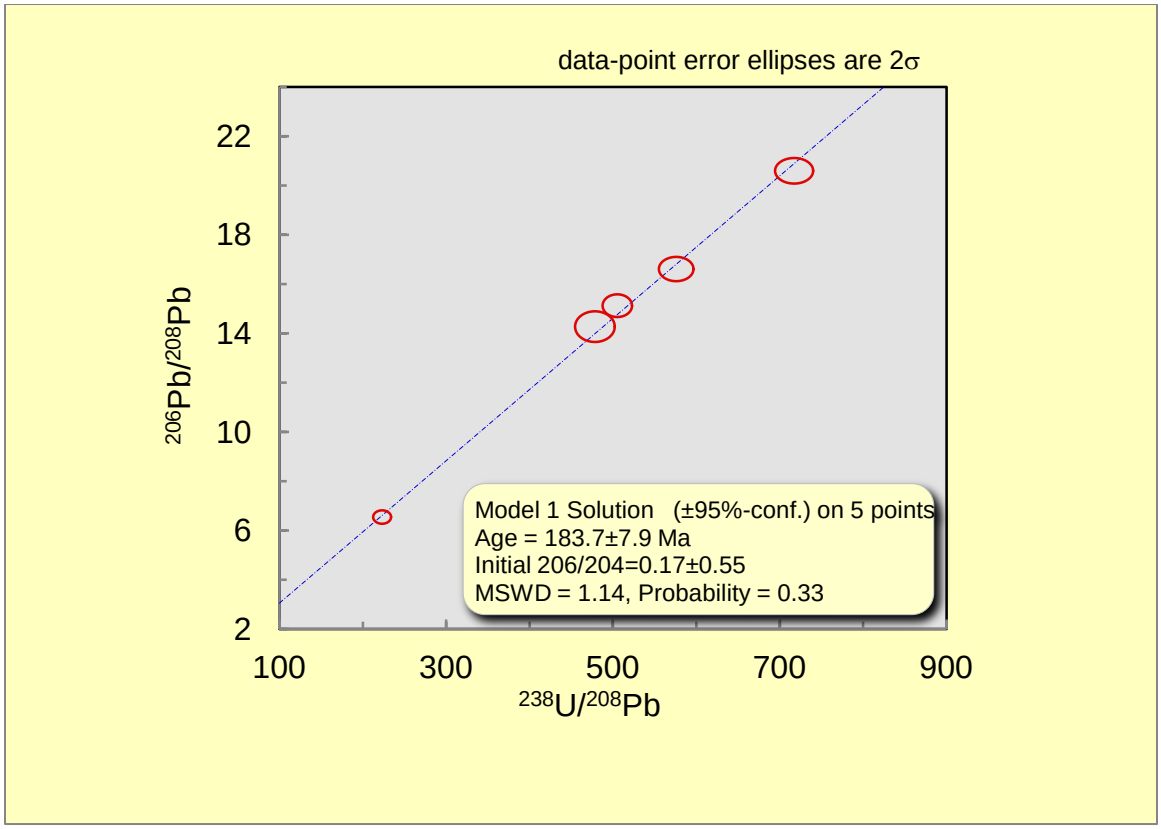
data-point error ellipses are 2σ
Model 1 Solution (±95%-conf.) on 5 points
Age = 183.7±7.9 Ma
Initial 206/204=0.17±0.55
MSWD = 1.14, Probability = 0.33
22
18
14
10
6
2
100
300
500
700
900
206Pb/208Pb
238U/208Pb

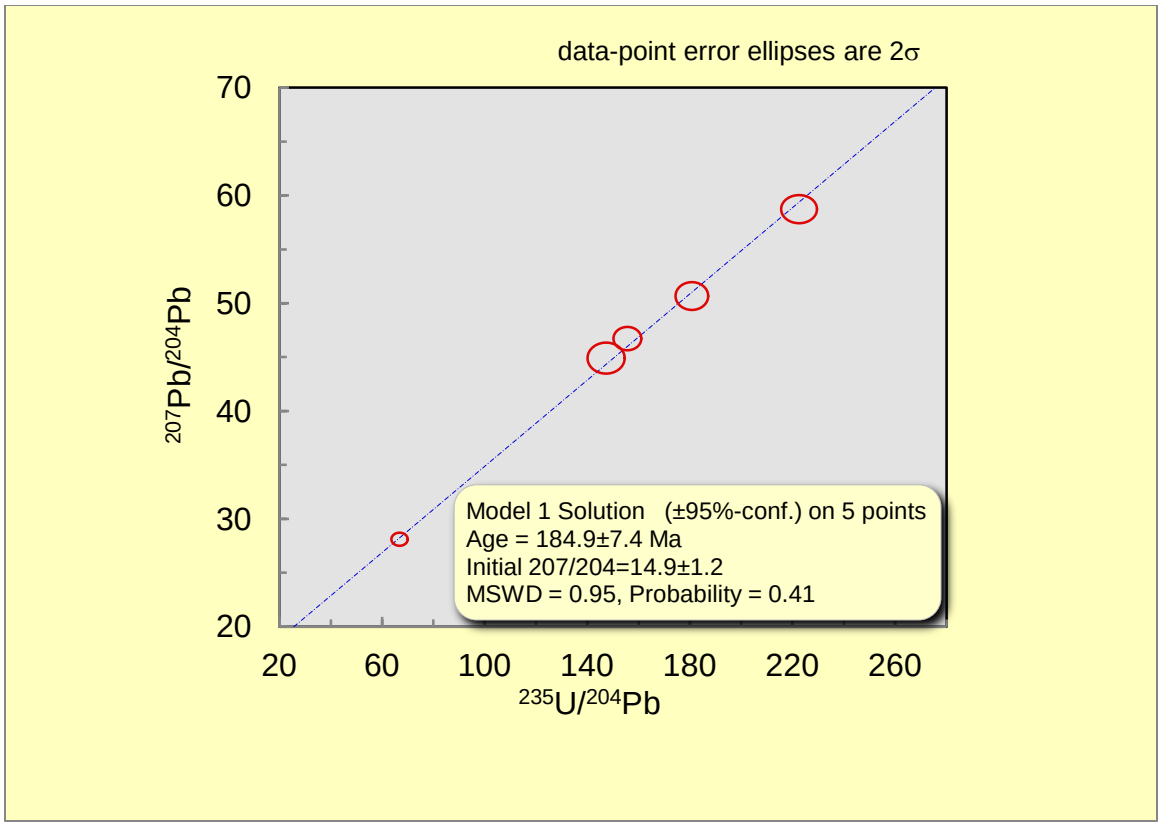
data-point error ellipses are 2σ
70
60
50
40
30
20
$^{207}Pb/^{204}Pb$
20
60
100
140
180
220
260
$^{235}U/^{204}Pb$
Model 1 Solution (±95%-conf.) on 5 points
Age = 184.9±7.4 Ma
Initial 207/204=14.9±1.2
MSWD = 0.95, Probability = 0.41

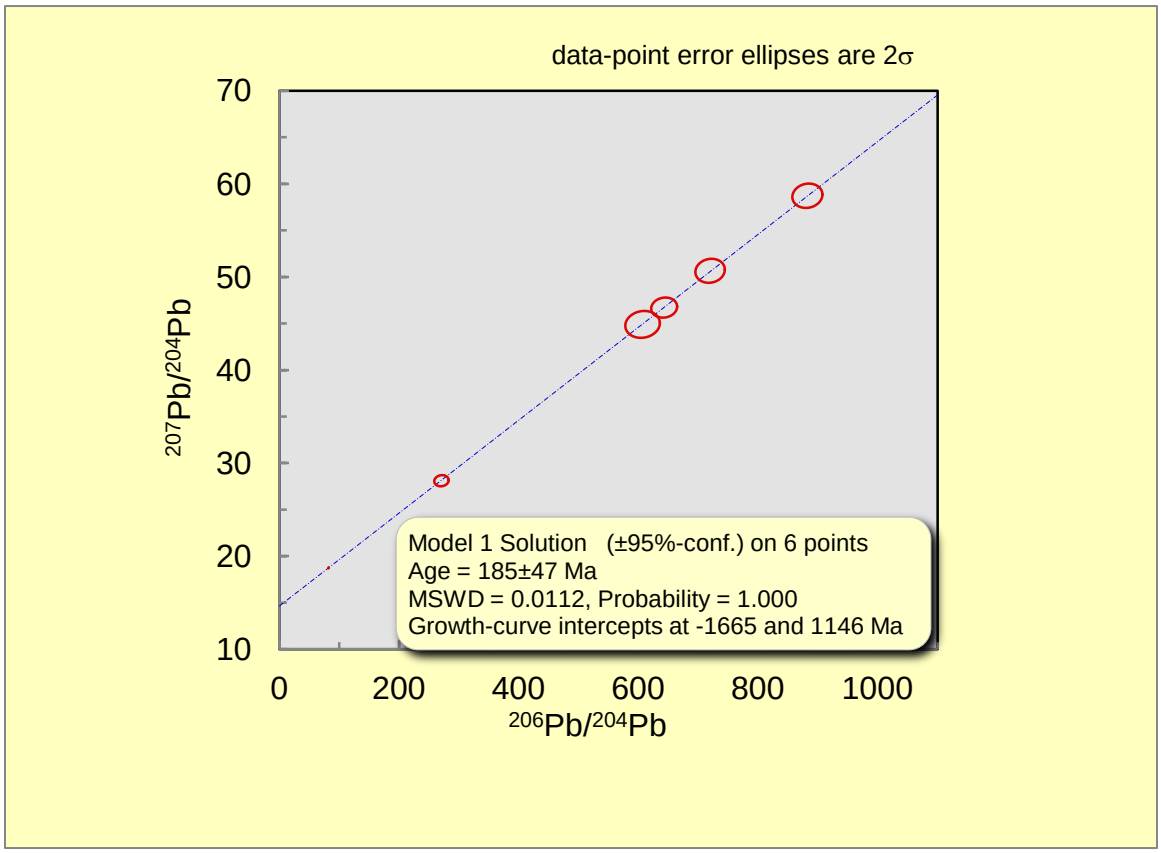
data-point error ellipses are 2σ
70
60
50
40
30
20
10
$^{207}Pb/^{204}Pb$
0
200
400
600
800
1000
$^{206}Pb/^{204}Pb$
Model 1 Solution (±95%-conf.) on 6 points
Age = 185±47 Ma
MSWD = 0.0112, Probability = 1.000
Growth-curve intercepts at -1665 and 1146 Ma

Figure 31: Sample CAVE-02399-003. Calcite spar. Scale bar is in cm. (Photo Credit: Dave Decker).

Cave ID Number: CAVE-C-1
Sample Number: CAVE-02399-003
Collection Date: 28 October, 2011
Collected By: Dave Decker

X-series U (ppm): 0.158
X-series Th (ppm): 0.063
X-series Pb (ppm): 0.019
U/Pb: 8.32

Weight (Kg): 1.100
Size (cm): 12 x 18
Curation Location: University of New Mexico

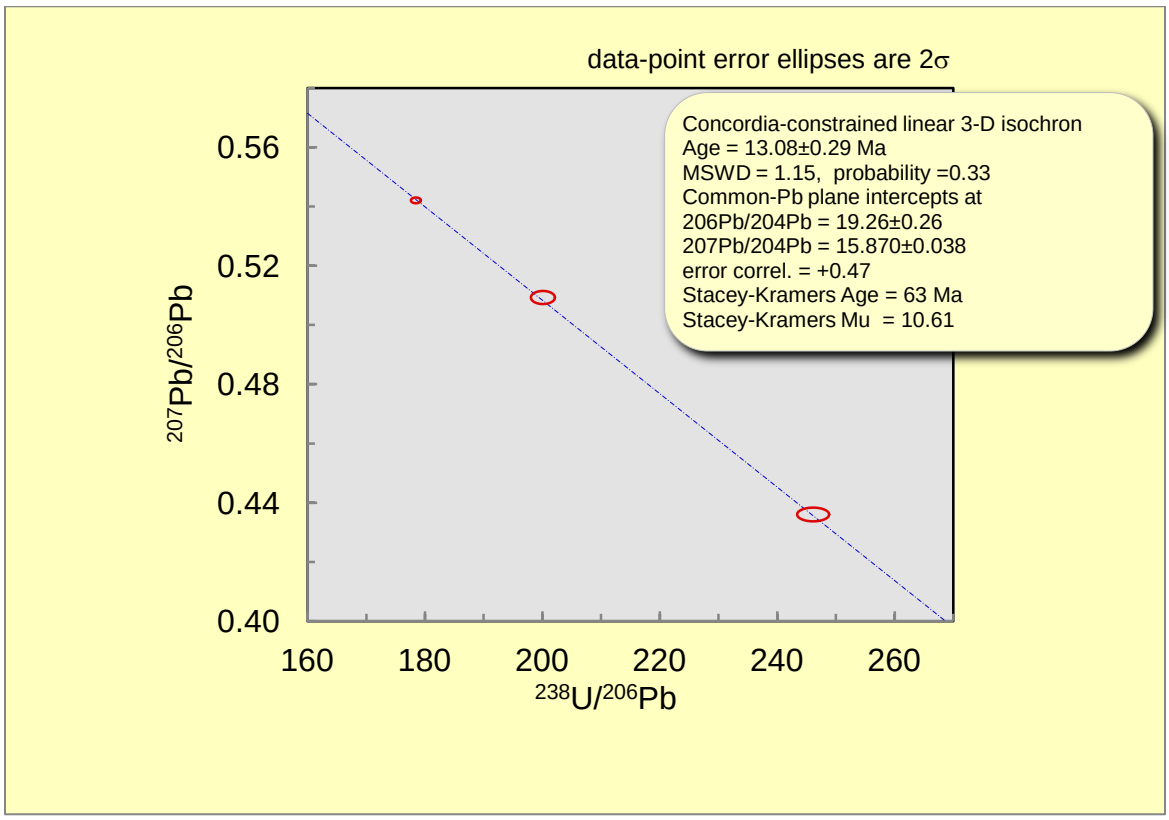

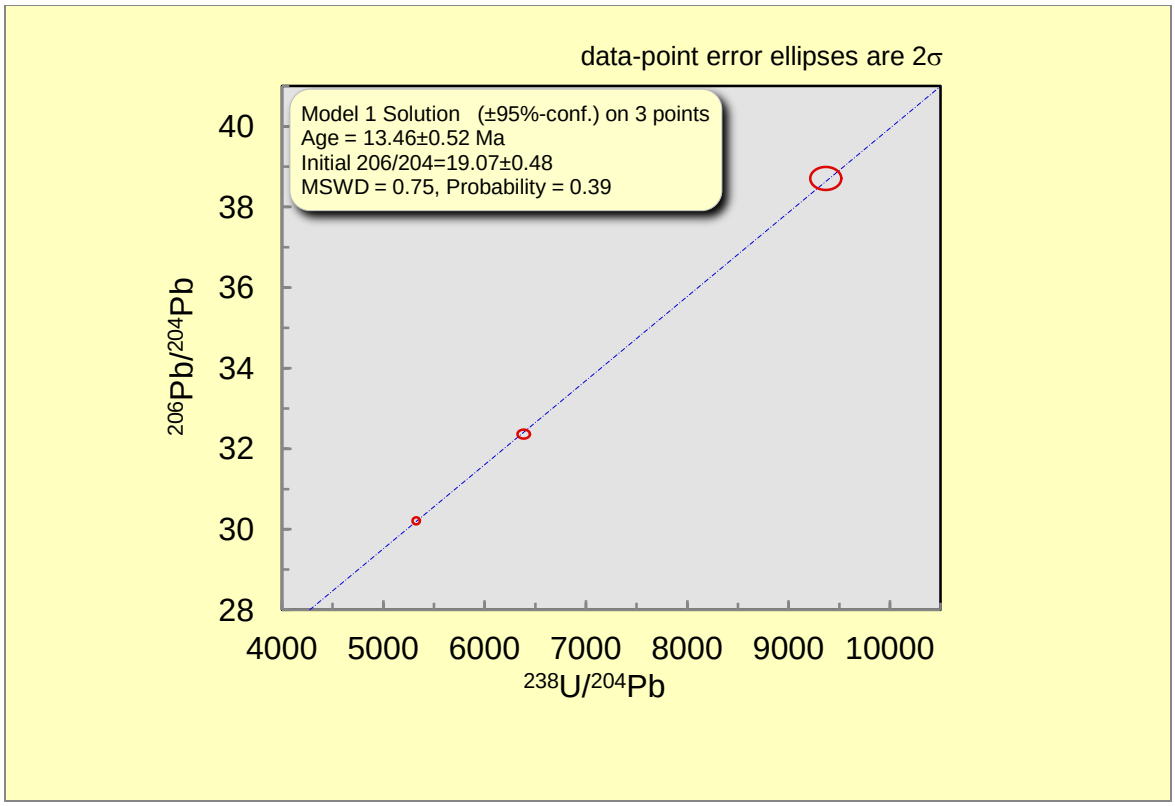
data-point error ellipses are 2σ
Model 1 Solution (±95%-conf.) on 3 points
Age = 13.46±0.52 Ma
Initial 206/204=19.07±0.48
MSWD = 0.75, Probability = 0.39
40
38
36
34
32
30
28
206Pb/204Pb
4000
5000
6000
7000
8000
9000
10000
238U/204Pb

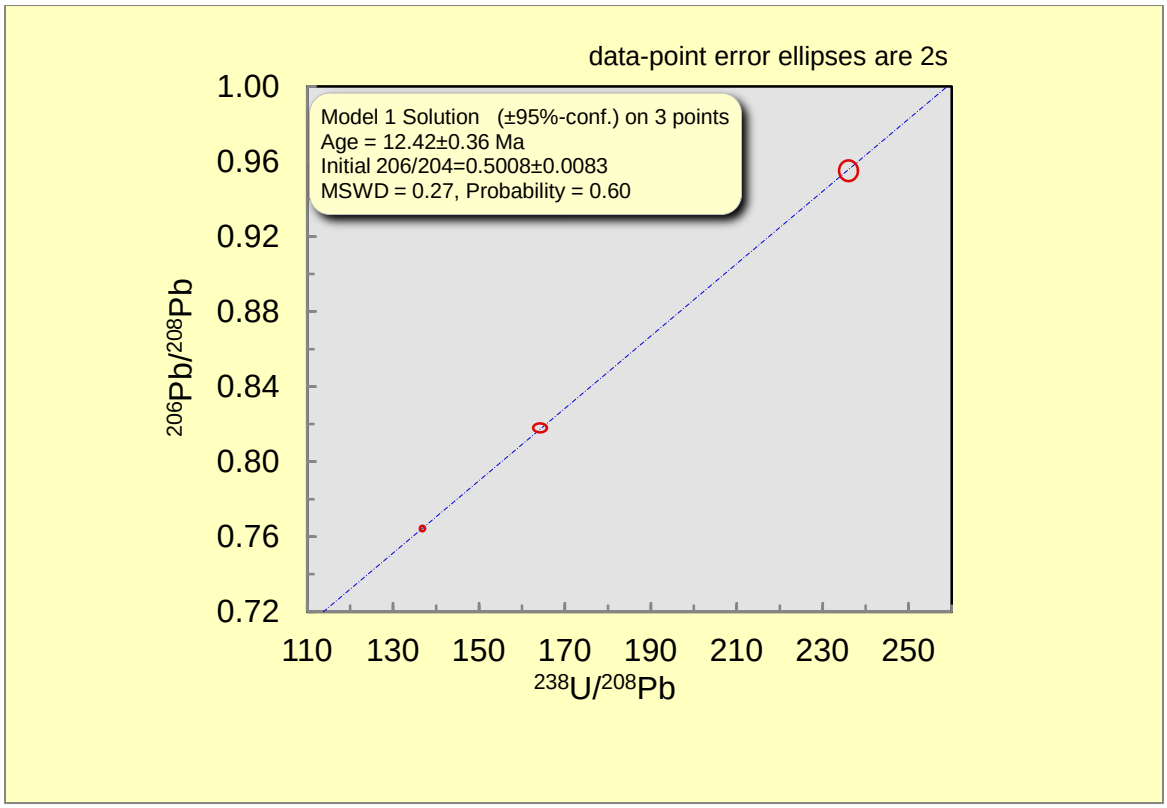
data-point error ellipses are 2s
Model 1 Solution (±95%-conf.) on 3 points
Age = 12.42±0.36 Ma
Initial 206/204=0.5008±0.0083
MSWD = 0.27, Probability = 0.60
1.00
0.96
0.92
0.88
0.84
0.80
0.76
0.72
206Pb/208Pb
110
130
150
170
190
210
230
250
238U/208Pb

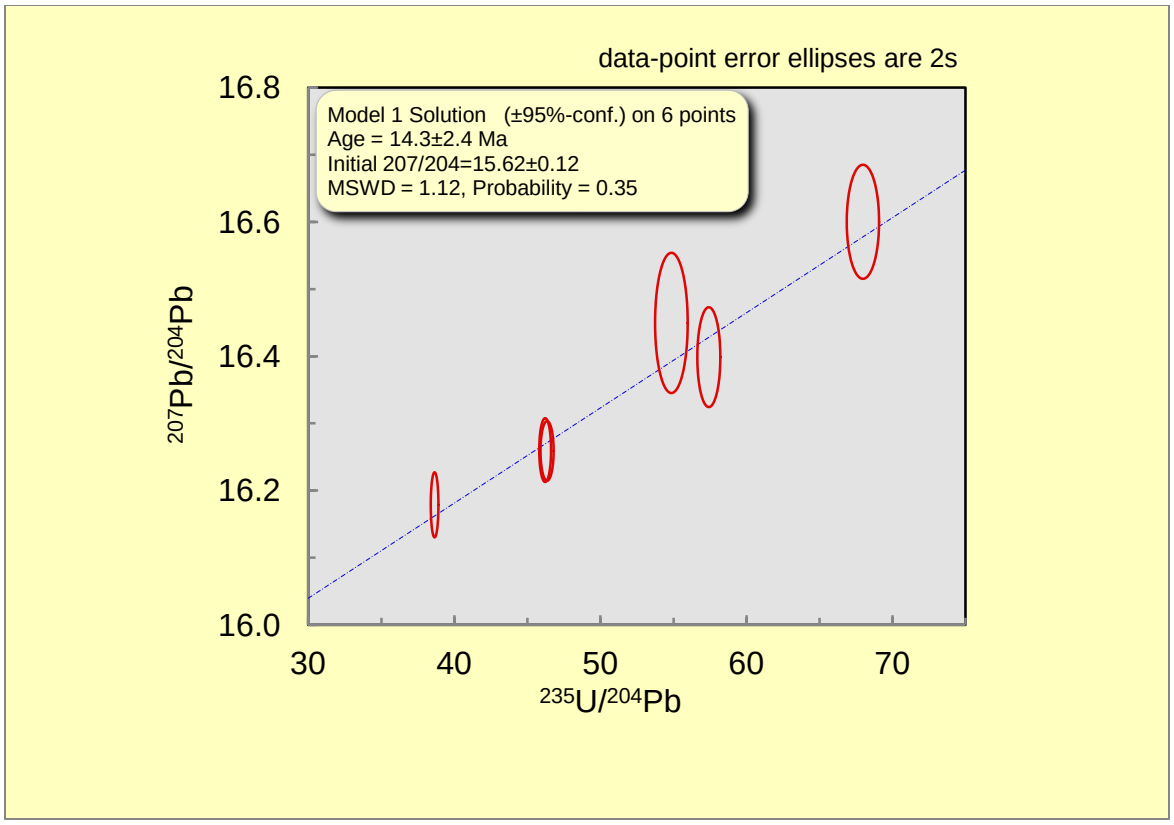
data-point error ellipses are 2s
Model 1 Solution (±95%-conf.) on 6 points
Age = 14.3±2.4 Ma
Initial 207/204=15.62±0.12
MSWD = 1.12, Probability = 0.35
16.8
16.6
16.4
16.2
16.0
30
40
50
60
70
207Pb/204Pb
235U/204Pb

Figure 32: Sample CAVE-02399-004. Calcite spar. Scale bar is in cm. (Photo Credit: Dave Decker).

Cave ID Number: CAVE-C-5
Sample Number: CAVE-02399-004
Collection Date: 19 July, 2012
Collected By: Dave Decker

X-series U (ppm): 1.193
X-series Th (ppm): 0.013
X-series Pb (ppm): 0.008
U/Pb: 149.125

Weight (Kg): 0.262
Size (cm): 10 x 7
Curation Location: University of New Mexico

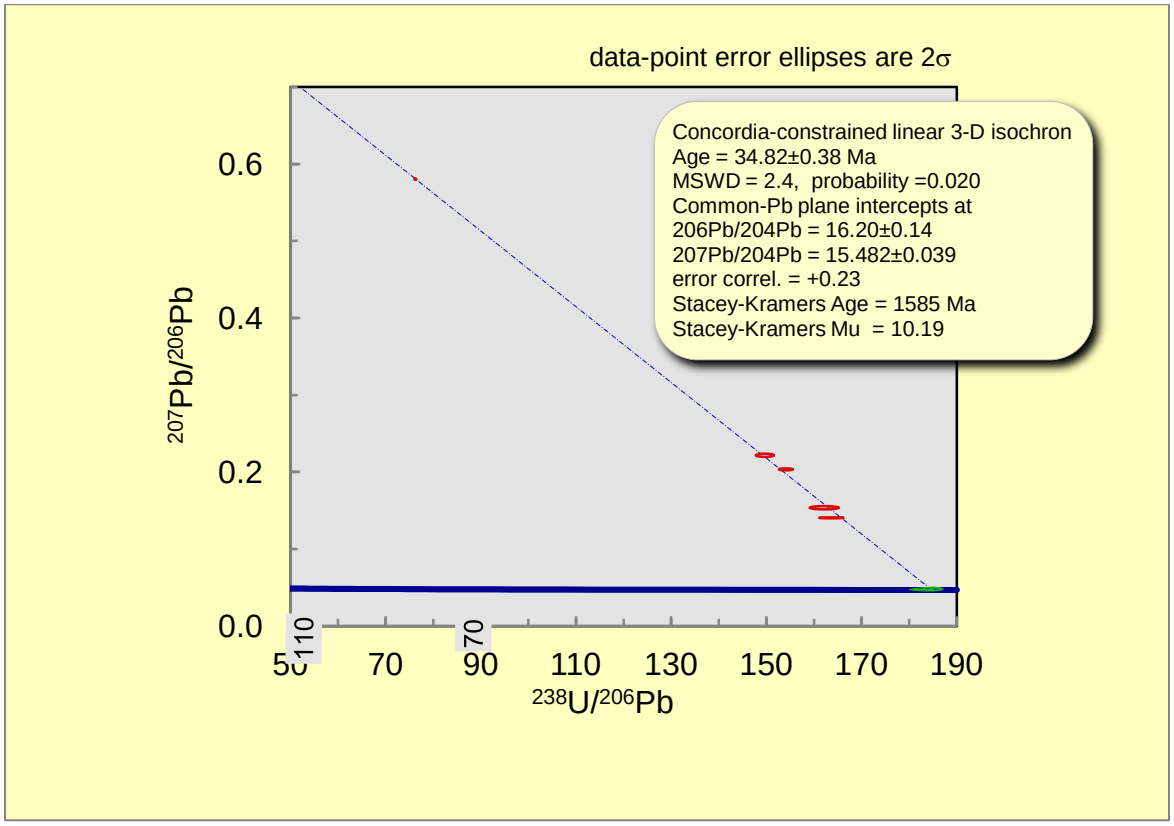

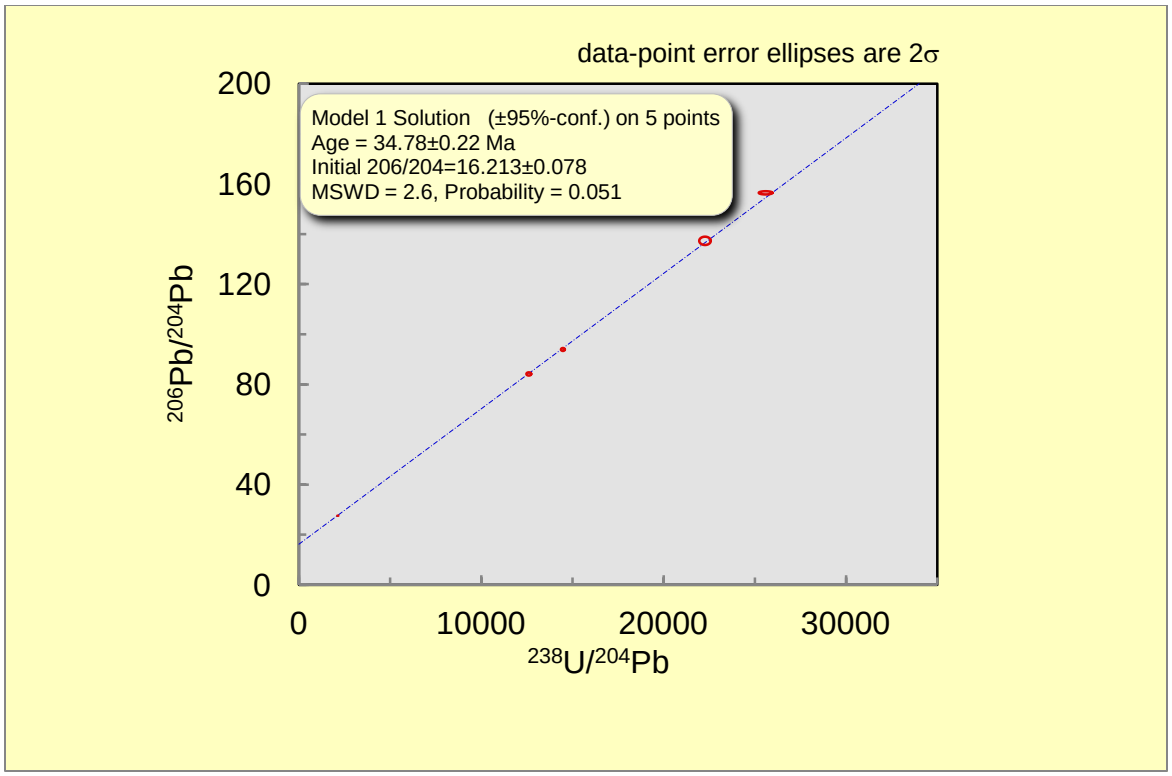
data-point error ellipses are 2σ
Model 1 Solution (±95%-conf.) on 5 points
Age = 34.78±0.22 Ma
Initial 206/204=16.213±0.078
MSWD = 2.6, Probability = 0.051
200
160
120
80
40
0
0
10000
20000
30000
206Pb/204Pb
238U/204Pb

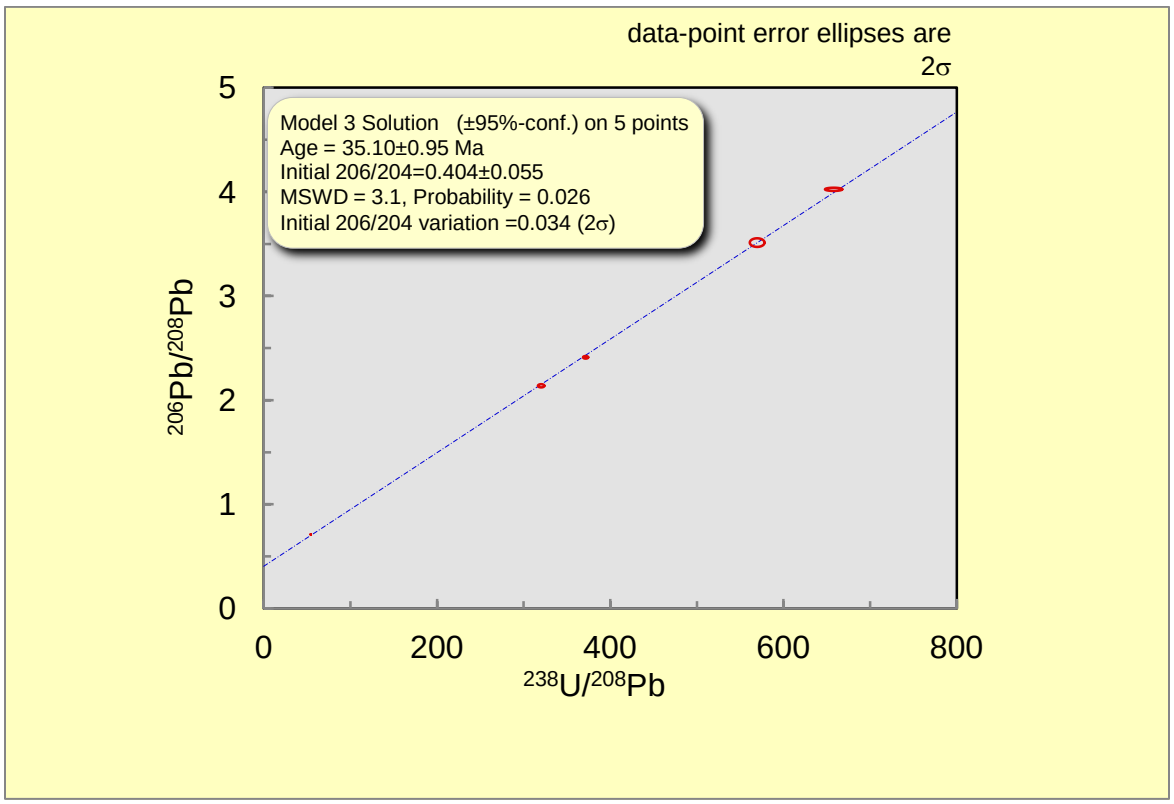
data-point error ellipses are 2σ
Model 3 Solution (±95%-conf.) on 5 points
Age = 35.10±0.95 Ma
Initial 206/204=0.404±0.055
MSWD = 3.1, Probability = 0.026
Initial 206/204 variation =0.034 (2σ)
5
4
3
2
1
0
0
200
400
600
800
206Pb/208Pb
238U/208Pb

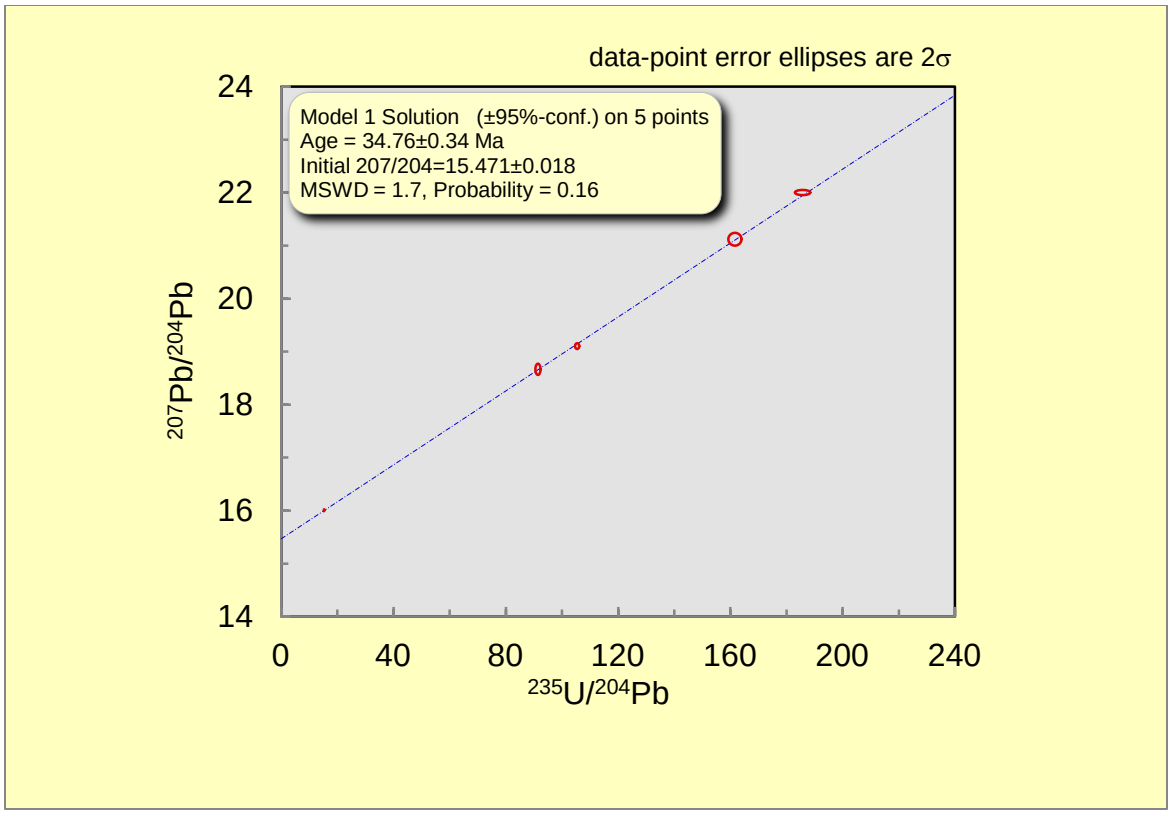
data-point error ellipses are 2σ
Model 1 Solution (±95%-conf.) on 5 points
Age = 34.76±0.34 Ma
Initial 207/204=15.471±0.018
MSWD = 1.7, Probability = 0.16
24
22
20
18
16
14
0
40
80
120
160
200
240
207Pb/204Pb
235U/204Pb

Figure 33: Sample CAVE-02399-006. Calcite spar. Scale bar is in cm. (Photo Credit: Dave Decker).

Cave ID Number: CAVE-C-5
Sample Number: CAVE-02399-006
Collection Date: 19 July, 2012
Collected By: Dave Decker

X-series U (ppm): 0.224
X-series Th (ppm): 0.007
X-series Pb (ppm): 0.010
U/Pb: 22.4

Weight (Kg): 0.040
Size (cm): 7 x 3.5
Curation Location: University of New Mexico

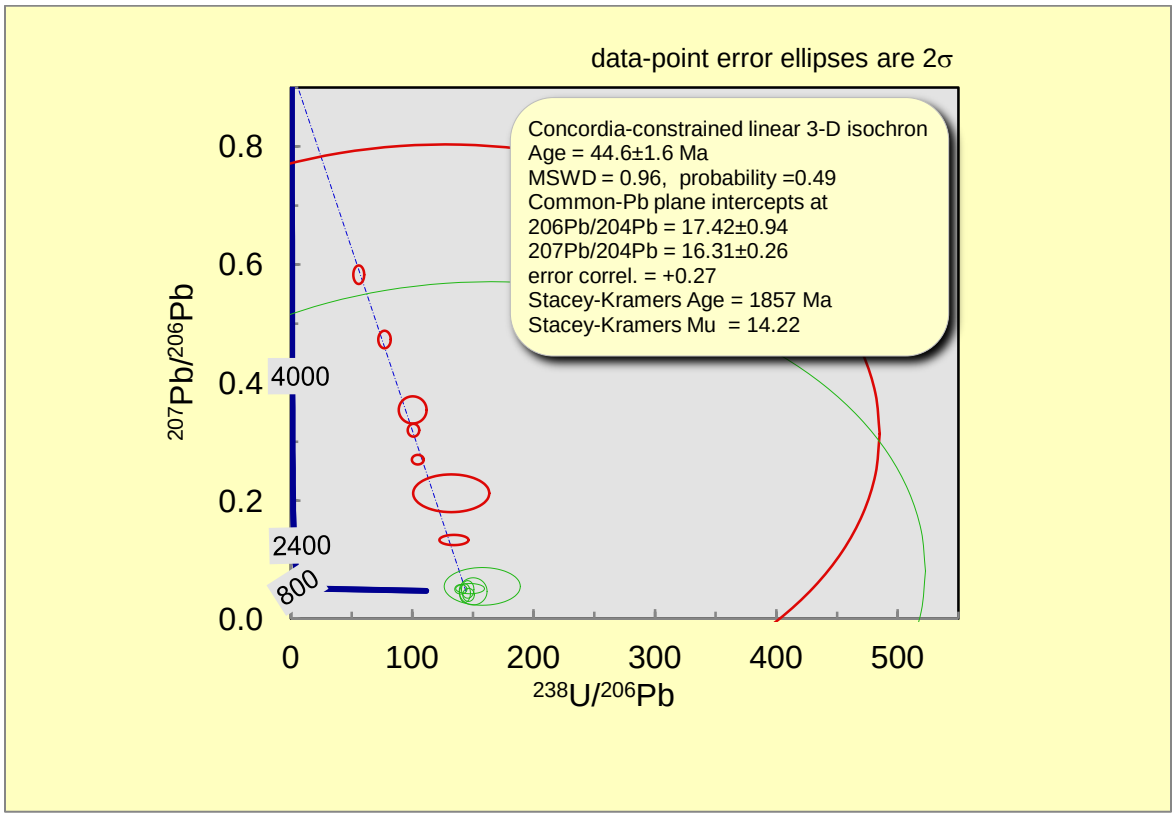

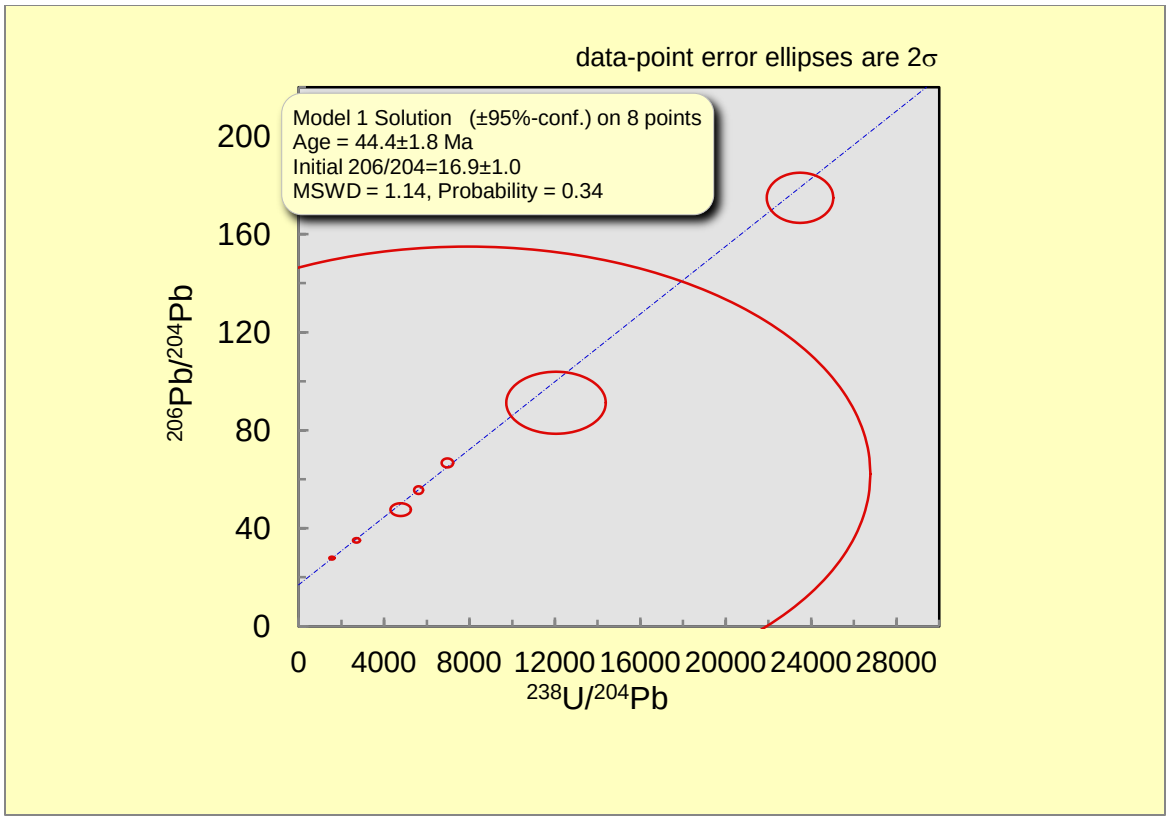
data-point error ellipses are 2σ
Model 1 Solution (±95%-conf.) on 8 points
Age = 44.4±1.8 Ma
Initial 206/204=16.9±1.0
MSWD = 1.14, Probability = 0.34
200
160
120
80
40
0
206Pb/204Pb
0
4000
8000
12000
16000
20000
24000
28000
238U/204Pb

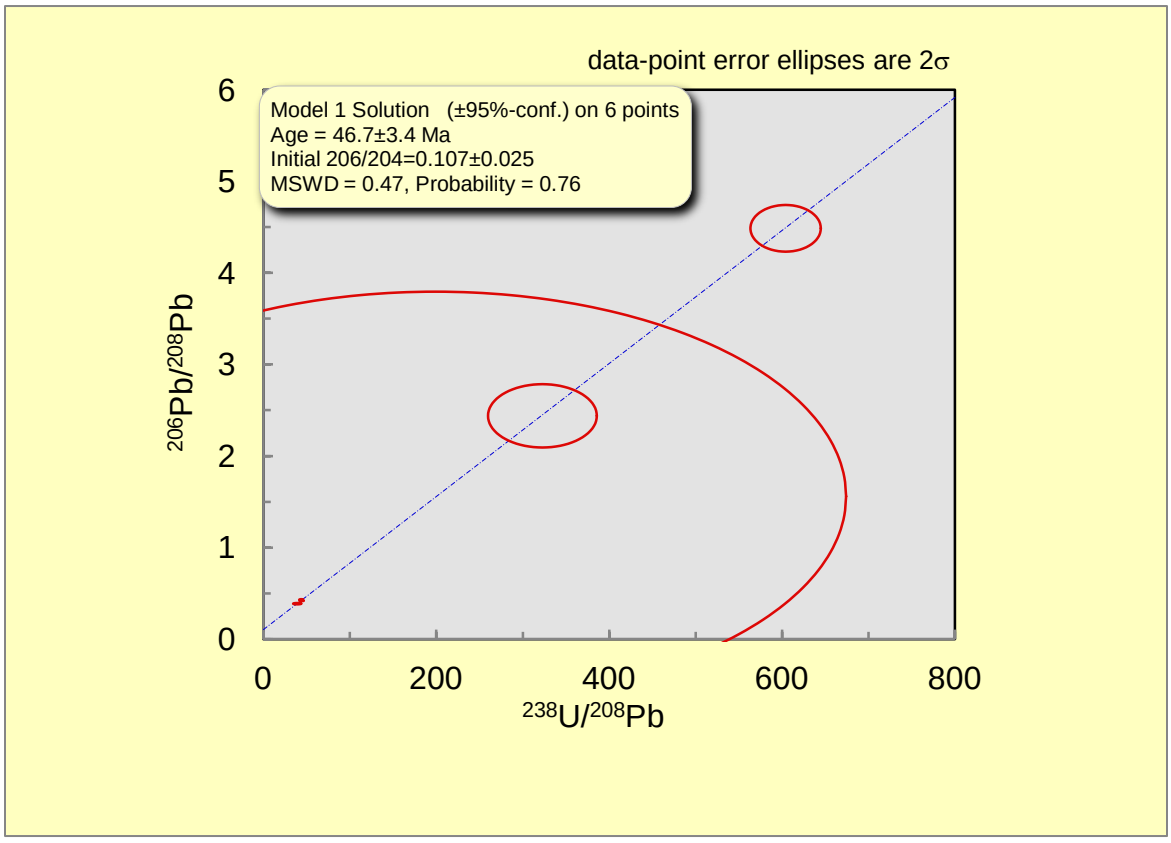
data-point error ellipses are 2σ
Model 1 Solution (±95%-conf.) on 6 points
Age = 46.7±3.4 Ma
Initial 206/204=0.107±0.025
MSWD = 0.47, Probability = 0.76
6
5
4
3
2
1
0
206Pb/208Pb
0
200
400
600
800
238U/208Pb

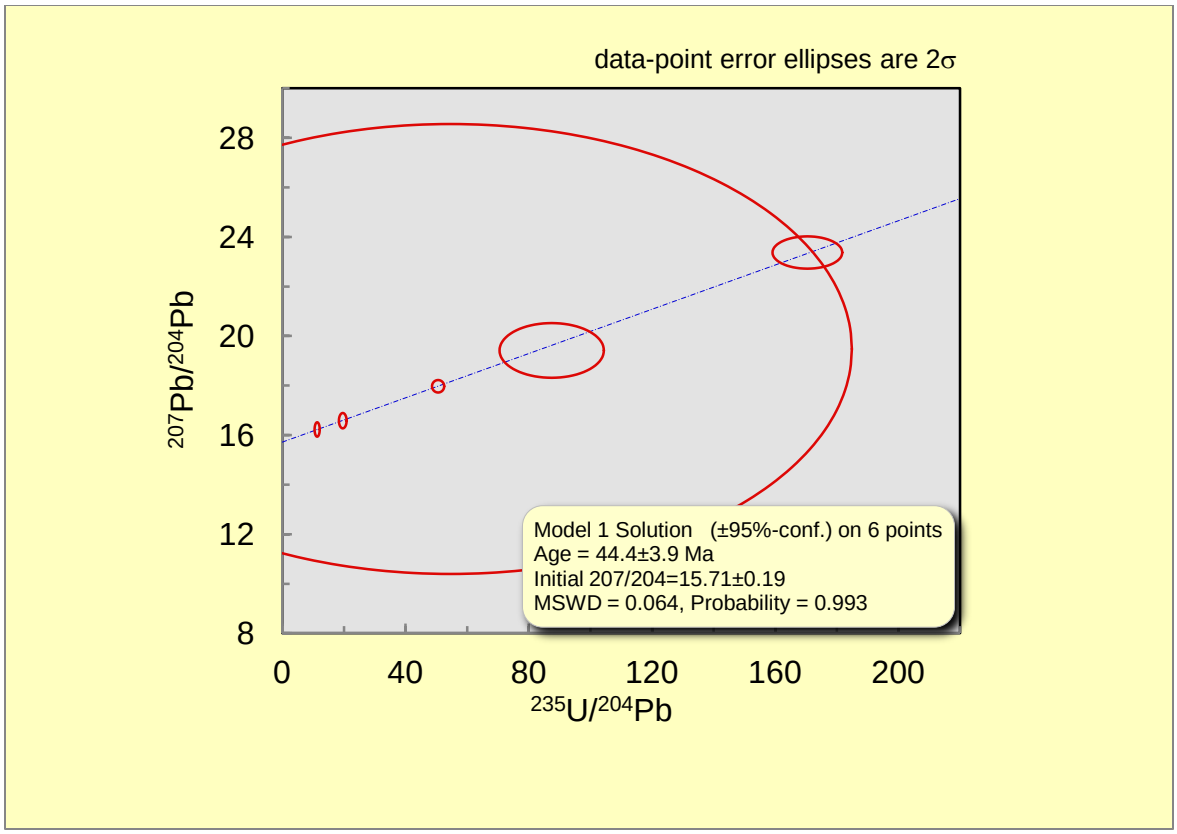
data-point error ellipses are 2σ
28
24
20
16
12
8
$^{207}Pb/^{204}Pb$
0
40
80
120
160
200
$^{235}U/^{204}Pb$
Model 1 Solution (±95%-conf.) on 6 points
Age = 44.4±3.9 Ma
Initial 207/204=15.71±0.19
MSWD = 0.064, Probability = 0.993

Figure 34: Sample CAVE-02399-008. Calcite spar. Scale bar is in cm. (Photo Credit: Dave Decker).

Cave ID Number: CAVE-C-1
Sample Number: CAVE-02399-008
Collection Date: 13 March, 2013
Collected By: Dave Decker

X-series U (ppm): 5.192
X-series Th (ppm): 0.247
X-series Pb (ppm): 0.790
U/Pb: 6.572
Weight (Kg): 0.005
Size (cm): Chips
Curation Location: University of New Mexico

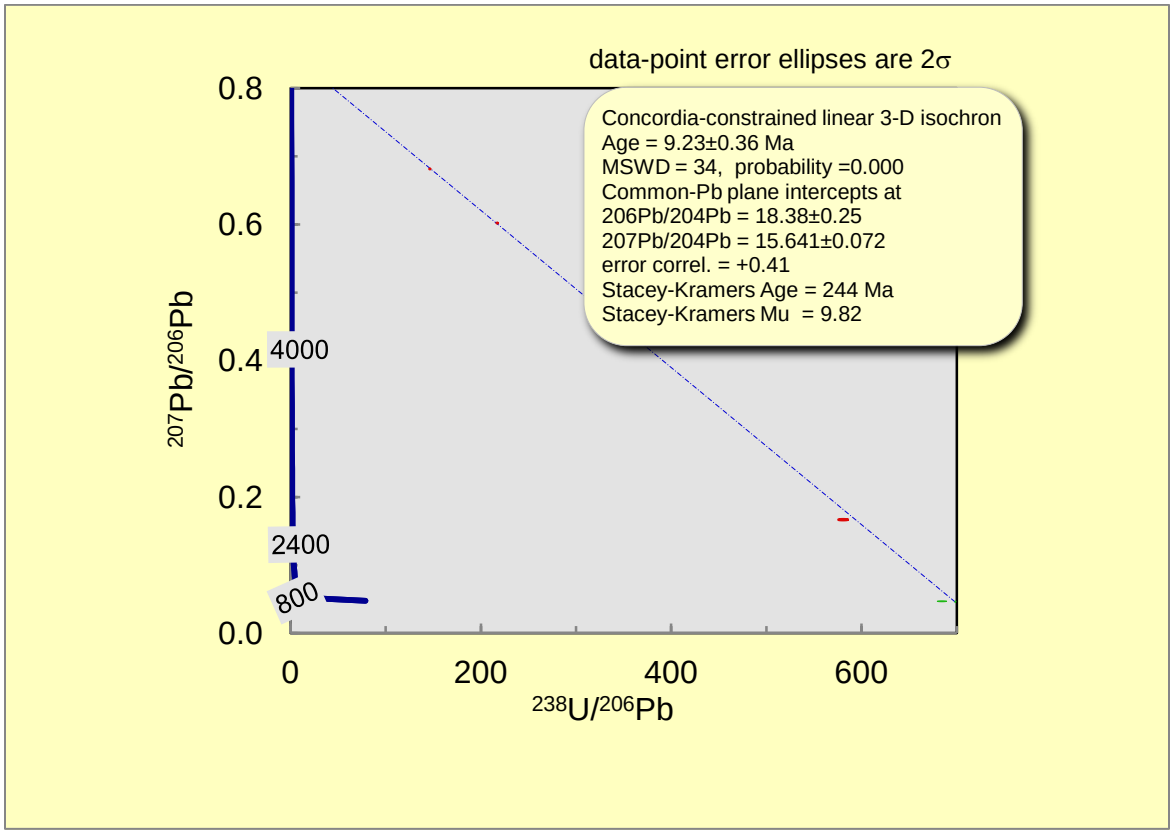

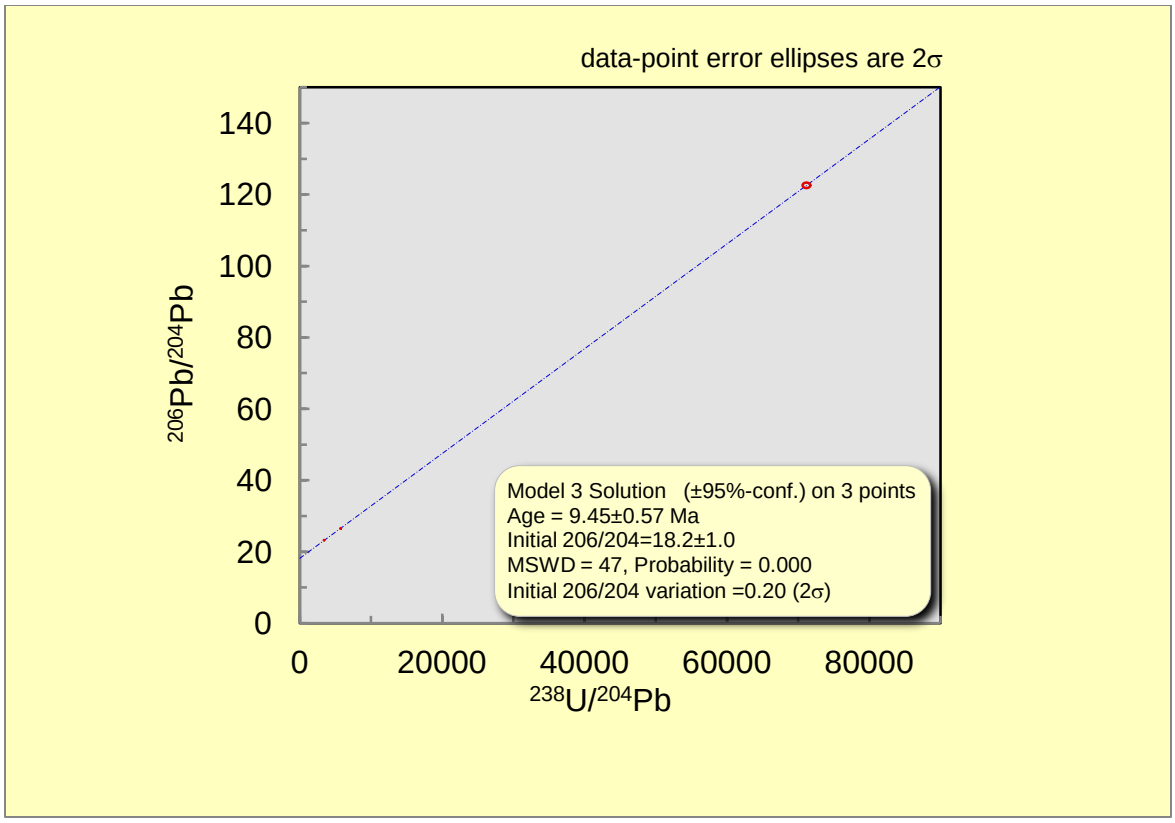
data-point error ellipses are 2σ
140
120
100
80
60
40
20
0
$^{206}Pb/^{204}Pb$
0
20000
40000
60000
80000
$^{238}U/^{204}Pb$
Model 3 Solution (±95%-conf.) on 3 points
Age = 9.45±0.57 Ma
Initial 206/204=18.2±1.0
MSWD = 47, Probability = 0.000
Initial 206/204 variation =0.20 (2σ)

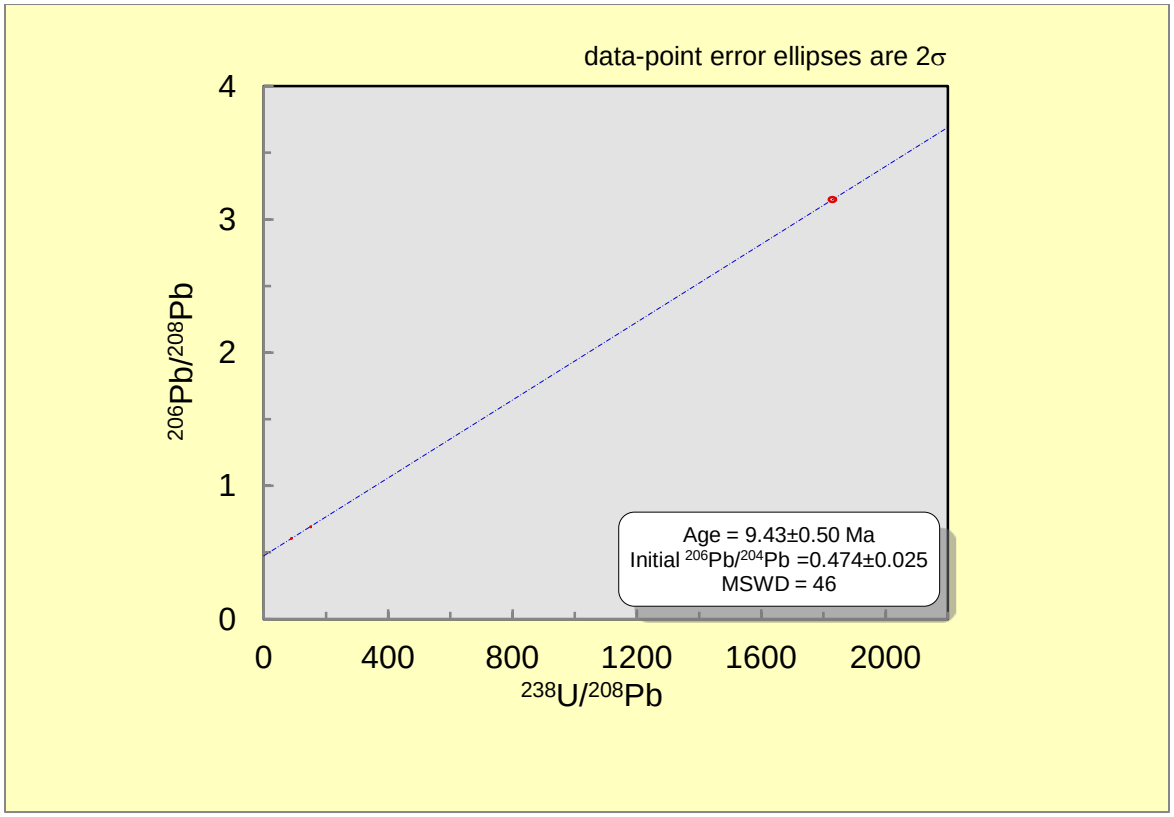
data-point error ellipses are 2σ
4
3
2
1
0
$^{206}Pb/^{208}Pb$
0
400
800
1200
1600
2000
$^{238}U/^{208}Pb$
Age = 9.43±0.50 Ma
Initial $^{206}Pb/^{204}Pb$ =0.474±0.025
MSWD = 46

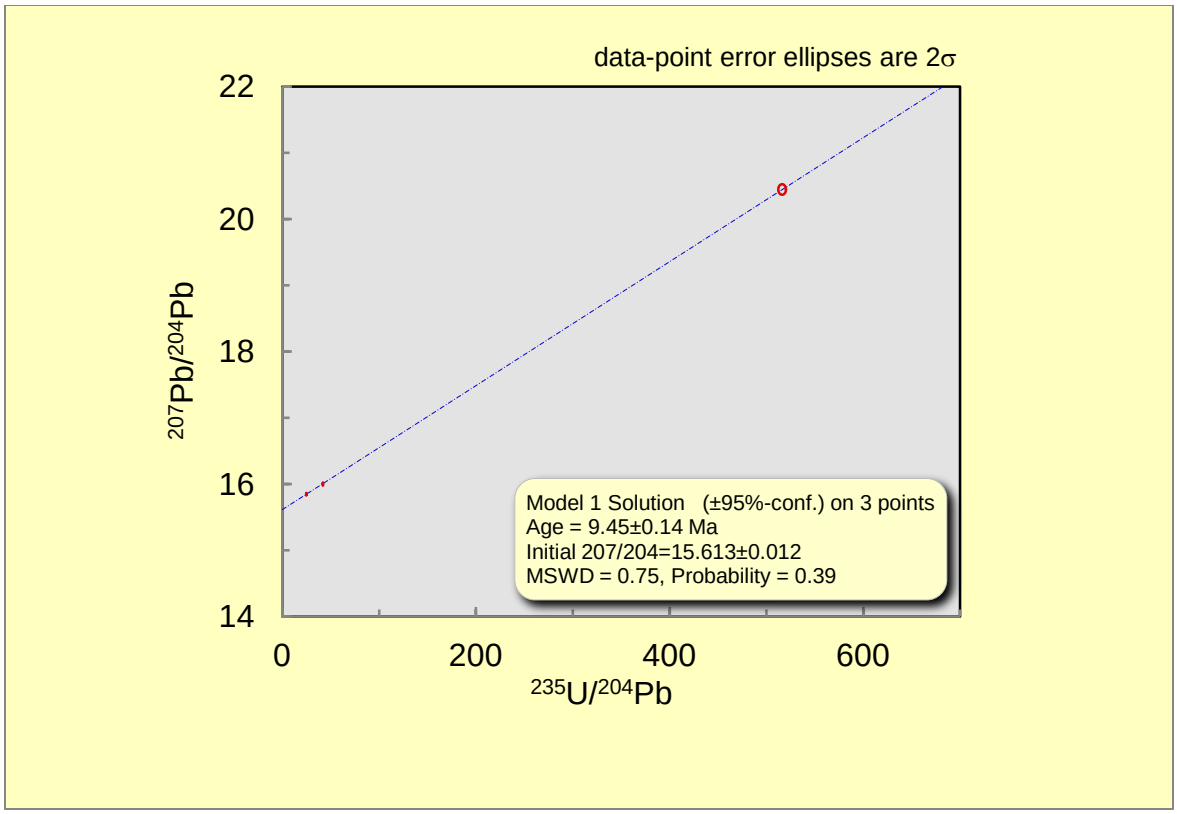
data-point error ellipses are 2σ
22
20
18
16
14
0
200
400
600
$^{207}Pb/^{204}Pb$
$^{235}U/^{204}Pb$
Model 1 Solution (±95%-conf.) on 3 points
Age = 9.45±0.14 Ma
Initial 207/204=15.613±0.012
MSWD = 0.75, Probability = 0.39

Figure 35: Sample CAVE-02399-009. Calcite spar. Scale bar is in cm. (Photo Credit: Dave Decker).

Cave ID Number: CAVE-C-5
Sample Number: CAVE-02399-009
Collection Date: 22 May, 2013
Collected By: Dave Decker

X-series U (ppm): 0.319
X-series Th (ppm): 0.030
X-series Pb (ppm): 0.161
U/Pb: 1.981

Weight (Kg): 0.119
Size (cm): 10x7
Curation Location: University of New Mexico

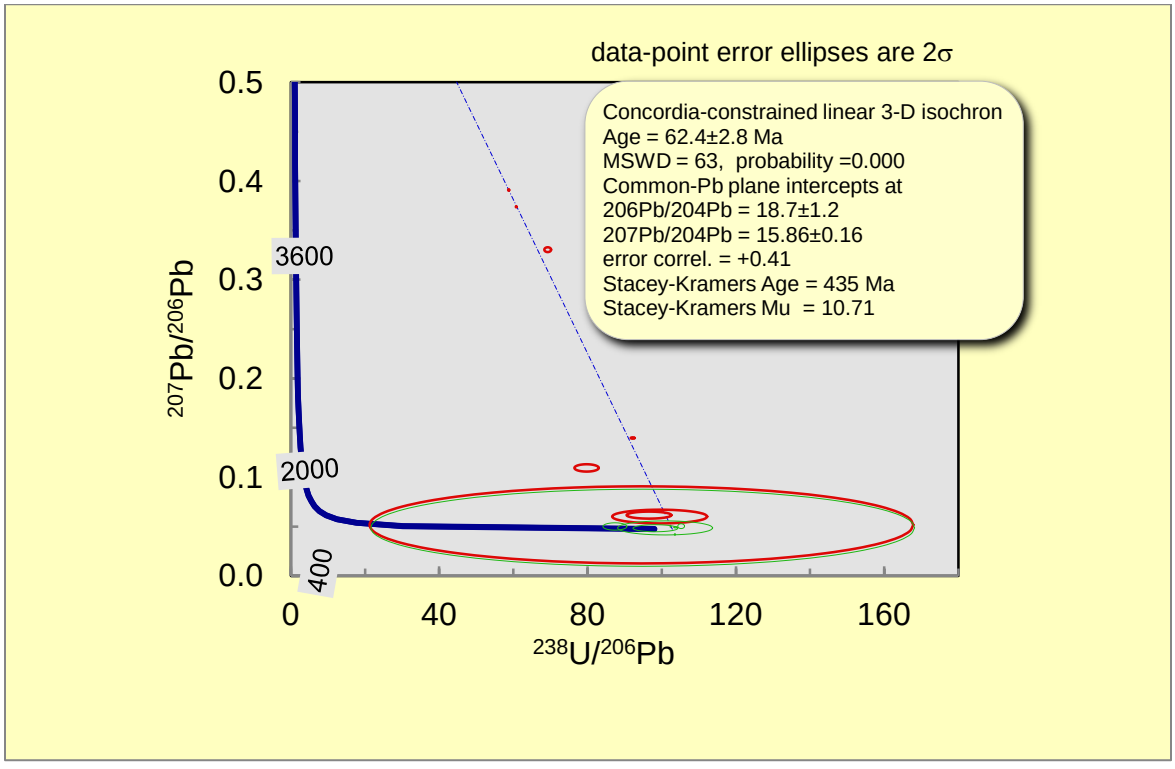

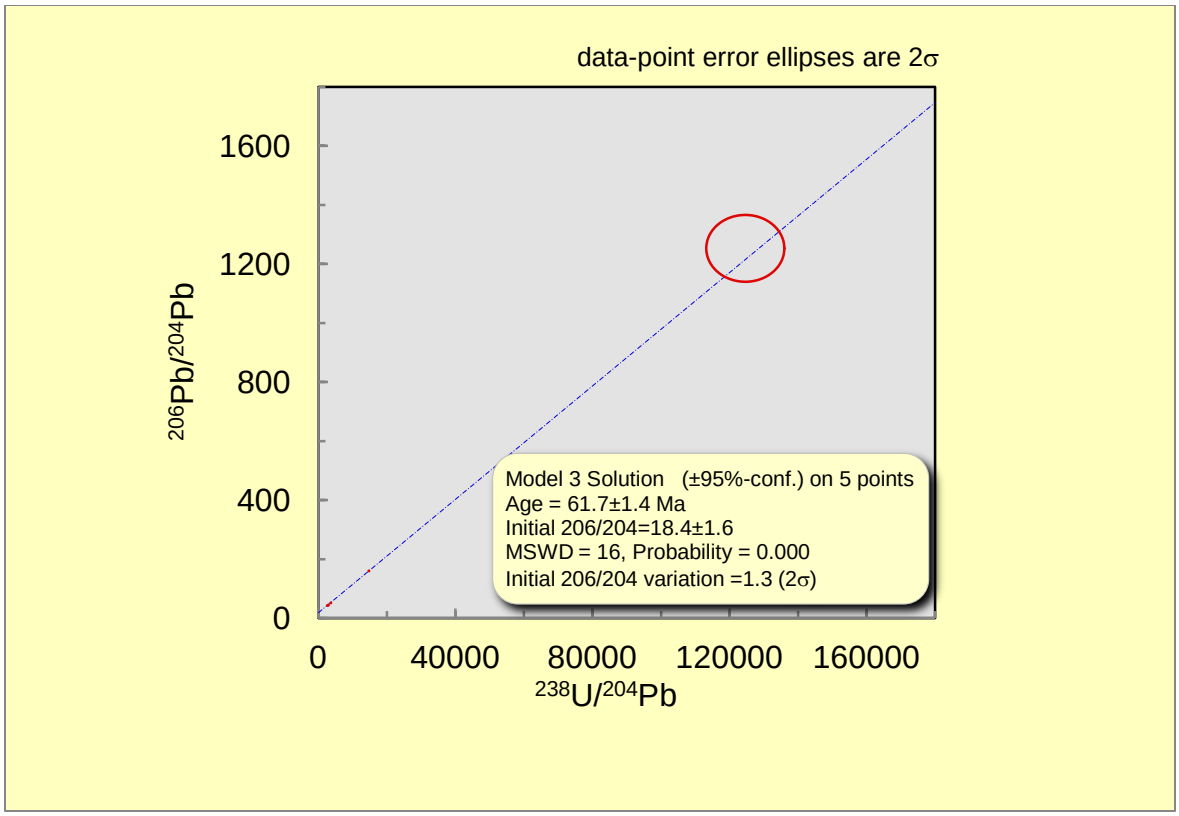
data-point error ellipses are 2σ
1600
1200
800
400
0
$^{206}Pb/^{204}Pb$
0
40000
80000
120000
160000
$^{238}U/^{204}Pb$
Model 3 Solution (±95%-conf.) on 5 points
Age = 61.7±1.4 Ma
Initial 206/204=18.4±1.6
MSWD = 16, Probability = 0.000
Initial 206/204 variation =1.3 (2σ)

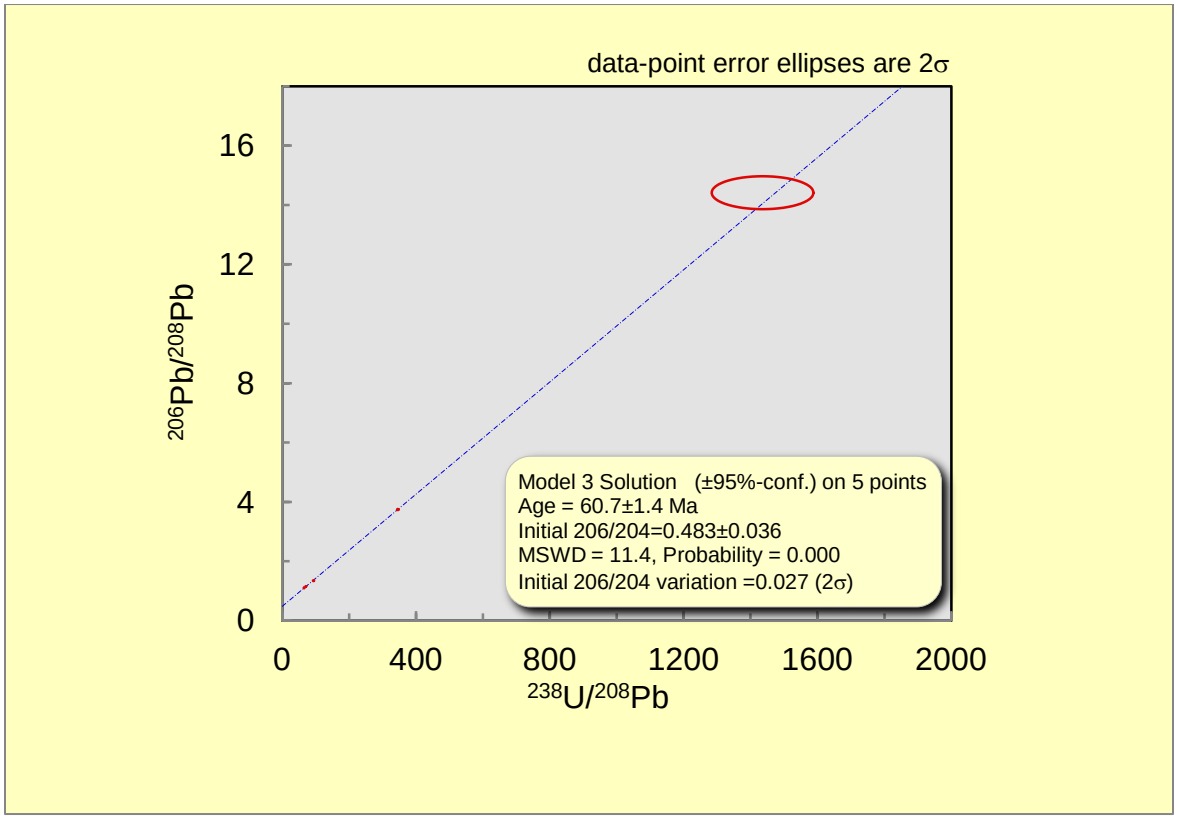
data-point error ellipses are 2σ
16
12
8
4
0
$^{206}Pb/^{208}Pb$
0
400
800
1200
1600
2000
$^{238}U/^{208}Pb$
Model 3 Solution (±95%-conf.) on 5 points
Age = 60.7±1.4 Ma
Initial 206/204=0.483±0.036
MSWD = 11.4, Probability = 0.000
Initial 206/204 variation =0.027 (2σ)

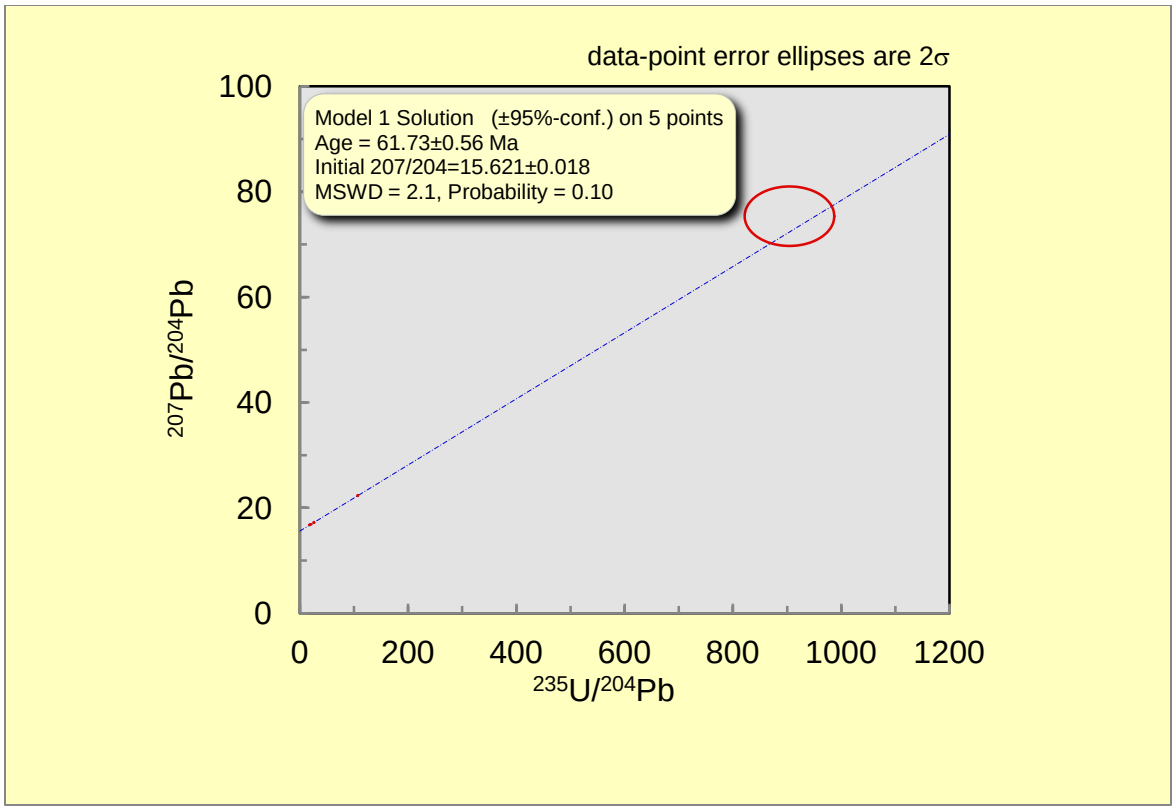
data-point error ellipses are 2σ
Model 1 Solution (±95%-conf.) on 5 points
Age = 61.73±0.56 Ma
Initial 207/204=15.621±0.018
MSWD = 2.1, Probability = 0.10
100
80
60
40
20
0
0
200
400
600
800
1000
1200
207Pb/204Pb
235U/204Pb

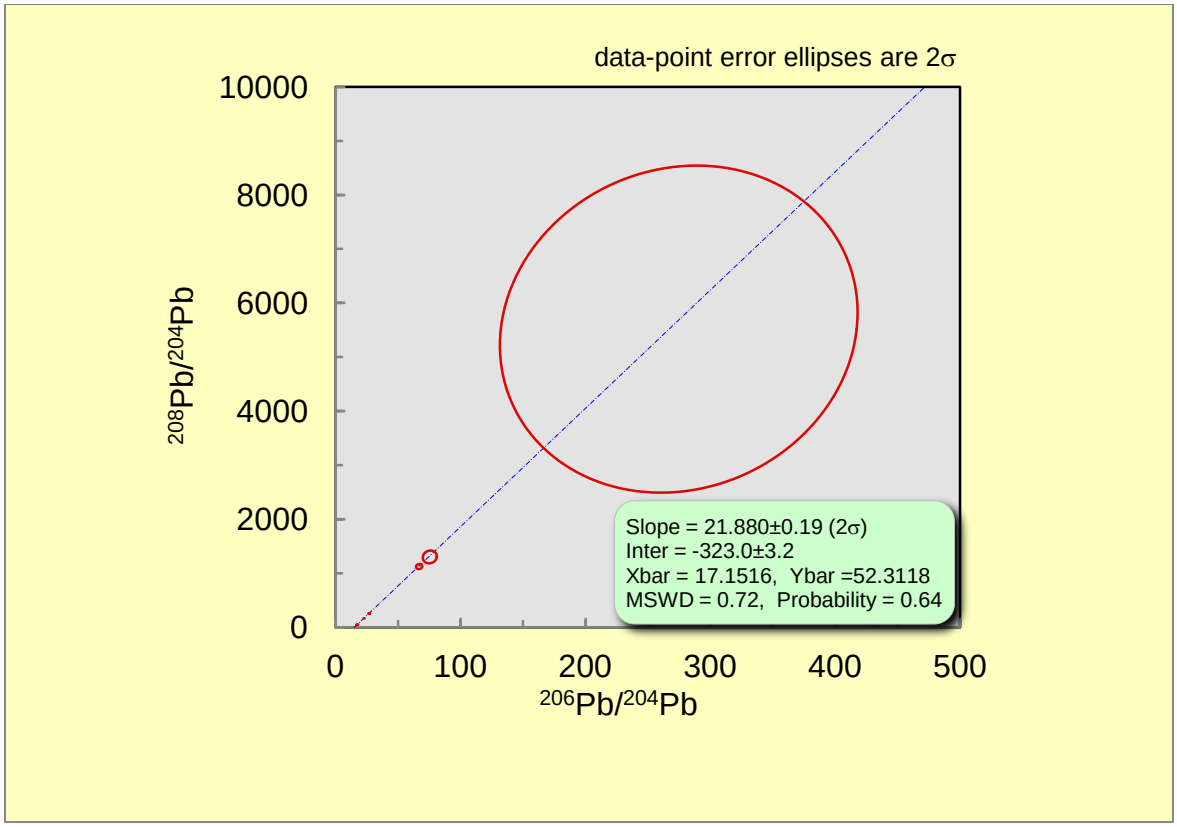
data-point error ellipses are 2σ
Slope = 21.880±0.19 (2σ)
Inter = -323.0±3.2
Xbar = 17.1516, Ybar =52.3118
MSWD = 0.72, Probability = 0.64
10000
8000
6000
4000
2000
0
0
100
200
300
400
500
208Pb/204Pb
206Pb/204Pb

Figure 36: Sample CAVE-02399-011. Calcite spar. Scale bar is in cm. (Photo Credit: Dave Decker).

Cave ID Number: CAVE-C-10
Sample Number: CAVE-02399-011
Collection Date: 10 May, 2014
Collected By: Dave Decker

X-series U (ppm): 5.443
X-series Th (ppm): 0.683
X-series Pb (ppm): 0.153
U/Pb: 35.575

Weight (Kg): 0.580
Size (cm): 14.0x9.5x6.4
Curation Location: University of New Mexico

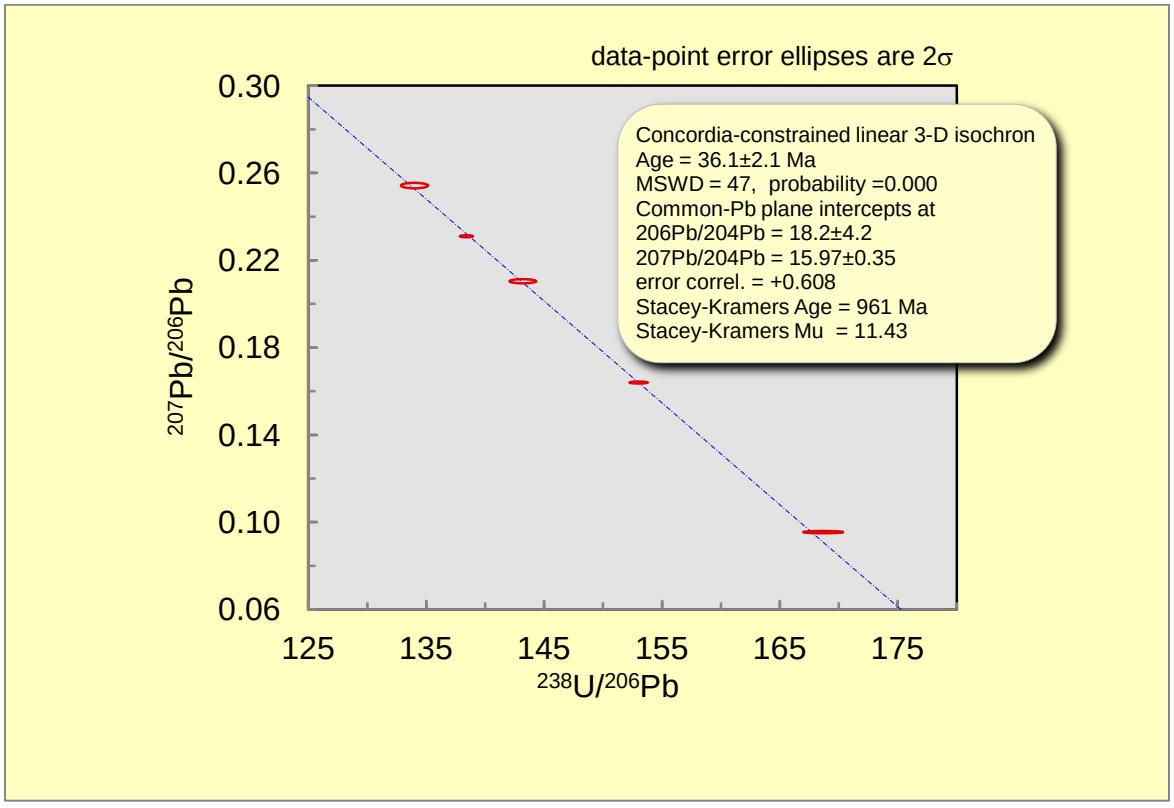

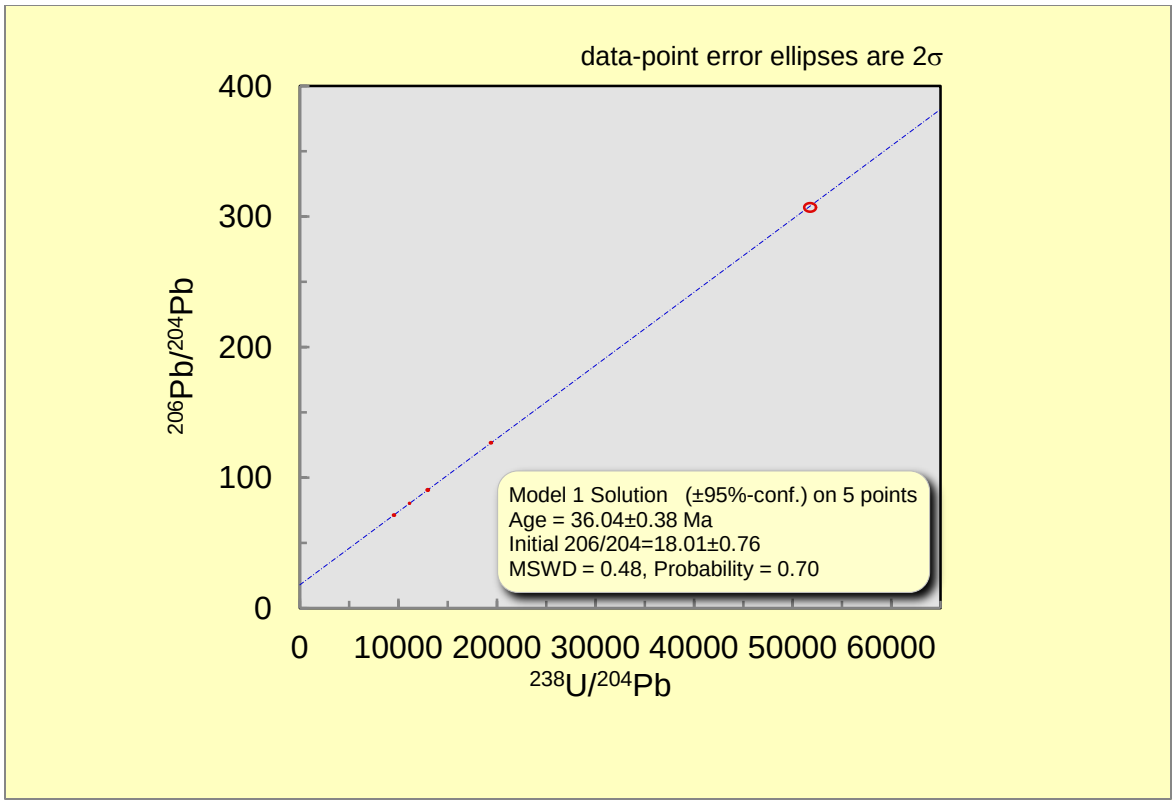
data-point error ellipses are 2σ
400
300
200
100
0
$^{206}Pb/^{204}Pb$
0
10000
20000
30000
40000
50000
60000
$^{238}U/^{204}Pb$
Model 1 Solution (±95%-conf.) on 5 points
Age = 36.04±0.38 Ma
Initial 206/204=18.01±0.76
MSWD = 0.48, Probability = 0.70

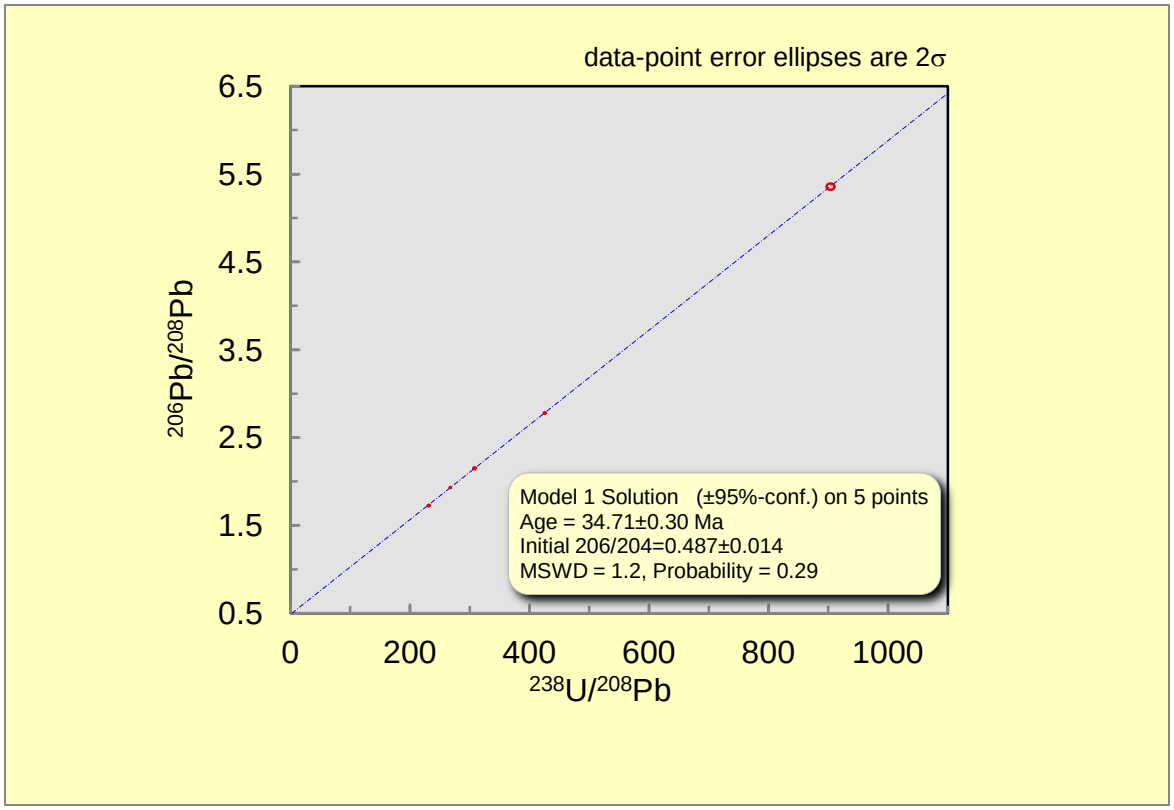
data-point error ellipses are 2σ
6.5
5.5
4.5
3.5
2.5
1.5
0.5
$^{206}Pb/^{208}Pb$
0
200
400
600
800
1000
$^{238}U/^{208}Pb$
Model 1 Solution (±95%-conf.) on 5 points
Age = 34.71±0.30 Ma
Initial 206/204=0.487±0.014
MSWD = 1.2, Probability = 0.29

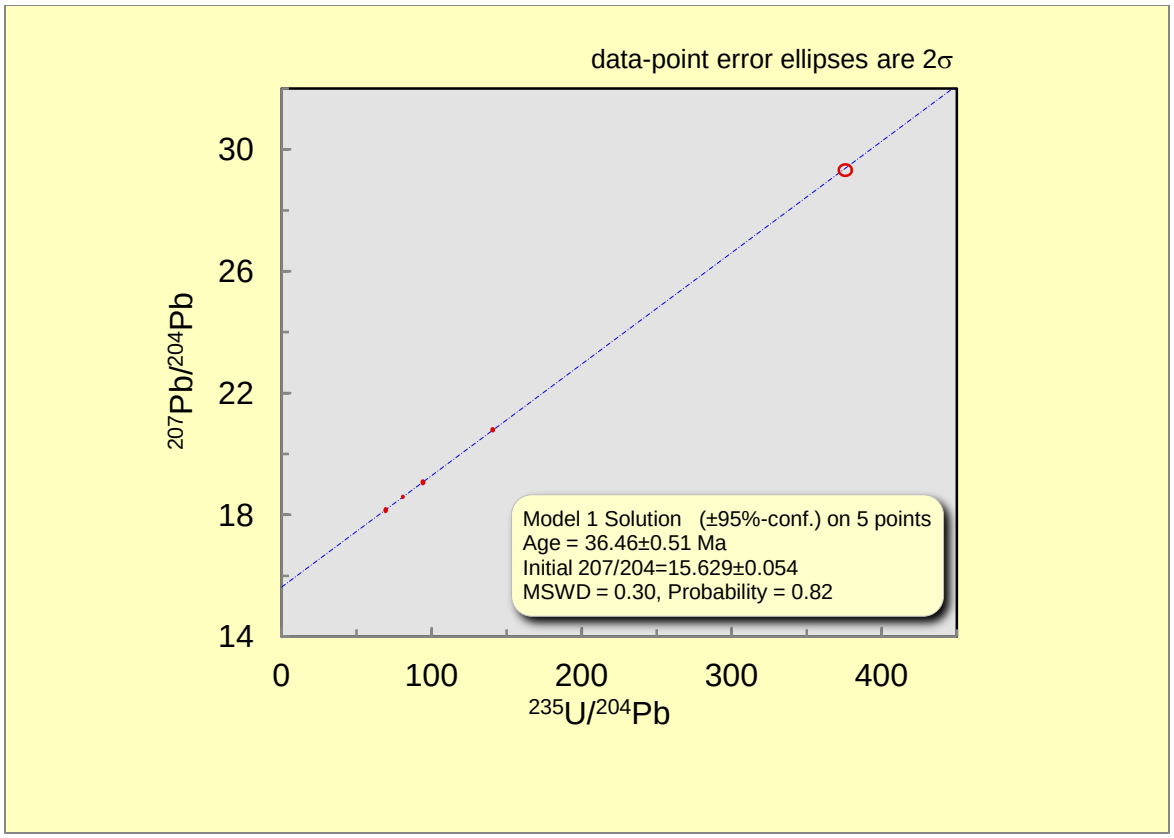
data-point error ellipses are 2σ
30
26
22
18
14
$^{207}Pb/^{204}Pb$
0
100
200
300
400
$^{235}U/^{204}Pb$
Model 1 Solution (±95%-conf.) on 5 points
Age = 36.46±0.51 Ma
Initial 207/204=15.629±0.054
MSWD = 0.30, Probability = 0.82

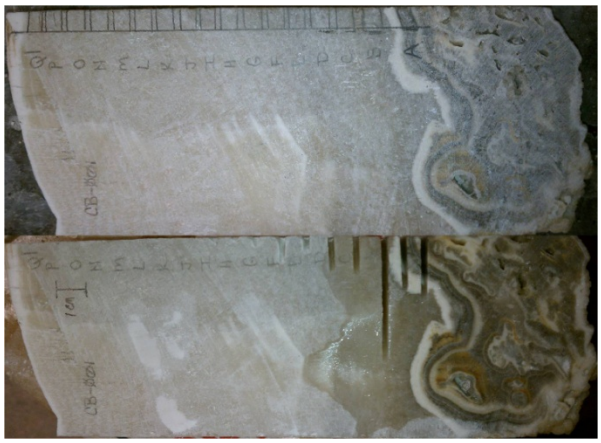

Figure 37: Sample CC-001. Mammillary spar. Age data from the lower brown area to the right on the photo. (Photo Credit: Dave Decker).

Cave ID Number: CAVE-C-1
Sample Number: CC-001
Collection Date: Unknown
Collected By: Carol Hill

X-series U (ppm): 0.760
X-series Th (ppm): 0.002
X-series Pb (ppm): 0.872
U/Pb: 0.872

Weight (Kg): Unknown
Size (cm): 15x7x2
Curation Location: University of New Mexico

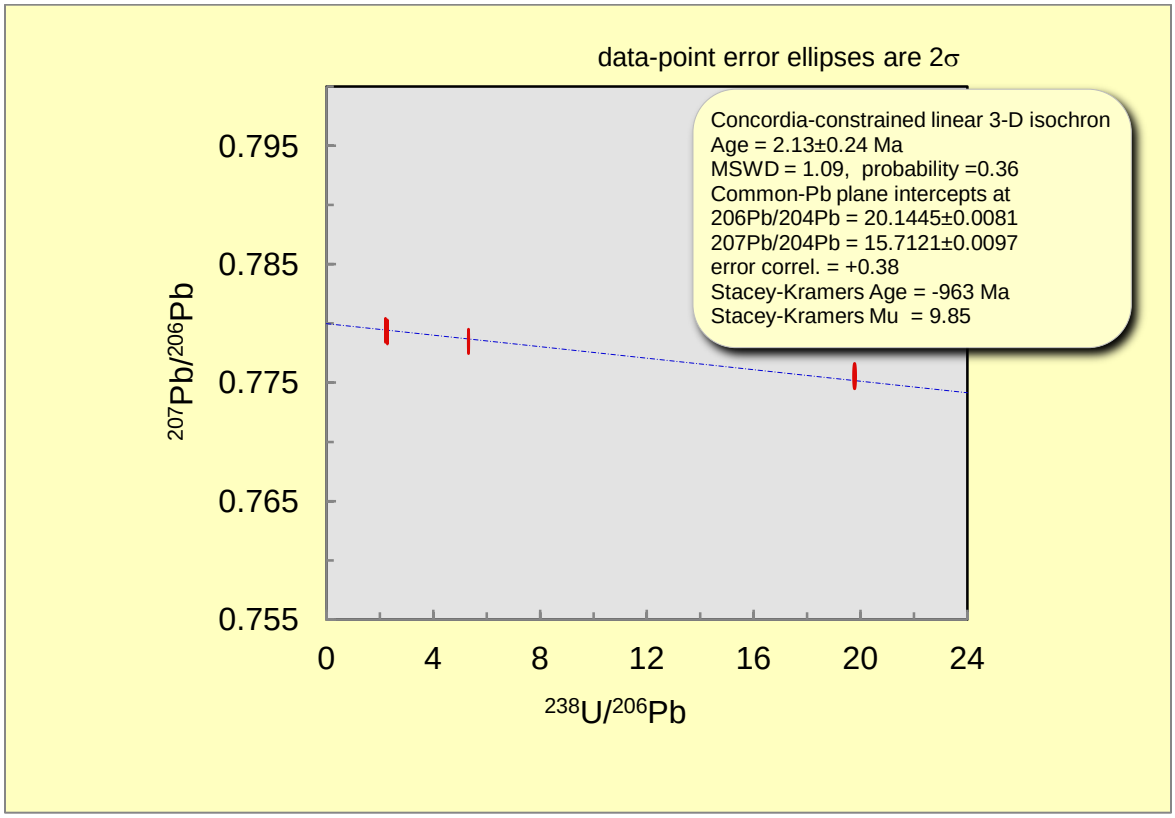

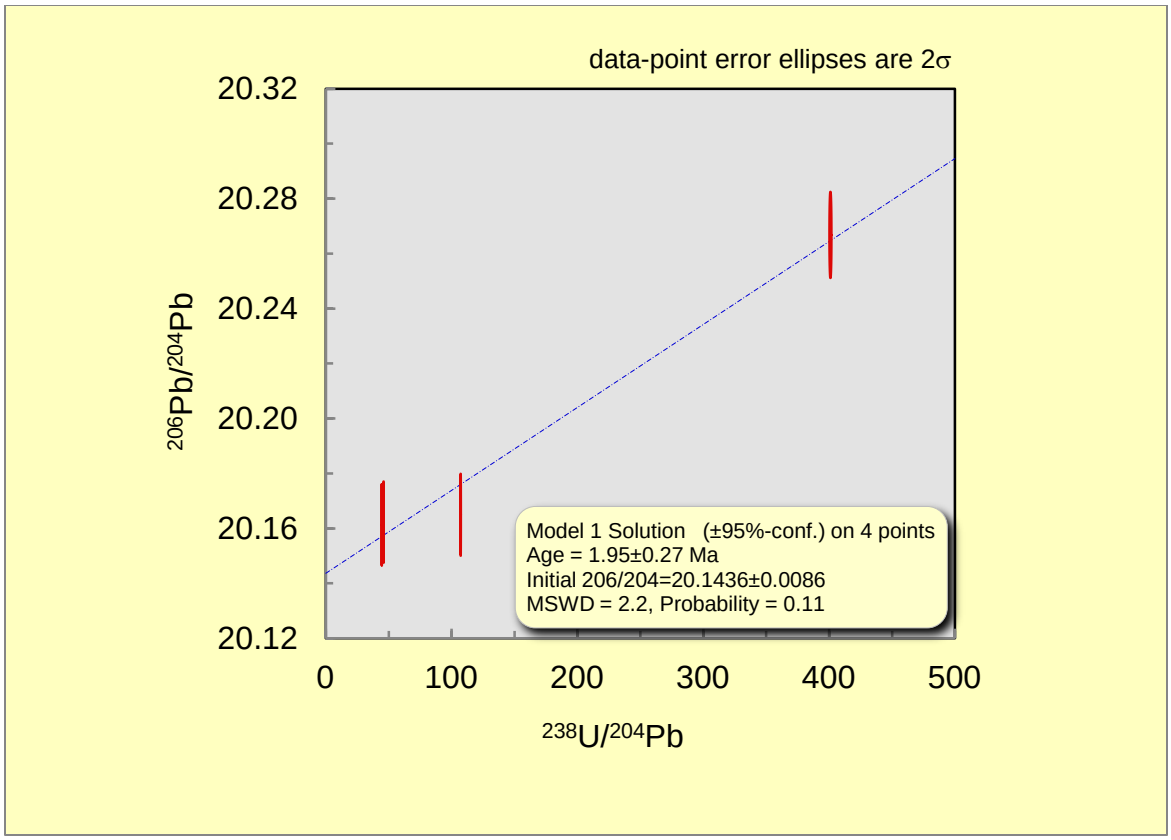
data-point error ellipses are 2σ
20.32
20.28
20.24
20.20
20.16
20.12
$^{206}Pb/^{204}Pb$
0
100
200
300
400
500
$^{238}U/^{204}Pb$
Model 1 Solution (±95%-conf.) on 4 points
Age = 1.95±0.27 Ma
Initial 206/204=20.1436±0.0086
MSWD = 2.2, Probability = 0.11

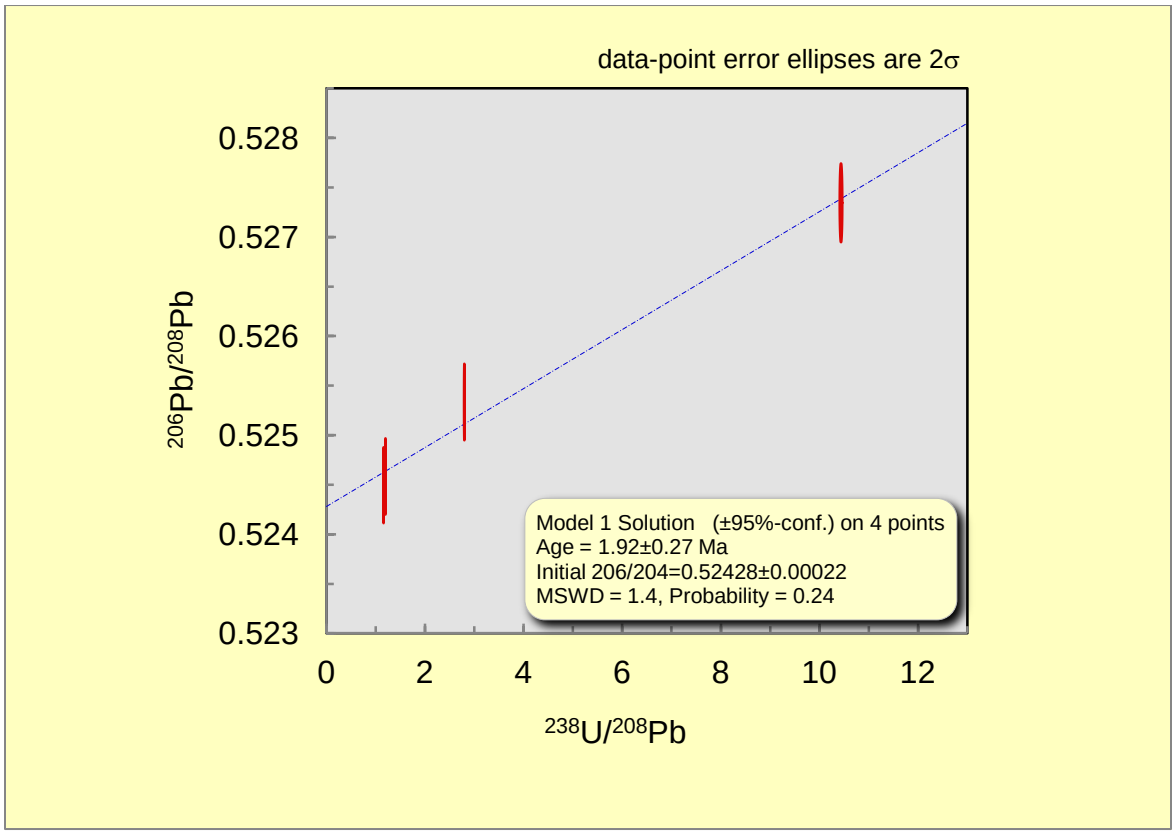
data-point error ellipses are 2σ
0.528
0.527
0.526
0.525
0.524
0.523
$^{206}Pb/^{208}Pb$
0
2
4
6
8
10
12
$^{238}U/^{208}Pb$
Model 1 Solution (±95%-conf.) on 4 points
Age = 1.92±0.27 Ma
Initial 206/204=0.52428±0.00022
MSWD = 1.4, Probability = 0.24

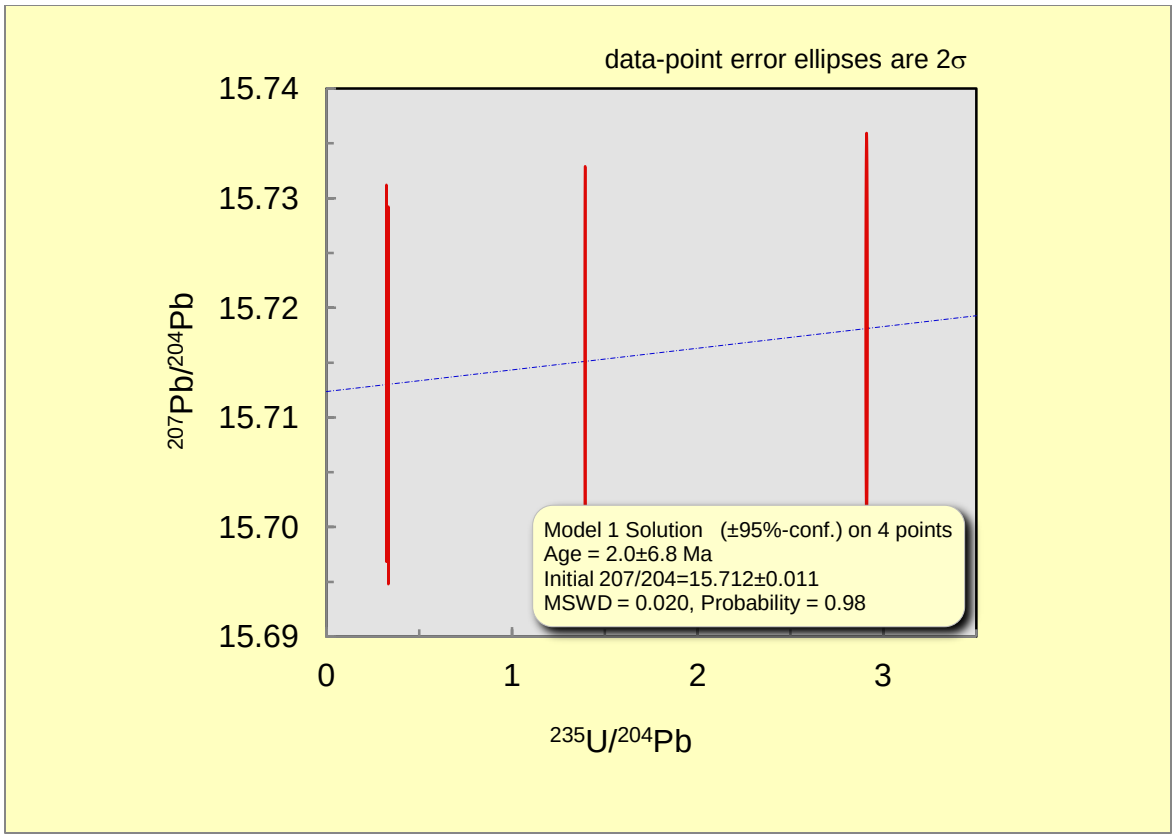
data-point error ellipses are 2σ
15.74
15.73
15.72
15.71
15.70
15.69
207Pb/204Pb
0
1
2
3
235U/204Pb
Model 1 Solution (±95%-conf.) on 4 points
Age = 2.0±6.8 Ma
Initial 207/204=15.712±0.011
MSWD = 0.020, Probability = 0.98

A.3.2 - GUMO

Figure 38: Sample GUMO-00549-001. Calcite spar. Scale bar is in cm. (Photo Credit: Dave Decker).

Cave ID Number: GUMO-GEO-00111
Sample Number: GUMO-00549-001
Collection Date: 3 January, 2012
Collected By: Dave Decker

X-series U (ppm): 0.934
X-series Th (ppm): 0.295
X-series Pb (ppm): 0.065
U/Pb: 14.369

Weight (Kg): 2.05
Size (cm): 20x20x15
Curation Location: University of New Mexico

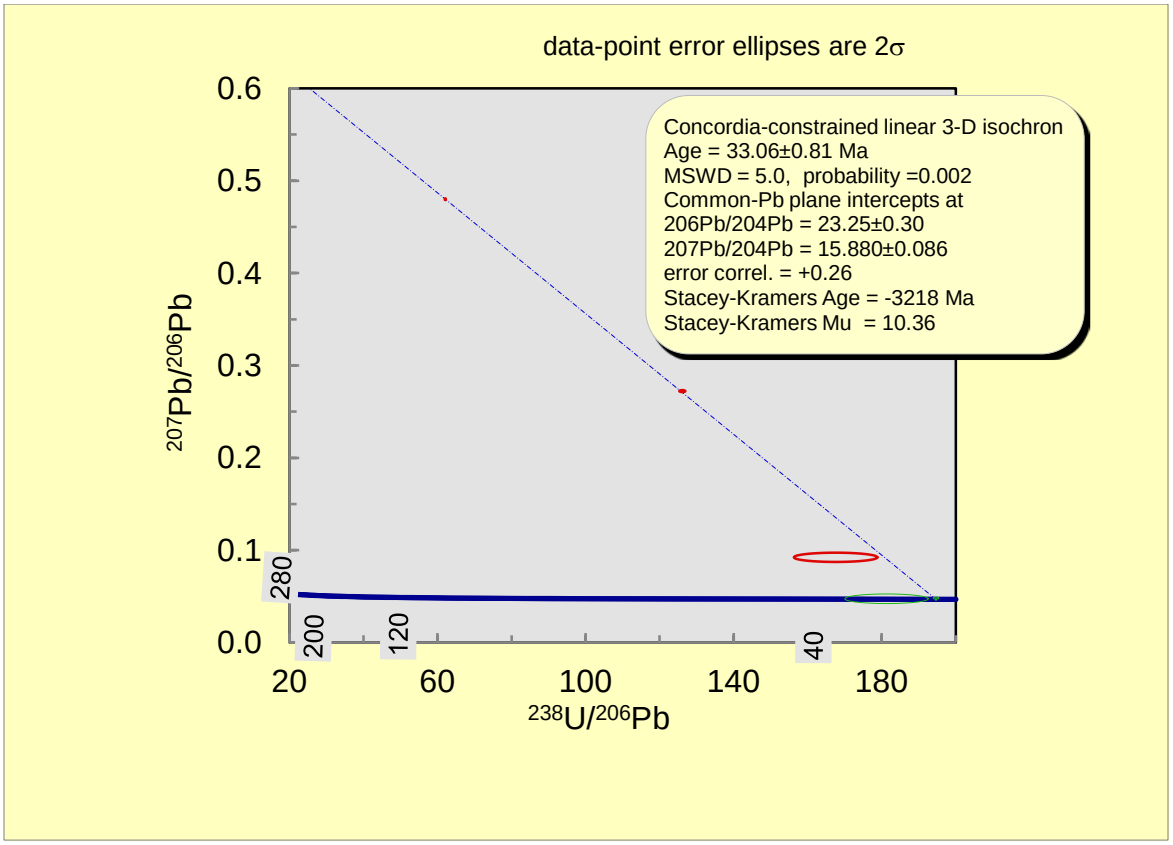

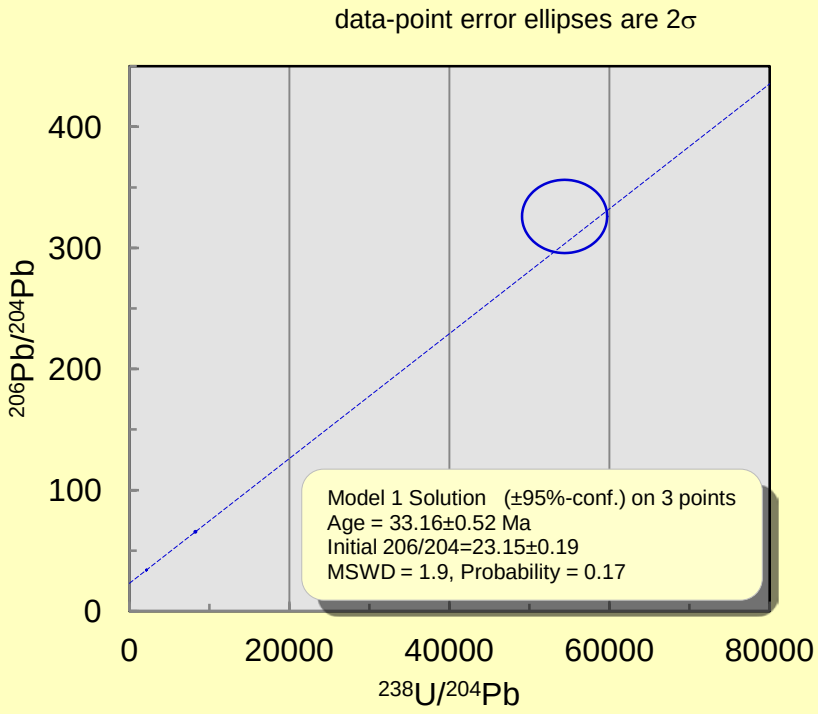

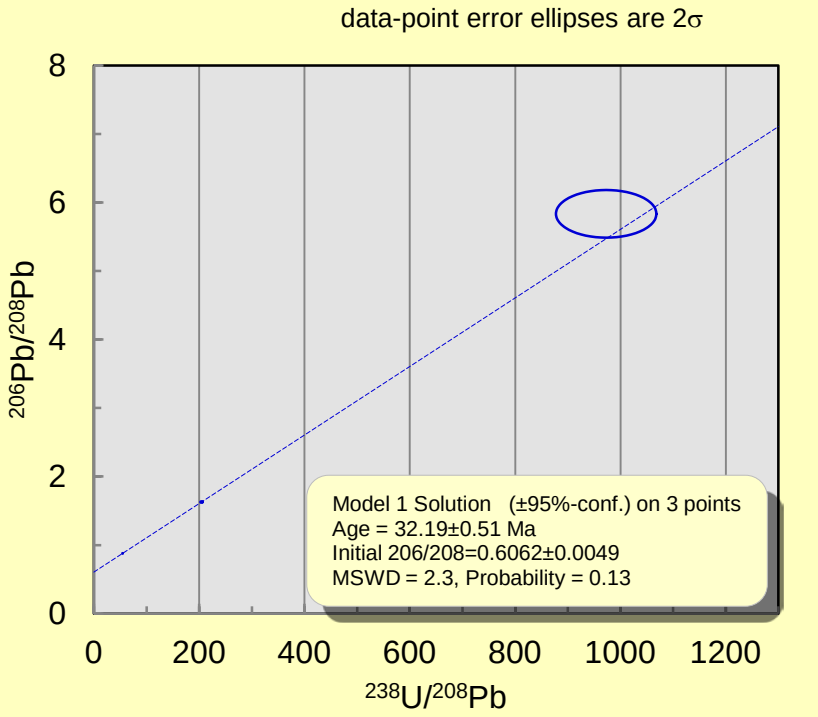

There was too much detrital ^{232}Th in the sample - causing an anomalously young age here.

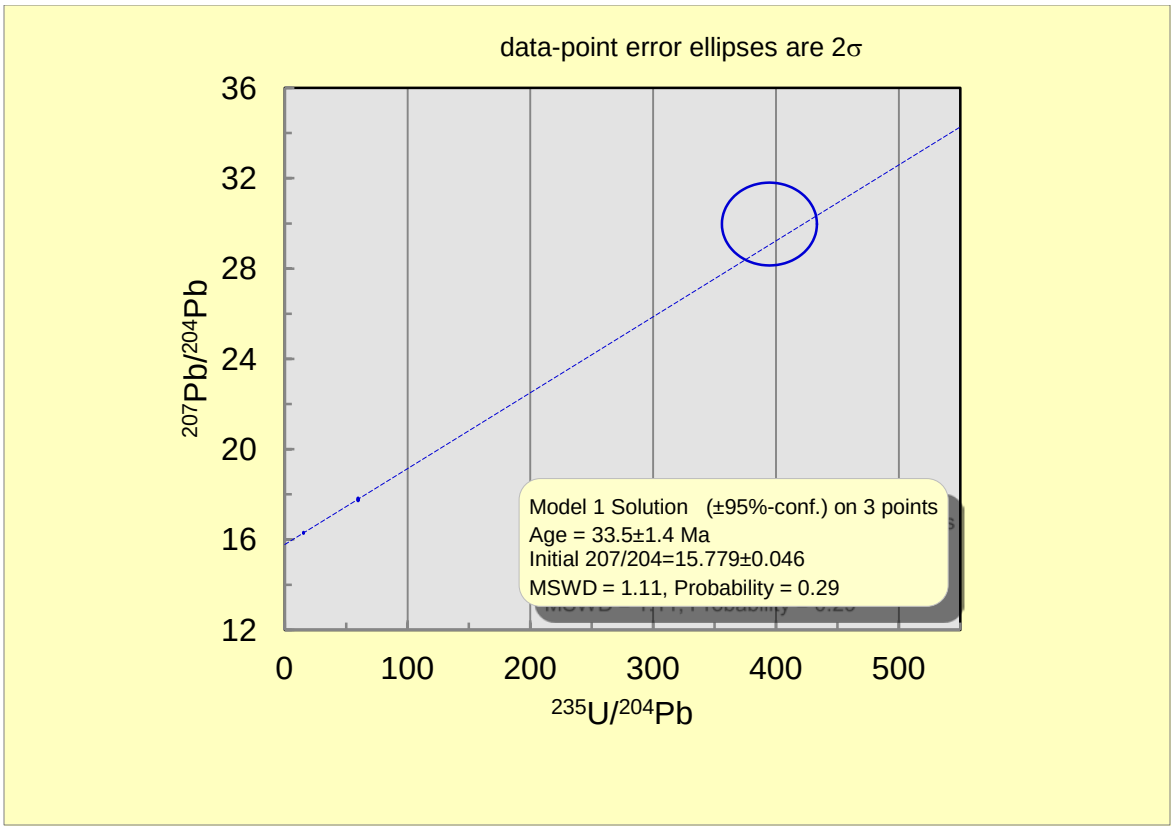
data-point error ellipses are 2σ
36
32
28
24
20
16
12
$^{207}Pb/^{204}Pb$
0
100
200
300
400
500
$^{235}U/^{204}Pb$
Model 1 Solution (±95%-conf.) on 3 points
Age = 33.5±1.4 Ma
Initial 207/204=15.779±0.046
MSWD = 1.11, Probability = 0.29

Figure 39: Sample GUMO-00549-002. Calcite spar. (Photo Credit: Dave Decker).

Cave ID Number: GUMO-GEO-00564
Sample Number: GUMO-00549-002
Collection Date: 9 March, 2012
Collected By: Dave Decker

X-series U (ppm): 3.689
X-series Th (ppm): 0.219
X-series Pb (ppm): 0.088
U/Pb: 41.920

Weight (Kg): 1.270
Size (cm): 15x10x8
Curation Location: University of New Mexico

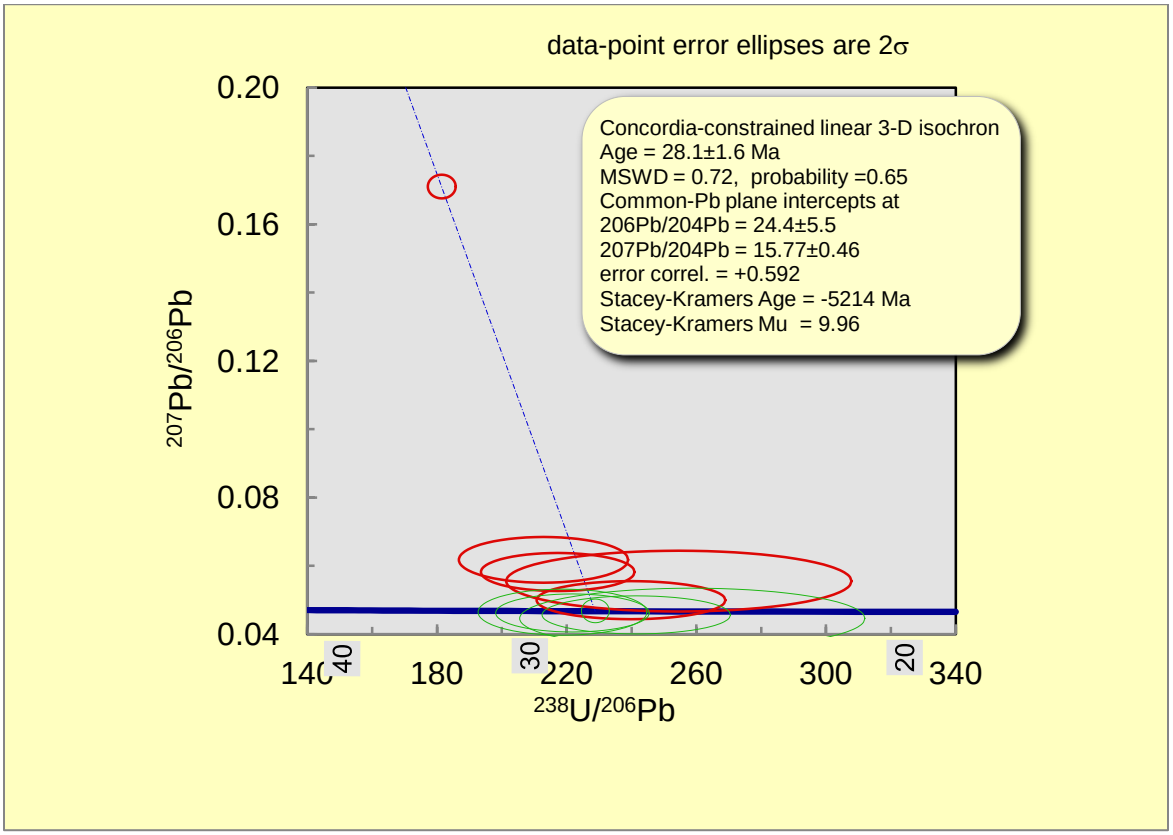

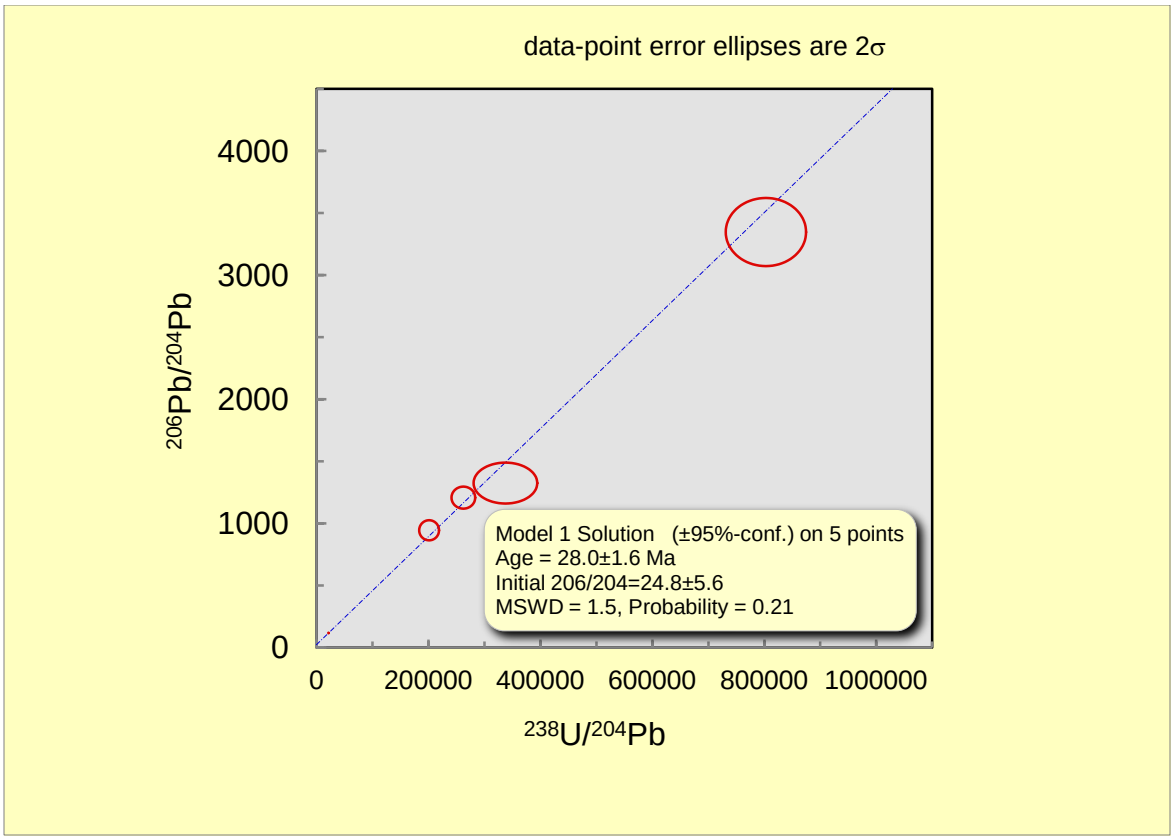
data-point error ellipses are 2σ
4000
3000
2000
1000
0
$^{206}Pb/^{204}Pb$
0
200000
400000
600000
800000
1000000
$^{238}U/^{204}Pb$
Model 1 Solution (±95%-conf.) on 5 points
Age = 28.0±1.6 Ma
Initial 206/204=24.8±5.6
MSWD = 1.5, Probability = 0.21

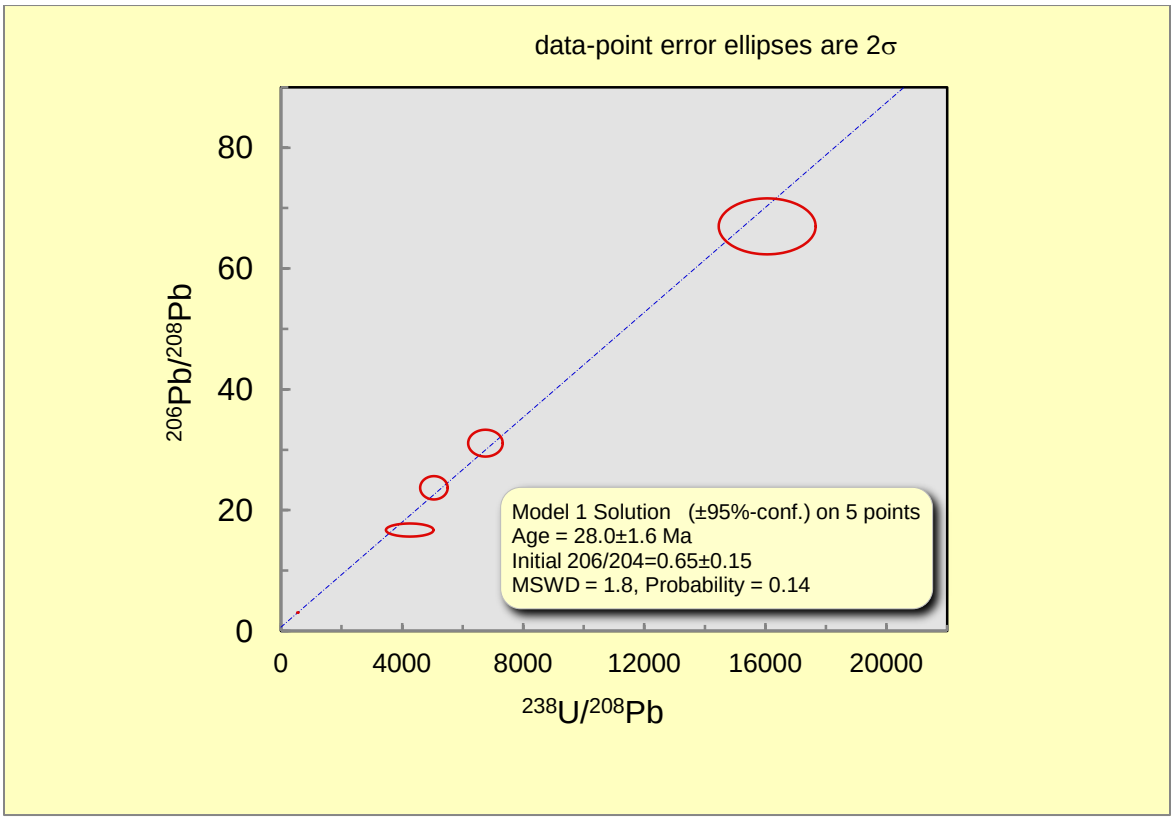
data-point error ellipses are 2σ
80
60
40
20
0
$^{206}Pb/^{208}Pb$
0
4000
8000
12000
16000
20000
$^{238}U/^{208}Pb$
Model 1 Solution (±95%-conf.) on 5 points
Age = 28.0±1.6 Ma
Initial 206/204=0.65±0.15
MSWD = 1.8, Probability = 0.14

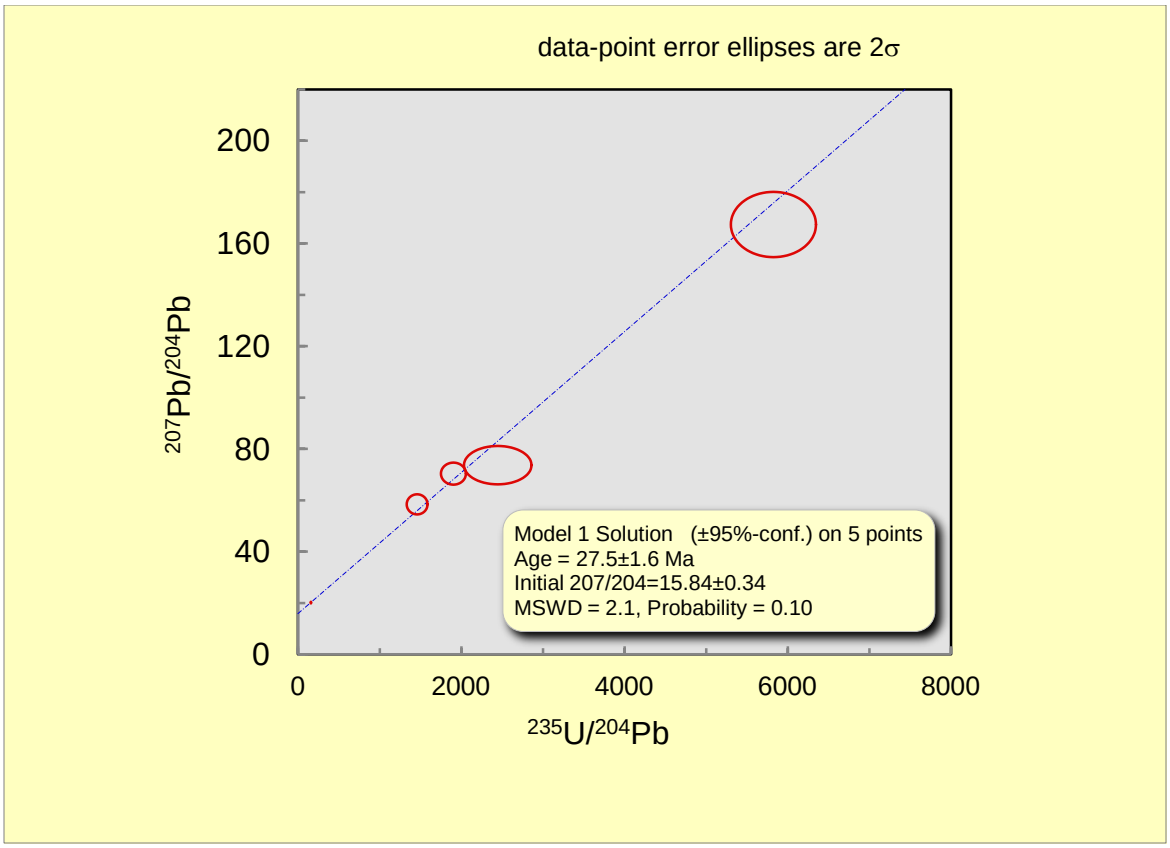
data-point error ellipses are 2σ
200
160
120
80
40
0
$^{207}Pb/^{204}Pb$
0
2000
4000
6000
8000
$^{235}U/^{204}Pb$
Model 1 Solution (±95%-conf.) on 5 points
Age = 27.5±1.6 Ma
Initial 207/204=15.84±0.34
MSWD = 2.1, Probability = 0.10

Figure 40: Sample GUMO-00549-003. Calcite spar. Scale bar in cm. (Photo Credit: Dave Decker).

Cave ID Number: GUMO-GEO-00108
Sample Number: GUMO-00549-003
Collection Date: 9 March, 2012
Collected By: Dave Decker

X-series U (ppm): 2.099
X-series Th (ppm): 0.034
X-series Pb (ppm): 0.062
U/Pb: 33.855

Weight (Kg): 0.625
Size (cm): 11x7x6
Curation Location: University of New Mexico

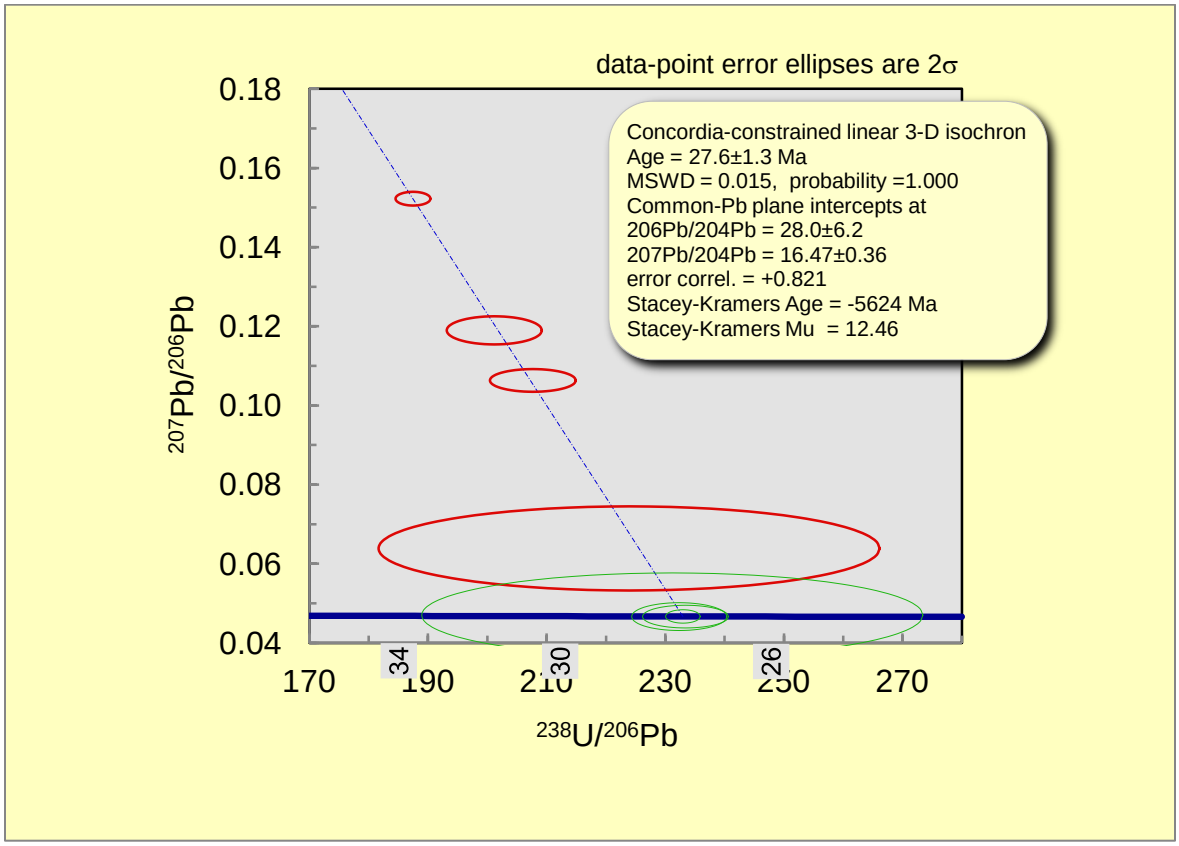

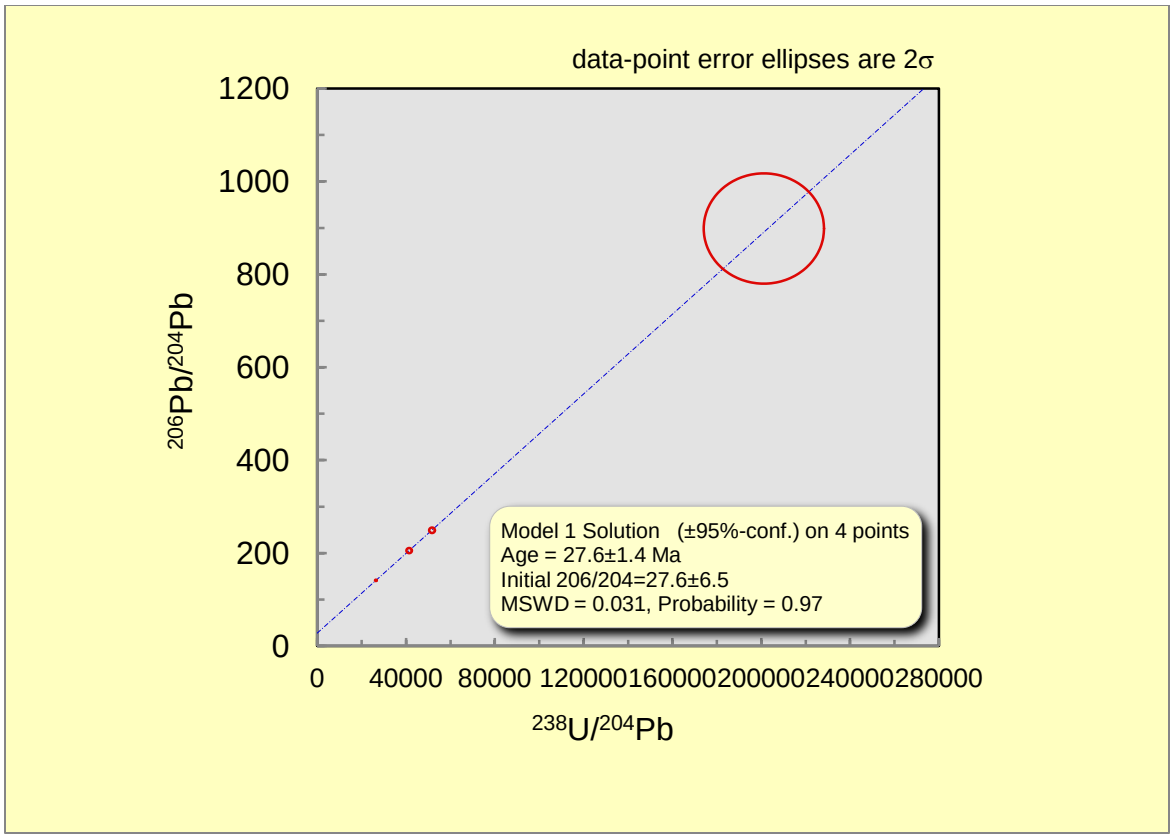
data-point error ellipses are 2σ
1200
1000
800
600
400
200
0
$^{206}Pb/^{204}Pb$
0
40000
80000
120000
160000
200000
240000
280000
$^{238}U/^{204}Pb$
Model 1 Solution (±95%-conf.) on 4 points
Age = 27.6±1.4 Ma
Initial 206/204=27.6±6.5
MSWD = 0.031, Probability = 0.97

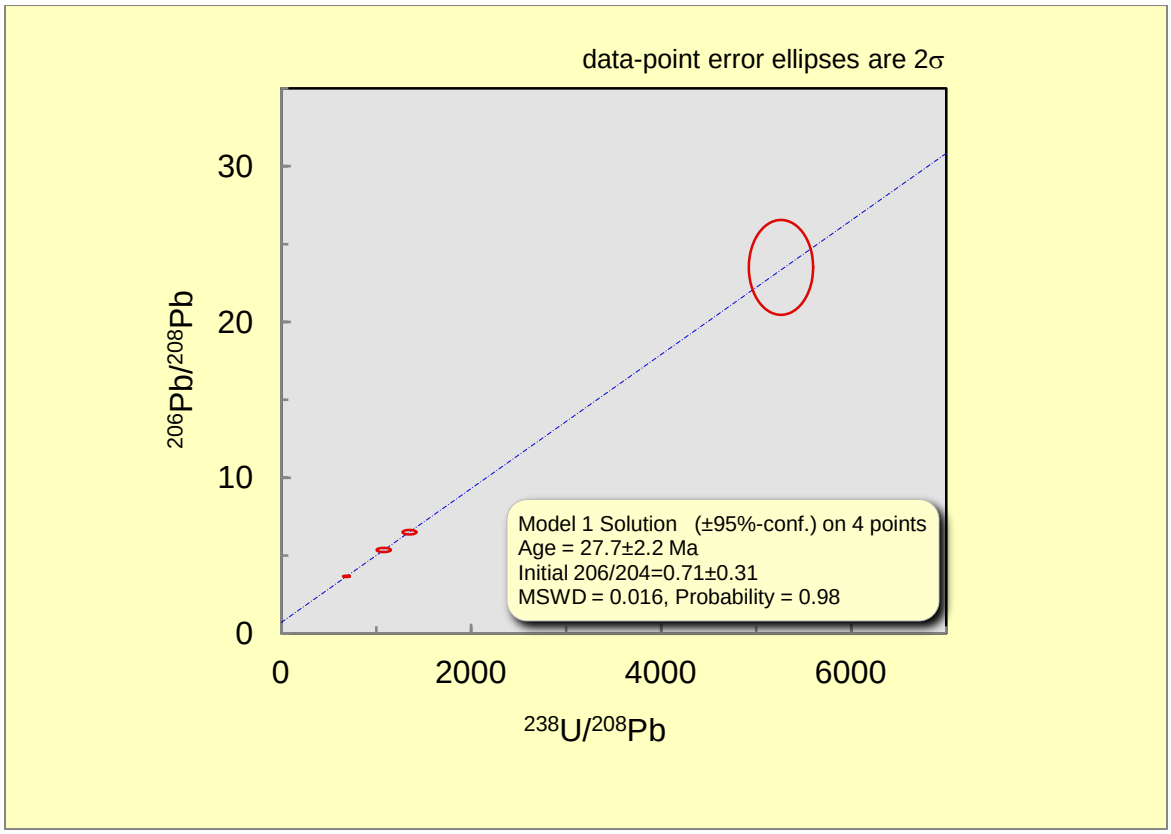
data-point error ellipses are 2σ
30
20
10
0
$^{206}Pb/^{208}Pb$
0
2000
4000
6000
$^{238}U/^{208}Pb$
Model 1 Solution (±95%-conf.) on 4 points
Age = 27.7±2.2 Ma
Initial 206/204=0.71±0.31
MSWD = 0.016, Probability = 0.98

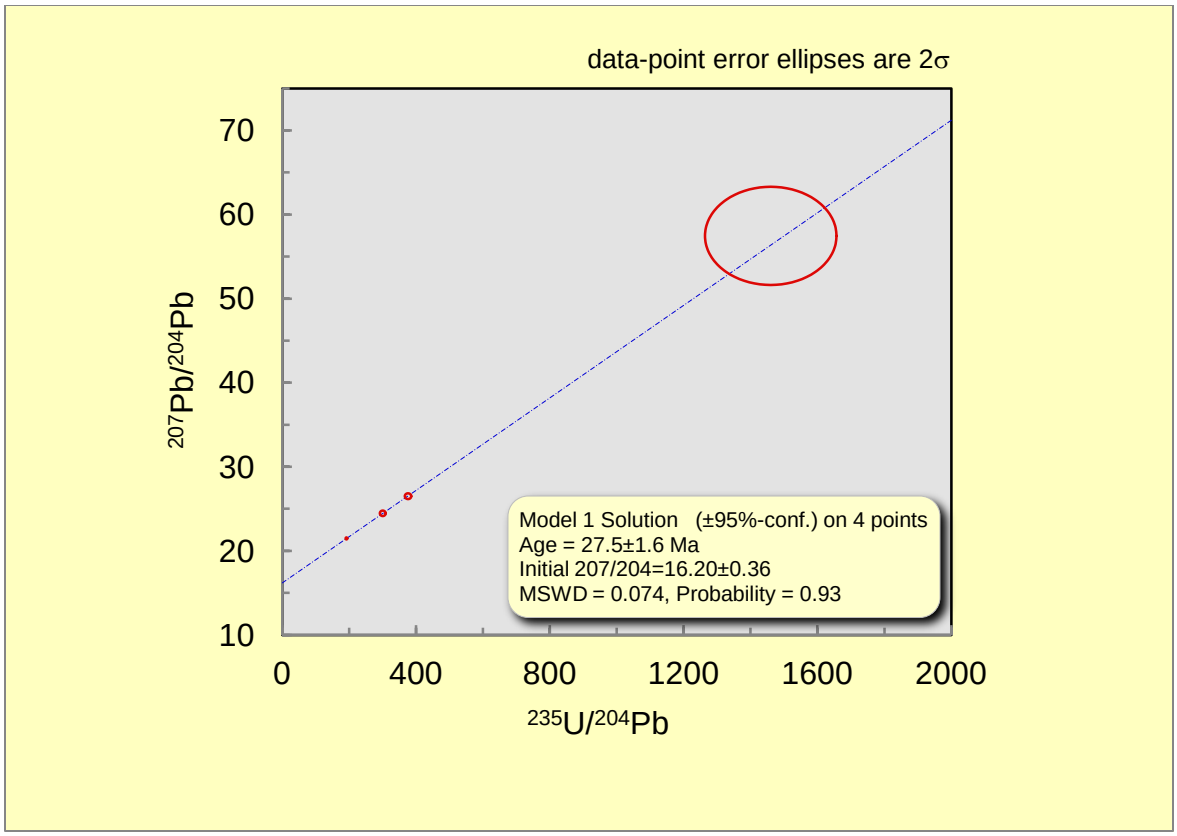
data-point error ellipses are 2σ
70
60
50
40
30
20
10
$^{207}Pb/^{204}Pb$
0
400
800
1200
1600
2000
$^{235}U/^{204}Pb$
Model 1 Solution (±95%-conf.) on 4 points
Age = 27.5±1.6 Ma
Initial 207/204=16.20±0.36
MSWD = 0.074, Probability = 0.93

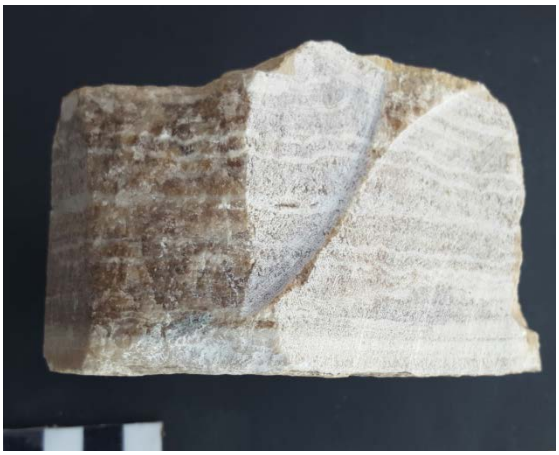

Figure 41: Sample GUPA-00001-001. Vein spar. Scale bar in cm. (Photo Credit: Dave Decker).

Cave ID Number:	Not Applicable
Sample Number:	GUPA-00001-001
Collection Date:	Unknown
Collected By:	Victor Polyak
X-series U (ppm):	0.354
X-series Th (ppm):	0.050
X-series Pb (ppm):	0.022
U/Pb:	16.091
Weight (Kg):	1.120
Size (cm):	13x6.5x8.5
Curation Location:	University of New Mexico

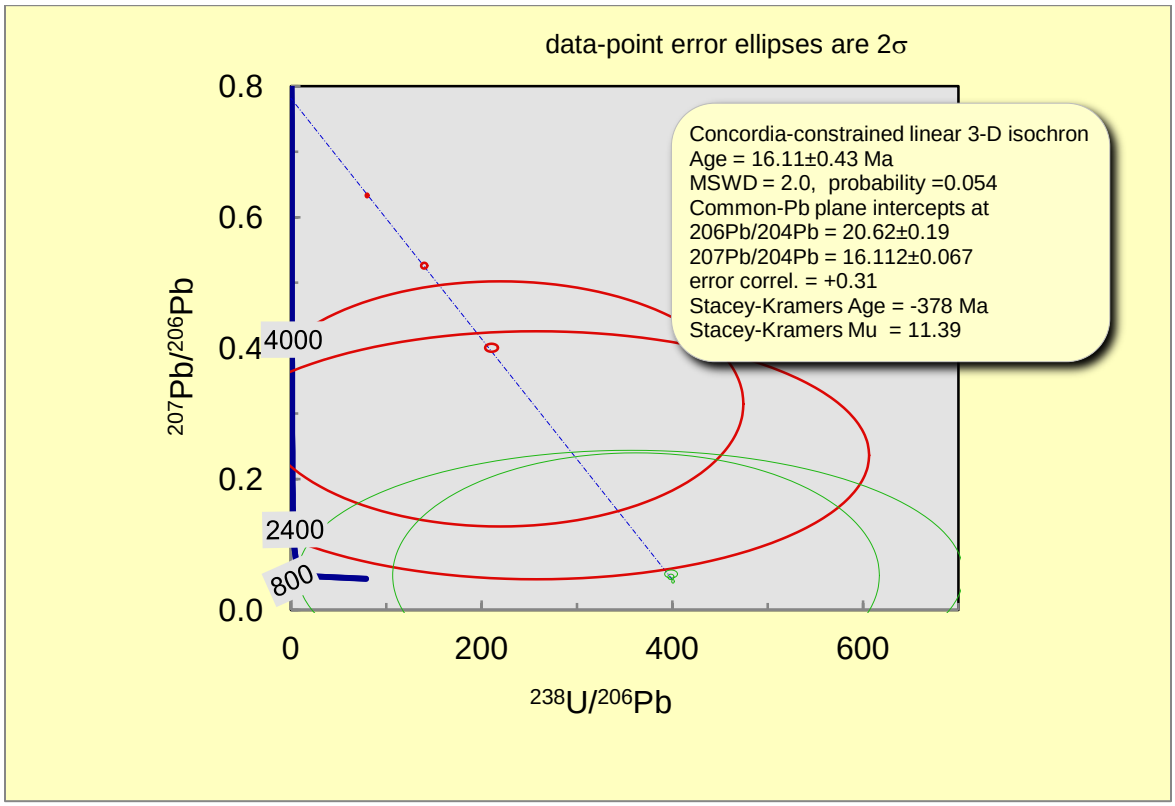

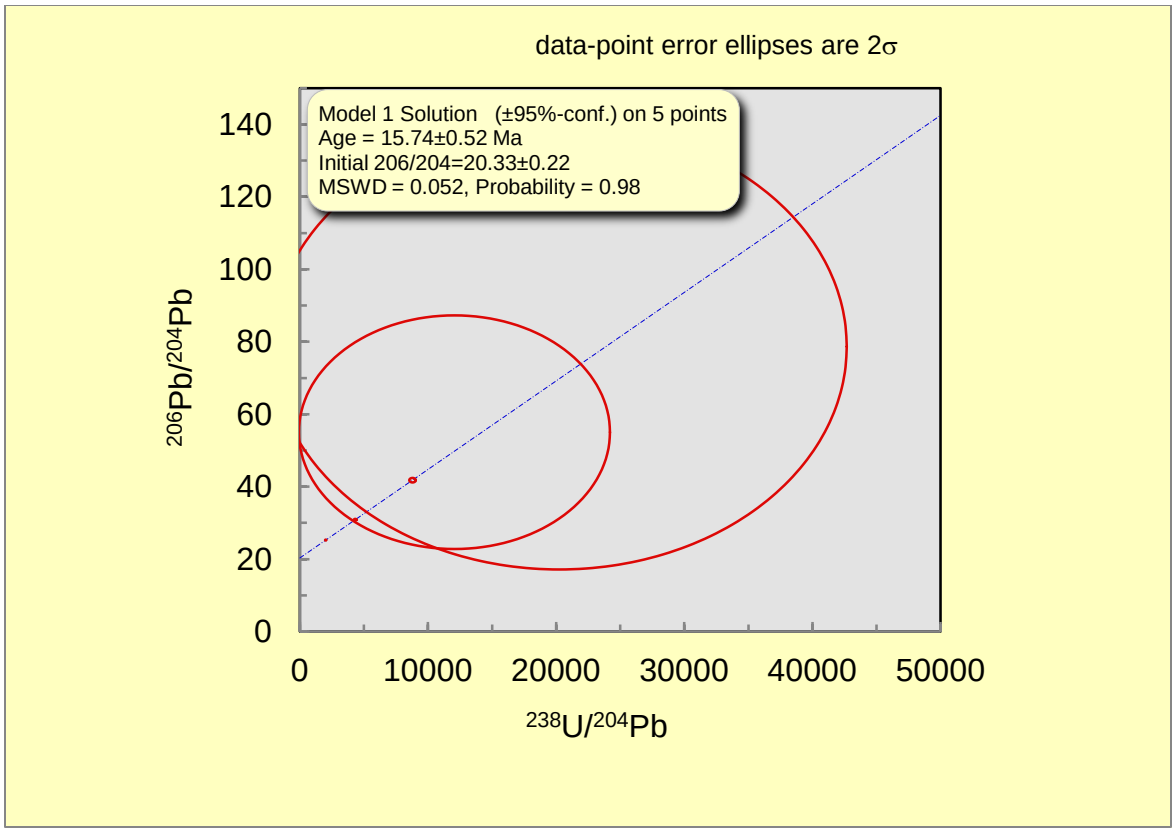
data-point error ellipses are 2σ
Model 1 Solution (±95%-conf.) on 5 points
Age = 15.74±0.52 Ma
Initial 206/204=20.33±0.22
MSWD = 0.052, Probability = 0.98
140
120
100
80
60
40
20
0
0
10000
20000
30000
40000
50000
206Pb/204Pb
238U/204Pb

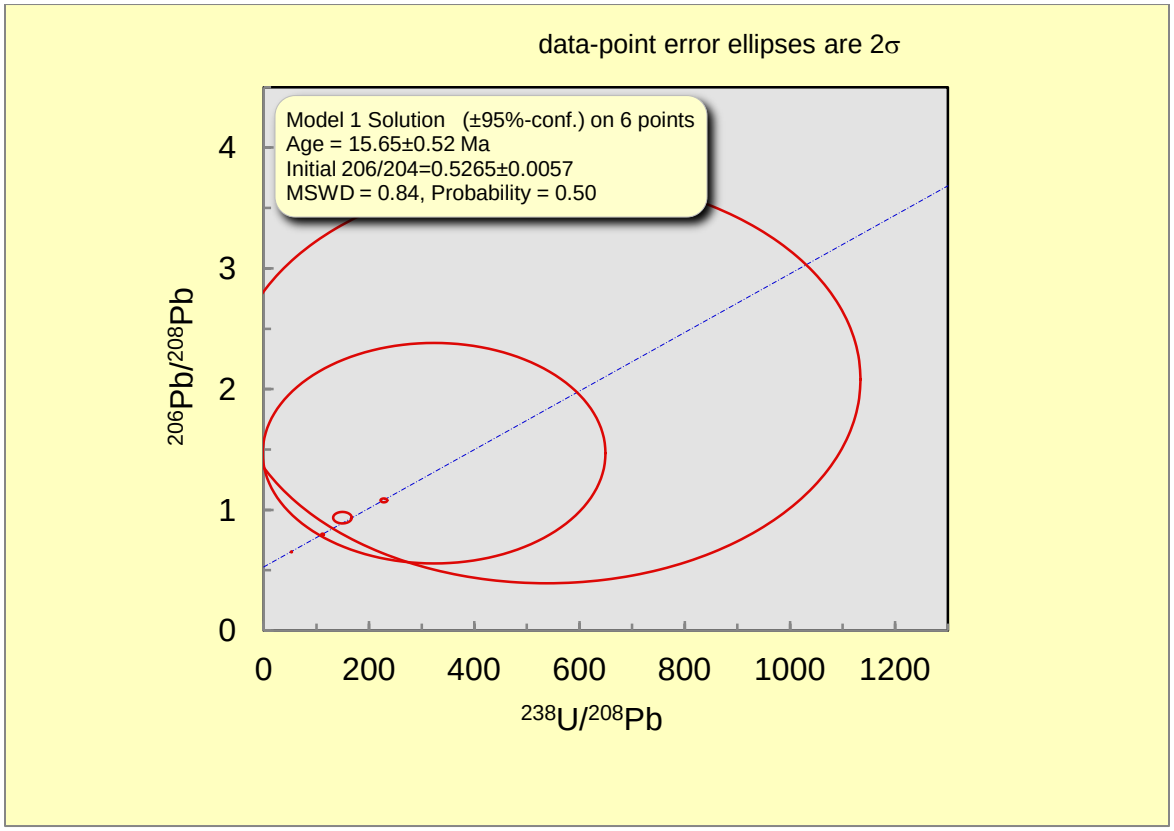
data-point error ellipses are 2σ
Model 1 Solution (±95%-conf.) on 6 points
Age = 15.65±0.52 Ma
Initial 206/204=0.5265±0.0057
MSWD = 0.84, Probability = 0.50
4
3
2
1
0
0
200
400
600
800
1000
1200
206Pb/208Pb
238U/208Pb

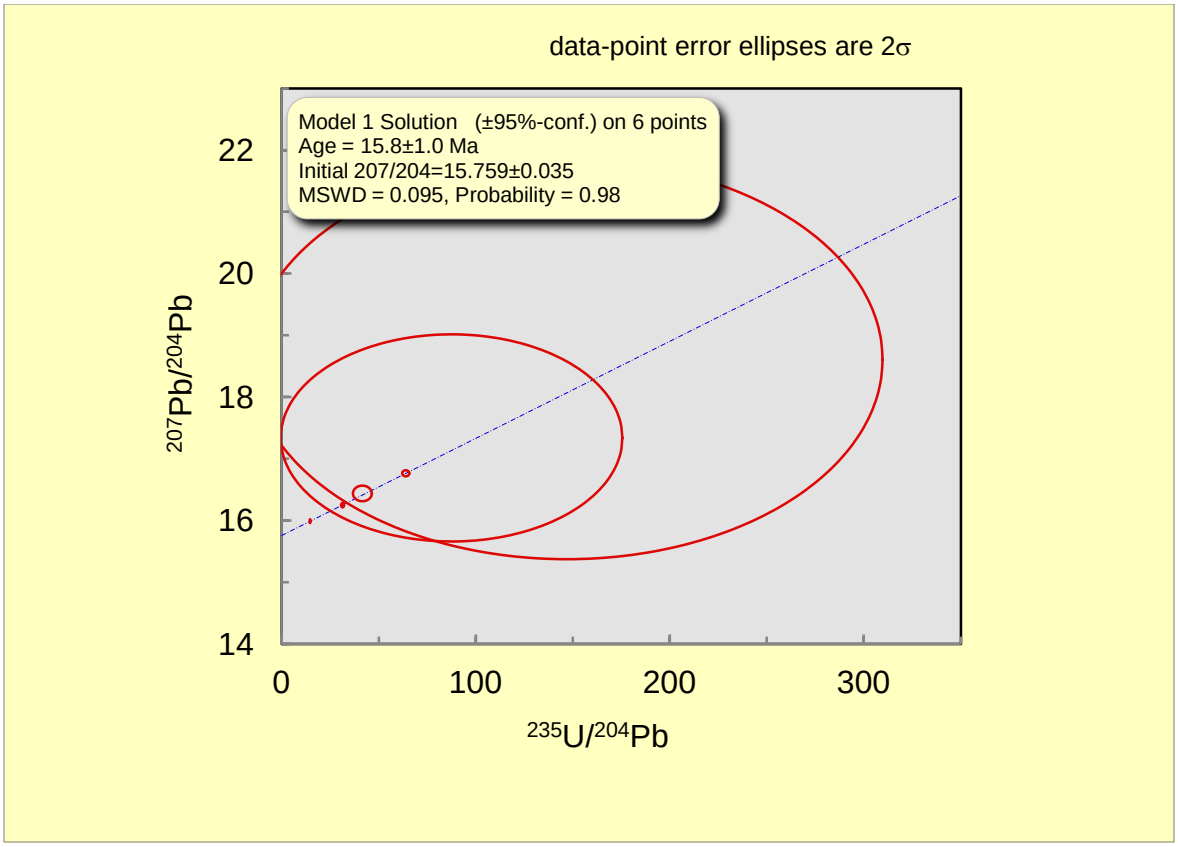
data-point error ellipses are 2σ
Model 1 Solution (±95%-conf.) on 6 points
Age = 15.8±1.0 Ma
Initial 207/204=15.759±0.035
MSWD = 0.095, Probability = 0.98
22
20
18
16
14
0
100
200
300
207Pb/204Pb
235U/204Pb

A.3.3 - BLMC

Figure 42: Sample BLMC-20122-001. Calcite spar. Scale bar is in cm. (Photo Credit: Dave Decker).

Cave ID Number: BLM-NM-060-0021
Sample Number: BLMC-20122-001
Collection Date: 18 November 2011
Collected By: Jim Goodbar

X-series U (ppm): 0.823
X-series Th (ppm): 1.289
X-series Pb (ppm): 0.046
U/Pb: 17.891

Weight (Kg): 0.029
Size (cm): 4x4x3
Curation Location: University of New Mexico

Figure 43: Sample BLMC-20122-003. Calcite spar. Scale bar is in cm. (Photo Credit: Dave Decker).

Cave ID Number: BLM-NM-060-0021
Sample Number: BLMC-20122-003
Collection Date: 18 November, 2011
Collected By: Jim Goodbar

X-series U (ppm): 0.472
X-series Th (ppm): 0.427
X-series Pb (ppm): 0.030
U/Pb: 15.733

Weight (Kg): 0.016
Size (cm): 2x2x3
Curation Location: University of New Mexico

Figure 44: Sample BLMC-20122-004. Calcite spar. Scale bar is in cm. (Photo Credit: Dave Decker).

Cave ID Number: BLM-NM-060-0030
Sample Number: BLMC-20122-004
Collection Date: 18 July, 2012
Collected By: Dave Decker

X-series U (ppm): 0.290
X-series Th (ppm): 0.071
X-series Pb (ppm): 3.105
U/Pb: 0.093

Weight (Kg): 0.020
Size (cm): 3x3x2 before fragmentation
Curation Location: University of New Mexico

Figure 45: Sample BLMC-20122-012. Calcite spar. Scale bar is in cm. (Photo Credit: Dave Decker).

Cave ID Number: BLM-NM-060-0027
Sample Number: BLMC-20122-012
Collection Date: 12 March, 2013
Collected By: Dave Decker

X-series U (ppm): 43.970
X-series Th (ppm): 6.819
X-series Pb (ppm): 30.480
U/Pb: 1.443

Weight (Kg): 2.60
Size (cm): 10x15x15
Curation Location: University of New Mexico

Figure 46: Sample BLMC-20122-002. Calcite spar. Scale bar is in cm. (Photo Credit: Dave Decker).

Cave ID Number:	BLM-NM-060-0021
Sample Number:	BLMC-20122-002
Collection Date:	18 November 2011
Collected By:	Jim Goodbar
X-series U (ppm):	0.838
X-series Th (ppm):	0.147
X-series Pb (ppm):	0.031
U/Pb:	27.032
Weight (Kg):	0.022
Size (cm):	3x2x2
Curation Location:	University of New Mexico

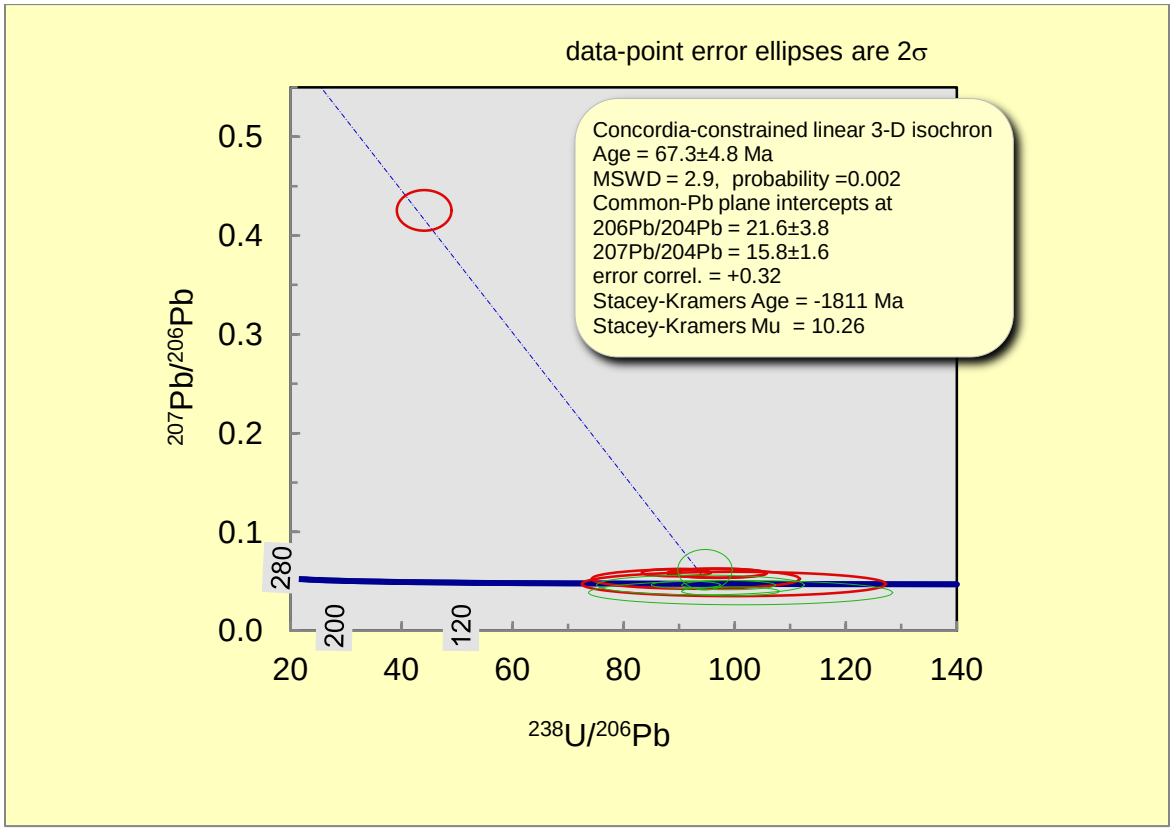

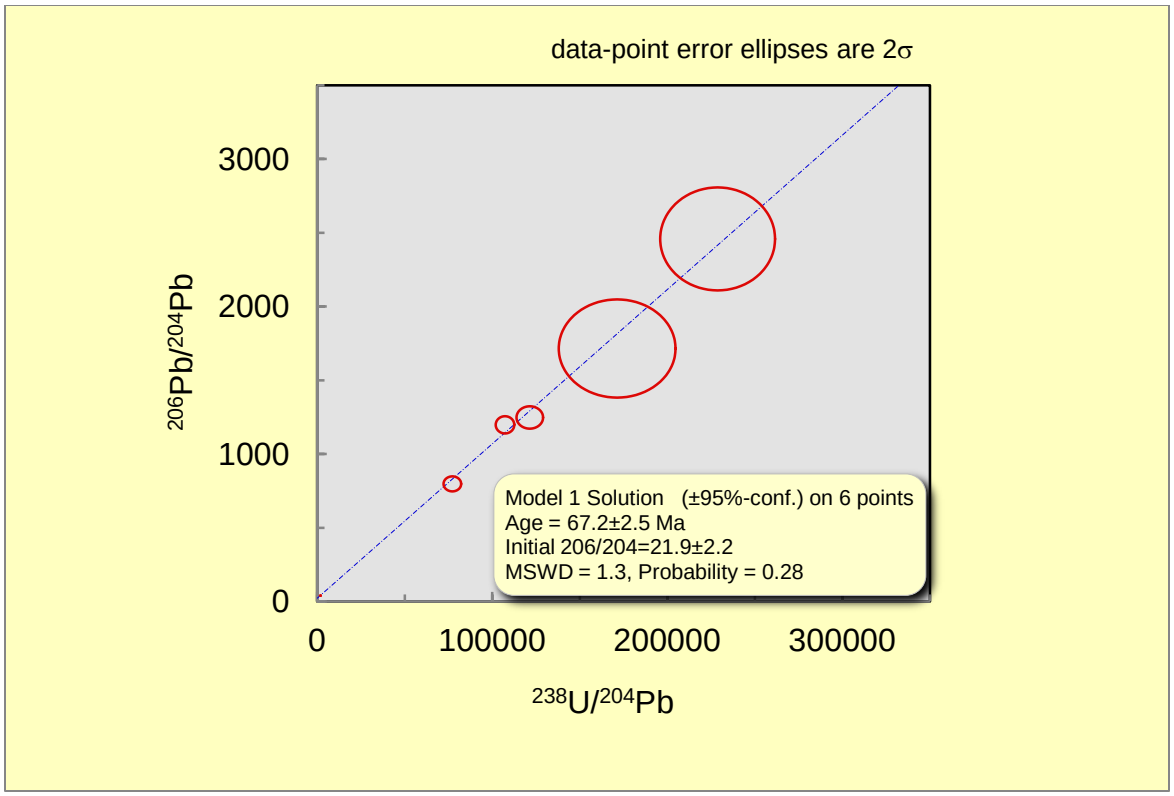
data-point error ellipses are 2σ
3000
2000
1000
0
$^{206}Pb/^{204}Pb$
0
100000
200000
300000
$^{238}U/^{204}Pb$
Model 1 Solution (±95%-conf.) on 6 points
Age = 67.2±2.5 Ma
Initial 206/204=21.9±2.2
MSWD = 1.3, Probability = 0.28

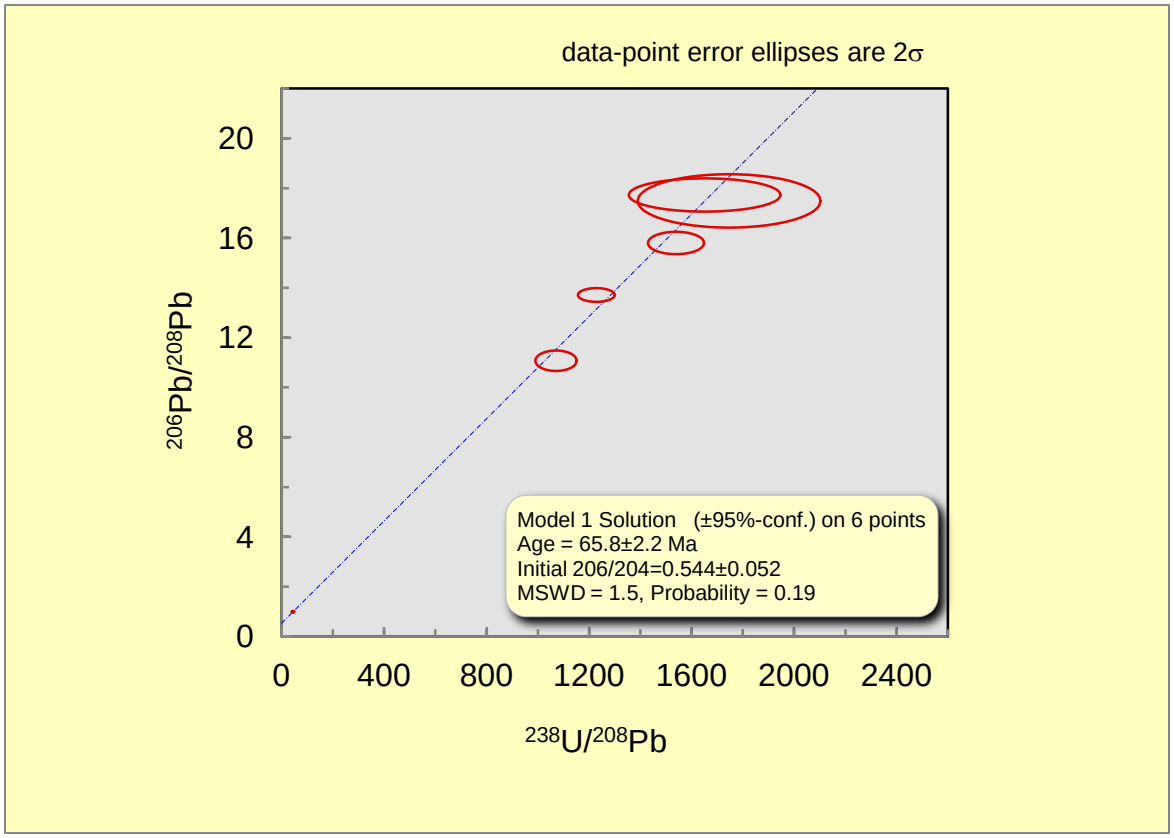
data-point error ellipses are 2σ
20
16
12
8
4
0
$^{206}Pb/^{208}Pb$
0
400
800
1200
1600
2000
2400
$^{238}U/^{208}Pb$
Model 1 Solution (±95%-conf.) on 6 points
Age = 65.8±2.2 Ma
Initial 206/204=0.544±0.052
MSWD = 1.5, Probability = 0.19

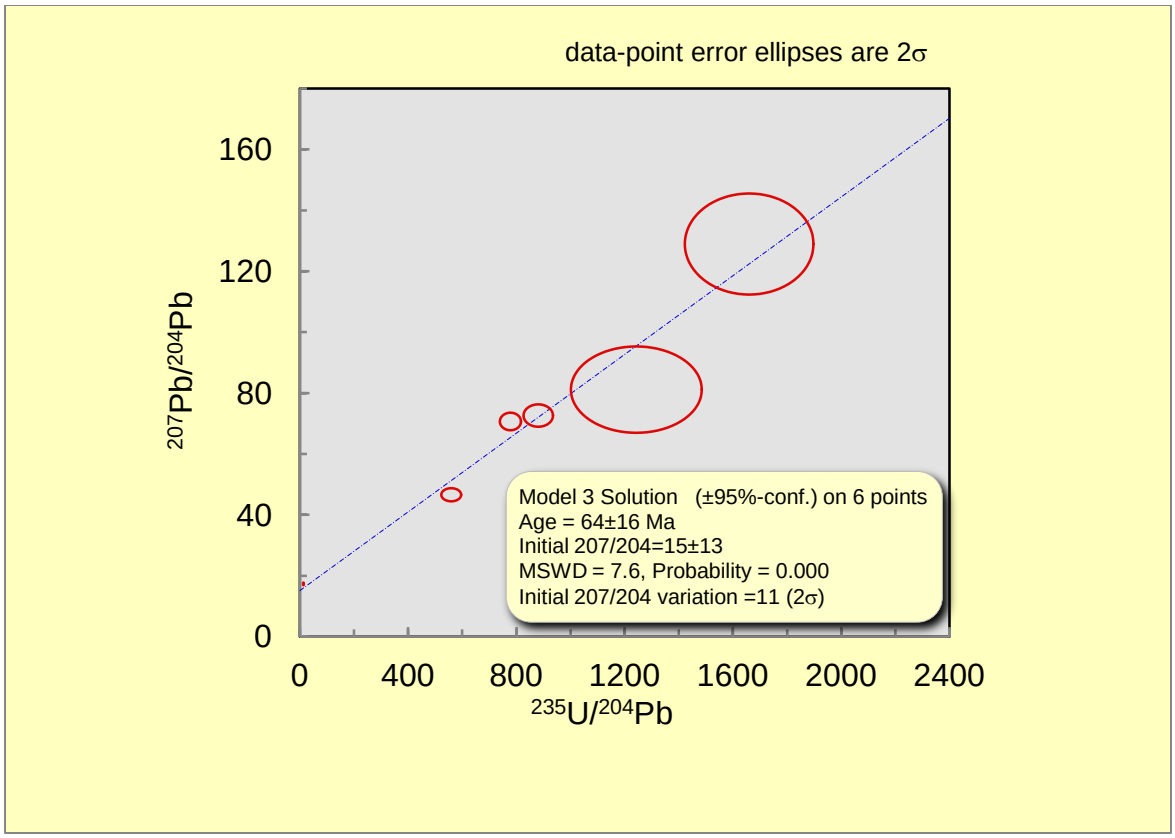
data-point error ellipses are 2σ
160
120
80
40
0
$^{207}Pb/^{204}Pb$
0
400
800
1200
1600
2000
2400
$^{235}U/^{204}Pb$
Model 3 Solution (±95%-conf.) on 6 points
Age = 64±16 Ma
Initial 207/204=15±13
MSWD = 7.6, Probability = 0.000
Initial 207/204 variation =11 (2σ)

Figure 47: Sample BLMC-20122-005. Calcite spar. Scale bar is in cm. Inset is a backlit close-up of petroleum inclusions in the largest fragment. (Photo Credit: Dave Decker).

Cave ID Number: BLM-NM-060-0030
Sample Number: BLMC-20122-005
Collection Date: 18 July, 2012
Collected By: Dave Decker

X-series U (ppm): 0.815
X-series Th (ppm): 0.021
X-series Pb (ppm): 0.009
U/Pb: 90.556

Weight (Kg): 0.025
Size (cm): 4x3x3 before fragmentation
Curation Location: University of New Mexico

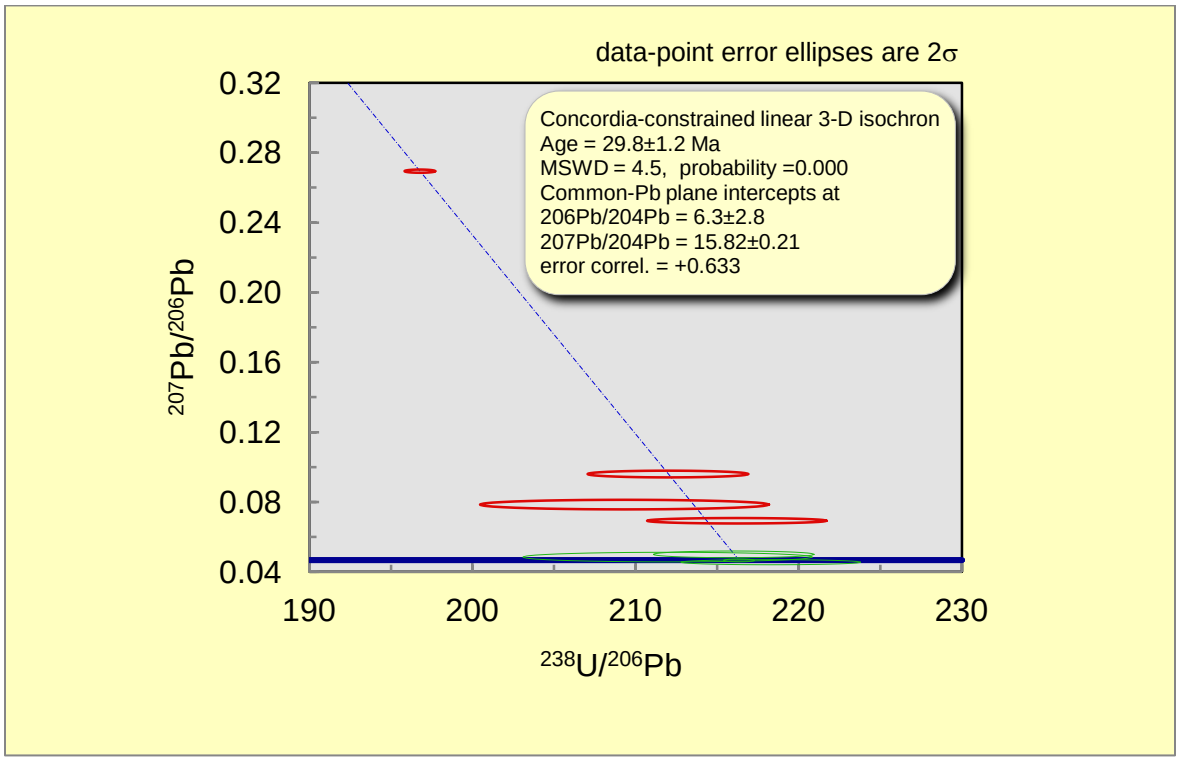

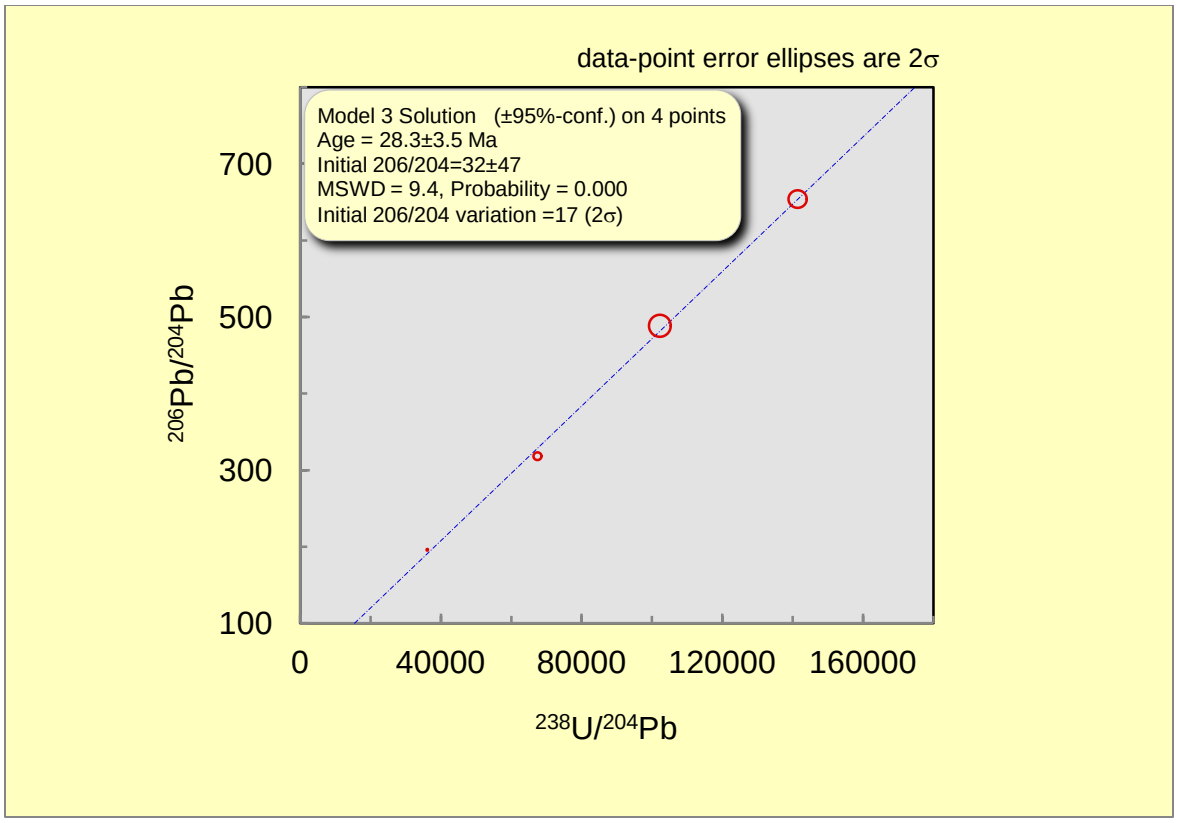
data-point error ellipses are 2σ
Model 3 Solution (±95%-conf.) on 4 points
Age = 28.3±3.5 Ma
Initial 206/204=32±47
MSWD = 9.4, Probability = 0.000
Initial 206/204 variation =17 (2σ)
700
500
300
100
0
40000
80000
120000
160000
206Pb/204Pb
238U/204Pb

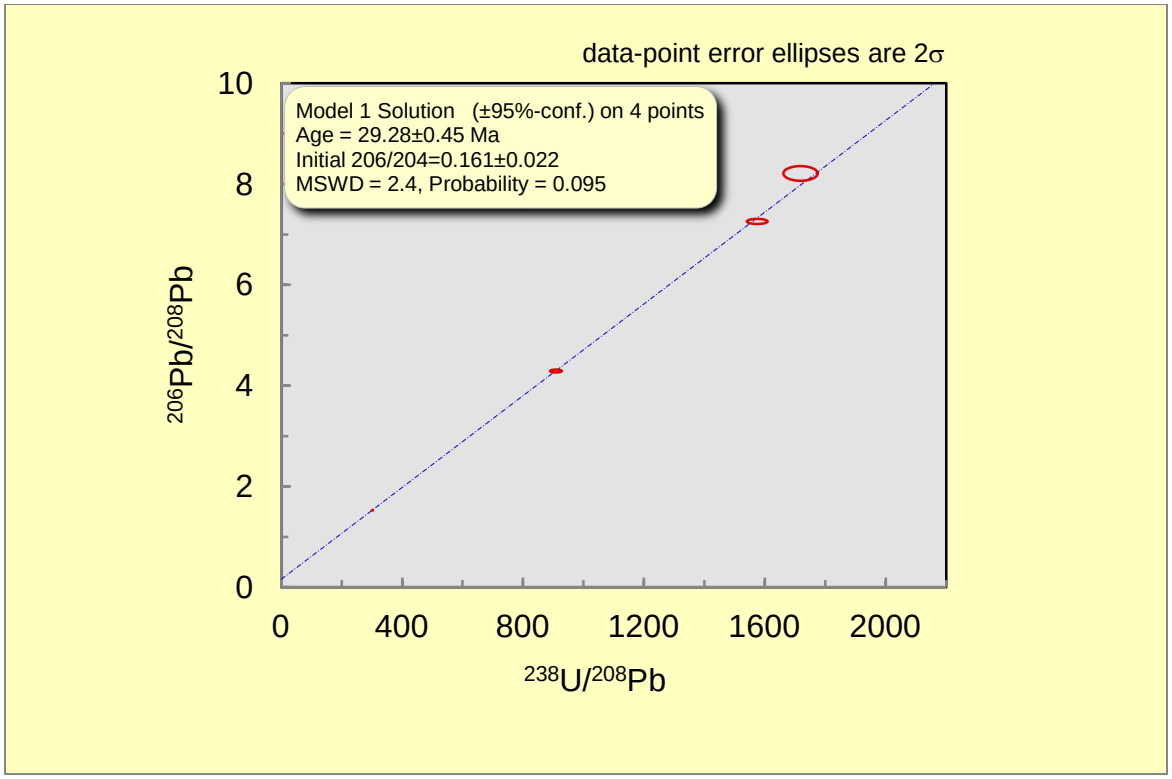
data-point error ellipses are 2σ
Model 1 Solution (±95%-conf.) on 4 points
Age = 29.28±0.45 Ma
Initial 206/204=0.161±0.022
MSWD = 2.4, Probability = 0.095
10
8
6
4
2
0
0
400
800
1200
1600
2000
206Pb/208Pb
238U/208Pb

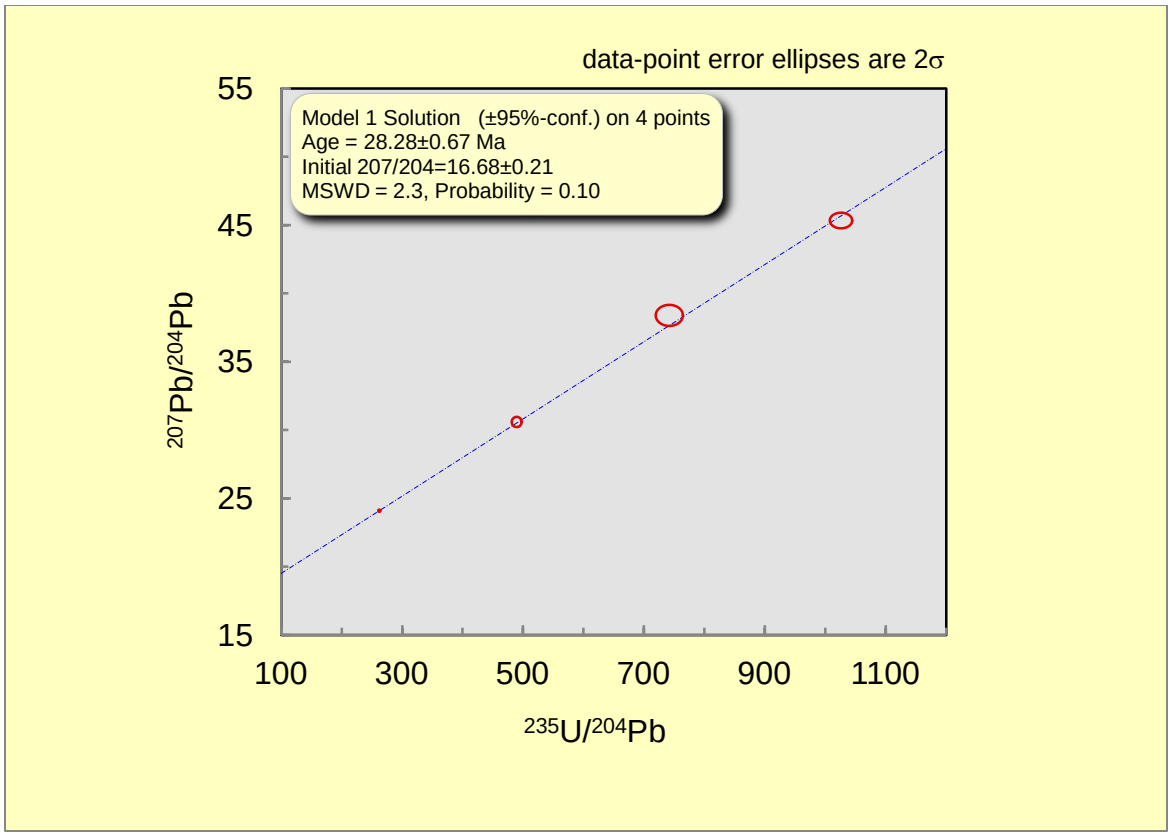
data-point error ellipses are 2σ
Model 1 Solution (±95%-conf.) on 4 points
Age = 28.28±0.67 Ma
Initial 207/204=16.68±0.21
MSWD = 2.3, Probability = 0.10
55
45
35
25
15
100
300
500
700
900
1100
207Pb/204Pb
235U/204Pb

Figure 48: Sample BLMC-20122-011. Calcite spar. Scale bar is in cm. (Photo Credit: Dave Decker).

Cave ID Number: BLM-NM-060-0027
Sample Number: BLMC-20122-011
Collection Date: 12 March, 2013
Collected By: Dave Decker

X-series U (ppm): 15.760
X-series Th (ppm): 0.607
X-series Pb (ppm): 0.197
U/Pb: 80.000

Weight (Kg): 1.00
Size (cm): 6x10x13
Curation Location: University of New Mexico

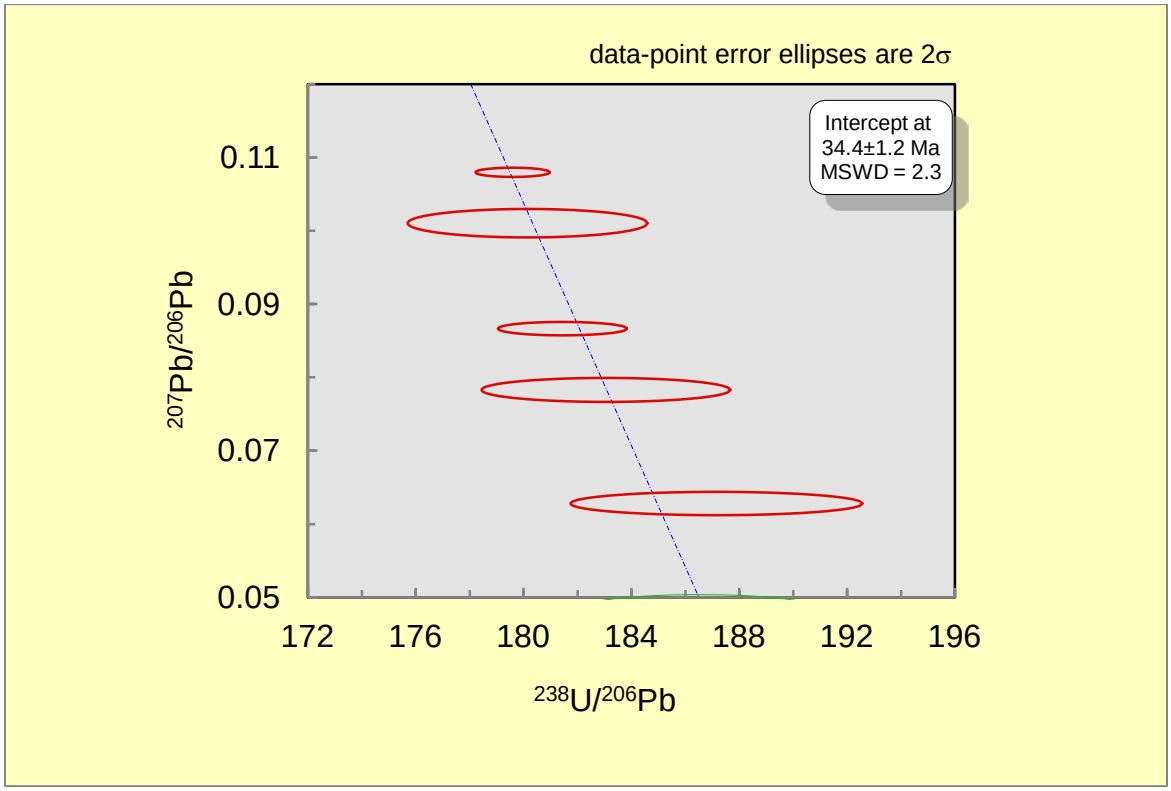

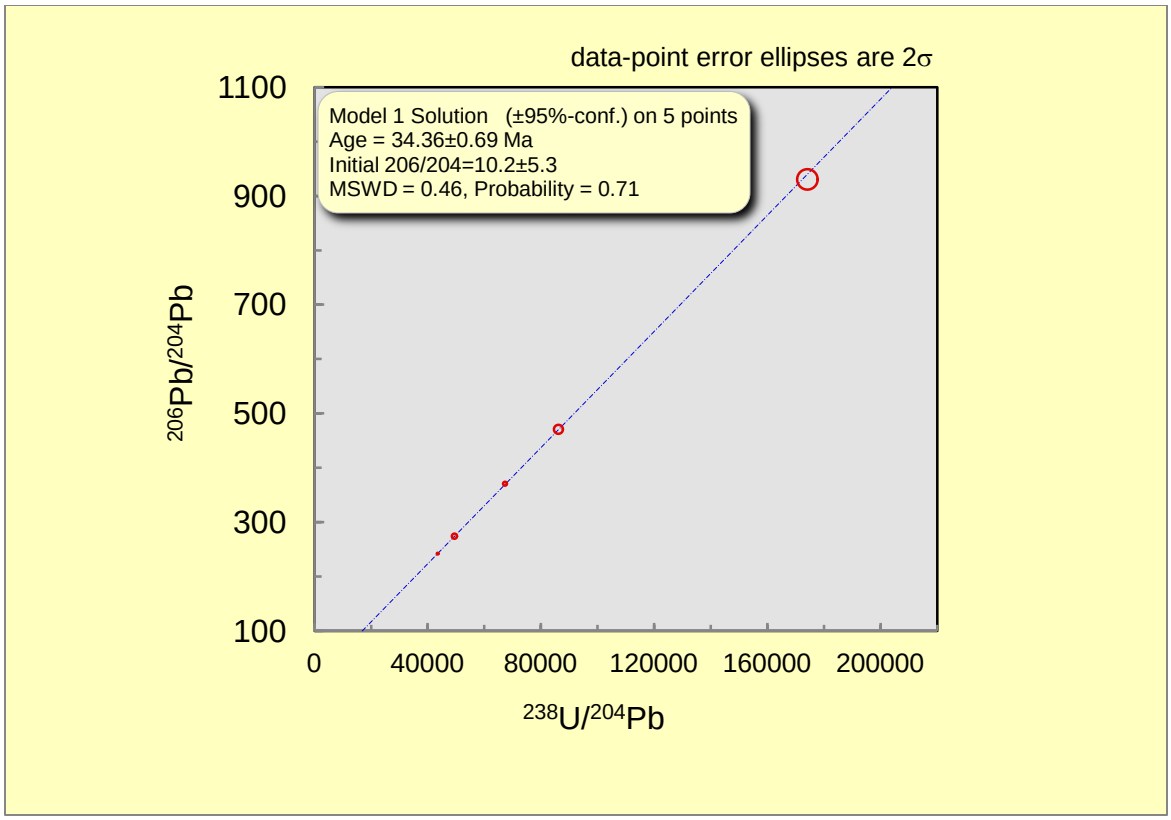
data-point error ellipses are 2σ
Model 1 Solution (±95%-conf.) on 5 points
Age = 34.36±0.69 Ma
Initial 206/204=10.2±5.3
MSWD = 0.46, Probability = 0.71
1100
900
700
500
300
100
0
40000
80000
120000
160000
200000
206Pb/204Pb
238U/204Pb

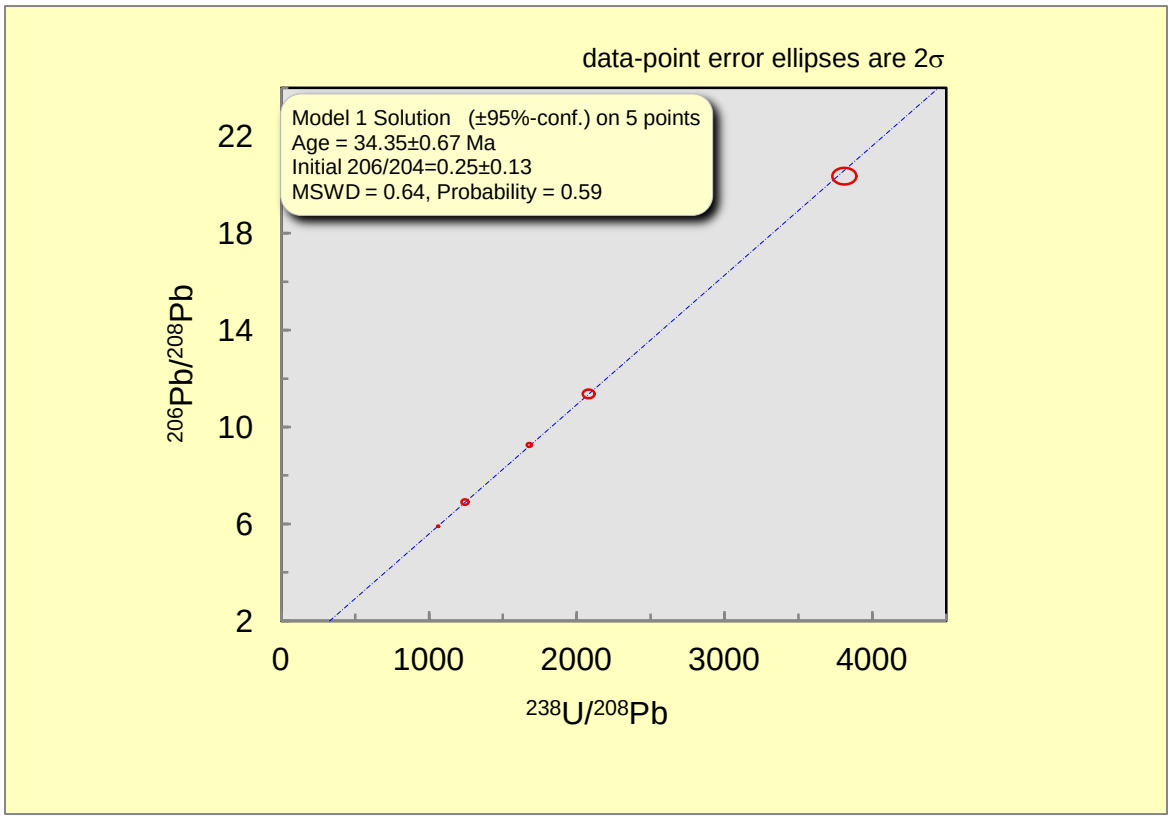
data-point error ellipses are 2σ
Model 1 Solution (±95%-conf.) on 5 points
Age = 34.35±0.67 Ma
Initial 206/204=0.25±0.13
MSWD = 0.64, Probability = 0.59
22
18
14
10
6
2
0
1000
2000
3000
4000
206Pb/208Pb
238U/208Pb

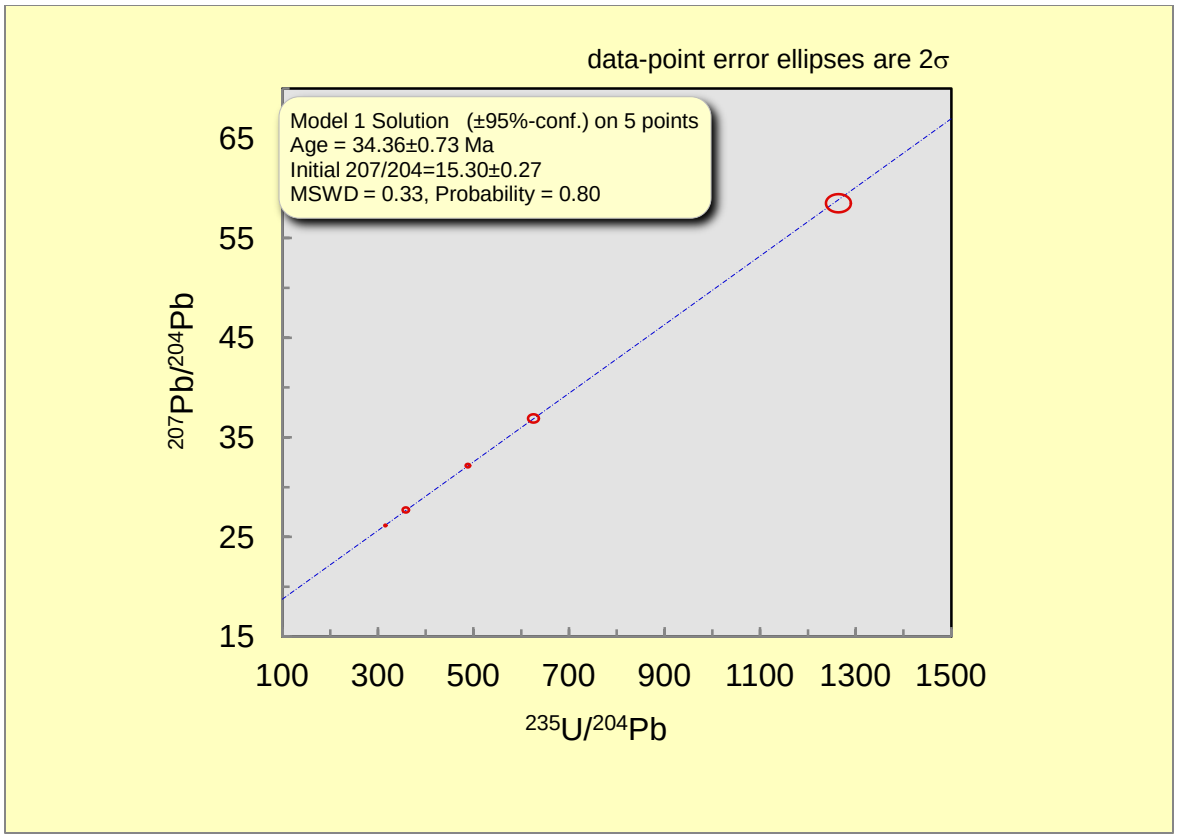
data-point error ellipses are 2σ
Model 1 Solution (±95%-conf.) on 5 points
Age = 34.36±0.73 Ma
Initial 207/204=15.30±0.27
MSWD = 0.33, Probability = 0.80
65
55
45
35
25
15
100
300
500
700
900
1100
1300
1500
207Pb/204Pb
235U/204Pb

A.3.4 - USFS

Figure 49: Sample USFS-11290-001. Calcite spar. Scale bar is in cm. (Photo Credit: Dave Decker).

Cave ID Number: FSGD-C-90
Sample Number: USFS-11290-001
Collection Date: 5 January, 2012
Collected By: Dave Decker

X-series U (ppm): 0.431
X-series Th (ppm): 0.160
X-series Pb (ppm): 0.053
U/Pb: 8.132

Weight (Kg): 0.205
Size (cm): 8x6x3
Curation Location: University of New Mexico

Figure 50: Sample USFS-11290-003. Calcite spar. Scale bar is in cm. (Photo Credit: Dave Decker).

Cave ID Number: FSGD-C-90
Sample Number: USFS-11290-003
Collection Date: 5 January, 2012
Collected By: Dave Decker

X-series U (ppm): 0.123
X-series Th (ppm): 0.026
X-series Pb (ppm): 0.037
U/Pb: 3.324

Weight (Kg): 0.710
Size (cm): 18x8x6
Curation Location: University of New Mexico

Figure 51: Sample USFS-11290-004. Calcite spar. Scale bar is in cm. (Photo Credit: Dave Decker).

Cave ID Number: FSGD-C-90
Sample Number: USFS-11290-004
Collection Date: 5 January, 2012
Collected By: Dave Decker

X-series U (ppm): Not Measured
X-series Th (ppm): Not Measured
X-series Pb (ppm): Not Measured
U/Pb: Not Applicable

Weight (Kg): 1.220
Size (cm): 15x8x7
Curation Location: University of New Mexico

Figure 52: Sample USFS-11290-005. Calcite spar from the surface above the cave. Scale bar is in cm. (Photo Credit: Dave Decker).

Cave ID Number: FSGD-C-202
Sample Number: USFS-11290-005
Collection Date: 12 March, 2012
Collected By: Dave Decker

X-series U (ppm): 0.141
X-series Th (ppm): 0.034
X-series Pb (ppm): 0.083
U/Pb: 1.699

Weight (Kg): 0.320
Size (cm): 5x5x4 and 6x5x4
Curation Location: University of New Mexico

Figure 53: Sample USFS-11290-002. Calcite spar. Scale bar is in cm. (Photo Credit: Dave Decker).

Cave ID Number:	FSGD-C-90
Sample Number:	USFS-11290-002
Collection Date:	5 January, 2012
Collected By:	Dave Decker
X-series U (ppm):	7.139
X-series Th (ppm):	0.976
X-series Pb (ppm):	0.043
U/Pb:	166.023
Weight (Kg):	0.105
Size (cm):	6x4.5x3
Curation Location:	University of New Mexico

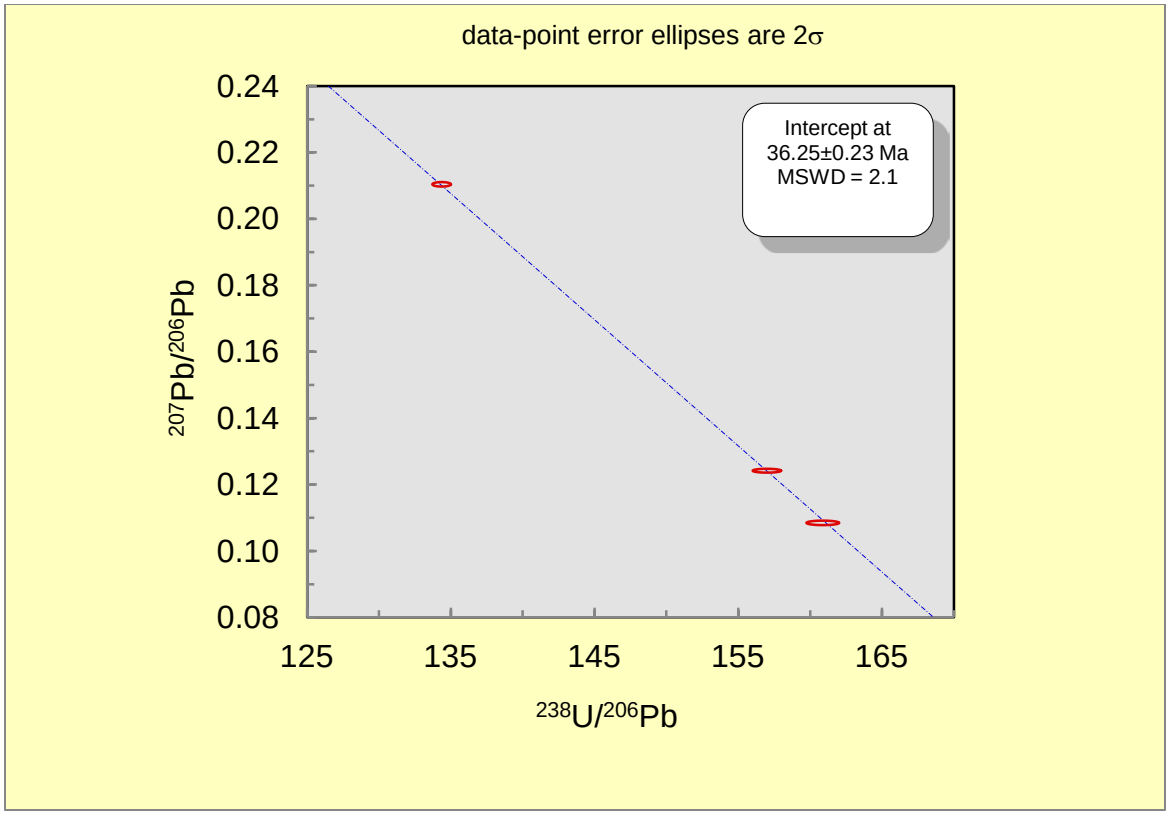

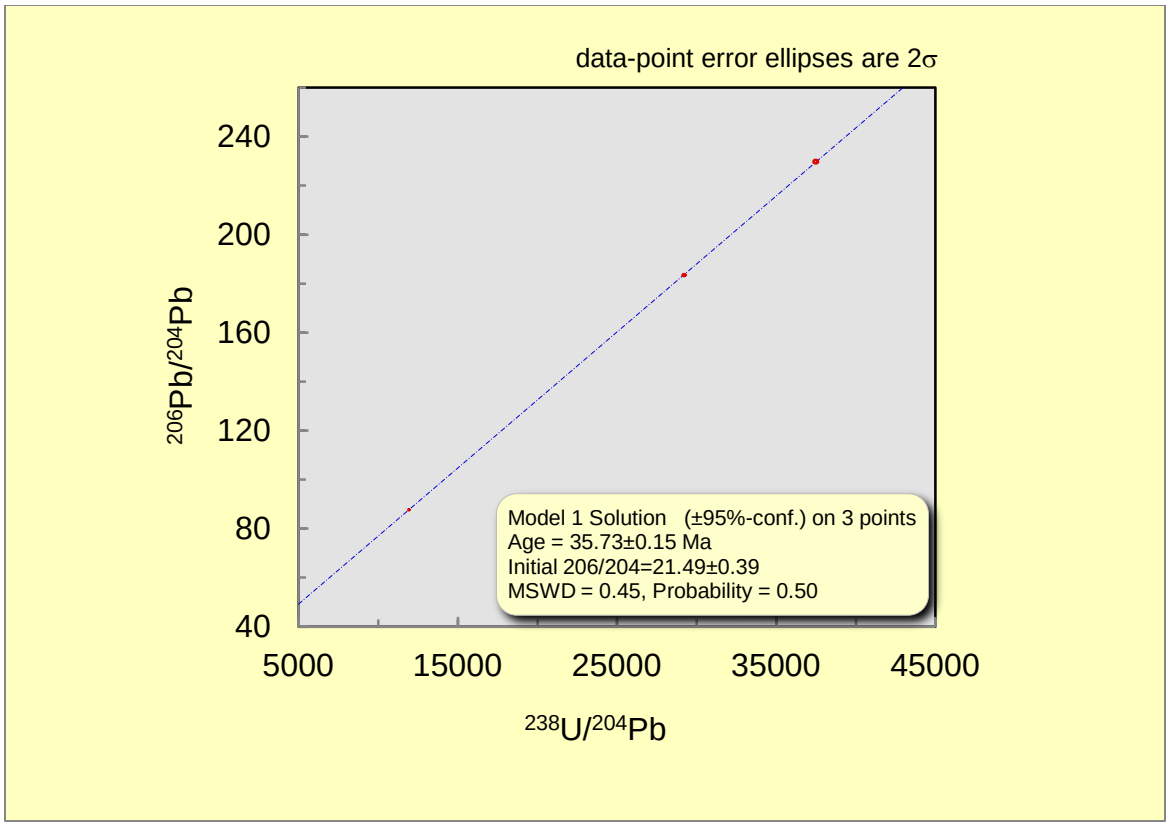
data-point error ellipses are 2σ
240
200
160
120
80
40
206Pb/204Pb
5000
15000
25000
35000
45000
238U/204Pb
Model 1 Solution (±95%-conf.) on 3 points
Age = 35.73±0.15 Ma
Initial 206/204=21.49±0.39
MSWD = 0.45, Probability = 0.50

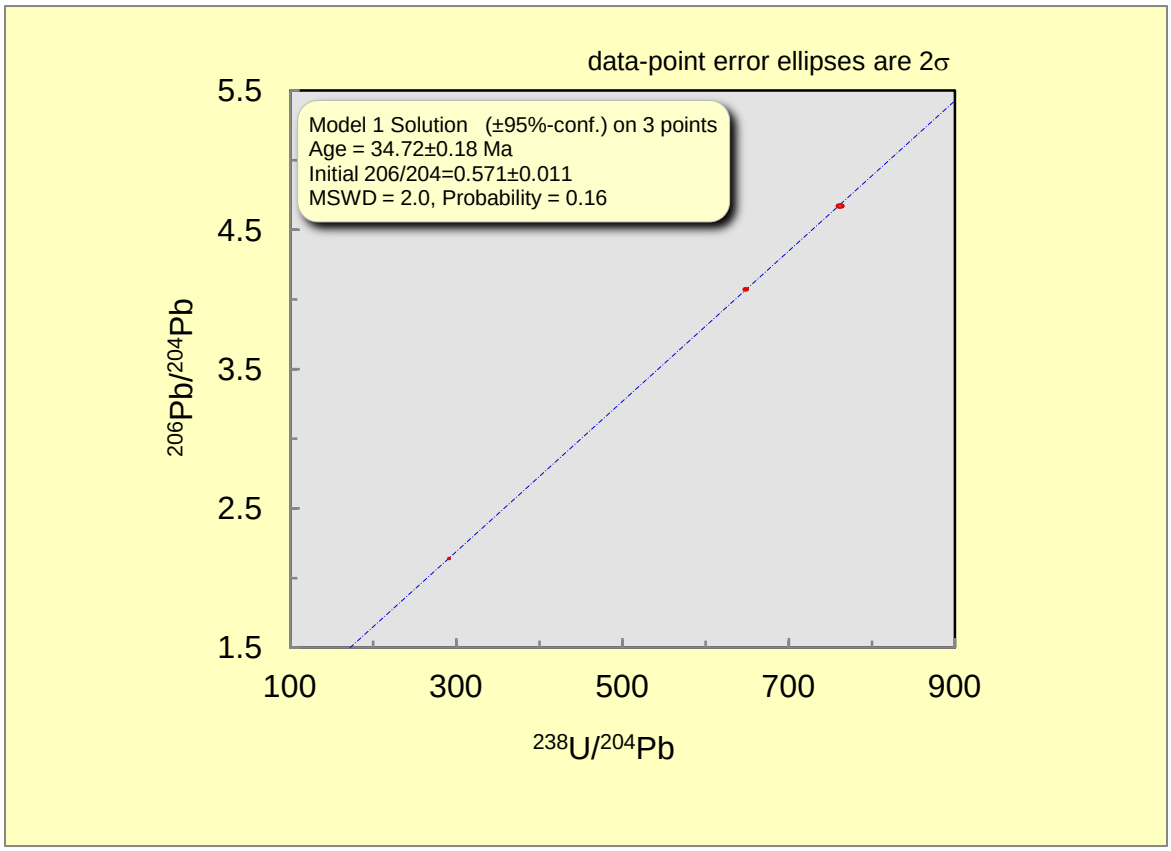
data-point error ellipses are 2σ
5.5
4.5
3.5
2.5
1.5
206Pb/204Pb
100
300
500
700
900
238U/204Pb
Model 1 Solution (±95%-conf.) on 3 points
Age = 34.72±0.18 Ma
Initial 206/204=0.571±0.011
MSWD = 2.0, Probability = 0.16

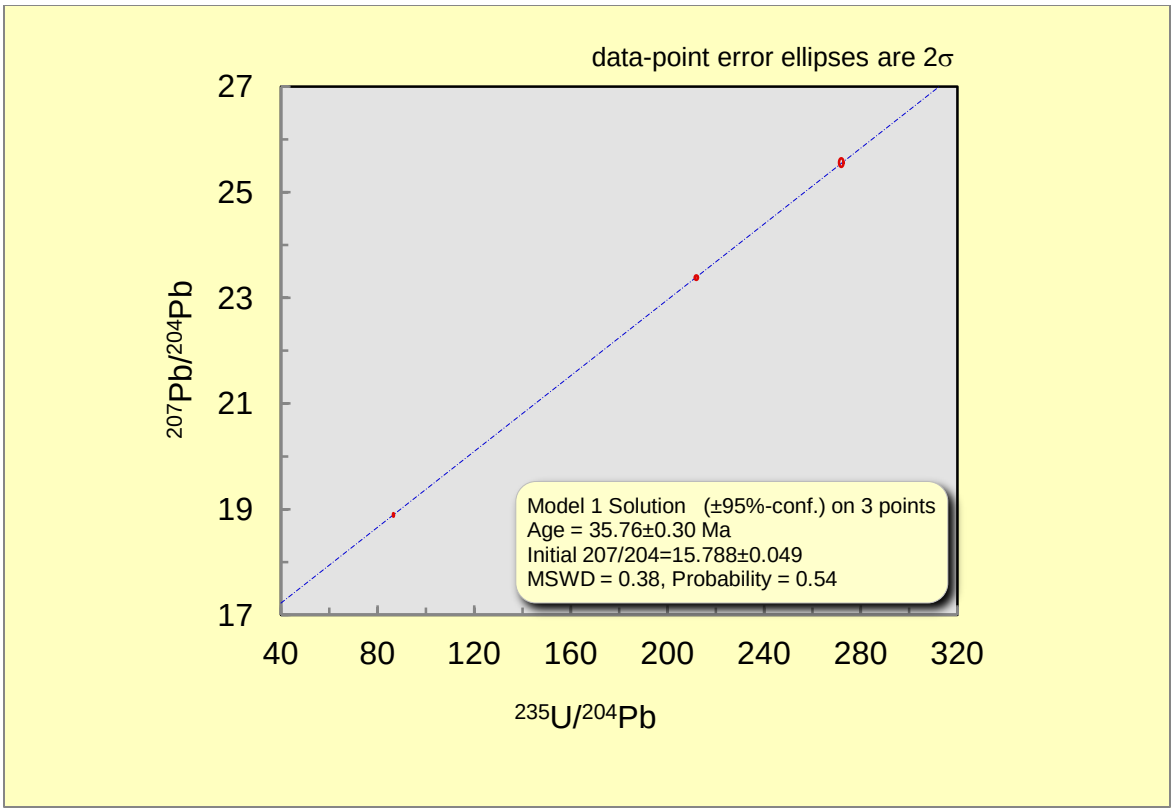
data-point error ellipses are 2σ
27
25
23
21
19
17
40
80
120
160
200
240
280
320
207Pb/204Pb
235U/204Pb
Model 1 Solution (±95%-conf.) on 3 points
Age = 35.76±0.30 Ma
Initial 207/204=15.788±0.049
MSWD = 0.38, Probability = 0.54

Figure 54: Sample USFS-11290-006. Calcite spar. Scale bar is in cm. (Photo Credit: Dave Decker).

Cave ID Number: FSGD-C-202
Sample Number: USFS-11290-006
Collection Date: 12 March, 2012
Collected By: Dave Decker

X-series U (ppm): 0.943
X-series Th (ppm): 0.014
X-series Pb (ppm): 0.039
U/Pb: 24.179

Weight (Kg): 0.740
Size (cm): 15x8x6
Curation Location: University of New Mexico

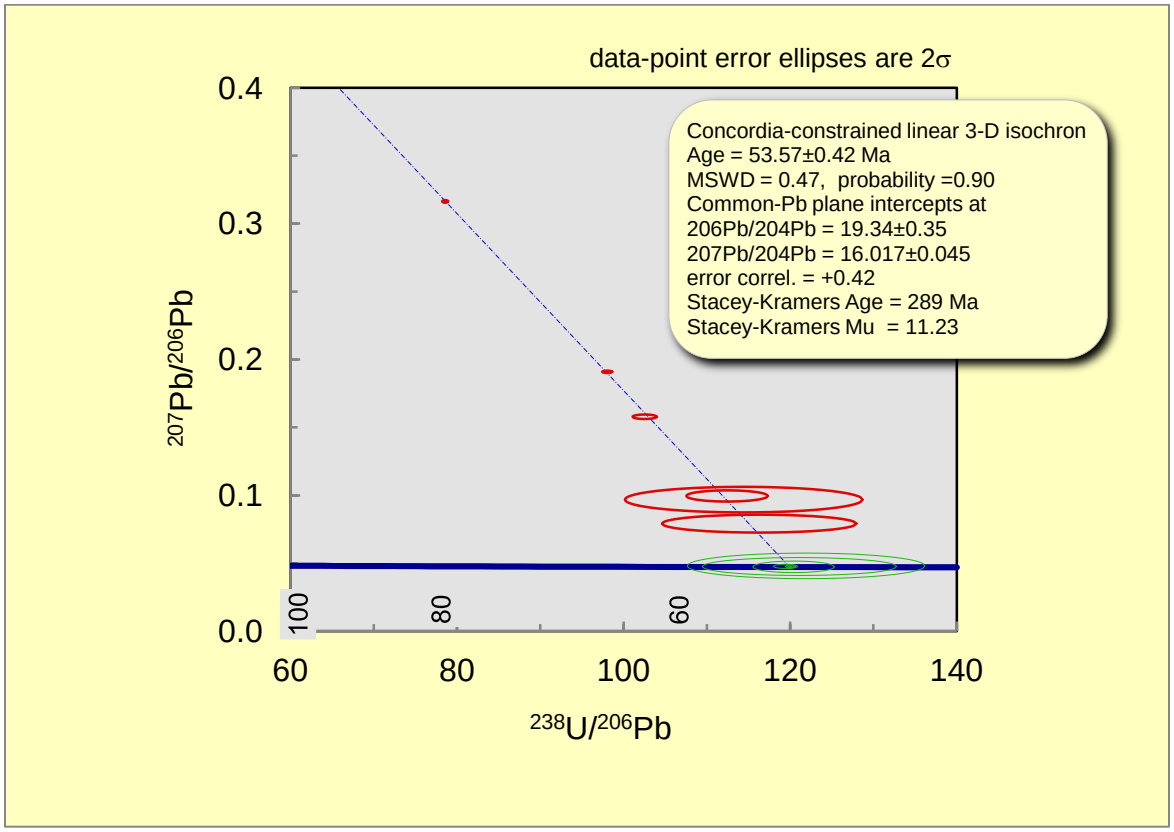

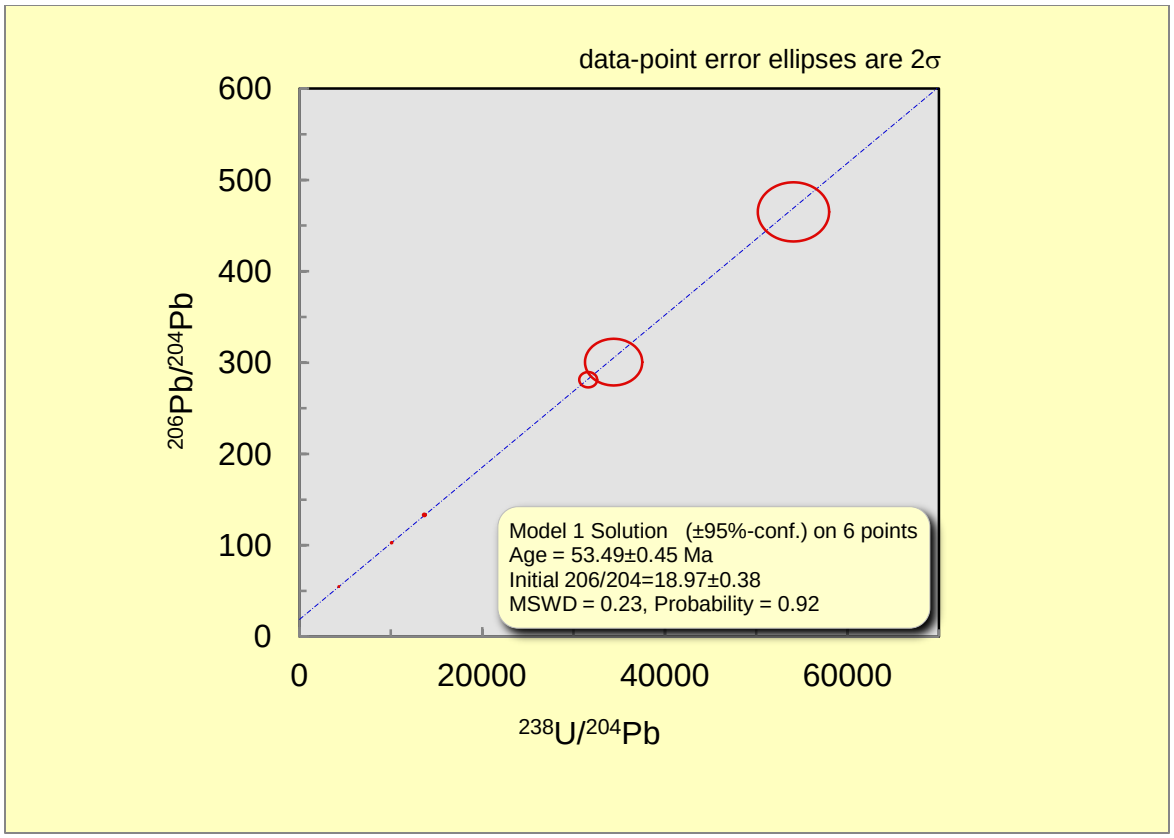
data-point error ellipses are 2σ
600
500
400
300
200
100
0
$^{206}Pb/^{204}Pb$
0
20000
40000
60000
$^{238}U/^{204}Pb$
Model 1 Solution (±95%-conf.) on 6 points
Age = 53.49±0.45 Ma
Initial 206/204=18.97±0.38
MSWD = 0.23, Probability = 0.92

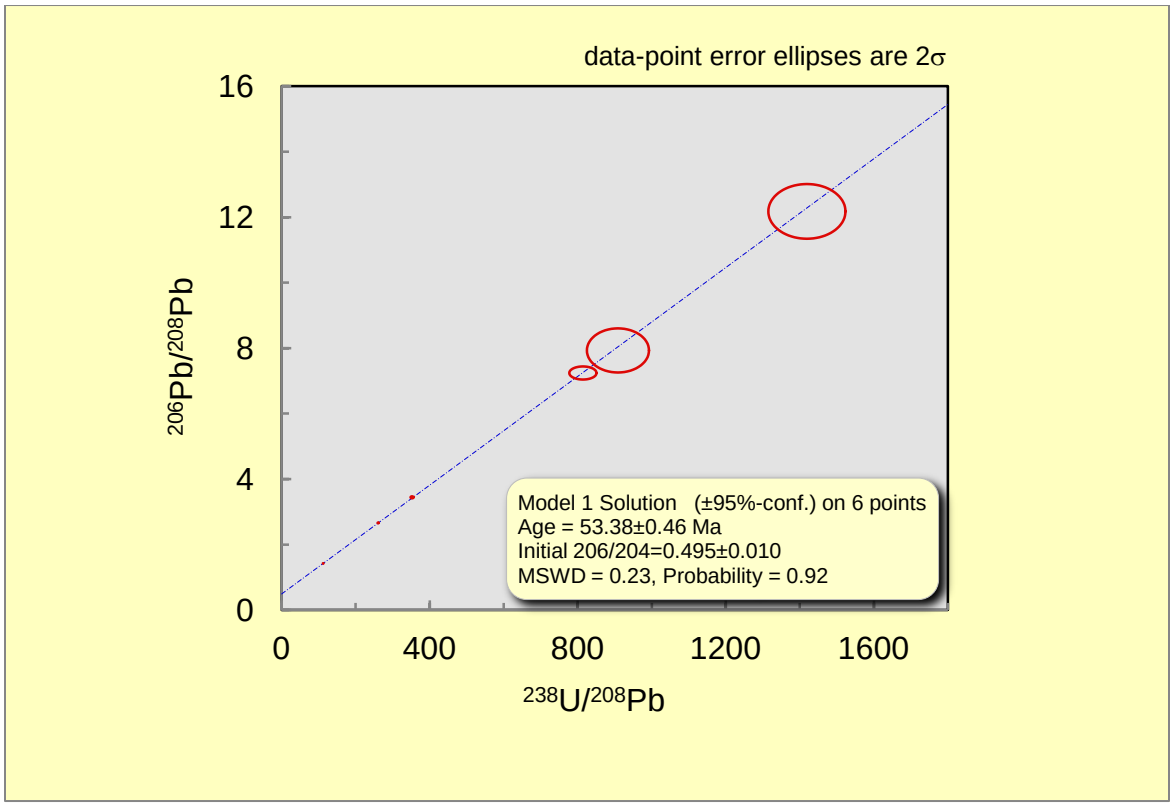
data-point error ellipses are 2σ
16
12
8
4
0
$^{206}Pb/^{208}Pb$
0
400
800
1200
1600
$^{238}U/^{208}Pb$
Model 1 Solution (±95%-conf.) on 6 points
Age = 53.38±0.46 Ma
Initial 206/204=0.495±0.010
MSWD = 0.23, Probability = 0.92

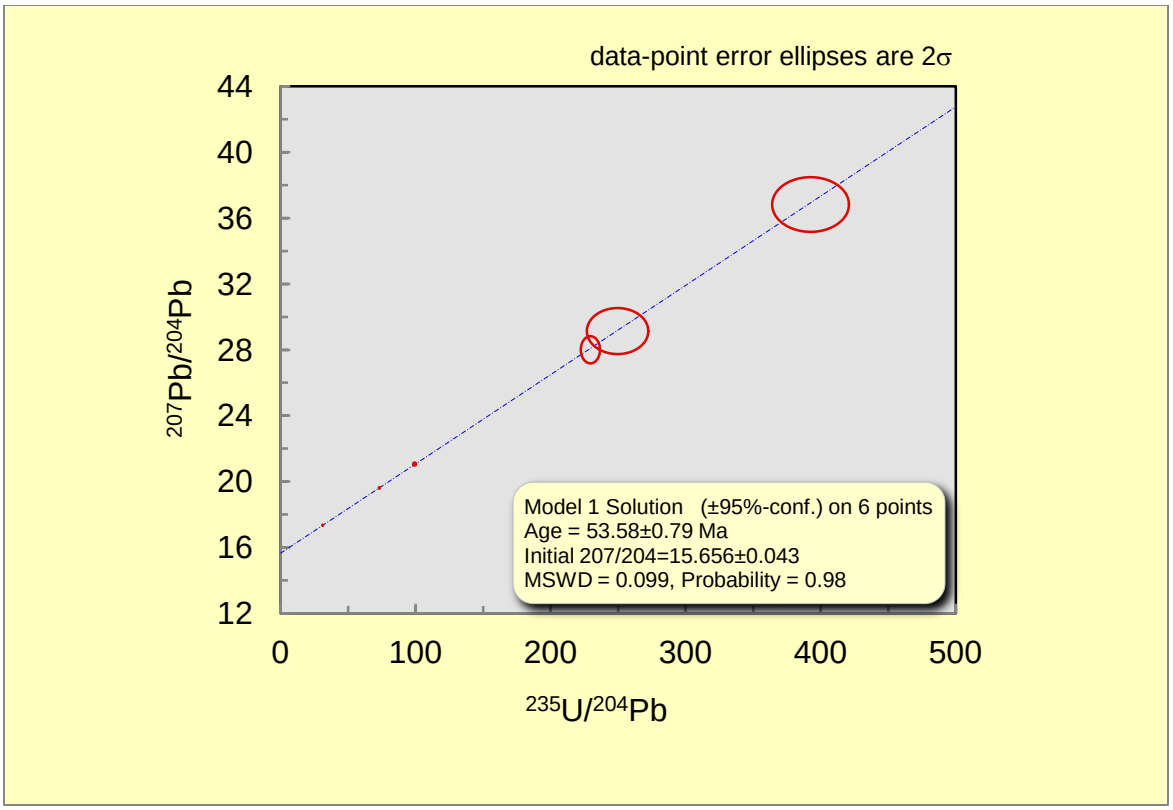
data-point error ellipses are 2σ
44
40
36
32
28
24
20
16
12
$^{207}Pb/^{204}Pb$
0
100
200
300
400
500
$^{235}U/^{204}Pb$
Model 1 Solution (±95%-conf.) on 6 points
Age = 53.58±0.79 Ma
Initial 207/204=15.656±0.043
MSWD = 0.099, Probability = 0.98

Figure 55: Sample USFS-11290-007. Calcite spar. Scale bar is in cm. (Photo Credit: Dave Decker).

Cave ID Number: FSGD-C-072
Sample Number: USFS-11290-007
Collection Date: 12 March, 2012
Collected By: Dave Decker

X-series U (ppm): 0.198
X-series Th (ppm): 0.009
X-series Pb (ppm): 0.039
U/Pb: 4.950

Weight (Kg): 0.360
Size (cm): 14x7x4
Curation Location: University of New Mexico

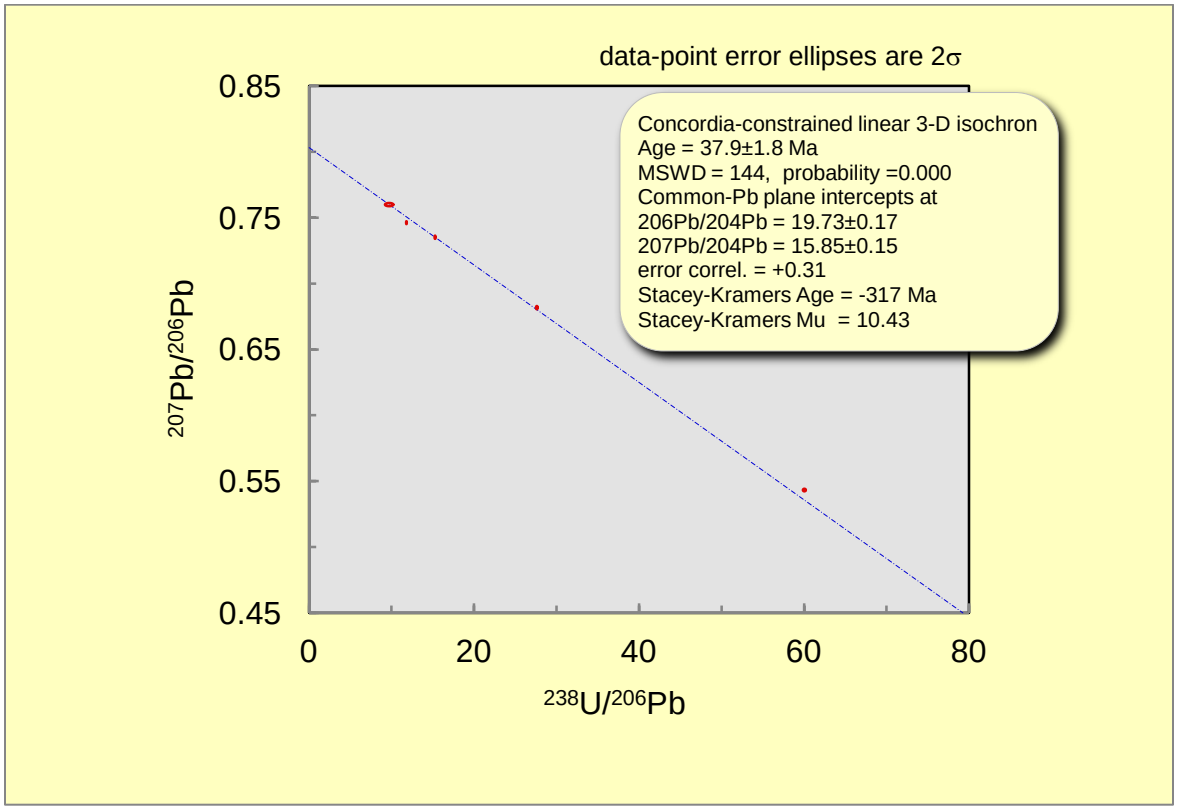

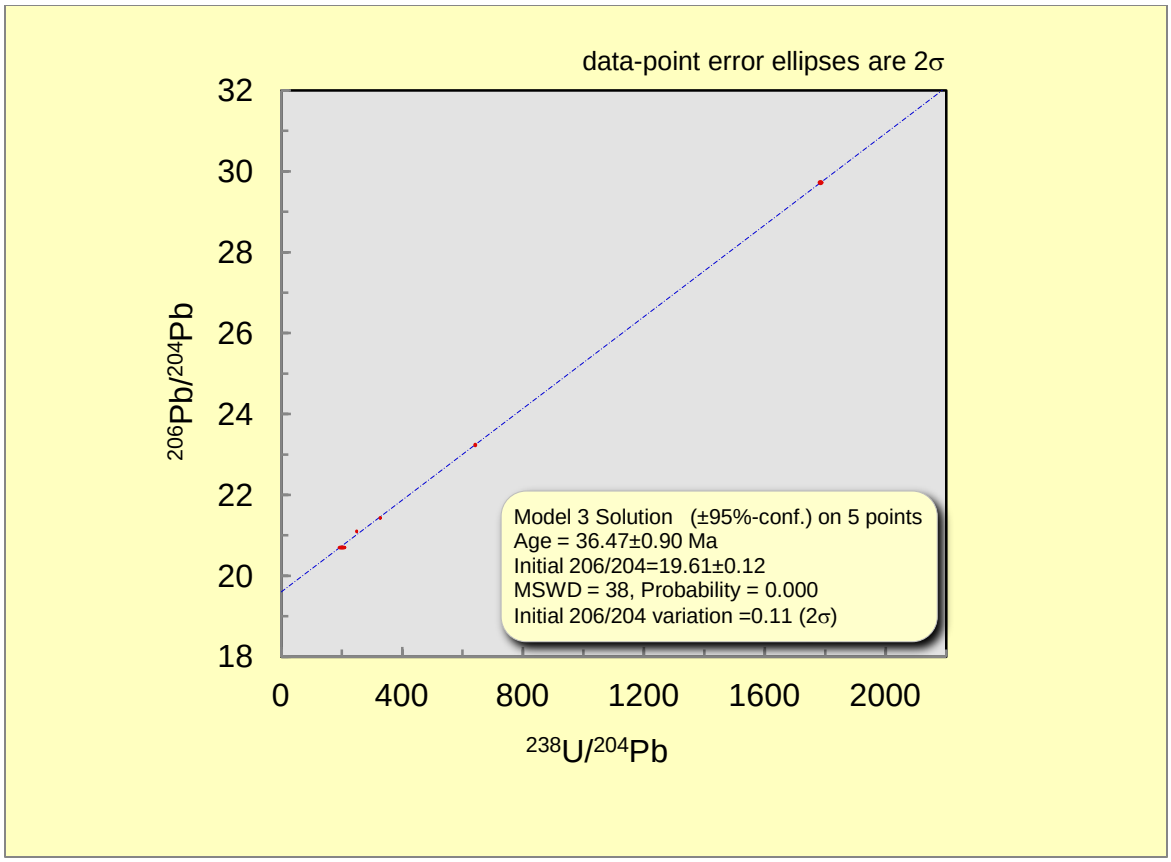
data-point error ellipses are 2σ
32
30
28
26
24
22
20
18
$^{206}Pb/^{204}Pb$
0
400
800
1200
1600
2000
$^{238}U/^{204}Pb$
Model 3 Solution (±95%-conf.) on 5 points
Age = 36.47±0.90 Ma
Initial 206/204=19.61±0.12
MSWD = 38, Probability = 0.000
Initial 206/204 variation =0.11 (2σ)

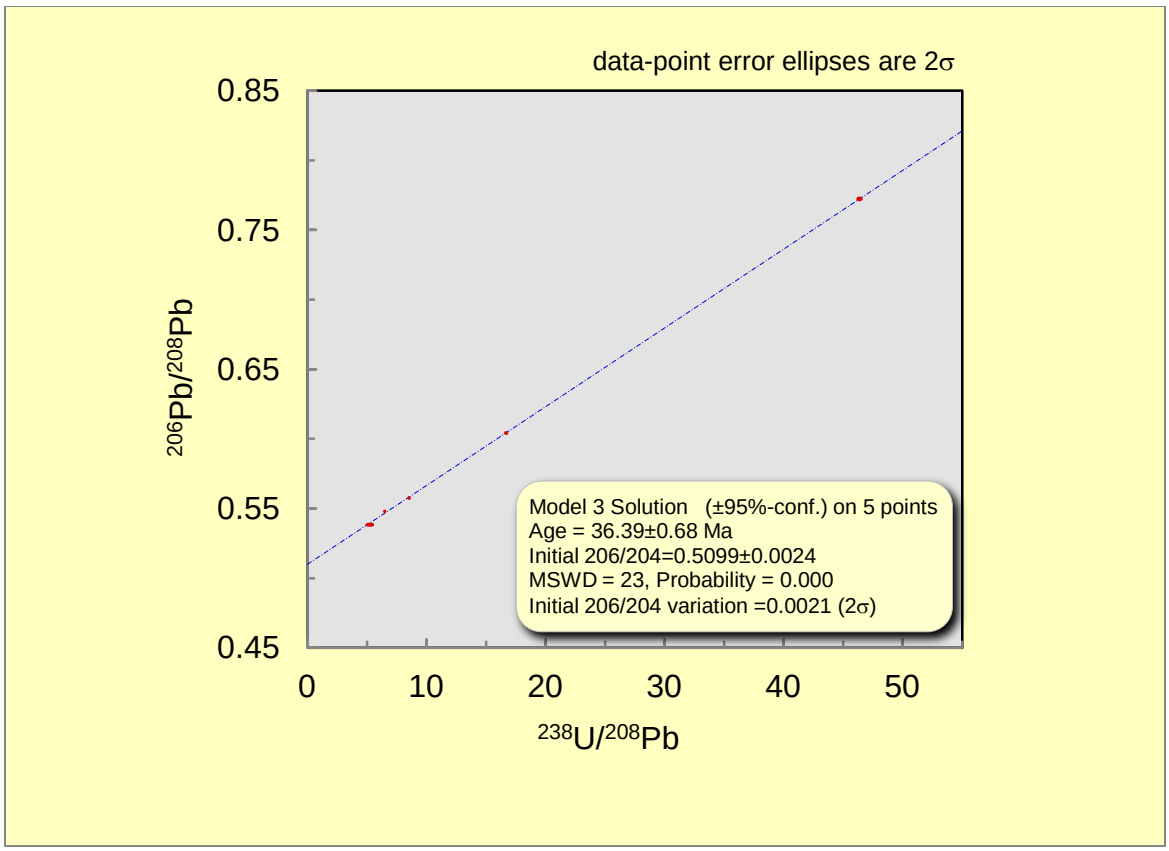
data-point error ellipses are 2σ
0.85
0.75
0.65
0.55
0.45
$^{206}Pb/^{208}Pb$
0
10
20
30
40
50
$^{238}U/^{208}Pb$
Model 3 Solution (±95%-conf.) on 5 points
Age = 36.39±0.68 Ma
Initial 206/204=0.5099±0.0024
MSWD = 23, Probability = 0.000
Initial 206/204 variation =0.0021 (2σ)

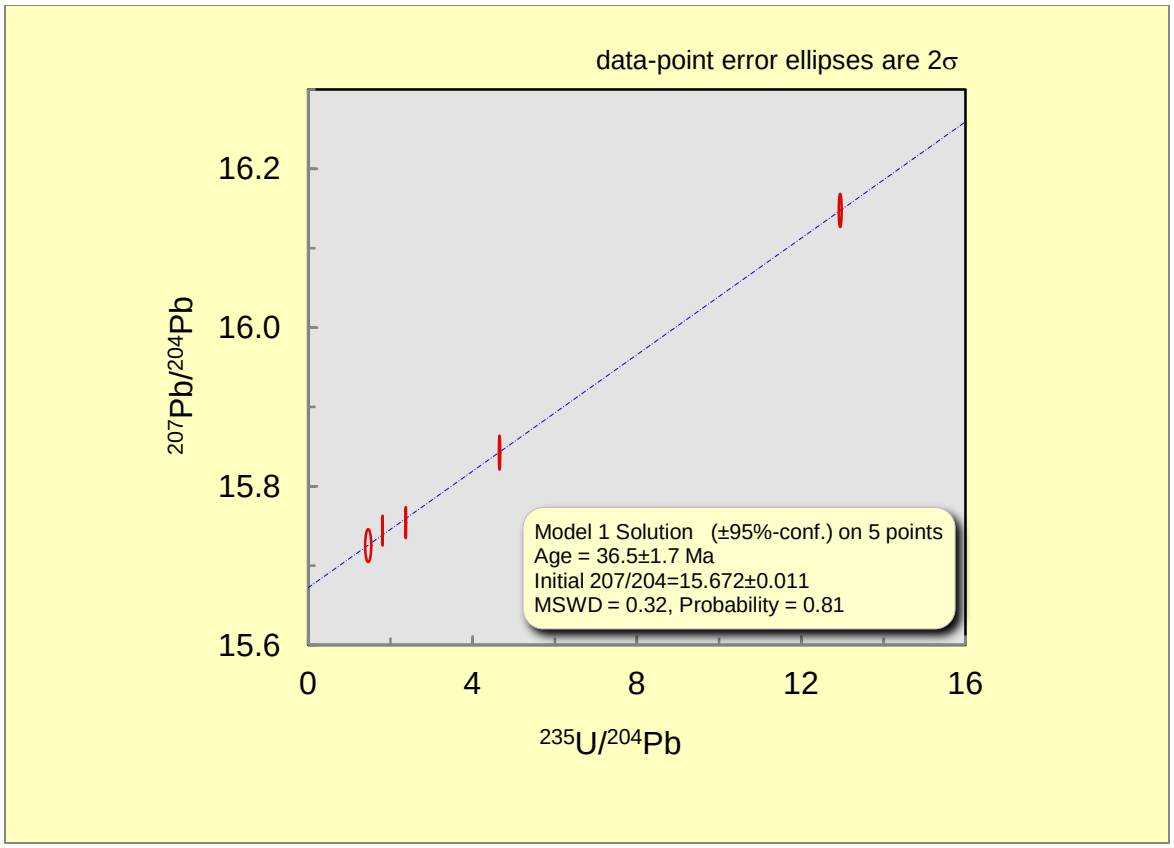
data-point error ellipses are 2σ
16.2
16.0
15.8
15.6
0
4
8
12
16
207Pb/204Pb
235U/204Pb
Model 1 Solution (±95%-conf.) on 5 points
Age = 36.5±1.7 Ma
Initial 207/204=15.672±0.011
MSWD = 0.32, Probability = 0.81

Figure 56: Sample USFS-11290-008. Calcite spar. Scale bar is in cm. (Photo Credit: Dave Decker).

Cave ID Number:	FSGD-C-040
Sample Number:	USFS-11290-008
Collection Date:	13 October, 2012
Collected By:	Dave Decker
X-series U (ppm):	1.300
X-series Th (ppm):	0.054
X-series Pb (ppm):	0.027
U/Pb:	48.148
Weight (Kg):	0.043
Size (cm):	3x3x5
Curation Location:	University of New Mexico

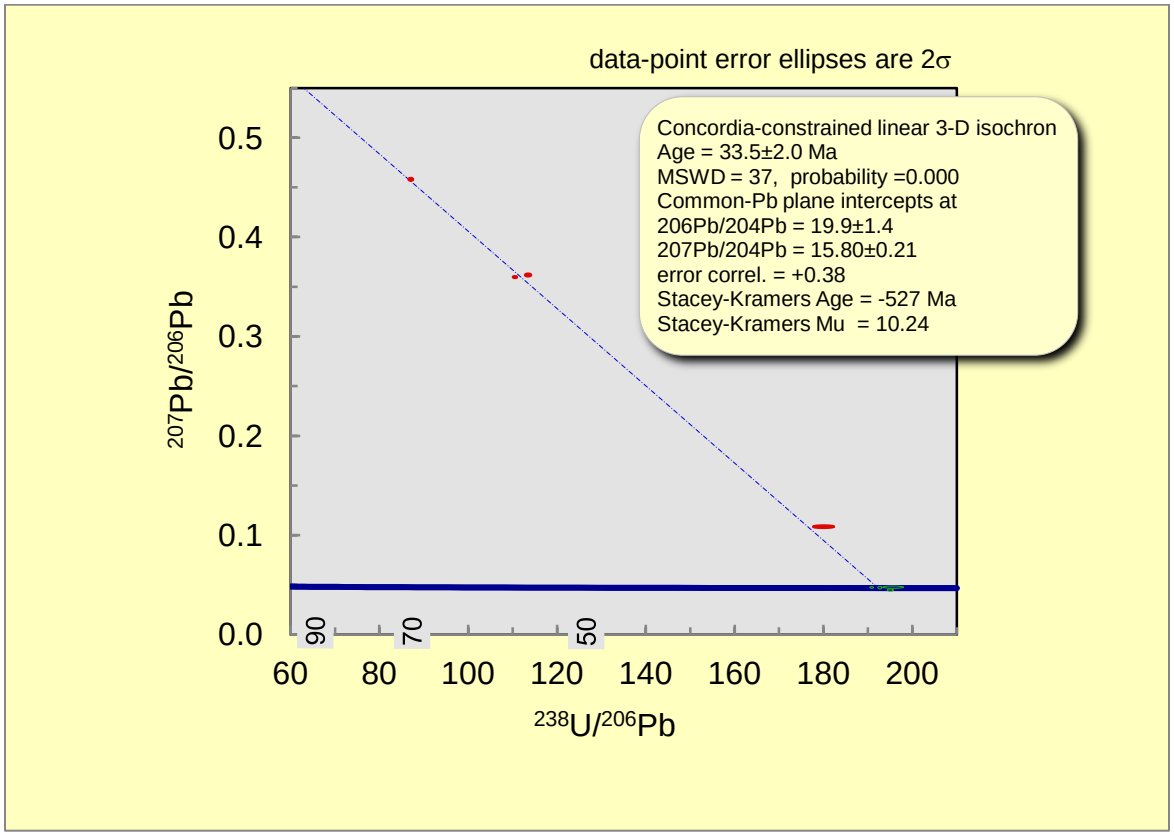

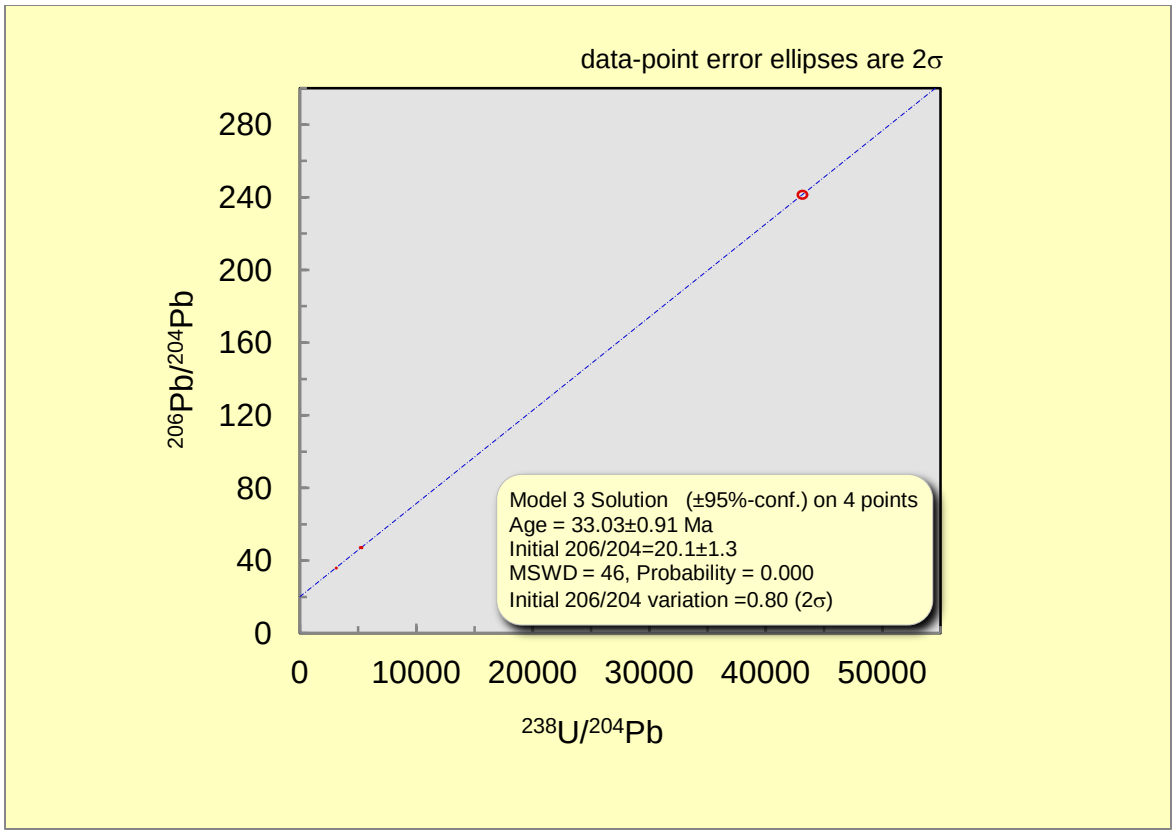
data-point error ellipses are 2σ
280
240
200
160
120
80
40
0
$^{206}Pb/^{204}Pb$
0
10000
20000
30000
40000
50000
$^{238}U/^{204}Pb$
Model 3 Solution (±95%-conf.) on 4 points
Age = 33.03±0.91 Ma
Initial 206/204=20.1±1.3
MSWD = 46, Probability = 0.000
Initial 206/204 variation =0.80 (2σ)

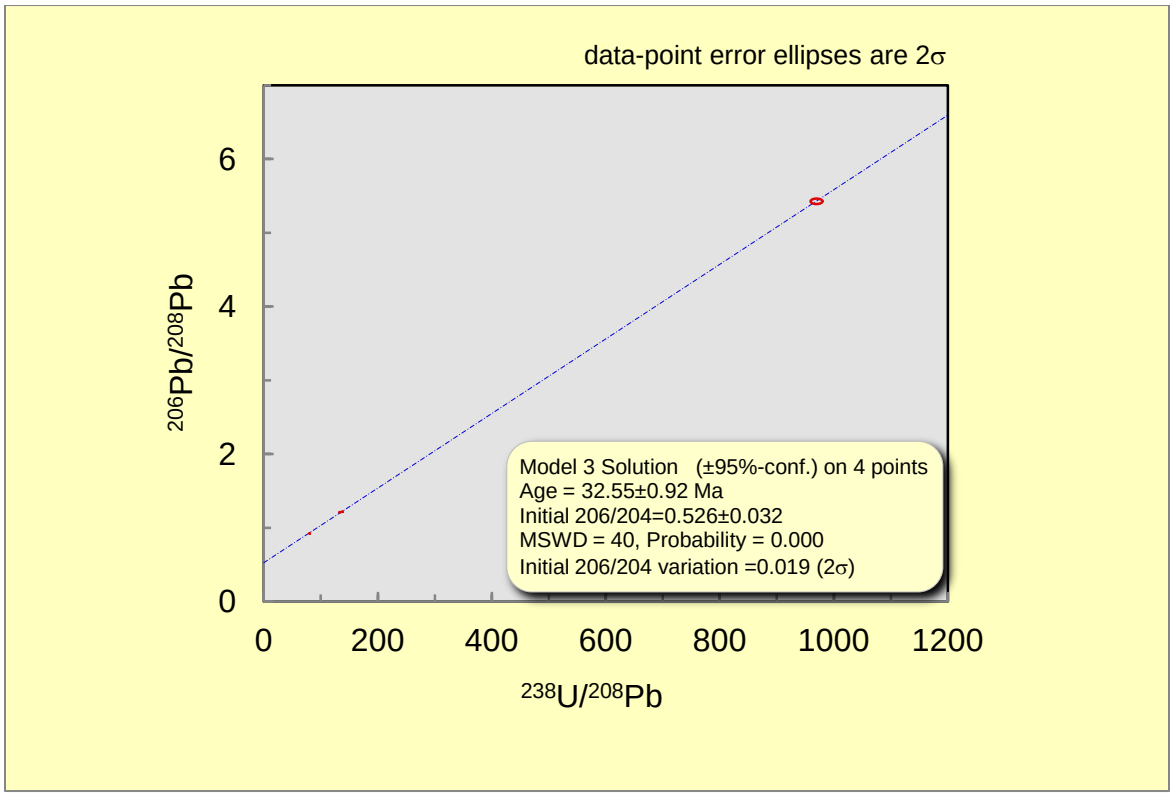
data-point error ellipses are 2σ
6
4
2
0
$^{206}Pb/^{208}Pb$
0
200
400
600
800
1000
1200
$^{238}U/^{208}Pb$
Model 3 Solution (±95%-conf.) on 4 points
Age = 32.55±0.92 Ma
Initial 206/204=0.526±0.032
MSWD = 40, Probability = 0.000
Initial 206/204 variation =0.019 (2σ)

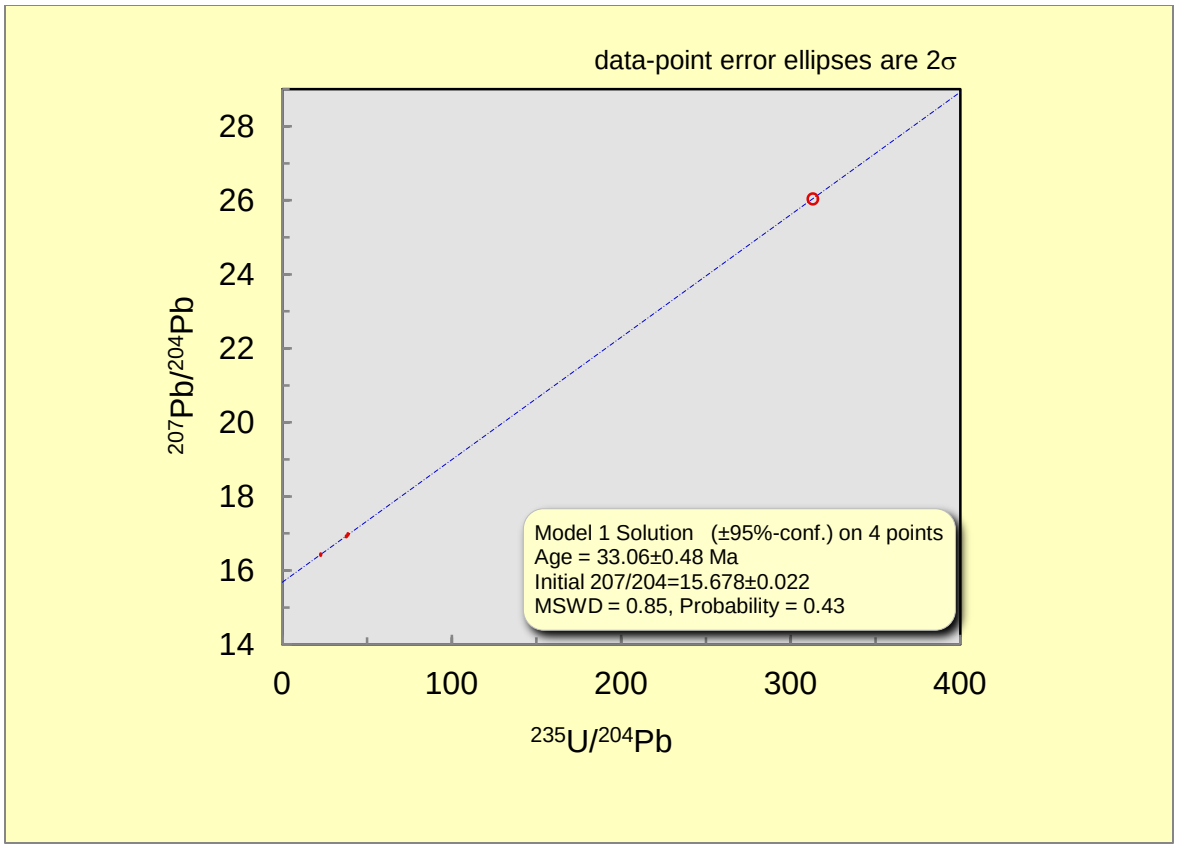
data-point error ellipses are 2σ
28
26
24
22
20
18
16
14
0
100
200
300
400
207Pb/204Pb
235U/204Pb
Model 1 Solution (±95%-conf.) on 4 points
Age = 33.06±0.48 Ma
Initial 207/204=15.678±0.022
MSWD = 0.85, Probability = 0.43

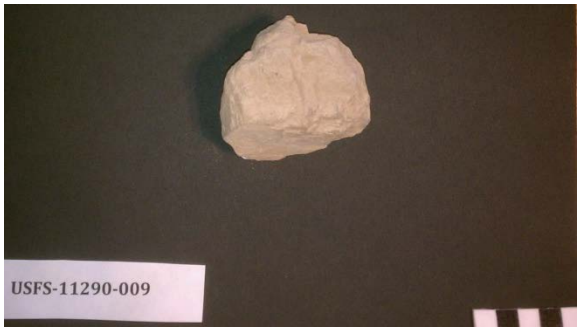

Figure 57: Sample USFS-11290-009. Calcite spar. Scale bar is in cm. (Photo Credit: Dave Decker).

Cave ID Number: FSGD-C-062
Sample Number: USFS-11290-009
Collection Date: 5 January, 2013
Collected By: Dave Decker

X-series U (ppm): 5.226
X-series Th (ppm): 0.012
X-series Pb (ppm): 0.039
U/Pb: 134.000

Weight (Kg): 0.240
Size (cm): 5x4x4
Curation Location: University of New Mexico

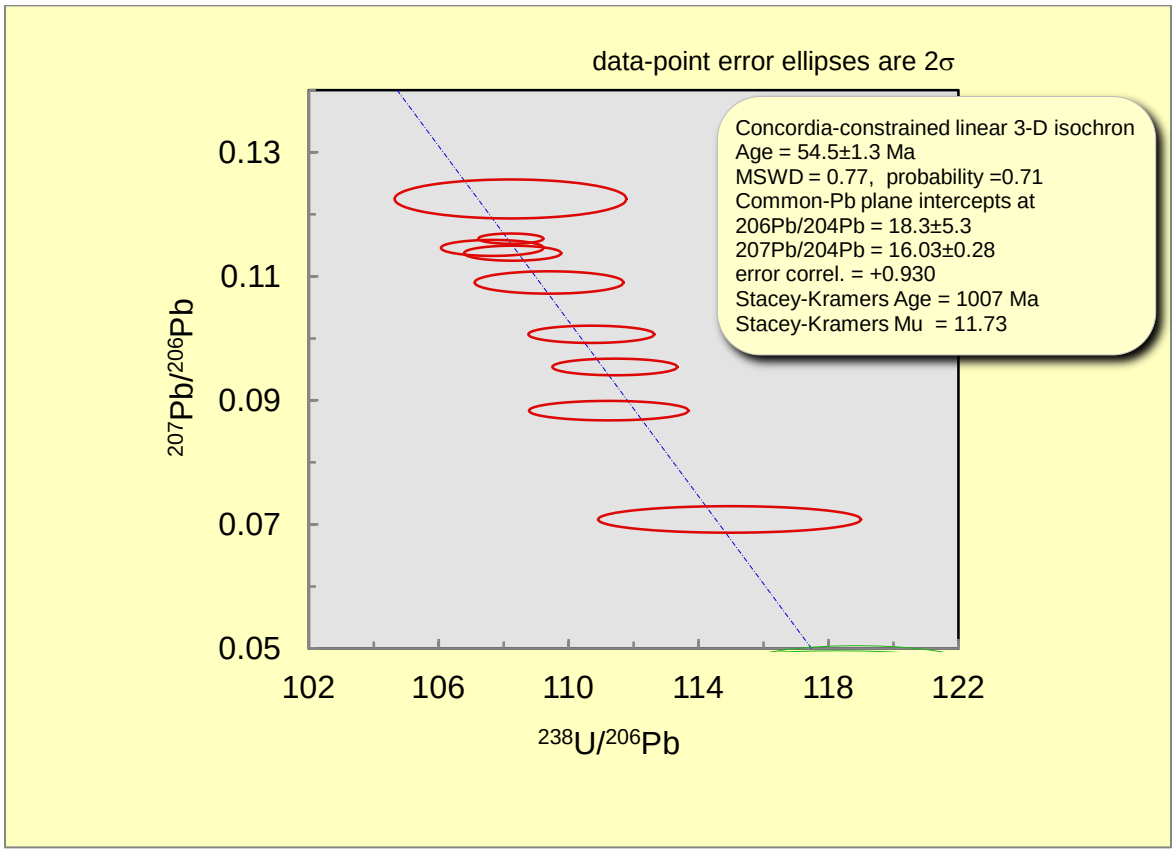

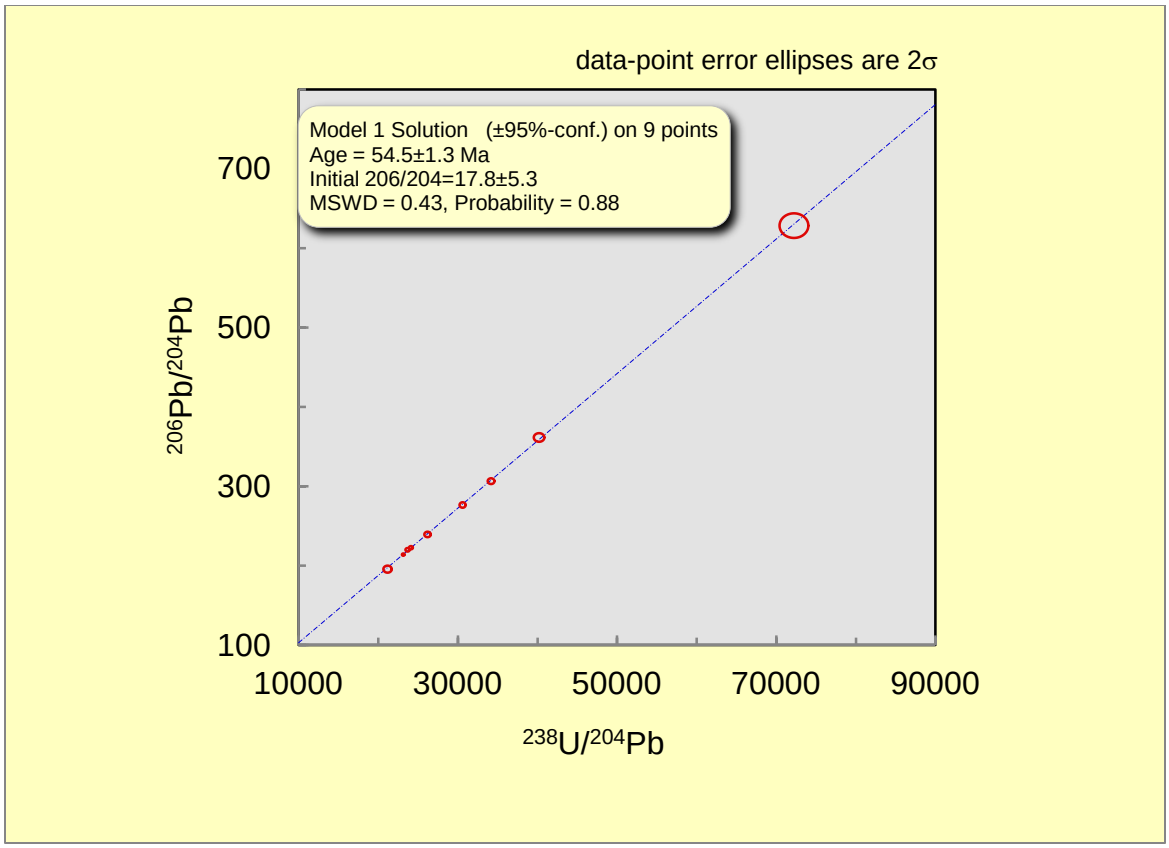
data-point error ellipses are 2σ
Model 1 Solution (±95%-conf.) on 9 points
Age = 54.5±1.3 Ma
Initial 206/204=17.8±5.3
MSWD = 0.43, Probability = 0.88
700
500
300
100
10000
30000
50000
70000
90000
206Pb/204Pb
238U/204Pb

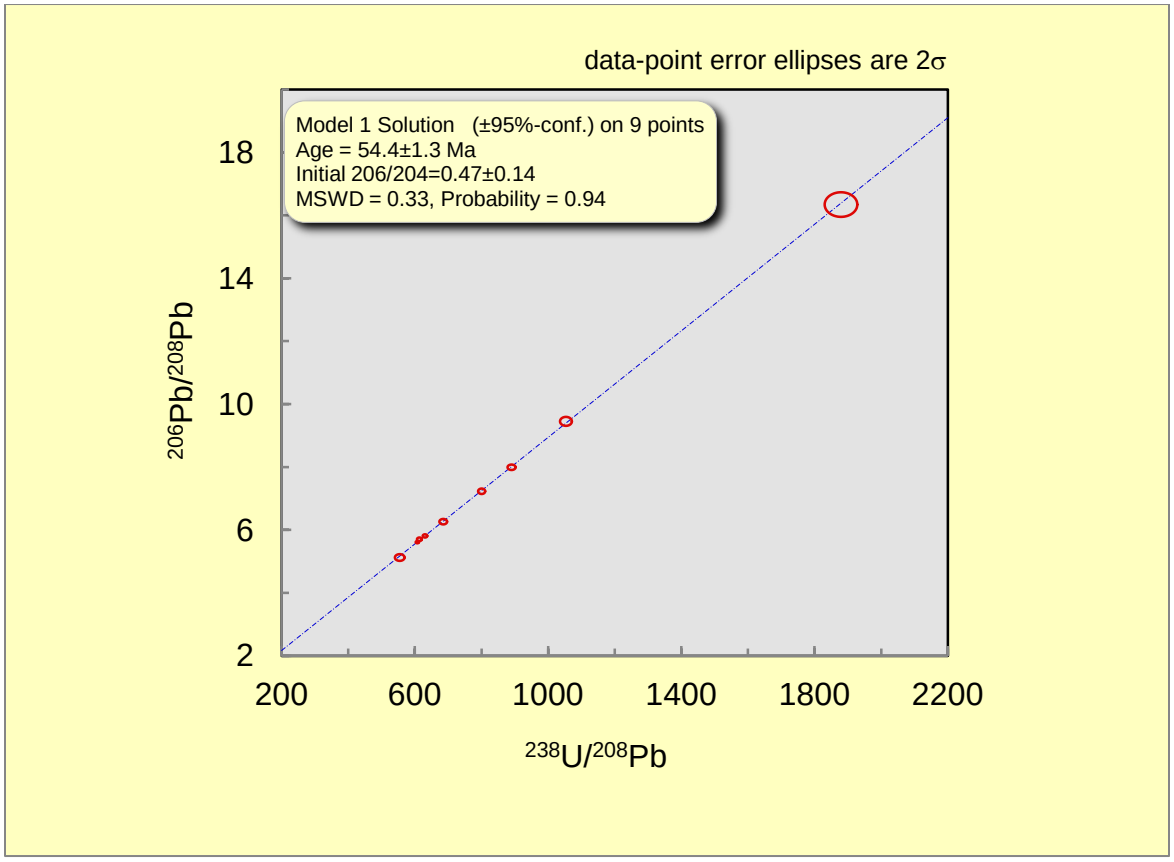
data-point error ellipses are 2σ
Model 1 Solution (±95%-conf.) on 9 points
Age = 54.4±1.3 Ma
Initial 206/204=0.47±0.14
MSWD = 0.33, Probability = 0.94
18
14
10
6
2
200
600
1000
1400
1800
2200
206Pb/208Pb
238U/208Pb

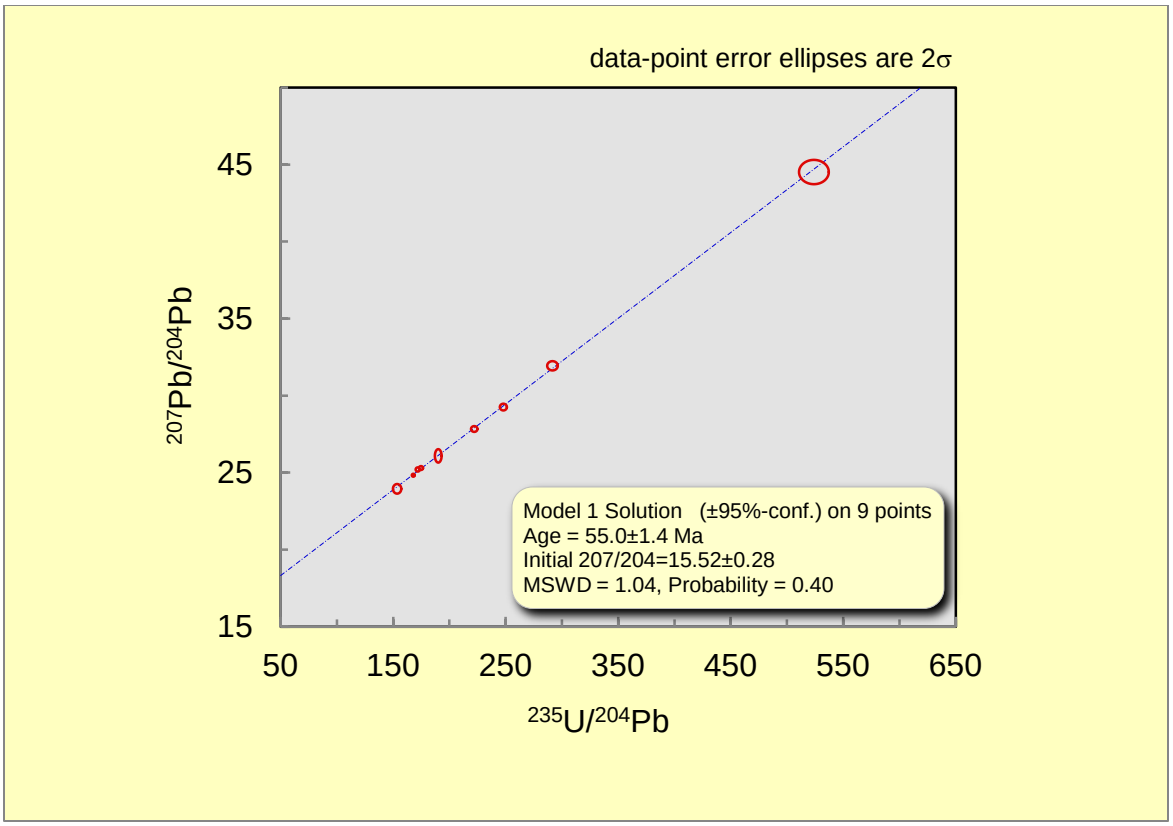
data-point error ellipses are 2σ
45
35
25
15
50
150
250
350
450
550
650
$^{207}Pb/^{204}Pb$
$^{235}U/^{204}Pb$
Model 1 Solution (±95%-conf.) on 9 points
Age = 55.0±1.4 Ma
Initial 207/204=15.52±0.28
MSWD = 1.04, Probability = 0.40

Figure 58: Sample USFS-11290-010. Calcite spar. Scale bar is in cm. (Photo Credit: Dave Decker).

Cave ID Number:	FSGD-C-011
Sample Number:	USFS-11290-010
Collection Date:	15 November, 2014
Collected By:	Dave Decker
X-series U (ppm):	Not Measured
X-series Th (ppm):	Not Measured
X-series Pb (ppm):	Not Measured
U/Pb:	Not Applicable
Weight (Kg):	0.470
Size (cm):	7x12x5.5
Curation Location:	University of New Mexico

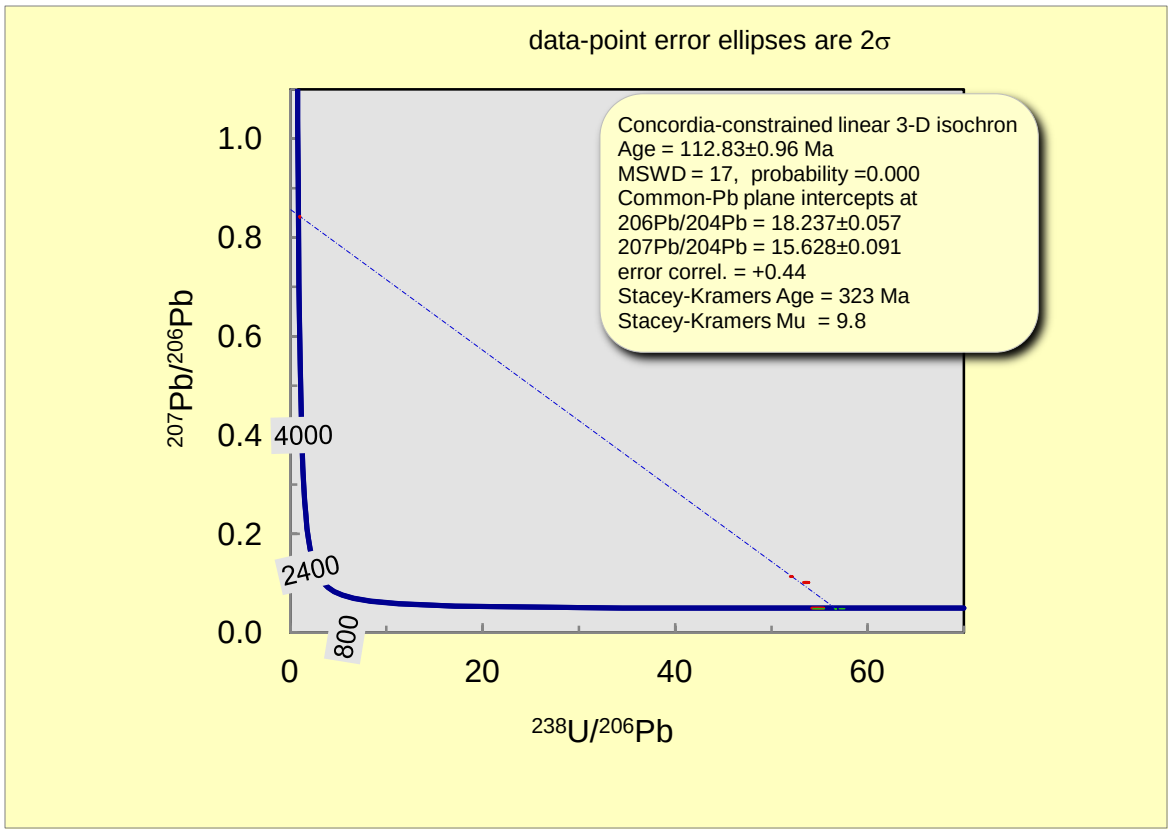

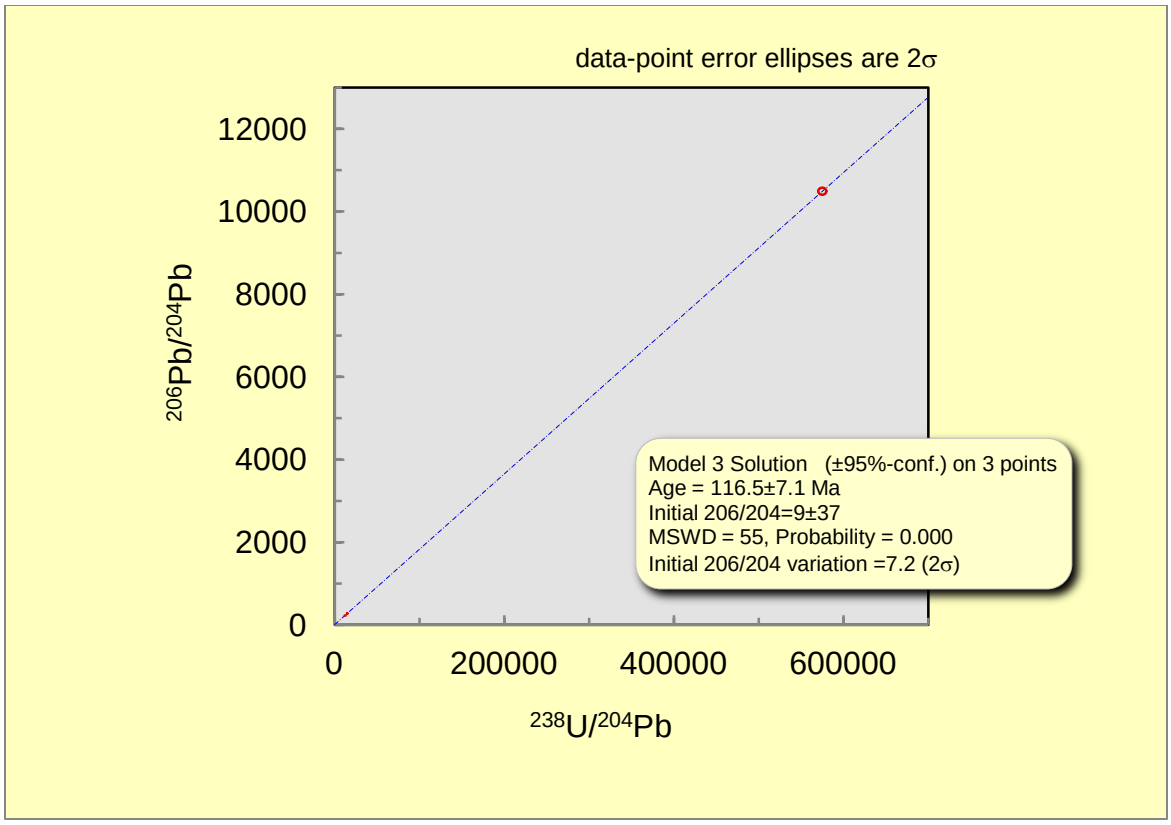
data-point error ellipses are 2σ
12000
10000
8000
6000
4000
2000
0
$^{206}Pb/^{204}Pb$
0
200000
400000
600000
$^{238}U/^{204}Pb$
Model 3 Solution (±95%-conf.) on 3 points
Age = 116.5±7.1 Ma
Initial 206/204=9±37
MSWD = 55, Probability = 0.000
Initial 206/204 variation =7.2 (2σ)

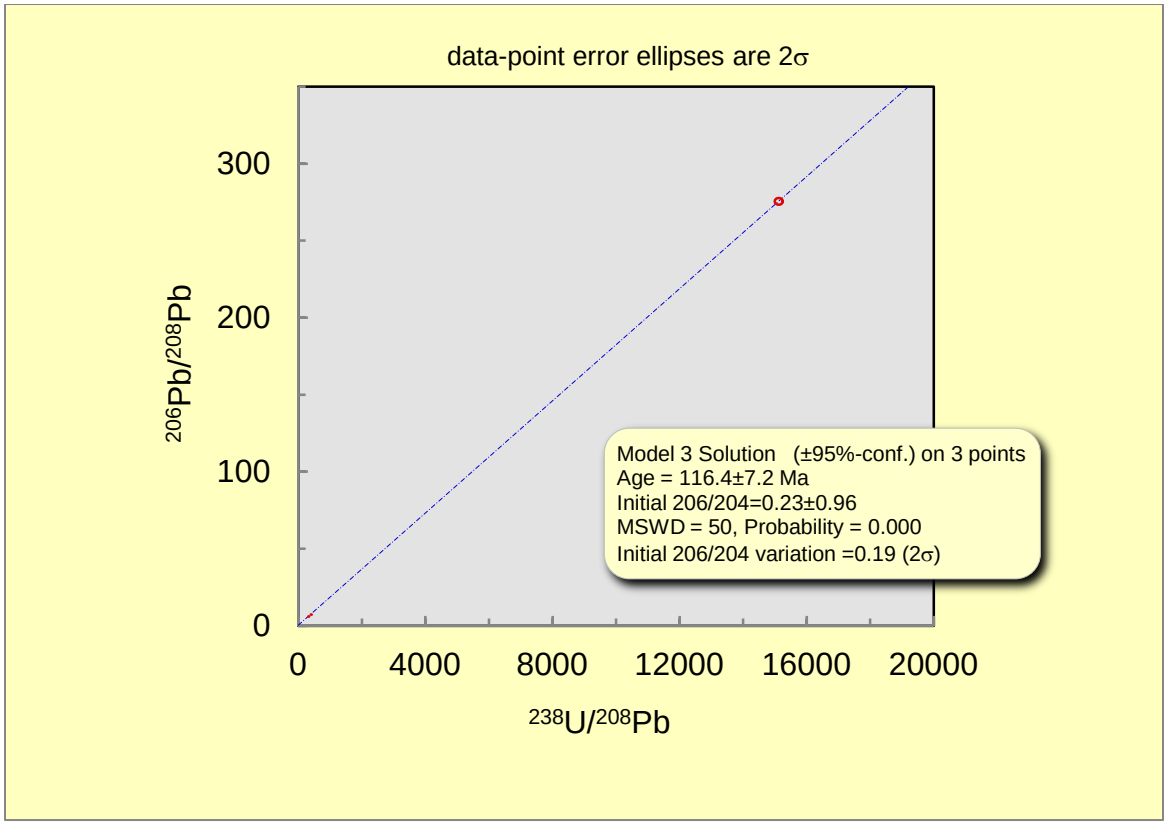
data-point error ellipses are 2σ
300
200
100
0
$^{206}Pb/^{208}Pb$
0
4000
8000
12000
16000
20000
$^{238}U/^{208}Pb$
Model 3 Solution (±95%-conf.) on 3 points
Age = 116.4±7.2 Ma
Initial 206/204=0.23±0.96
MSWD = 50, Probability = 0.000
Initial 206/204 variation =0.19 (2σ)

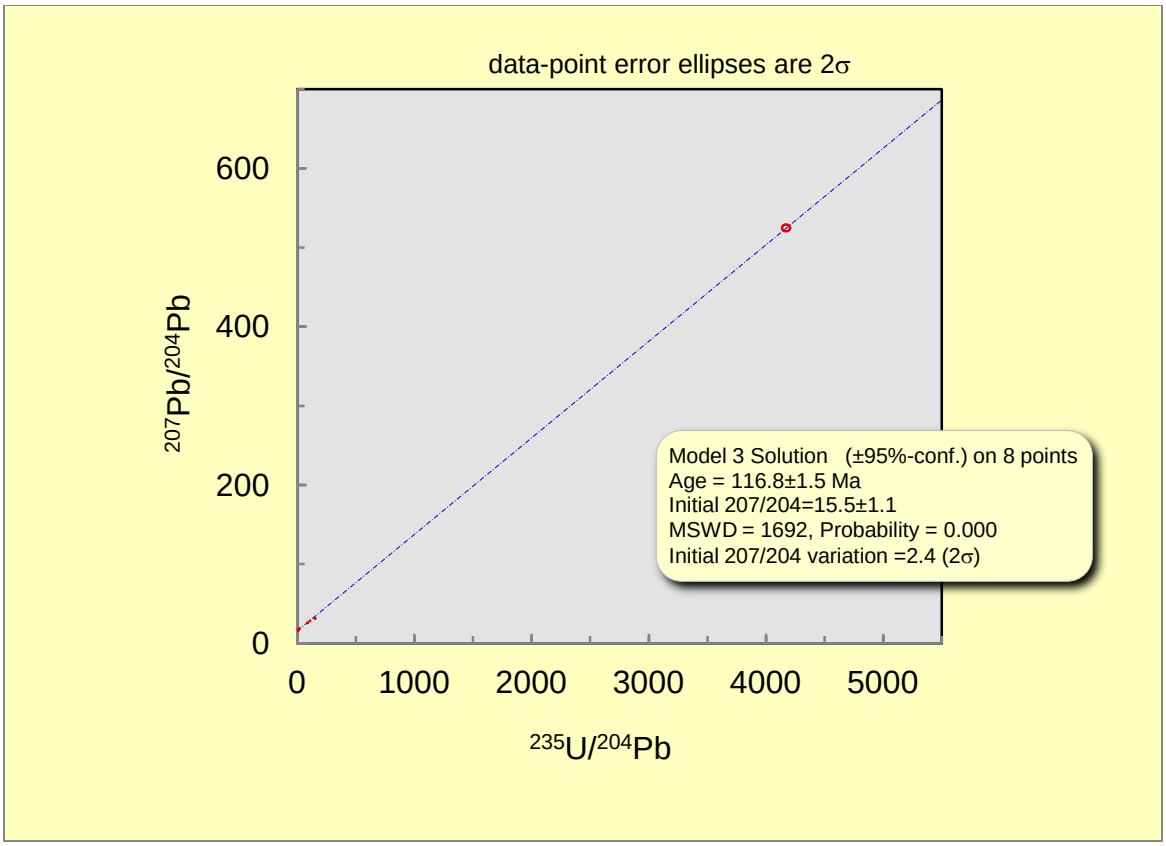
data-point error ellipses are 2σ
600
400
200
0
$^{207}Pb/^{204}Pb$
0
1000
2000
3000
4000
5000
$^{235}U/^{204}Pb$
Model 3 Solution (±95%-conf.) on 8 points
Age = 116.8±1.5 Ma
Initial 207/204=15.5±1.1
MSWD = 1692, Probability = 0.000
Initial 207/204 variation =2.4 (2σ)

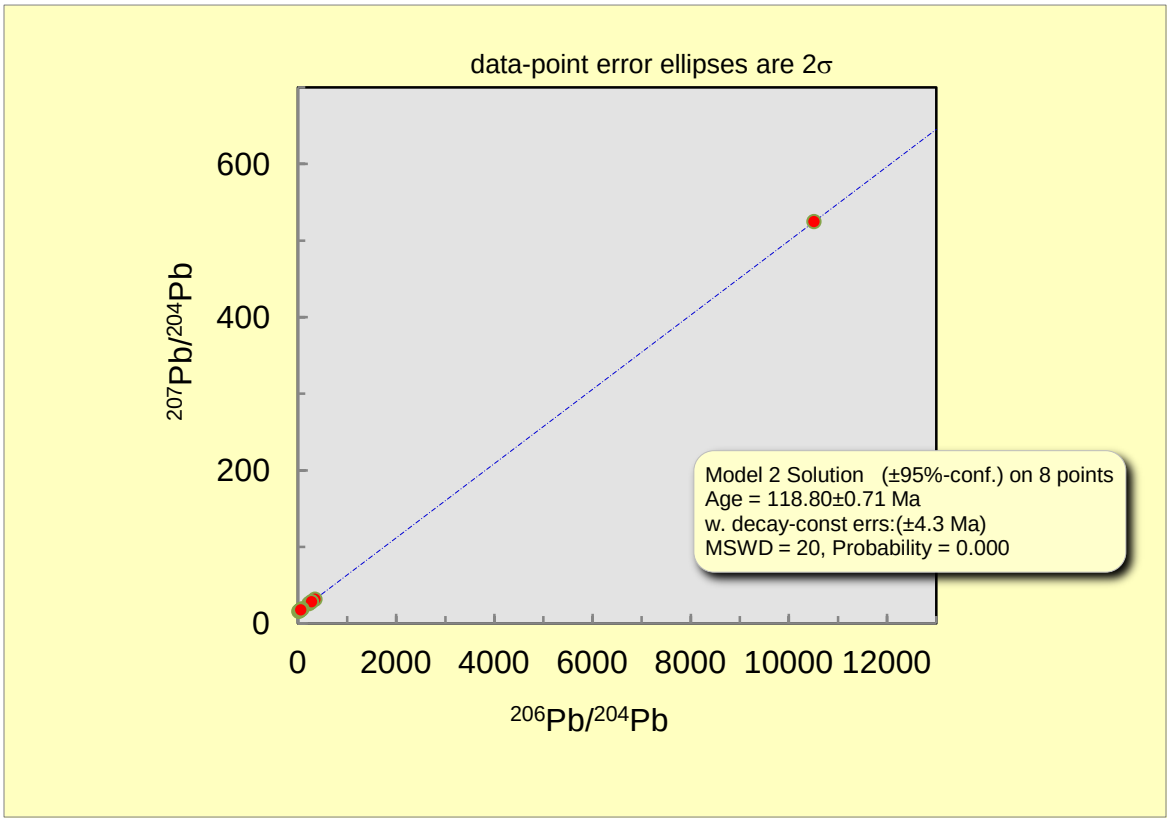
data-point error ellipses are 2σ
600
400
200
0
$^{207}Pb/^{204}Pb$
0
2000
4000
6000
8000
10000
12000
$^{206}Pb/^{204}Pb$
Model 2 Solution (±95%-conf.) on 8 points
Age = 118.80±0.71 Ma
w. decay-const errs:(±4.3 Ma)
MSWD = 20, Probability = 0.000

Figure 59: Sample USFS-11290-011. Calcite spar. Scale is knife at 10 cm in length. (Photo Credit: Dave Decker).

Cave ID Number: FSGD-C-0XX*
Sample Number: USFS-11290-011
Collection Date: Unknown
Collected By: Victor Polyak

X-series U (ppm): Not Run
X-series Th (ppm): Not Run
X-series Pb (ppm): Not Run
U/Pb: Not Applicable

Weight (Kg): 1.810
Size (cm): 20x8.5x8.5
Curation Location: University of New Mexico

*No Cave ID Number assigned.

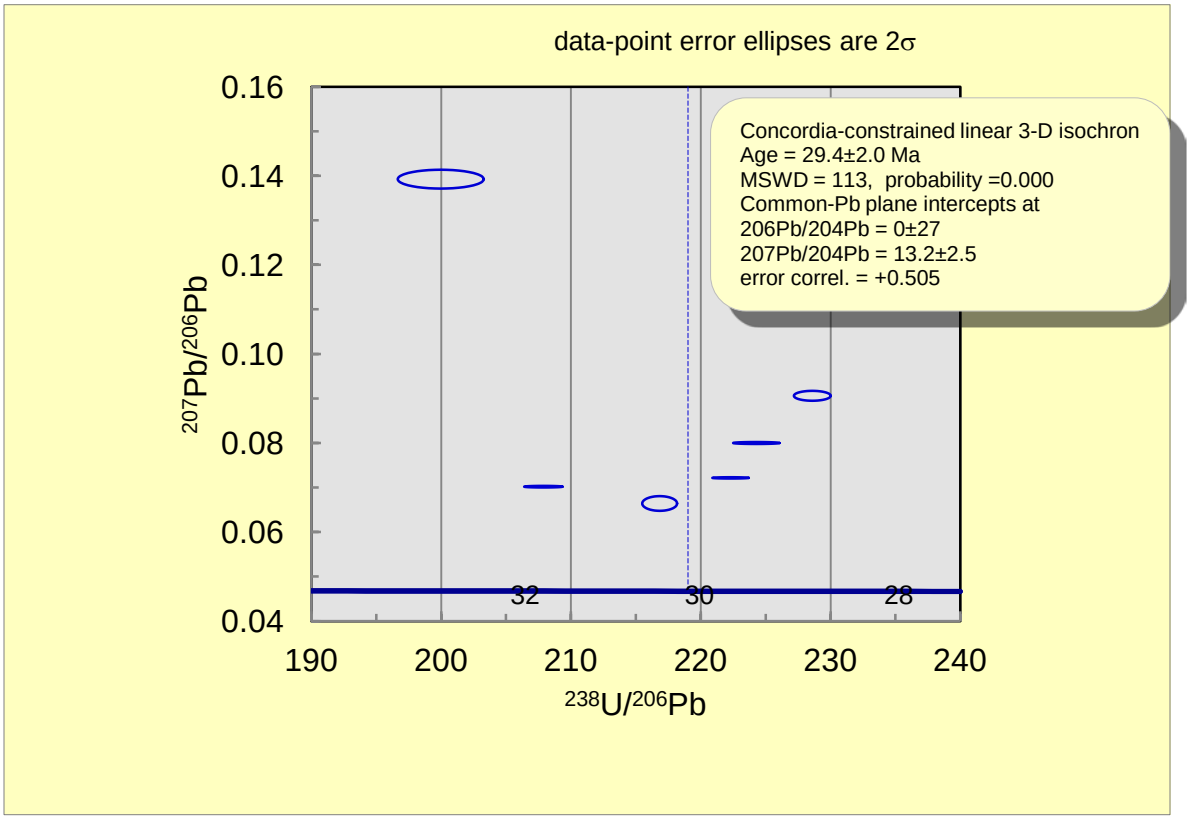

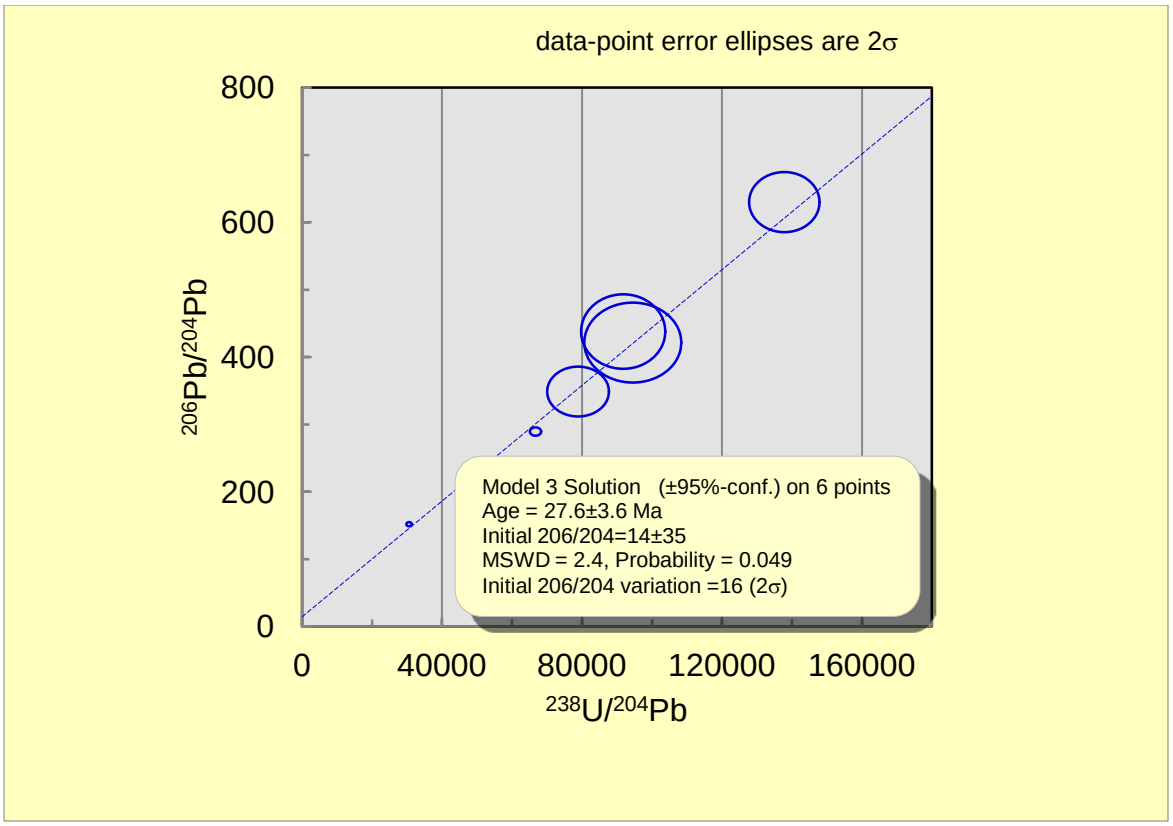
data-point error ellipses are 2σ
800
600
400
200
0
$^{206}Pb/^{204}Pb$
0
40000
80000
120000
160000
$^{238}U/^{204}Pb$
Model 3 Solution (±95%-conf.) on 6 points
Age = 27.6±3.6 Ma
Initial 206/204=14±35
MSWD = 2.4, Probability = 0.049
Initial 206/204 variation =16 (2σ)

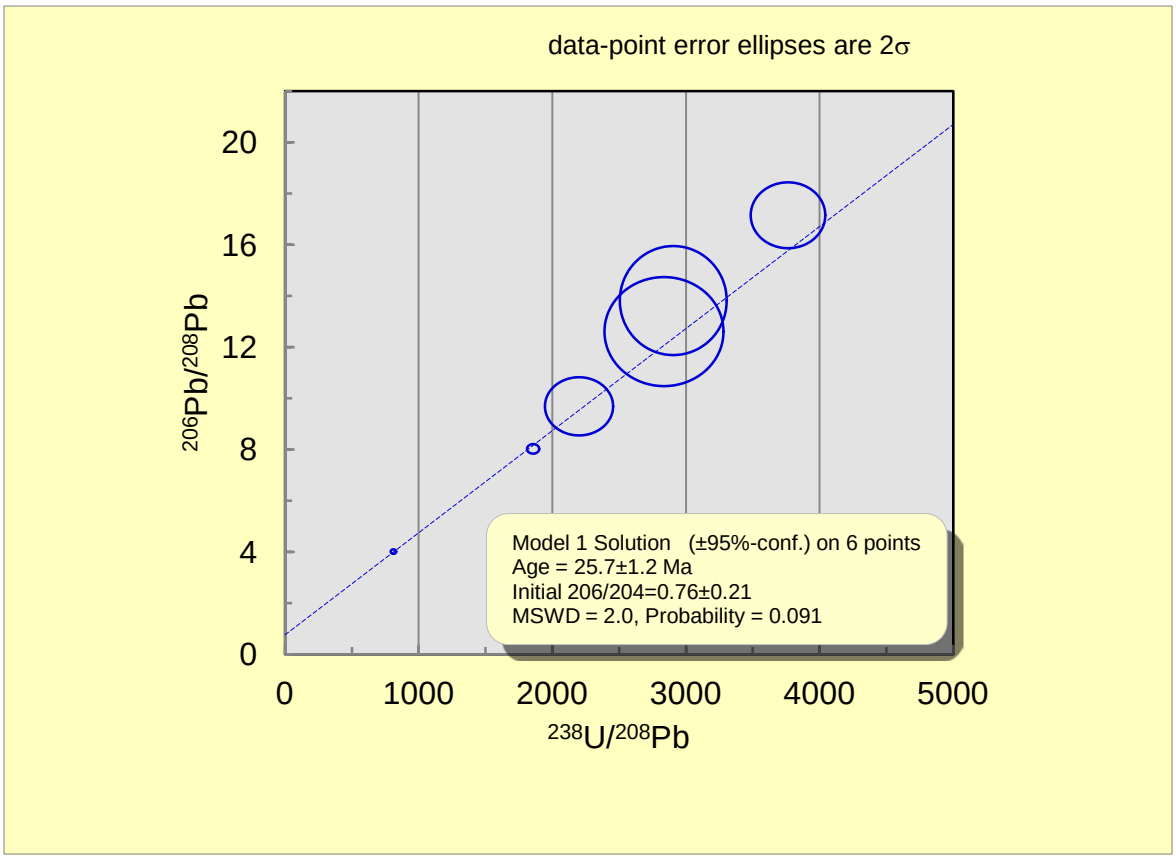
data-point error ellipses are 2σ
20
16
12
8
4
0
$^{206}Pb/^{208}Pb$
0
1000
2000
3000
4000
5000
$^{238}U/^{208}Pb$
Model 1 Solution (±95%-conf.) on 6 points
Age = 25.7±1.2 Ma
Initial 206/204=0.76±0.21
MSWD = 2.0, Probability = 0.091

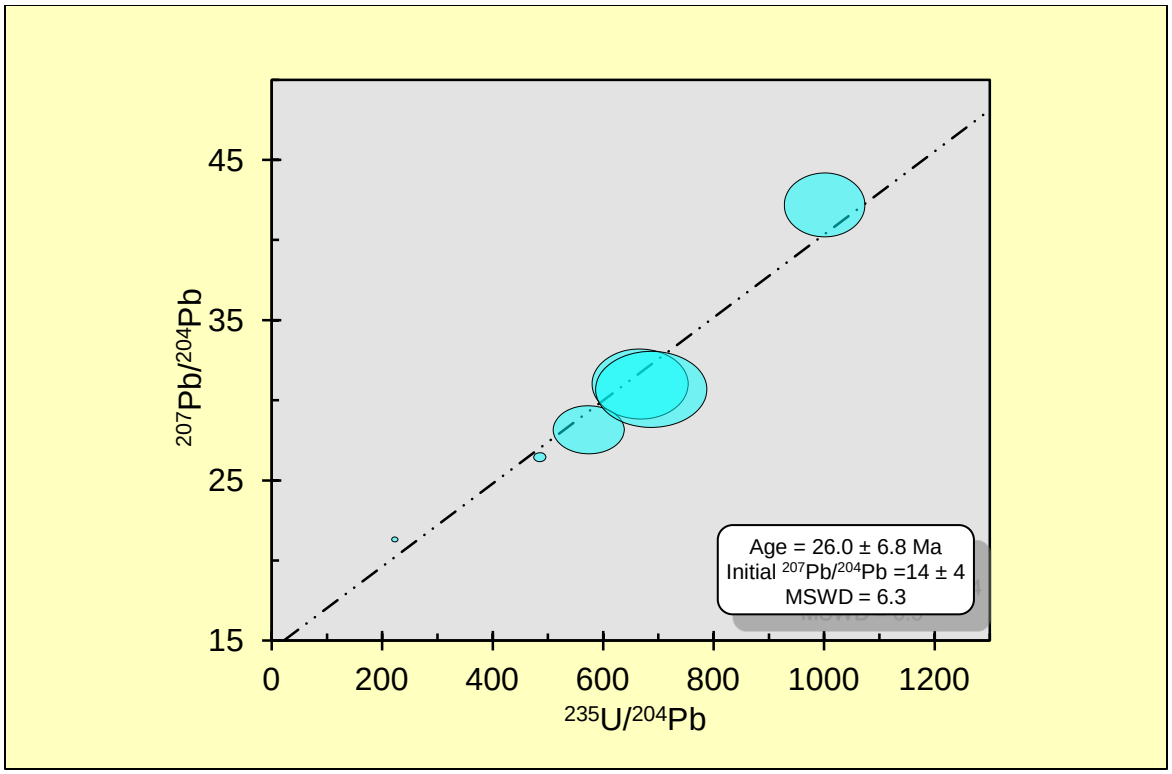
45
35
25
15
0
200
400
600
800
1000
1200
$^{207}Pb/^{204}Pb$
$^{235}U/^{204}Pb$
Age = 26.0 ± 6.8 Ma
Initial $^{207}Pb/^{204}Pb$ =14 ± 4
MSWD = 6.3

APPENDIX A.4 - SAMPLE DESCRIPTIONS AND TRIP REPORTS

A.4.1 - CAVE

Data, Trip Reports, and Sample Descriptions for Carlsbad Caverns have been redacted. These items are available upon request from the author.

A.4.2 - GUMO

Guadalupe Mountains National Park
Cave Sample Tracking Form

Collector Dave Decker
Principal Investigator Dave Decker
Permit Number GUMO-2011-SCI-0047

Cave Name GUMO-GEO-00111
Date Collected 1/3/2012

Sample Type

Mineral - Calcite Spar

Notes:
Sample collected from above a loose block of spar. Sample itself was also loose.

Equipment left in cave

Type	Tracking #	Date Removed
N/A		

Survey to Sample or Science Station

From Station	To Station (sample site)	Distance (m)	Azimuth (°)	Inclination (°)	Sample Notes
D2	D2a	3.3	325	+10	To intermediate station
D2a	D2b	4.0	220	+10	Sample was loose on top
					of a piece of the wall that
					had broken off.

Individual Sample Tracking

Sample Number	Amount of sample (kg)	Type of test	Date sample returned to park	Date results reported to park
GUMO-00549-001	2.05	U/Pb Dating		3/7/2012
		Sr Isotopes		
		FIA Analysis		
		O Isotopes		
		C Isotopes		

TRIP REPORT FORM

GUADALUPE MOUNTAINS NATIONAL PARK

DATE: 1/3/2012
ENTERED/EXITED: 12:10/12:50

PERMIT NUMBER: GUMO-2011-SCI-047

CAVE: GUMO-GEO-00111
SPECIFIC AREA: Above deer skull

TEAM LEADER: Dave Decker (Lead Investigator)
TEAM MEMBERS: Garrett Jorgensen (Logistical Support)

PURPOSE OF TRIP

SCIENCE (SPECIFY): Spar collection

Sample Name	Size (cm)	Weight (g)	Station	Distance (m)	Azimuth (°)	Inclination (%)
GUMO-00549-001	20X20X15	2050	D2	3.3	325	+10
			D2a	4.0	220	+10

NOTES:

I parked the Jeep at the double water tanks just past the Ship of the Desert. We left the car at approximately 10:40 and arrived at the cave at approximately 12:10. The hike was 1.5 miles with 1500 feet of elevation gain and took 1.5 hours. At the cave we donned helmets and conducted a quick recon trip into both sections. Garrett also explored above the left hand branch in the bell canopy, the lead noted on the map didn't go. I selected a chunk of spar approximately 20 cm by 20 cm by 15 cm, directly above the deer skull in the small alcove of the left hand branch. We then surveyed in two new stations, D2a and D2b in order to locate the collection spot (D2b). No graffiti, trash or other evidence of human

visitation was noted. No permanent survey markers were found, though all of the survey points were located. This cave is a large vug formed along two orthogonal joints. The cave is 95% covered in 3 to 4 cm long gray to yellow dog tooth spar. In some areas the spar has a secondary coating of flowstone, stalagmites or stalactites. Additionally, a red-brown mud covers the floor and overlies the spar. After approximately 40 minutes (12:50), we departed and made our way down toward another small cave. On the way we checked out a small void in the cliff on the south wall of the drainage, nothing of interest was noted. Once at this cave, we entered to look for spar, but found none. Lots of porcupine feces were seen, amberat was visible on several of the ledges along with possible ringtail cat feces. There was no graffiti, trash or other evidence of human visitation in this cave either, except a helmet mounted LED light found at the back of the cave. This was brought out and turned over to the park Geologist, Dr. Jonena Hearst. We spent about five minutes in this small cave and then made our way back down to the Jeep, arriving at approximately 14:20.

Guadalupe Mountains National Park
Cave Sample Tracking Form

Collector Dave Decker
Principal Investigator Dave Decker
Permit Number GUMO-2011-SCI-0047

Cave Name GUMO-GEO-00564
Date Collected 3/9/2012

Sample Type

Mineral - Calcite Spar

Notes:

Equipment left in cave

Type	Tracking #	Date Removed
N/A		

Survey to Sample or Science Station

From Station	To Station (sample site)	Distance (m)	Azimuth (°)	Inclination (°)	Sample Notes
A1	A1a	1.05	175	-5	Loose in ceiling

Individual Sample Tracking

Sample Number	Amount of sample (g)	Type of test	Date sample returned to park	Date results reported to park
GUMO-00549-002	1270	U/Pb Dating		5/9/2012
		Sr Isotopes		
		FIA analysis		
		O Isotopes		
		C isotopes		

Guadalupe Mountains National Park
Cave Sample Tracking Form

Collector Dave Decker
Principal Investigator Dave Decker
Permit Number GUMO-2011-SCI-0047

Cave Name GUMO-GEO-108
Date Collected 3/9/2012

Sample Type

Mineral - Calcite Spar

Notes:

Equipment left in cave

Type	Tracking #	Date Removed
N/A		

Survey to Sample or Science Station

From Station	To Station (sample site)	Distance (m)	Azimuth (°)	Inclination (°)	Sample Notes
Drip Line	N/A	0.61	005	N/A	Loose on floor

Individual Sample Tracking

Sample Number	Amount of sample (g)	Type of test	Date sample returned to park	Date results reported to park
GUMO-00549-003	625	U/Pb Dating		5/17/2012
		Sr Isotopes		
		FIA Analysis		
		O Isotopes		
		C Isotopes		

TRIP REPORT FORM

GUADALUPE MOUNTAINS NATIONAL PARK

DATE: 3/9/2012
PERMIT NUMBER: GUMO-2011-SCI-047

CAVE(S): GUMO-GEO-00564)/GUMO-GEO-108
SPECIFIC AREA: Camp Wilderness Ridge/Permian Reef Trail

TEAM LEADER: Dave Decker (Lead Investigator)
TEAM MEMBERS: Michael Queen (Support Team)
Garrett Jorgensen (Support Team)
Bill Mason (Support Team)

PURPOSE OF TRIP

SCIENCE (SPECIFY): Spar Collection

Sample Name	Size (cm)	Weight (g)	Station	Distance (m)	Azimuth (°)	Inclination (%)
GUMO-00549-002	15x10x8	1270	A1	3.45	175	-5
GUMO-00549-003	11x7x6	625	Dripline	2.00	005	N/A

NOTES:

The team left the McKittrick Canyon visitor's center at approximately 8:20 AM. The sky was overcast with a ceiling of approximately 1000 feet and temperature of 1° C. We followed the Permian Reef Trail (PRT) to the top where we left the trail heading south toward the USGS survey marker. Upon arrival we headed east down the ridge until we ran into a cliff, at which time we backtracked until we found a way down. We arrived at GUMO-GEO-00564 at approximately 12:30 PM. At the entrance of the cave we noted that there was no permanent cave marker. There were no signs of visitation, no graffiti and no trash. We could see the entrance of GUMO-GEO-00561, but couldn't access it without rigging a hand line, which we chose not to do. Upon entry into GUMO-GEO-00564, we noted that the entrance chamber was approximately 3 meters across by 10 meters

deep and 0.6 meters tall. There were mammillaries covering the walls and ceiling and in some locations, spar could be seen underneath the mammillaries. A thorough search of the cave was conducted to try to find loose spar, but none was found. A loose piece was, however, located in the ceiling about midway into the room from the entrance and behind a ceiling pendant. A chisel was used to pry the piece from its spot in the ceiling; the location was photographed and logged. We left the cave at approximately 1 PM and retraced our steps back to the PRT.

We followed the PRT back down to just below the cloud base where we again left the trail and followed the bottom of the cliff toward GUMO-GEO-00108, another small cave and GUMO-GEO-00106. At GUMO-GEO-00108, we noticed quite a bit of graffiti scratched into the walls, no trash and one bullet casing (caliber unknown). GUMO-GEO-00108 is a large vug breached by the cliff face approximately 240 meters below GUMO-GEO-00564. The surfaces of this cave were covered with spar and mammillaries and in some areas, cave rafts. The original void was then breached by the down cutting and formation of McKittrick Canyon. Spar is found in one small pocket on the cave wall, cave rafts in another. Cave mammillaries cover the entire ceiling and most of the walls and cover more spar. The floor of the cave is covered by broken mammillaries and spar, so it was a simple matter of choosing a good piece to collect from the floor. Once this was accomplished, the cave was photographed, the collection logged and we moved on. We spotted another small cave just a few meters away from GUMO-GEO-00108. Garrett was the only one of us that could fit into the small entrance, so we rigged a hand line and he climbed down the blind pit to look for more spar. None was noted, so he returned to the surface, we derigged the handline and moved on to a cave further down the cliff face. Bill volunteered to check this cave, and again, no spar was noted with a quick check into the entrance chamber. Due to the exposure of this entrance, we didn't push the cave to find the spar, since we already had two samples from other caves very nearby. We made our way back to the PRT and back to the visitor's center by 4:30 PM.

A.4.3 - BLMC

Bureau of Land Management – Carlsbad Field Office
Cave Sample Tracking Form

Collector Jim Goodbar Cave Name BLM-NM-023-0021
Principal Investigator Dave Decker Date Collected 11/18/2011
Permit Number BLM-2012-2

Sample Type

Mineral - Calcite Spar

Notes:

Equipment left in cave

Type	Tracking #	Date Removed
N/A		

Survey to Sample or Science Station

From Station	To Station (sample site)	Distance (m)	Azimuth (°)	Inclination (°)	Sample Notes
AB37					260 feet below datum

Individual Sample Tracking

Sample Number	Amount of sample (g)	Type of test	Date sample returned to BLM	Date results reported to BLM
BLMC-20122-001	29.5	U/Pb Dating		
BLMC-20122-002	22.2	U/Pb Dating		3/3/2012
BLMC-20122-003	15.7	U/Pb Dating		

Bureau of Land Management - Carlsbad Field Office
Trip Report

BLM Trip Report: CFO-2012-2-001

Date: 10/13/2011
Entered/Exited: 11:50/15:15
Total Trip Time: 3.4 hours

Cave Number: BLM-NM-CFO-0021

Participants: David Decker (Lead Investigator)
James Goodbar (Guide, Technical Support)
Patricia Seiser (Photographer)

Weather: Sunny, 70°F

Description: BLM-NM-CFO-0021 is a multi-level maze cave with abundant boneyard. The upper levels of the cave are accessible without a rope. The lower levels require a 50' handline for safety.

Purpose: This was a reconnaissance trip to the bottom of BLM-NM-CFO-0021 looking for possible areas of dogtooth spar to sample. No dogtooth spar was found. Some small nailhead spar was noted in the intermediate level of the cave. Other speleothems noted include corrosion residue, cave coral, "purple dots" (unknown mineral formation on the surface of flowstone), flowstone, aragonite needles, and sulfur deposits. Many fossils were noted in the intermediate level where there was little to no secondary deposits on the walls and ceiling, including a group of five unusual dome-shaped fossils approximately 15 - 20 cm in diameter.

Notes: The surface around the cave has been burned badly by a recent fire. Fauna noticed in the cave include Harvestman arachnids, two frogs (possibly Rio Grande Leopard Frog?), and crickets.

Bureau of Land Management – Carlsbad Field Office
Cave Sample Tracking Form

Collector Dave Decker Cave Name BLM-NM-060-030
Principal Investigator Dave Decker Date Collected 7/18/2012
Permit Number BLM-2012-2

Sample Type

Mineral - Calcite Spar

Notes: This cave has been heavily vandalized with numerous broken formations and trash. The bat counter solar panels have been shot out.

Equipment left in cave

Type	Tracking #	Date Removed
N/A		

Survey to Sample or Science Station

From Station	To Station (sample site)	Distance (m)	Azimuth (°)	Inclination (°)	Sample Notes
AB2	AB2a	0	0	0	Station AB2 was where
AB2	AB2b	0.2	345	0	the spar vugs were
					located, see attached map

Individual Sample Tracking

Sample Number	Amount of sample (g)	Type of test	Date sample returned to park	Date results reported to park
BLMC-20122-004	20g	U/Pb Dating		
BLMC-20122-005	25g	U/Pb Dating		8/17/2012

Bureau of Land Management - Carlsbad Field Office
Trip Report

BLM Permit No.: CFO-2012-2

Date: 20120718
Entered/Exited: 17:10/18:20
Total Trip Time: 1.2 hours

Cave Name: BLM-NM-060-030

Participants: David Decker (Lead Investigator)
Garrett Jorgensen (Technical Support)

Weather: 35° C, clear and sunny, no wind, low humidity.

Description: This is a small linear cave approximately 80 meters long with an entrance that is approximately a meter square underneath a mesquite tree. The cave trends generally to the east from the entrance. This cave is well known to the locals and shows signs of heavy use. There are broken bottles and trash in the cave, all of the formations have been broken or otherwise vandalized. The cave is developed along a ceiling joint which is also where the majority of the speleothems have formed. The terminal room is the largest in the cave and contains some breakdown. There is a beautiful nautiloid fossil (Bellerophontidae) in a small alcove near the back. The cave itself is rather warm and humid and at the time of the visit contained numerous Harvestmen, crickets and beetles. There were no bats in the cave, though there was a coating of guano on the floor in the back room, but it could not be determined how old it was.

Purpose: Purpose of the trip was to collect scalenohedral calcite spar from two small vugs located in a parallel side passage. Two samples were collected, one each from two separate vugs located within a meter of each other. Both samples were collected from inside their respective vugs from a location that is difficult to see from the

passage. The vugs have already sustained heavy damage from mineral collectors who left little available for scientific collection. Both samples fragmented upon collection (see photos in sample tracking form). Sample one (BLMC-20122-004) was a light yellow calcite with no visible inclusions, weighed20 grams and was approximately 3 x 3 x 2 cm before fragmentation. Sample two (BLMC-20122-005) was a clear color with numerous petroleum inclusions visible to the eye. It weighed 25 grams and was approximately 4 x 3 x 3 cm before it fragmented. This cave was resurveyed for the purpose of this collection. Both samples were collected from survey point AB2.

Notes: There is a bat counter in the entrance of the cave that is powered by a solar panel in the mesquite tree that grows at the entrance. The solar panel has been shot up and the bat counter appears to no longer be working.

Bureau of Land Management – Carlsbad Field Office
Cave Sample Tracking Form

Collector Dave Decker Cave Name BLM-NM-060-027
Principal Investigator Dave Decker Date Collected 3/12/2013
Permit Number BLM-2012-2

Sample Type

Mineral - Calcite Spar

Notes:

Equipment left in cave

Type	Tracking #	Date Removed
N/A		

Survey to Sample or Science Station

From Station	To Station (sample site)	Sample Notes
		This cave has not been surveyed and has no survey stations.
		Samples were collected from breakdown near the back of the
		cave.

Individual Sample Tracking

Sample Number	Amount of sample (g)	Type of test	Sample Notes
BLMC-20122-011	1000	U/Pb Dating	Brown to yellow etched spar
BLMC-20122-012	2600	U/Pb Dating	Sample has wall rock, spar and mammillary

Bureau of Land Management - Carlsbad Field Office
Trip Report - BLM-NM-023-027

BLM Permit No.: CFO-2012-2

Date: 20130312
Entered/Exited: 11:55/13:25
Total Trip Time: 1.5 hours

Cave Number: BLM-NM-023-027

Participants: David Decker (Lead Investigator)
Jim Goodbar (Guide, Technical Support)

Weather: Clear, wind 20 knots from the west, 60° F

Description: BLM-NM-060-027 Cave is a large (100 X 100 X 50 meters?), single room cavern, modestly decorated with large stalagmites (two of which are roughly 5 to 6 meters tall, all measurements are estimates), stalactites and curtains. The cave also contains pool fingers as well as remnant shelf stone, flowstone and rimstone dams. The largest dams were approximately 20 cm in height. There is currently no standing water in the cave. The spar lines all of the walls of the cave from floor to ceiling in the places where the wall rock has not spalled off. In the lower portions of the cave, the spar has been covered by mammillary calcite, which in turn, in many places, has been eroded away to reveal circular patterns with mammillary calcite on the outside and spar on the inside. It appears that this cavern is a large vug.

Purpose: Purpose of this trip was to collect scalenohedral spar for U-Pb dating, Sr geochemical analysis and fluid inclusion analysis. Two samples were collected, BLMC-20122-011 showed a deep brown color with etching, weighed 1 Kg and measured 6 X 10 X 13 cm. Sample BLMC-20122-012 included wall rock, spar and mammillary calcite, weighed 2.6 Kg and measured 10 X 15 X 15 cm. Both samples were

collected from breakdown near the rear of the lower section of the cave.

Notes: The cave had piles of deep bird guano in many places. There were also burned and broken yucca stumps in the cave that appeared to have been eaten. There were many footprints that looked like sheep or goat within the guano. An evaporated milk can that contained a register reported by Jim Goodbar on his last visit to the cave was searched for, but not located. No paleontological or archeological artifacts were noted other than a large tin can that appears to have been there for some number of years.

A.4.4 - USFS

US Forest Service – Guadalupe District
Cave Sample Tracking Form

Collector Dave Decker Cave Name FSGD-C-90
Principal Investigator Dave Decker Date Collected 1/5/2012
Permit Number USFS-11290

Sample Type

Mineral - Calcite Spar

Notes: Collected along route to Lake Room in lower level.

Equipment left in cave

Type	Tracking #	Date Removed
N/A		

Survey to Sample or Science Station

From Station	To Station (sample site)	Distance (m)	Azimuth (°)	Inclination (°)	Sample Notes
P2	-001	11.21	179.0	+9.0	USFS-11290-001
P2	-002	11.21	179.0	+9.0	USFS-11290-002
P2	-003	3.0	090.0	-29.0	USFS-11290-003
Pw	-004	7.0	075.0	-23.0	USFS-11290-004

Individual Sample Tracking

Sample Number	Amount of sample (g)	Type of test	Date sample returned to USFS	Date results reported to USFS
USFS-11290-001	205	U/Pb Dating	N/A	
USFS-11290-002	105	U/Pb Dating	N/A	3/8/2012
USFS-11290-003	710	U/Pb Dating	N/A	
USFS-11290-004	1,220	U/Pb Dating	N/A	

US Forest Service - Guadalupe District
Trip Report

USFS Permit No.: USFS-11290

Date: 1/5/2012
Entered/Exited: 11:40/15:10
Total Trip Time: 3.5 hours

Cave Name: FSGD-C-90

Participants: David Decker (Lead Investigator)
Jason Walz (Guide, Photographer)
Michael Queen (Scientific Support)
Garrett Jorgensen (Technical Support)

Weather: Clear, 50°F, no precipitation,

Description: FSGD-C-90 is developed in two directions. The main corridor is a large, three level sloping trunk passage, heavily decorated, developed along the reef front. Three secondary passages are developed orthogonal to the main passage and are deep rifts. FSGD-C-90 is, at minimum, a second generation cave, as the main cave passage cuts across brecciated fill that has been cemented together by calcite spar. The cave is located at the contact of the Capitan Limestone and the Seven Rivers formation. On this trip, we entered the cave and then rappelled the 70' drop to the lower level where we took the marked trail toward the Lake Room. We looked for spar along the way, but all we noted was the spar that cements the breccia together. Near survey station P2, we located a vug that contained large (3 to 30 cm) scalenohedral dogtooth spar crystals. The vug was located on top of a breakdown block. Upon looking up, we noticed that the rest of the vug was in the ceiling of the room we were in and actually ran quite a distance. It was evident that the spar had formed in a fracture striking 040°, parallel to the main passage trend. This fracture was filled with spar crystals and ran for approximately 10 meters. Four samples were collected (Figure 1a, 1b, 1c &

1d), cataloged and bagged for return to the surface. We then continued to the Lake Room so that Jason could evaluate the need for restoration of the route and determine if the route was suitable for recreational trips. The return to the surface was uneventful, the entire trip took 3.5 hours.

Purpose: Purpose of the trip was to collect dog tooth spar samples for U-Pb age dating and evaluate the route for restoration recreation. Four samples were collected: USFS-11290-001 (205 g, 8x6x3 cm), -002 (105 g, 6x4.5x3 cm), -003 (710 g, 18x8x6 cm) & -004 (1220 g, 15x8x7 cm). The nearest survey marker was P2, see sample collection form for azimuth, elevation and distance for each sample collection point.

Notes: None.

US Forest Service – Guadalupe District
Cave Sample Tracking Form

Collector Dave Decker Cave Name FSGD-C-202
Principal Investigator Dave Decker Date Collected 3/11/2012
Permit Number USFS-11290

Sample Type

Mineral - Calcite Spar

Notes:

Equipment left in cave

Type	Tracking #	Date Removed
N/A		

Survey to Sample or Science Station

From Station	To Station (sample site)	Distance (m)	Azimuth (°)	Inclination (°)	Sample Notes
					Cave unsurveyed
					Sample taken from
					directly below the drop
					under an overhang to the
					right as you're looking at
					the entrance

Individual Sample Tracking

Sample Number	Amount of sample (g)	Type of test	Date sample returned to USFS	Date results reported to USFS
USFS-11290-006	740	U/Pb Dating		7/21/2012

US Forest Service - Guadalupe District
Trip Report

USFS Permit No: USFS-11290

Date: 20120312
Entered/Exited: 15:15/16:45
Total Trip Time: 1.5 hours

Cave Name: FSGD-C-202

Participants: David Decker (Lead Investigator)
Michael Queen (Technical Support)
Garrett Jorgensen (Logistics Support)

Weather: Clear, 80° F, slight breeze

Description: FSGD-C-202 is located at the base of a cliff on the north side of one of the smaller ridges between Guadalupe Ridge and Lonesome Ridge. The cave is developed along a fracture and has at least two levels. FSGD-C-202 is moderately decorated with stalactites, stalagmites and dog tooth spar. The dog tooth spar ranges in size from 2 to 30 centimeters in length (Figure 61). The spar is concentrated in a small room in the bottom of the cave that is approximately 1.8 meters wide, 6 meters long and 8 meters high. The route out to FSGD-C-202 is approximately 3.6 kilometers, one way, through thick brush and down steep ledges. The last 120 meters of elevation loss in nearly straight down along a treacherous, extremely steep descent through very heavy brush. A hand line may be required for the last part, which is a 10 meter climb down over a cliff. Once at the cave, there are two small entrances, both require climbing up into the cave, but can be done without rigging. Both entrances lead to the same pit which is a 2.5 meter climb down to a small room and then a drop off of approximately six meters into the lower level of the cave. A 15 meter rope or longer is required for rigging the drop to the lower level.

Purpose: The purpose of the trip was to collect dog tooth spar for uranium-lead dating, fluid inclusion analysis and stable isotope analysis. One sample was collected from the bottom of the drop (this cave has not been surveyed, so no survey stations were available for a reference). Sample USFS-11290-006 weighed 740 g. A sample of surface spar was also collected on this trip. Sample USFS-11290-005 weighed 320 g.

Notes: At the time of this visit, the log contained the names of only two other groups, one lead by Victor Polyak, the other by Aaron Stockton.

Photos:

Figure 60: In situ spar in FSGD-C-202, Guadalupe Mountains, New Mexico. (Photo Credit: Dave Decker).

US Forest Service – Guadalupe District
Cave Sample Tracking Form

Collector Dave Decker Cave Name FSGD-C-72
Principal Investigator Dave Decker Date Collected 3/12/2012
Permit Number USFS-11290

Sample Type

Mineral - Calcite Spar

Notes:

Equipment left in cave

Type	Tracking #	Date Removed
N/A		

Survey to Sample or Science Station

From Station	To Station (sample site)	Distance (m)	Azimuth (°)	Inclination (°)	Sample Notes
H4	H4a	0.30	320	-5	Sample loose in wall
					Swallow tail twinning

Individual Sample Tracking

Sample Number	Amount of sample (g)	Type of test	Date sample returned to USFS	Date results reported to USFS
USFS-11290-007	360	U/Pb Dating		7/21/2012

US Forest Service - Guadalupe District
Trip Report

USFS Permit No: USFS-11290

Date: 20120313
Entered/Exited: 10:20/11:00
Total Trip Time: 0.7 hours

Cave Name: FSGD-C-72

Participants: David Decker (Lead Investigator)
Jason Walz (Guide, Technical Support)
Garrett Jorgensen (Technical Support)

Weather: Sunny, clear, slight breeze, approximately 72° F/20° C.

Description: FSGD-C-72 is a large vug cave further developed along a fracture parallel to the reef front. The cave is heavily decorated with stalactites and stalagmites toward the back of the entrance chamber and the walls near the front of the entrance chamber are coated in scalenohedral dog tooth spar ranging in size from four to thirty centimeters. Some of the spar exhibits swallow-tail twinning. All of the speleothems in the cave are heavily corroded. The entrance to FSGD-C-72 is located on a steep south facing slope and is difficult to see due to the orientation of the opening. The cave has a 30- to 40-foot (9 – 12-meter) drop directly inside the entrance and requires a 100' rope minimum due to rigging restrictions. The drop was rigged to a small bush several meters downslope from the entrance using both friction on the surface and a wrap around the trunk of the bush as an anchor. Due to the orientation of the entrance, a substantial amount of sunlight shines into the entrance chamber allowing a great deal of moss to grow on the walls (the origin of the name perhaps?).

Purpose: Purpose of the trip was to collect a sample of the dog tooth spar located in the cave for U-Pb dating. A sample

(USFS-11290-007) was located at the base of the drop, underneath the overhang toward the southwest. The sample was loose in the wall and exhibits the swallow-tail twinning mentioned above. The sample was 14 X 7 X 4 cm and weighed 360 g.

Notes: The log was signed after collection of the sample and we departed the cave. Garrett explored a little, but did not go beyond daylight.

US Forest Service – Guadalupe District
Cave Sample Tracking Form

Collector Dave Decker
Principal Investigator Dave Decker
Permit Number USFS-11290

Cave Name FSGD-C-40
Date Collected 10/13/2012

Sample Type

Mineral - Calcite Spar

Notes:

Equipment left in cave

Type	Tracking #	Date Removed
N/A		

Survey to Sample or Science Station

From Station	To Station (sample site)	Distance (m)	Azimuth (°)	Inclination (°)	Sample Notes
N/A	N/A	--	--	--	Collected from underneath large breakdown block in second

Individual Sample Tracking

Sample Number	Amount of sample (g)	Type of test	Date sample returned to USFS	Date results reported to USFS
USFS-11290-008	42.5	U/Pb Dating		

US Forest Service - Guadalupe District
Trip Report

USFS Permit No: USFS-11290

Date: 20121013
Entered/Exited: 12:15/14:45
Total Trip Time: 2.5 hours

Cave Name: FSGD-C-40

Participants: David Decker (Lead Investigator)
Jason Walz (Guide, Technical Support)
Michael Queen (Guide, Technical Support)
Jed Haldeman (Photographer)

Weather: Partly cloudy, 16.1 °C, high winds (approximately 50 kph with up to 95 kph gusts.

Description: FSGD-C-40 is a small cave located approximately 150 meters below the ridge crest, one mile south of the parking area (Figure 62). There is a 12 meter drop into the entrance room. A 33 meter rope is sufficient to tie off to a large boulder at the lip and then use as a hand line to cross a ledge that leads to a small alcove where the drop can be safely rigged from a 30 cm diameter column. There are four rooms to this cave. The entrance room is a large chamber with a breakdown pile near the entrance drop. The rest of the room is floored with deep bird guano. A small room and side passage near the top of the breakdown pile on the west side of the entrance chamber were given a cursory look, but not fully explored. Midway along the entrance chamber on the west side, a hand line was rigged on a stalactite to facilitate the climb down into the third chamber. This chamber was moderately decorated and also floored with bird guano. A large breakdown block with small passages underneath was the main feature of this room. Beneath this breakdown block is where the spar is located. The spar covers the ceiling of the room created by the breakdown block and is small mm

to cm size euhedral scalenohedral crystals. A 3 X 3 X 5 cm group of loose crystals was collected from a crack in the floor. A fourth large room was located to the southwest of the third room. This fourth room was heavily decorated with flow stone, helictites, totem pole stalactites (one of which reached at least 3.7 meters tall) and popcorn. There are three entrances to this room from the third room, a low crawl through popcorn, probably the quickest and safest route, a steep climb down through delicate totem pole stalactites which has high potential for damage; and a longer crawl route that passes by a breathing hole with a breath frequency of approximately 20 breaths per minute. This caught us off guard as it sounded like either a person or other large mammal breathing right in your ear!

Purpose: Purpose of the trip was to collect spar for the Guadalupe Spar Project. One sample was collected (USFS-11290-008), a group of euhedral, scalenohedral crystals (one doubly terminated) approximately 3 X 3 x 5 cm and weight 42.5 grams. This cave has not been surveyed, but the sample was collected at the location noted above.

Notes: A bird skeleton was noted in a crack in the floor in the third room. A snake skeleton and a rusty tin can were noted on the west side of the entrance chamber near the top of the breakdown pile. A small vug like opening approximately two meters off the breakdown pile on the east side of the entrance chamber contained an unusual speleogen that is possibly etched coral? See Figure 63 below.

Photos:

Figure 61: Trip participants from left to right: Jed Haldeman, Jason Walz, Michael Queen, Dave Decker (not pictured).

Figure 62: Odd texture in ceiling of 1.5 X 1.5 X 1.5 meter vug on east side of entrance chamber approximately two meters off of the breakdown pile. Photo is approximately 25 cm across. (Photo credit: Dave Decker)

US Forest Service – Guadalupe District
Cave Sample Tracking Form

Collector Dave Decker
Principal Investigator Dave Decker
Permit Number USFS-11290

Cave Name FSGD-C-62
Date Collected 1/5/2013

Sample Type

Mineral - Calcite Spar

Notes: Sample taken from small vug at the entrance of FSGD-C-62. Sample was found laying loose on the floor of the vug (Figure 63).

Equipment left in cave

Type	Tracking #	Date Removed
N/A		

Survey to Sample or Science Station

From Station	To Station (sample site)	Distance (m)	Azimuth (°)	Inclination (°)	Sample Notes

Individual Sample Tracking

Sample Number	Amount of sample (g)	Type of test	Date sample returned to USFS	Date results reported to USFS
USFS-11290-009	239.4	U/Pb Dating		

Sample Photo:

Figure 63: Spar sample and collection location, FSGD-C-62, Guadalupe Mountains, New Mexico. (Photo credit: Dave Decker)

US Forest Service - Guadalupe District
Trip Report

USFS Permit No: USFS-11290

Date: 20130105
Entered/Exited: 13:30/14:30
Total Trip Time: 1.0 hour in cave (hike up: 2.5 hours, hike down: 1.0 hour)

Cave Name: FSGD-C-62

Participants: David Decker (Lead Investigator)
Jason Walz (Guide, Technical Support)
Tami Walz (Field Assistant)
Brent Hall (Photographer)
Jeramiah Johnson (Photographer's Assistant)

Weather: Clear, 42° F/ 5.5° C, Wind 10 knots out of the SSE, 5" of snow on the ground which had melted in the areas that received sun, but not in the shade.

Description: FSGD-C-62 is a large opening in the cliff side 750' above the wash in Black Canyon (Figure 64). It is reached via a steep (52° maximum incline) one mile hike/scramble from the wash through scrub and cactus. The main part of the cave is a large, dome shaped passage with two large stalagmites near the back. Each of these stalagmites is easily 5 meters tall, but were not formally measured during this trip. The back of the cave slopes down in dirt floored passage and ends abruptly. It looks as if a dig could open it up to more cave. The walls of the cave are covered in rhodochrosite ($MnCO_3$) which give a pink hue to the walls. There are two holes in the floor near the entrance, both of which lead down. The one nearest the south wall has white, opaque spar lining. The passage continues down in a too-tight hole floored with sharp gravel. The second hole (near the middle of the main passage) blows a substantial amount of warm air. The ceiling of this passage is covered with 20 cm diameter mammillaries that in turn cover white, opaque spar. This room has another body size passage

leading through the floor from which the air was coming. It is obvious that this passage continues, but due to lack of time we had to abandon the lead. The main passage is very flat floored and alternates between soil and breakdown. The soil is imprinted almost everywhere with goat tracks and goat feces are prevalent. No bats or other animals were noted in the cave at the time we were there. Beneath the entrance to FSGD-C-62, there are numerous small (10 centimeter to 3 meter) spar vugs with translucent to opaque white scalenohedral dog tooth spar (Figure 65).

Purpose: The sample collected during this trip was found laying loose on the floor of one of these small vug. The sample collected (USFS-11290-009) was approximately 5 X 4 X 4 cm and weighed 239.4 grams. This sample has been exposed to the elements.

Notes: One instance of graffiti was noted near the back of the cave: "Donnie1976". One piece of wood with burned ends and a small drill hole was also found near the north side, close to the entrance.

Photos:

Figure 64: Entrance to FSGD-C-62. (Photo credit: Dave Decker)

Figure 65: Scalenohedral dogtooth spar in small vug near entrance. (Photo credit: Dave Decker)

Figure 66: Rhodochrosite on wall of FSGD-C-62. (Photo credit: Brent Hall, Lightbender's Visuals)

US Forest Service – Guadalupe District
Cave Sample Tracking Form

Collector Dave Decker
Principal Investigator Dave Decker
Permit Number USFS-11290

Cave Name FSGD-C-011
Date Collected 11/15/2014

Sample Type

Mineral - Calcite Spar

Notes:

Equipment left in cave

Type	Tracking #	Date Removed
N/A		

Survey to Sample or Science Station

From Station	To Station (sample site)	Distance (m)	Azimuth (°)	Inclination (°)	Sample Notes
					No survey stations noted
					Sample was collected
					Loose from a 0.5 meter
					Vug on a large rock at
					The back of the cave. See
					Attached sketch for
					Approximate location

Individual Sample Tracking

Sample Number	Amount of sample (g)	Type of test	Date sample returned to USFS	Date results reported to USFS
USFS-11290-010	47	U/Pb Dating		

US Forest Service - Guadalupe District Trip Report

USFS Permit No: USFS-11290

Date: 20141115
Entered/Exited: 12:30/15:00
Total Trip Time: 2.5 hours

Cave Name: FSGD-C-011

Participants: David Decker (Lead Investigator)
Kevin Lorms (Technical Support)
Chris Sipfle (Technical Support, Undergraduate Student)
Jenna Burgess (EMS, Undergraduate Student)
Chrissy Allen (Graduate Student)
Justin Peinado (Graduate Student)

Weather: Clear day with few clouds. Temperature approximately 55 to 60 degrees Fahrenheit. Winds 25 to 30 knots from the southwest.

Description: FSGD-C-011 is a large entrance facing east on the side of cliff. The cave is aligned SE-NW along the same trend as the surface valleys and is cut orthogonally by two parallel fractures that also parallel the reef front. It appears to be of sulfuric acid speleogenetic origin and truncates small (10 to 50 cm) voids that contain scalenohedral dogtooth spar anywhere from 2 to 10 cm along the C-axis. These vugs are also in much of the breakdown that floors the cave. The cave has active formations in the lower, back section, but also many dead, dry formations.

Purpose: This trip was to collect a sample of the dogtooth spar for the purpose of U-Pb dating, $\delta^{18}O$, $\delta^{13}C$, and $\delta^{88}Sr$ analysis and fluid inclusion assemblage analysis under permit USFS-11290. One piece of spar was collected from a 0.5 meter vug in a large breakdown block at the back of the cave (Figure 70). The piece collected was already loose and did not require any mechanical means to

remove it. The sample is designated sample USFS-11290-010, is 470 grams and 70 x 120 x 55 mm. We were to also look for bats, only one was spotted and that was on a breakdown block near the back of the cave. An identification of the bat was not attempted, but it appeared to be a Little Brown. Fresh guano was noted.

Notes: In addition to the bat, two mummified Barbary sheep were located at the back of the cave as well as many pieces of wood with burned tips. One word of graffiti was also noted on a breakdown block near the middle of the cave before dropping off into the back. It was five or six letters long, appeared to be in pencil, but was unreadable. A great deal of speleothem breakage was noted, mostly stalagmites, but also some stalactites and columns. Breakage appears to be natural. The cave is obviously used by the Barbary sheep as a sheltering location as footprints and sheep dung abounded. One bird was heard within the cave, but not seen or identified.

Photos:

Figure 67: Participants from left to right: Jenna Burgess, Kevin Lorms, Chrissy Allen, Chris Sipfle, Justin Peinado. Not pictured, Dave Decker. (Photo credit: Dave Decker)

Figure 68: Typical Vug in breakdown block. (Photo credit: Dave Decker)

Figure 69: Sunset hiking out from the cave. (Photo credit: Dave Decker)

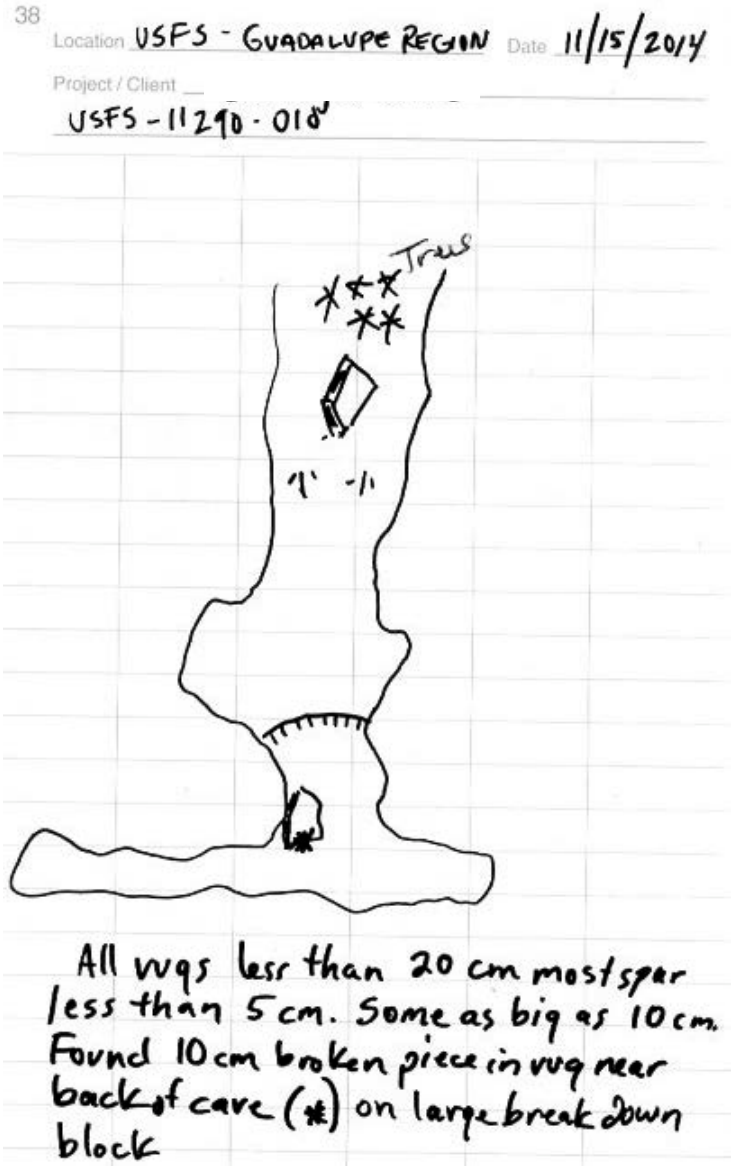

Figure 70: Sketch of FSGD-C-011 to show approximate location where sample was collected. This sketch is NOT to scale.

APPENDIX A.5 - DESCRIPTION OF COLLECTION LOCATIONS

Designations are regional, not specific caves. See detailed description for cave number associated with the sample number (CAVE: Carlsbad Caverns National Park; GUMO: Guadalupe Mountains National Park; BLMC: Bureau of Land Management, Carlsbad Field Office; USFS: US Forest Service, Guadalupe District).

CAVE-02399-002: Small[1] vug exposed in fracture in intermediate level of CAVE-C-1 truncated by later cave formation. Spar of centimeter size. Elevation of sample is approximately 1115 meters above sea level (mASL).

CAVE-02399-003: Small to medium[2] vugs exposed in bone yard at bottom of medium sized room in the intermediate level of CAVE-C-1, room truncated by later cave formation. Spar of decimeter size. Elevation of sample is approximately 1095 mASL.

CAVE-02399-004: Large[3] vug, heavily encrusted with large (decimeter) spar crystals in the upper levels of CAVE-C-5 truncated by later cave formation. Elevation of sample is approximately 1330 mASL.

CAVE-02399-006: Spar encrusting small vugs and fractures in the intermediate level of CAVE-C-5 exposed by later cave formation. Spar of centimeter size. Elevation of sample is approximately 1050 mASL.

CAVE-02399-007: Spar encrusting small vugs and fractures in the intermediate level of CAVE-C-1 exposed by later cave formation. Spar of centimeter to decimeter size. Elevation of sample is approximately 1205 mASL.

CAVE-02399-008: Spar encrusting very small vug in the lower level of CAVE-C-1 truncated by later cave formation. Spar of millimeter to centimeter size. Elevation of sample is approximately 1135 mASL.

CAVE-02399-009: Spar encrusting small vugs and fractures in the intermediate to lower level of CAVE-C-5 truncated by later cave formation. Spar of centimeter size. Elevation of sample is approximately 1075 mASL.

CAVE-02399-011: Two large vugs heavily encrusted with large (decimeter) spar crystals. Vugs exposed by canyon down cutting and surface erosion. CAVE-C-10. sample location is half-way up a ridge at approximately 1630 mASL.

BLMC-20122-002: Collection site not seen directly by author, collection made by BLM representative on author's behalf. Spar of centimeter size. BLM-NM-060-0021. Sample elevation approximately 1030 mASL.

BLMC-20122-005: Small spar encrusted vugs truncated by later cave formation. Spar is of centimeter size with visible petroleum inclusions. BLM-NM-060-0030. Sample location is approximately 1085 mASL.

BLMC-20122-011: Large vug truncated by canyon down-cutting and surface erosion. Spar is of the "linoleum spar" variety, heavily corroded, most probably by later sulfuric acid speleogenesis. BLM-NM-060-27. Sample location near the top of the Guadalupe escarpment at approximately 1975 mASL.

USFS-11290-002: Small vugs truncated by later cave formation in the intermediate level of the cave. Spar of decimeter size. FSGD-C-90. Sample elevation approximately 2035 mASL.

USFS-11290-006: Intermediate[2] vug truncated by canyon down-cutting and surface erosion. Spar of decimeter size. FSGD-C-202. Sample location at approximately 1855 mASL.

USFS-11290-007: Intermediate vug truncated by canyon down-cutting and surface erosion. Spar of decimeter to meter size. Spar exposed to sunlight had moss or algae growing on it. Some spar crystals were swallow tail twins. Much of the spar was heavily corroded, most likely from subsequent sulfuric acid speleogenesis. FSGD-C-72. Sample location at approximately 2040 mASL.

USFS-11290-008: Intermediate vug truncated by subsequent cave formation. Spar of centimeter size. FSGD-C-211. Sample location at approximately 1805 mASL.

USFS-11290-009: Spar in small vugs beneath the entrance of the cave, possibly in break down. Vugs are exposed at the surface and truncated by surface erosion. Spar is of centimeter size. FSGD-C-62. Sample location at approximately 1815 mASL.

GUMO-00549-001: Intermediate vug in two orthogonal passages entirely encrusted with centimeter size spar crystals located near the top of the Guadalupe escarpment. GUMO-GEO-00111. Sample location at the top of the Guadalupe escarpment at approximately 2080 mASL.

GUMO-00549-002: Small vug truncated by canyon down-cutting. Spar was acicular and centimeter in size. GUMO-GEO-00564. Sample location at the top of the Guadalupe escarpment at approximately 2065 mASL.

GUMO-00549-003: Intermediate vug truncated by canyon down-cutting. Spar was acicular and centimeter in size. GUMO-GEO-00108. Sample location in the middle of the Guadalupe escarpment at approximately 1946 mASL.

GUPA-00001-001: Laminar spar collected from a fault exposed in a road cut through the Castile formation by second author. First author has not personally seen the site. Elevation approximately 1650 mASL.

CC-001: Mammillary formation collected from lower levels of CAVE-C-1. First author has not personally seen the site. From photographs of the collection site, it appears to be an intermediate size room covered in mammillary calcite with a small pool at the bottom. Sample elevation approximately 1010 mASL.

1. Small vug defined as a vug with a volume of less than 10 m^3.
2. Intermediate vug with a volume of between 10 m^3 and 100 m^3.
3. Large vug defined as a vug with a volume of greater than 100 m^3.
4. All samples were encrusted with a thin outer layer of hydrated calcite. This layer has not yet been dated.

REFERENCES

Albarede, F., 2006, Geochemistry, An Introduction, Cambridge, UK, Cambridge University Press, 248 p.:

Alkattan, M., Oelkers, E. H., Dandurand, J.-L., and Schott, J., 1998, An experimental study of calcite and limestone dissolution rates as a function of pH from -1 to 3 and temperature from 25 to 80 C: Chemical Geology, v. 151, p. 199 - 214.

Andre, B. J., and Rajaram, H., 2005, Dissolution of limestone fractures by cooling waters: Early development of hypogene karst systems: Water resources research, v. 41, no. 1.

André, L., Audigane, P., Azaroual, M., and Menjoz, A., 2007, Numerical modeling of fluid–rock chemical interactions at the supercritical CO< sub> 2</sub>–liquid interface during CO< sub> 2</sub> injection into a carbonate reservoir, the Dogger aquifer (Paris Basin, France): Energy Conversion and Management, v. 48, no. 6, p. 1782-1797.

Asmerom, Y., Polyak, V., Schwieters, J., and Bouman, C., 2006, Routine high-precision U–Th isotope analyses for paleoclimate chronology: Geochemica et Cosmochimica Acta, v. 70, no. 18, p. A24.

Asmerom, Y., Polyak, V. J., and Lachniet, M. S., 2017, Extrapolar climate reversal during the last deglaciation: Scientific Reports, v. 7, p. 1 - 7.

Austin, G. S., 1978, Geology and mineral deposits of Ochoan rocks in Delaware Basin and adjacent areas, Socorro, NM, New Mexico Bureau of Mines and Mineral Resources, 88 p.:

Bakalowicz, J. M., Ford, D. C., Miller, T. E., Palmer, A. N., and Palmer, M. V., 1987, Thermal genesis of dissolution caves in the Black Hills, South Dakota: Geological Society of America Bulletin, v. 99, p. 729 - 738.

Baldridge, S. W., Olsen, K. H., and Callender, J. F., 1984, Rio Grande Rift: Problems and Perspectives: Los Alamos National Laboratories

New Mexico Museum of Natural History.

Banner, J. L., Musgrove, M., Asmerom, Y., Edwards, R. L., and Hoff, J. A., 1996, High-resolution temporal record of Holocene ground-water chemistry: Tracing links between climate and hydrology: Geology, v. 24, p. 1049 - 1053.

Barker, C. E., and Pawlewicz, M. J., 1987, The effects of igneous intrusions and higher heatflow on the thermal maturity of Leonardian and younger rocks, western Delaware Basin, Texas, *in* Cromwell, D. W., and Mazullo, L., eds., Glass Mountains, Society of Economic Paleontologists and Mineralogists, p. 69 - 83.

Barker, D. S., Long, L. E., Hoops, G. K., and Hodges, F. N., 1977, Petrology and Rb-Sr isotope geochemistry of intrusions in the Diablo Plateau, northenr Trans-Pecos magmatic province, Texas and New Mexico: Geological Society of America Bulletin, v. 88, no. 10, p. 1437 - 1446.

Barnes, V. E., 1983, Geologic Atlas of Texas, Van Horn and El Paso Sheet: Texas Bureau of Geology.

Befus, K. S., Hanson, R. E., Lehman, T. M., and Griffin, W. R., 2008, Cretaceous basaltic phreatomagmatic volcanism in West Texas: Maar complex at Pena Mountain, Big Bend National Park: Journal of Volcanology and Geothermal Research, v. 173, p. 245 - 264.

Belski, D., 1993, Parks Ranch Cave System: National Speleological Society.

Blakey, R. C., and Middleton, L. T., 2012, Geologic History and Paleogeography of Paleozoic and Mesozoic Sedimentary Rocks, Eastern Grand Canyon, Arizona, *in* Timmons, J. M., and Karlstrom, K., E., eds., Grand Canyon Geology -Two Billion Years of Earth's History, Volume 489: Boulder, CO, Geological Society of America, p. 81 - 92.

Böhm, F., Eisenhauer, A., Tang, J., Dietzel, M., Krabbenhöft, A., Kisakürek, B., and Horn, C., 2012, Strontium isotope fractionation of planktic foraminifera and inorganic calcite: Geochimica et Cosmochimica Acta, v. 93, no. 0, p. 300-314.

Bourg, I. C., Richter, F. M., Christensen, J. N., and Sposito, G., 2010, Isotopic mass dependence of metal cation diffusion coeffecients in liquid water: geochemica et Cosmochimica Acta, v. 74, p. 2249 - 2256.

Box, E. T., 2014, The Engineering Toolbox, Volume 2014.

Breyer, J. A., Busbey, A. B., Hanson, R. E., Befus, K. E., Griffin, W. R., Hargrove, U. S., and Bergman, S. C., 2007, Evidence for Late Cretaceous Volcanism in Trans-Pecos Texas: The Journal of Geology, v. 115, p. 243 - 251.

Brown, K. L., and Simmons, S. F., 2003, Precious metals in high-temperature geothermal systems in New Zealand: Geothermics, v. 32, no. 4-6, p. 619 - 625.

Budd, D. A., Frost, E. L., Huntington, K. W., and Allwardt, P. E., 2013, Syndepostional Deformation Features in High-Relief Carbonate Platforms: Long-Lived Conduits for Diagenetic Fluids: Journal of Sedimentary Research, v. 82, p. 12 - 36.

Burke, W. H., Denison, R. E., Hethreington, E. A., Koepnick, R. B., Nelson, H. F., and Otto, J. B., 1982, Variations of seawater 87Sr/86Sr throughout Phanerozoic time: Geology, v. 10, p. 516 - 519.

Calzia, J. P., and Hiss, W. L., 1978, Igneous Rocks in Northern Delaware Basin, New Mexico and Texas: New Mexico Bureau of Mines and Mineral Resources, v. 159, p. 39 - 45.

Cather, S. M., Chapin, C. E., and Kelley, S. A., 2012, Diachronous episodes of Cenezoic erosion in southwestern North America and their relationship to surface uplift, paleoclimate, paleodrainage, and paleoaltimitry: Geosphere, v. 8, no. 6, p. 1177 - 1206.

Chamberlin, R. M., Chapin, C. E., and McIntosh, W. C., 2002, Westward migrating ignimbrite calderas and a large radiating mafic dike swarm of Oligocene age, central Rio Grande Rift, New Mexico: Surface expression of an upper mantle diapir?, Geological Society of America Annual Meeting: Denver, CO.

Chapin, C. E., 1989, Volcanism along the Socorro accomodation zone, Rio Grande rift, New Mexico: New Mexico Bureau of Mines and Mineral Resources, v. 46, p. 46 - 57.

Chapin, C. E., and Cather, S., 1994, Tectonic settings of the axial basins of the northern and central Rio Grande rift: Geological Society of America Special Papers, v. 291, p. 5 - 26.

Chapin, C. E., Wilks, M., and McIntosh, W. C., 2004, Space-time patterns of Late Cretaceous to present magmatism in New Mexico - comparison with Andean volcanism and potential for future volcanism: New Mexico Bureau of Geology & Mineral Resources, v. 160, p. 13-40.

Cheng, H., Edwards, R. L., Shen, C.-C., Polyak, V. J., Asmerom, Y., Woodhead, J., Hellstrom, J., Wang, Y., Kong, X., Spotl, C., Wang, X., and Alexander, E. C., 2013, Improvements in 230Th dating, 230Th and 234U half-life values,and U–Th isotopic measurements by multi-collector inductively coupled plasma mass spectrometry: Earth and Planetary Science Letters, v. 371-372, p. 82 - 91.

Chew, D. M., and Spikings, R. A., 2015, Geochronology and Thermochronology Using Apatite: Time and Temperature, Lower Crust to Surface: Elements, v. 11, no. 3, p. 189 - 194.

Coplen, T. B., 2007, Calibration of the calcite–water oxygen-isotope geothermometer at Devils Hole, Nevada, a natural laboratory: Geochemica et Cosmochimica Acta, v. 71, p. 3948 - 3957.

Crysdale, B. L., 1987, Fluid inclusion evidence for the origin, diagenesis and thermal history of sparry calcite cement in the Capitan Limestone, McKittrick Canyon, West Texas [Master of Science Master of Science]: University of Colorado, 78 p.

de Laeter, J. R., Böhlke, J. K., Bièvre, P. D., Hidaka, H., Peiser, H. S., Rosman, K. J. R., and Taylor, P. D. P., 2003, Atomic Weights of the Elements: Review 2000: Pure and Applied Chemistry, v. 75, no. 6, p. 683 - 800.

De Muynck, D., Huelga-Auarez, G., Van Heghe, L., Degryse, P., and Vanhaecke, F., 2009, Systematic evaluation of a strontium-specific extraction

chromatographic resin for obtaining a purified Sr fraction with quantitative recovery from complex and Ca-rich matrices: Journal of Analytical Atomic Spectrometry, v. 24, p. 1498 - 1510.

Decker, D. D., Polyak, V. J., and Asmerom, Y., 2012, U-Pb dates of scalenohedral calcite spar from the Guadalupe Mountains of west Texas and southeastern New Mexico, University of New Mexico Albuquerque.

Decker, D. D., Polyak, V. J., and Asmerom, Y., 2016, Depth and timing of calcite spar and 'spar cave' genesis: Implications for landscape evolution studies, GSA Special Publication 516 - Caves and Karst Across Time, Geological Society of America.

Decker, D. D., Polyak, V. J., Asmerom, Y., and Lachniet, M. S., 2017, U-Pb dating of cave spar: A new shallow crust landscape evolution tool: Tectonics, v. 36.

Decker, D. D., Polyak, V. J., Hill, C. A., and Asmerom, Y., 2011, Determining Landscape Evolution using Isotope Data from Pre-Pleistocene-aged Speleothems in the Guadalupe Mountains, New Mexico, Phase I: How Deep Does Cave Spar Form?, *in* Kolstad, R., ed., National Speleological Society Convention 2011: Glenwood Springs, CO, National Speleological Society.

Denniston, R. F., Asmerom, Y., Polyak, V. J., McNiel, D. F., Klaus, J. S., Cole, P., and Budd, A. F., 2008, Caribbean chronostratigraphy refined with U-Pb dating of a Miocene coral: Geology, v. 36, no. 2, p. 151 - 154.

DePaolo, D. J., 2011, Surface kinetic model for isotopic and trace element fractionation during precipitation of calcite from aqueous solutions: Geochemica et Cosmochimica Acta, v. 75, p. 1039 - 1056.

Dietzel, M., Tang, J., Leis, A., and Kohler, S. J., 2009, Oxygen isotopic fractionation during inorganic calcite precipitation - Effects of temperature, precipitation rate and pH: Chemical Geology, v. 268, p. 107 - 115.

Domingo, C., García-Carmona, J., Loste, E., Fanovich, A., Fraile, J., and Gómez-Morales, J., 2004, Control of calcium carbonate morphology by precipitation in compressed and supercritical carbon dioxide media: Journal of Crystal Growth, v. 271, no. 1, p. 268-273.

Donelick, R. A., O'Sullivan, P. B., and Ketcham, R. A., 2005, Apatite-Fission Track Analysis, Reviews in Mineralology and Geochemistry, Volume 58, p. 49 - 94.

Dublyansky, Y. V., 2000, Dissolution of Carbonates by Geothermal Waters, *in* Klimchouk, A. B., Ford, D. C., Palmer, A. N., and Dreybrodt, W., eds., Speleogenesis - Evolution of Karst Aquifers: Huntsville, AL, National Speleological Society, p. 158 - 159.

-, 2014, Hypogene Speleogenesis - Discussion of Definitions, *in* Klimchouk, A. B., Sasowsky, I. D., Mylroie, J., Engel, S. A., and Engel, A. S., eds., Hypogene Cave Morphologies: San Salvadore, Bahamas, Karst Waters Institute.

DuChene, H., R., 2009, The Relationship of Oil Field-Derived Hydrogen Sulfide in the Permian (Guadalupian) Artesia Group to Sulfuric Acid Speleogenesis in the Guadalupe Mountains, New Mexico and Texas, USA, Advances in Hypogene Karst Studies, National Cave and Karst Reasearch Institute, p. 111 - 120.

DuChene, H., R., and Cunningham, K. L., 2006, Tectonic Influences on Speleogenesis in the Guadalupe Mountains, New Mexico and Texas, New Mexico Geological Society Guidebook, 57th Field Conference, Caves and Karst of Southeastern New Mexico: Soccorro, NM, New Mexico Geological Society, p. 211 - 218.

DuChene, H., R., and Martinez, R., 2000, Post-Speleogenetic Erosion and its Effect on Caves in the Guadalupe Mountains, New Mexico and West Texas: Journal of Cave and Karst Studies, v. 62, no. 2, p. 75 - 79.

Dumitru, T. A., 2000, Fission-Track Geochronology, *in* Noller, J. S., Sowers, J. M., and Lettis, W. R., eds., Quaternary Geochronology - Methods and Applications, Volume 4: Washington D.C., American Geophysical Union, p. 582.

Eaton, G. P., 1986, Tectonic redefinition of the Southern Rocky Mountains: Tectonophysics, v. 132, p. 163 - 193.

-, 2008, Epeirogeny in the Southern Rocky Mountains region: Evidence and origin: Geosphere, v. 4, no. 5, p. 764.

Ehlers, T. A., and Farley, K. A., 2003, Apatite (U-Th)/He thermochronometry: methods and applications to problems in tectonics and surface processes: Earth and Planetary Science Letters, v. 206, no. 1 - 2, p. 1 - 14.

El Desouky, H., Soete, J., Claes, H., and Ozkul, M., 2015, Novel applications of fluid inclusions and isotope geochemistry in unravelling the genesis of fossil travertine systems: Sedimentology, v. 62, p. 27 - 56.

Ely, J. F., Haynes, W. M., and Bain, B. C., 1989, Isochoric (p, Vm, T) measurements on CO2 and on (0.982CO2+0.018N2) from 250 to 330 K at pressures to 35 MPa: Journal of Chemical Thermodynamics, v. 21, p. 879 - 894.

Farley, K. A., 2002, (U-Th)/He dating: Techniques, Calibrations, and Applications, Reviews in Mineralogy and Geochemistry: Noble Gases, Volume 47, Mineralogical Society of America, p. 819 - 844.

Farley, K. A., and Flowers, R. M., 2012, (U–Th)/Ne and multidomain (U–Th)/He systematics of a hydrothermal hematite from eastern Grand Canyon: Earth and Planetary Science Letters, v. 359–360, p. 131-140.

Farley, K. A., and Stockli, D. F., 2002, (U-Th)/He dating of phosphates: apatite, monazite, and xenotime, Reviews in Mineralogy and Geochemistry: Phosphates, Volume 48, Mineralogical Society of America, p. 559 - 577.

Faure, G., and Powell, J. L., 1972, Strontium Isotope Geology, New York, Springer-Verlag, Minerals, Rocks and Inorganic Materials, Monograph Series of Theoretical and Experimental Studies, 189 p.:

Fietzke, J., and Eisenhauer, A., 2006a, Determination of temperature-dependent stable strontium isotope (88Sr/86Sr) fractionation bia bracketing standard MC-ECP-MS: Geochemistry Geophysics Geosystems, v. 7, no. 8, p. 6.

-, 2006b, Determination of temperature-dependent stable strontium isotope (88Sr/86Sr) fractionation via bracketing standard MC-ICP-MS: Geochemistry, Geophysics, Geosystems, v. 7, no. 8, p. 6.

Finney, B., and Jacobs, M., 2010, Carbon dioxide pressure-temperature phase diagram, Volume 2015, p. Carbon Dioxide pressure-temperature phase diagram.

Flawn, P. T., 1955, Summary of Southeast New Mexico Basement Rocks: New Mexico Geological Society Fifth Field Conference Guidebook, p. 114-117.

Flawn, P. T., 1956, Basement Rocks of Texas and Southeast New Mexico, University of Texas, Austin, Texas Bureau of Economic Geology, 261 p.:

Flowers, R. M., and Farley, K. A., 2012, Apatite 4He/3He and (U-Th)/He Evidence for an Ancient Grand Canyon: Science, v. 338, no. 6114, p. 1616-1619.

-, 2013, Response to Comments on "Apatite 4He/3He and (U-Th)/He Evidence for an Ancient Grand Canyon": Science, v. 340, p. 143.

Fossen, H., 2010, Structural Geology, Cambridge, England, Cambridge University Press, 463 p.:

Garber, R. A., Grover, G. A., and Harris, P. M., 1989, Geology of the Capitan Shelf Margin - subsurface data from the northern Delaware Basin, *in* Harris, P. M., and Grover, G. A., eds., Subsurface and outcrop examination of the Capitan shelf margin, northern Delaware Basin, Volume 13: San Antonio, TX, Society of Economic Paleontology and Mineralogy, p. 3 - 269.

Gary, M. O., Sharp, J. M., and Havens, R. S., 2002, Identifying the Connection Between Volcanic Activity and Hypogenic Karst in a Hydrothermal Phreatic Cave System: Geo2, v. 29, no. 3-4, p. 1 - 14.

Gilmer, A. K., Kyle, J. R., Connelly, J. N., Mathur, R. D., and Henry, C. D., 2003, Extension of Laramide magmatism in southwestern North America into Trans-Pecos Texas: Geology, v. 31, no. 5, p. 447 - 450.

Goff, F., Dunbar, N. W., Kelley, S. A., Peters, L., McIntosh, W. C., Heizler, L. L., and Goff, C. J., ABSTRACT: Three Rivers Stock and Palisades Tuff: Correlating Intrusive Source with Ignimbrite Sheet in the Tectonically Disrupted Sierra Blanca Igneous Complex, New Mexico, *in* Proceedings 2011 GSA Annual Meeting, Minneapolis, MN, 2011, Geological Society of America.

Goff, F., Shevenell, L., and Gardner, J. N., 1988, The Hydrothermal Outflow Plume of Valles Caldera, New Mexico, and a Comparison with other Outflow Plumes: Journal of Geophysical Research, v. 93, no. B6, p. 6041 - 6058.

Green, P. F., Crowhurst, P. V., Duddy, I. R., Japsan, P., and Holford, S. P., 2006, Conflicting (U-Th)-He and fission track ages in apatite - Enhanced retention, not anomolous annealing behavior: Earth and Planetary Science Letters, v. 250, p. 407 - 427.

Gregory, K. M., and Chase, C. G., 1992, Tectonic significance of paleobotanically estimated climate and altitude of the late Eocene erosion surface, Colorado: Geology, v. 20, p. 581-585.

Gries, J. C., 1979, Problems of Delineation of the Rio Grande Rift into the Chihuahua Tectonic Belt of Northern Mexico, *in* Riecker, R. E., ed., Rio Grande Rift: Tectonics and Magmatism: Washington D.C., American Geophysical Union, p. 107 - 113.

Gussone, N., Eisenhauer, A., Heuser, A., Dietzel, M., Bock, B., Böhm, F., Spero, H. J., Lea, D. W., Bijma, J., and Nägler, T. F., 2003, Model for kinetic effects on calcium isotope fractionation (δ44Ca) in inorganic aragonite and cultured planktonic foraminifera: Geochimica et Cosmochimica Acta, v. 67, no. 7, p. 1375-1382.

Halicz, L., Segal, I., Fruchter, N., Stein, M., and Lazar, B., 2008, Strontium stable isotopes fractionate in the soil environments: Earth and Planetary Science Letters, v. 272, no. 1, p. 406-411.

Harris, P. M., and Grover, G. A., 1989, Subsurface and Outcrop Examination of the Capitan Shelf Margin, Northern Delaware Basin, San Antonio, TX, Society of Economic Paleontologists and Mineralogists, 481 p.:

Hay, W. W., 1984, The breakup of Pangaea, climatic, erosional and sedimentological effects, *in* Proceedings Geology of Ocean Basins, Moscow, Russia, 1984, Volume 6: Utrecht, the Netherlands, VNU Science Press, p. 15 - 38.

Hayes, P. T., 1964, Geology of the Guadalupe Mountains, New Mexico, U.S. Government Printing Office, Washington D.C., U.S. Department of the Interior, Geological Survey Professional Paper 446, 69 p.:

Hayes, P. T., and Adams, J. E., 1962, Permian of the Central Guadalupe Mountains, Eddy County, New Mexico, Carlsbad, NM, West Texas, Roswell and Hobbs Geological Societies, 116 p.:

Hendricks, B. W. H., and Redfield, T. F., 2005, Apatite fission track and (U-Th)/He data from Fennoscandia: An example of underestimation of fission track annealing in apatite: Earth and Planetary Science Letters, v. 236, p. 443 - 458.

-, 2006, Reply to: Comment on “Apatite Fission Track and (U–Th)/He data from Fennoscandia: An example of underestimation of fission track annealing in apatite” by B. W. H. Hendriks and T. F. Redfield: Earth and Planetary Science Letters, v. 248, no. 1 - 2, p. 569 - 577.

Henry, C. D., and Price, J. G., 1986, Early Basub and Range Development in Trans-Pecos Texas and Adjacent Chihuahua: Magmatism and Orientation, Timing, and Style of Extension: Journal of Geophysical Research, v. 91, no. B6, p. 6213 - 6224.

Henry, C. D., Price, J. G., and James, E. W., 1991, Mid-Cenozoic Stress Evolution and Magmatism in the Southern Cordillera, Texas and Mexico: Transition from Continental Arc to Intraplate Extension: Journal of Geophysical Research, v. 96, no. B8, p. 13,545 - 513,560.

Herzog, L. F., Pinson, W. H., and Cormier, R. F., 1958, Sediment Age Determination by Rb/Sr Analysis of Glauconite: AAPG Bulletin, v. 42, no. 4, p. 717 - 733.

Hill, C. A., 1987, Geology of Carlsbad Cavern and other caves in the Guadalupe Mountains, New Mexico and Texas, Socorro, NM, New Mexico Bureau of Mines and Mineral Resources, 150 p.:

-, 1990, Sulfuric Acid Speleogenesis of Carlsbad Cavern and Its Relationship to Hydrocarbons, Delaware Basin, New Mexico and Texas: AAPG Bulletin, v. 74, no. 11, p. 1685-1694.

Hill, C. A., 1993, Sulfide/barite/fluorite mineral deposits, Guadalupe Mountains, New Mexico and west Texas: New Mexico Geology, no. August, p. 56 - 71.

-, 1996, Geology of the Delaware Basin, Guadalupe, Apache and Glass Mountains, New Mexico and West Texas, Albuquerque, NM, Permian Basin Seciton - SEPM, 480 p.:

Hill, C. A., 2000, Overview of the geologic history of cave development in the Guadalupe Mountains: Journal of Cave and Karst Studies, v. 62, no. 2, p. 60 - 71.

Hills, J. M., 1984, Sedimentation, Tectonism, and Hydrocarbon Generation in Delaware Basin, West Texas and Southeastern New Mexico: The American Association of Petroleum Geologists Bulletin, v. 68, no. 3, p. 250-267.
Hiss, W. L., 1976, Structure of the Permian Guadalupian Capitan Aquifer, Southeast New Mexico and West Texas: USGS.
Horak, R. L., 1985, Tectonic and Hydrocarbon Maturation History in the Permian Basin: Oil and Gas Journal, v. 83, no. 21, p. 124 - 129.
Huff, G. F., 2004, An Overview of the Hydrology of Saline Groundwater in New Mexico, Water Desalinization and Reuse Strategies for New Mexico, New Mexico Water Resources Research Institute.
Ingebritsen, S., Sanford, W., and Neuzil, C., 2006, Groundwater in Geologic Processes, New York, NY, Cambridge University Press.
Jagnow, D. H., 1977, Geologic factors influencing speleogenesis in the Capitan Reef complex, New Mexico and Texas [MSc: University of New Mexico, 197 p.
Karlstrom, K. E., Coblentz, D., Dueker, K., Ouimet, W., Kirby, E., Van Wijk, J., Schmandt, B., Kelley, S., Lazear, G., Crossey, L. J., Crow, R. S., Aslan, A., Darling, A., Aster, R., MacCarthy, J., Hansen, S. M., Stachnik, J., Stockli, D. F., Garcia, R. V., Hoffman, M., McKeon, R., Feldman, J., Heizler, M., Donahue, M. S., and CREST, 2012, Mantle-driven dynamic uplift of the Rocky Mountains and Colorado Plateau and its surface response: Toward a unified hypothesis: Lithosphere, v. 4, no. 1, p. 3 - 22.
Karlstrom, K. E., Lee, J. P., Kelley, S., Crow, R. S., Young, R. A., Lucchitta, I., Beard, L. S., Dorsey, R., Ricketts, J. W., Dickinson, W. R., and Crossey, L. J., 2013, Comment on "Apatite 4He/3He and (U-Th)/He Evidence for an Ancient Grand Canyon": Science, v. 340, p. 143.
Karlstrom, K. E., Lee, J. P., Kelley, S. A., Crow, R. S., Crossey, L. J., Young, R. A., Lazear, G., Beard, L. S., Ricketts, J. W., Fox, M., and Shuster, D. L., 2014, Formation of the Grand Canyon 5 to 6 million years ago through integration of older palaeocanyons: Nature Geosci, v. 7, no. 3, p. 239-244.
Kelley, S., Koning, D. J., Goff, F., Cikoski, C., Peters, L., and McIntosh, W. C., 2014, Stratigraphy of the northwestern Sierra Blanca volcanic field, *in* Rawling, G., McLemore, V. T., Timmons, S., and Dunbar, N. W., eds., Geology of the Sacramento Mountains Region, Volume 65: Socorro, NM, New Mexico Geological Society.
Kelley, V. C., 1971, Geology of the Pecos country, southeastern New Mexico: New Mexico Bureau of Mines and Mineral Resources, v. 24, p. 78.
Kharaka, Y., Cole, D., Hovorka, S., Gunter, W., Knauss, K., and Freifeld, B., 2006, Gas-water-rock interactions in Frio Formation following CO2

injection: Implications for the storage of greenhouse gases in sedimentary basins: Geology, v. 34, no. 7, p. 577-580.
King, P. B., 1948, Geology of the Southern Guadalupe Mountains, Texas: United States Department of the Interior, 215.
Kirkland, D. W., 2014, Role of Hydrogen Sulfide in the Formation of Cave and Karst Phenomena in the Guadalupe Mountains and Western Delaware Basin, New Mexico and Texas, Carlsbad, NM, National Cave and Karst Research Institute, NCKRI Special Paper, 77 p.:
Klimchouk, A. B., 2007, Hypogene Speleogenesis: Hydrogeological and Morphogenetic Perspective. Special Paper No. 1, Carlsbad, NM, National Cave and Karst Research Institute, 106 p.:
-, 2009, Morphogenesis of Hypogenic Caves: Geomorphology, v. 106, p. 100 - 117.
Klimchouk, A. B., Ford, D. C., Palmer, A. N., and Dreybrodt, W., 2000, Speleogenesis: Evolution of Karst Aquifers, Huntsville, AL, National Speleological Society, 527 p.:
Kolesar, P. T., and Riggs, A. C., 2004, Influence of Depositional Environment on Devil's Hole Calcite Morphology and Petrology, *in* Sasowsky, I. D., and Mylroie, J., eds., Studies of Cave Sediments: Physical and Chemical Records of Paleoclimates: New York, NY, Springer Science + Business Media, p. 227 - 242.
Lachniet, M., 2009, Climatic and environmental controls on speleothem oxygen isotope values: Quaternary Science Reviews, v. 28, no. 5 - 6, p. 412 - 432.
Larson, S. A., Cederbom, C., E., Tullborg, E.-L., and Stiberg, J.-P., 2006, "Comment on Apatite fission track and (U-Th)/He data fro Fennoscandia: An example of underestimation of fission track annealing in apatite" by Hendricks and Redfield: Earth and Planetary Science Letters, v. 248, p. 561 - 568.
Lauritzen, S.-E., and Lundberg, J. L., 2000, Solutional and Erosional Morphology, *in* Klimchouk, A. B., Ford, D. C., Palmer, A. N., and Dreybrodt, W., eds., Speleogenesis - Evolution of Karst Aquifers: Huntsville, AL, National Speleological Society, p. 408 - 426.
Lawton, T. F., and McMillan, N. J., 1999, Arc abandonment as a cause for passive continental rifting: Comparison of the Jurassic Mexican Borderland rift and the Cenozoic Rio Grande rift: Geology, v. 27, no. 9, p. 779 - 782.
Lipman, P. W., Mehnert, H. H., and Naeser, C. W., 1986, Evolution of the Latir Volcanic Field, Northern New Mexico, and Its Relation to the Rio Grande Rift, as Indicated by Potassium-Argon and Fission Track Dating: Journal of Geophysical Research, v. 91, no. B6, p. 6329 - 6345.

Lowenstern, J. B., 2001, Carbon dioxide in magmas and implications for hydrothermal systems: Mineralium Deposita, v. 36, no. 6, p. 490-502.
Loyd, S. J., Dickson, J. A. D., Scholle, P. A., and Tripati, A. K., 2013, Extensive Uplift-related and Non-fault-controlled Spar Precipitation in the Permian Capitan Formation: Sedimentary Geology, v. 298, p. 17 - 27.
Ludwig, K. R., 1993, PBDAT: A computer program for processing Pb-U-Th isotope data, U.S. Geological Survey, US Geological Survey Open-File Report 88-542, 30 p.:
-, 2000, Users Manual for Isoplot/Ex Version 2.2: A geochronological toolkit for Microsoft Excel, Berkely, CA, Berkely Geochronolgy Center, 47 p.:
Lundberg, J. L., Ford, D. C., and Hill, C. A., 2000, Preliminary U-Pb Date on Cave Spar, Big Canyon, Guadalupe Mountains, New Mexico, USA: Journal of Cave and Karst Studies, v. 62, no. 2, p. 144 - 148.
Ma, J., Wei, G., Liu, Y., Ren, Z., Xu, Y., and Yang, Y., 2013, Precise measurement of stable (δ 88/86Sr) and radiogenic (87Sr/86Sr) strontium isotope ratios in geological standard reference materials using MC-ICP-MS: Chinese Science Bulletin, p. 1-8.
Malinin, S., 1979, Physical chemistry of hydrothermal systems with carbon dioxide, Nauka, Moscow.
Maynard, S. R., 1995, Gold mineralization associated with mid-Tertiary magmatism and tectonism, Ortiz Mountains, Santa Fe County, New Mexico, *in* Bauer, P. W., Kues, B. S., Dunbar, N. W., Karlstrom, K. E., and Harrison, B., eds., Geology of the Santa Fe Region, Volume 46, New Mexico Geolological Society, p. 161 - 166.
McIntosh, W. C., Chapin, C. E., Ratte, J. C., and Sutter, J. F., 1992, Time-stratigraphic framework for the Eocene-Oligocene Mogollon-Datil volcanic field, southwest New Mexico: Geological Society of America Bulletin, v. 104, no. July, p. 851 - 871.
McKnight, C. L., 1986, Descriptive Geomorphology of the Guadalupe Mountains, South-Central New Mexico and West Texas: Baylor University.
McLemore, V. T., McIntosh, W. C., and Pease, T. C., 1995, 40Ar/39Ar age determinations of four plutons associated with mineral deposits in southwestern New Mexico: New Mexico Tech.
Meyer, R., F., 1966, Geology of the Pennsylvanian and Wolfcampian Rocks in Southeast New Mexico, Socorro, NM, New Mexico Bureau of Mines and Mineral Resources.
Mruk, D. H., 1985, Cementation and Dolomitization of the Capitan Limestone (Permian), McKittrick Canyon, West Texas [Master of Science: University of Colorado, Boulder, CO, 155 p.

-, 1989, Dianenesis of the Capitan Limestone, Upper Permian, McKittrick Canyon, West Texas, Subsurface and Outcrop Examination of the Capitan Shelf Margin, Northern Delaware Basin, Volume 13: San Antonio, TX, SEPM, p. 387 - 473.

Nehrke, G., Reichart, G. J., Van Cappellen, P., Meile, C., and Bijma, J., 2007, Dependence of calcite growth rate and Sr partitioning on solution stoichiometry: Non-Kossel crystal growth: Geochemica et Cosmochimica Acta, v. 71, p. 2240 - 2249.

NOAA, N. O. a. A. A., 2014, Cavern City Air Terminal Average Temperature Record 1942 - 2014, Volume 2014.

Ohno, T., and Hirata, T., 2007, Simultaneous Determination of Mass-dependent Isotopic Fractionation and Radiogenic Isotope Variation of Strontium in Geochemical Samples by Multiple Collector-ICP-Mass Spectrometry: Analytical Sciences, v. 23, p. 1275 - 1280.

Palmer, A. N., 2007a, Cave Geology, Dayton, OH, Cave Books, 454 p.:

-, 2007b, Caves and Time, *in* Watson, R. A., ed., Cave Geology: Dayton Ohio, Cave Book, p. 347 - 363.

-, 2011, Distinction Between Epogenic and Hypogenic Maze Caves: Geomorphology, v. 134, p. 9 - 22.

Palmer, A. N., and Palmer, M. V., 2000, Hydrochemical Interpretations of Cave Patterns in the Guadalupe Mountains, New Mexico: Journal of Cave and Karst Studies, v. 62, no. 2, p. 91 - 108.

-, 2012, Petrographic and isotopic evidence for late-stage processes in sulfuric acid caves of the Guadalupe Mountains, New Mexico, USA: International Journal of Speleology, v. 41, no. 2, p. 22-34.

Pokrovksy, O. S., Golubev, S. V., Schott, J., and Castillo, A., 2009, Calcite, dolomite and magnesite dissolution kinetics in aqueous solutions at acid to circumnuetral pH, 25 to 150 C and 1 to 55 atm pCO2: New constraints on CO2 sequestration in sedimentary basins: Chemical Geology, v. 265, p. 20 - 32.

Polyak, V. J., Guven, Necip, 2000, Clays in Caves of the Guadalupe Mountains, New Mexico: Journal of Cave and Karst Studies, v. 62, no. 2, p. 120-126.

Polyak, V. J., Hill, C. A., and Asmerom, Y., 2008, Age and Evolution of the Grand Canyon Revealed by U-Pb Dating of Water Table-Type Speleothems: Science, v. 319, p. 1377 - 1380.

Polyak, V. J., Hill, C. A., and Decker, D. D., 2017, A conceptual model for Grand Canyon hypogene speleogenesis, *in* Klimchouk, A. B., Palmer, A. N., De Waele, J., Auler, A., and P., A., eds., Hypogene karst regions and caves of the world, Springer, p. 555-564.

Polyak, V. J., McIntosh, W. C., Guven, N., and Provencio, P., 1998, Age and Origin of Carlsbad Cavern and Related Caves from 40Ar/39Ar of Alunite: Science, v. 279, no. 5358, p. 1919-1922.

Polyak, V. J., and Provencio, P., 2001, By-Product Materials Related to H2S-H2SO4 Influenced Speleogenesis of Carlsbad, Lechuguilla, and other Caves of the Guadalupe Mountains, New Mexico: Journal of Cave and Karst Studies, v. 63, no. 1, p. 23-32.

Rasmussen, J., 2006, Late Holocene Climate Variability in the Southwestern United Sates from High-Resolution Speleothem Data [PhD Dissertation]: University of New Mexico, 99 p.

Reilinger, R. E., Brown, L. D., and Oliver, J. E., 1979, Recent Vertical Crustal Movements from Leveling Observations in the Vicinity of the Rio Grande Rift, *in* Riecker, R. E., ed., Rio Grande Rift: Tectonics and Magmatism: Washington D.C., American Geophysical Union, p. 223 - 236.

Reiners, P. W., Ehlers, T. A., and Zeitler, P. K., 2005, Past, Present & Future of Thermochronology, *in* Reiners, P. W., and Ehlers, T. A., eds., Low-Temperature Thermochronology: Techniques, Interpretations, and Applications, Volume 58: Chantilly, VA, Mineralogical Society of America, p. 622.

Renne, P. R., 2000, K-Ar and 40Ar/39Ar Dating, *in* Noller, J. S., Sowers, J. M., and Lettis, W. R., eds., Quaternary Geochronology - Methods and Applications, Volume 4: Washington D.C., American Geophysical Union, p. 582.

Reynolds, T. J., 1994, Fluid Inc. Adapted U.S.G.S. Gas-Flow Heating/Freezing System Instruction Manual, Denver, CO, Fluid Inc., 33 p.:

Ricketts, J. W., Kelley, S. A., Karlstrom, K. E., Schmandt, B., Donahue, M. S., and van Wijk, J., 2016, Synchrounous opeing of the Rio Grande rift along its entire length at 25 - 10 Ma supported by apatite (U-Th)/He and fission-track thermochronology, and evaluation of possible driving mechanisms: GSA Bulletin, v. 128, no. 3/4, p. 397-424.

Roberts, N. M. W., and Walker, R. J., 2016, U-Pb geochronology of calcite-mineralized faults: Absolute timing of rift-related fault events o the northeast Atlantic margin: Geology, v. 44, no. 7, p. 531 - 534.

Roedder, E., 1983a, Fluid Inclusions, Washington D.C., Mineralogical Society of America, Reviews in Mineralogy, 646 p.:

-, 1983b, The Origin of Inclusions, *in* Roedder, E., ed., Fluid Inclusions, Volume 12: Reston, VA, Mineralogical Society of America, p. 11 - 46.

Romanek, C. S., Brossman, E. L., and Morse, J. W., 1992, Carbon isotopic fractionation in synthetic aragonite and calcite: Effects of temperature and precipitation rate: Geochemica et Cosmochimica Acta, v. 56, p. 419 - 430.

Rüggeberg, A., Fietzke, J., Liebetrau, V., Eisenhauer, A., Dullo, W.-C., and Freiwald, A., 2008, Stable strontium isotopes (δ88/86Sr) in cold-water corals — A new proxy for reconstruction of intermediate ocean water temperatures: Earth and Planetary Science Letters, v. 269, no. 3–4, p. 570-575.

Ruppel, S. C., Jones, R. H., Breton, C. L., and Kane, J. A., 2005, Preparation of maps depicting geothermal gradients and Precambrian structure in the Permian Basin: Bureau of Economic Geology, Jackson School of Geosciences, University of Texas, Austin.

Savin, S. M., 1977, The History of the Earth's Surface Temperatures During the Past 100 Million Years: Annual Reviews, Earth and Planetary Science Letters, v. 5, p. 319 - 355.

Scher, H. D., Griffith, E. N., and Buckly, W. P., 2014, Accuracy and precision of 88Sr/86Sr and 87Sr/86Sr measurements by MC-ICPMS compromised by high barium concentrations: Geochemstry, Geophysics, Geosystems, v. 15, no. 2, p. 499-508.

Schmidt, M. W., Vautravers, M. J., and Spero, H. J., 2006, Western Caribbean sea surface temperatures during the late Quaternary: Geochemistry Geophysics Geosystems, v. 7, no. 2, p. 1 - 17.

Schoene, B., Crowley, J. L., Condon, D. J., Schmitz, M. D., and Bowring, S. A., 2006, Reassessing the uranium decay constants for geochronology using ID-TIMS U-Pb data: Geochemica et Cosmochimica Acta, v. 70, p. 426 - 445.

Scholle, P. A., Ulmer, D. S., and Melim, L. A., 1992, Late-stage calcites in the Permian Capitan Formation and its equivalents, Delaware Basin margin, west Texas and New Mexico: evidence for replacements of precursor evaporites: Sedimentology, v. 39, p. 207 - 234.

Seager, W. R., and Morgan, P., 1978, Rio Grande rift in southern New Mexico, west Texas, and northern Chihuahua: American Geophysical Union Special Publication - Rio Grand Rift: Tectonics and Magmatism, v. 14, p. 87 - 106.

Shalev, N., Lazar, B., Halicz, L., Stein, M., Gavrieli, I., Sandler, A., and Segal, I., 2013, Strontium Isotope Fractionation in Soils and Pedogenic Processes: Procedia Earth and Planetary Science, v. 7, no. 0, p. 790-793.

Sharp, Z., 2007a, Biogenic Carbonates: Oxygen, *in* Burns, P., ed., Principles of Stable Isotope Geochemistry: Upper Saddle River, NJ, Prentice-Hall, p. 120 - 148.

-, 2007b, Principles of Stable Isotope Geochemistry, New Jersey, Pearson Prentice Hall, 344 p.:

Simmons, S. F., and Brown, K. L., 2006, Gold in Magmatic Hydrothermal Solutions and the Rapid Formation of a Giant Ore Deposit: Science, v. 314, no. 5797, p. 288 - 291.

Sims, K. W. W., Gill, J. B., Dosseto, A., Hoffmann, D. L., Lundstrom, C. C., Williams, R. W., Ball, L., Tollstrup, D., Turner, S., Prytulak, J., Glessner, J. J. G., Standish, J. J., and Elliot, T., 2008, An Inter-Laboratory Assessment of the Thorium Isotopic Composition of Synthetic and Rock Reference Materials: Geostandards and Geoanalytical Research, v. 32, no. 1, p. 65 - 91.

Stevenson, E. I., Hermoso, M., Rickaby, R. E. M., Tyler, J. J., Minoletti, F., Parkinson, I. J., Mokadem, F., and Burton, K. W., In Publication, Controls on Stable strontium isotope fractionation in coccolithophores with implications for the marine Sr cycle: Geochimica et Cosmochimica Acta.

Tang, J., Kohler, S. J., and Dietzel, M., 2008, Sr2+/Ca2+ and 44Ca/40Ca fractionation during inorganic calcite formation: I. Sr incorporation: Geochemica et Cosmochimica Acta, v. 72, p. 3718 - 3732.

Todd, V., Silberman, M., and Armstrong, A., Geochemistry, petrology, and K-Ar ages of igneous rocks in the central Peloncillo Mountains, Hidalgo County, New Mexico: New Mexico Geol, *in* Proceedings Soc. Guidebook, 26th Field conf1975, p. 343-344.

Turin, H. J., and Plummer, M. A., 2000, Lechuguilla Cave Pool Chemistry, 1986-1999: Journal of Cave and Karst Studies, v. 62, no. 2, p. 135 - 143.

Wasserburg, G. J., Wetherill, G. W., Silver, L. T., and Flawn, P. T., 1962, A Study of the Ages of the Precambrian of Texas: Journal of Geophysical Research, v. 67, no. 10, p. 4021 - 4047.

Watson, E. B., and Muller, T., 2009, Non-equilibrium isotopic and elemental fractionation during diffusion-controlled crystal growth under static and dynamic conditions: Chemical Geology, v. 267, p. 111 - 124.

White, W. B., 1988, Geomorphology and Hydrology of Karst Terrains, New York, NY, Oxford University Press, 464 p.:

Whitmeyer, S. J., and Karlstrom, K. E., 2007, Tectonic Model for the Proterozoic Growth of North America: Geosphere, v. 3, p. 220 - 259.

Wilks, M., and Chapin, C. E., 1997, New Mexico Geochronology Database, *in* Resources, N. M. B. o. G. a. M., ed.: Socorro, NM.

Zeebe, R. E., 1999, An explanation of the effect of seawaer carbonate concentration on foraminiferal oxygen isotopes: Geochemica et Cosmochimica Acta, v. 63, no. 13/14, p. 2001 - 2007.

Zeebe, R. E., Bijma, J., Honisch, B., Sanyal, A., Spero, H. J., and Wolf-Gladrow, D. A., 2006, Vital Effects and Beyond: A Modeling Perspective on Developing Paleoceanographic Proxy Relationships in Foraminifera, *in*

Austin, J. R., Clarke, W. E. N., and Rickaby, R. E. M., eds., Biogeochemical Controls on Palaeoceanographic Proxies, The Geological Society of London.

Zimmerman, J. B., 1962, Permian of the Central Guadalupe Mountains, Eddy County, New Mexico, West Texas, Roswell and Hobbs Geological Societies, 115 p.: